(2)

Growth and Characterization of Self-Assembled InGaAs/GaAs Quantum Dots and Their Application to Lasers

June, 2000

Kohki Mukai

CONTENTS

Chapter 1

Introduction

Artificial fabrication of semiconductor nanostructures has been inciting novel interest in physics and providing a valuable application. Its beginning was a proposal about superlattice and quantum wells in 1970 [1], which broke new ground in the concept of nanostructure creation and attracted a great deal of attention because of its potential in designing the band structure of semiconductors. Development of thin-film growth techniques using molecular beam epitaxy (MBE) and metalorganic vapor phase epitaxy (MOVPE) has enabled growth of nanometer-thick semiconductor layers, and electrical and optical properties of carriers in two-dimensional systems have been experimentally investigated [2, 3]. With two-dimensional nanostructures, new electronic and optical devices have been invented, such as the high-electron mobility transistor (HEMT) [4] and quantum well lasers [5, 6]. By the mid-1990s, the main properties of quantum wells and superlattices were rather well understood, and the interest of researchers shifted toward structures that are further reduced dimensionally -- quantum wires and quantum dots.

Reducing the remaining two-dimensional extension of quantum wells to the nanoscale leads to carrier localization in all three dimensions and a breakdown of the classical band structure model of a continuous dispersion of energy as a function of momentum. The resulting energy level structure is discrete, like in an atom. Quantum dots enable laboratory studies of textbook quantum structures at the extreme limit of the zero dimension, and also, the unusual behavior seen there appears to be translatable into novel device concepts [7, 8]. Thus, this field is exciting to quantum theorists, spectroscopic experimentalists, and electronic and optoelectronic device researchers alike.

One of the most attractive concepts for a quantum dot device is quantum dot lasers [9, 10]. The predicted advantages of these lasers are ultra-low electric power consumption, stability against temperature variations, and high-speed and high-efficiency operation. In the

ideal quantum dot laser (i.e., a dot ensemble has an identical state density and infinite barriers for carrier confinement), all injected carriers contribute to swift lasing and the threshold current is insensitive to temperature. The very narrow material gain spectrum of quantum dots causes a high differential gain, and the maximum gain is expected to be more than one order higher than that for higher-dimensional systems. These distinct effects of low dimensionality on lasing properties have motivated extensive experimental and further theoretical research on quantum dots.

Since the 1980s, considerable effort has been devoted to the realization of semiconductor microstructures that provide carrier confinement in all three directions and behave as electronic quantum dots. The first realization of quantum dots were nano-sized semiconductor inclusions (e.g., CdSe) in glass [11], which have been commercially available as color filters for decades and were used to investigate physics in the zero dimension. The size of these molecules can be controlled during growth, and their shape is nearly spherical. Colloidal techniques have been perfected mostly for ionic II-VI systems (CdS, CdSe) and more recently for III-V semiconductors (InP, GaP, InAs) [12 - 14]. An electrically isolating matrix, however, prohibits electric injection and use in electronic and optoelectronic devices. To eliminate the problem, many alternative semiconductor nanofabrication approaches have been developed based on thin-layer epitaxial techniques, such as selective intermixing of quantum wells, the use of stressors, controlled coarsening during epitaxial growth, and fluctuations of quantum well thickness [15 - 17].

By the end of the 1980s, the fabrication of quantum dots by patterning quantum wells was the most common method in the field. Patterning attracts much attention because the lateral shape, size and arrangement of dots can be controlled within the resolution of the particular lithographic technique used and a variety of processing techniques, like dry and wet etching, that are continuously improving at a researcher's disposal. The lithographic techniques comprise optical lithography and holography, X-ray lithography, electron and focused ion beam lithography, and scanning tunneling microscopy [18 - 21]. The techniques, however, still continue to suffer from low uniformity in dot size, poor interface quality, and low numerical density. High uniformity is required to achieve an identical state density in a dot ensemble. High quantum efficiency and high density are required to obtain a large optical gain. Quantum dot lasers using artificial nanofabrication techniques, therefore, have difficulty achieving room-temperature operation [22].

A breakthrough occurred at the beginning of the 1990s. Through the employment of a self-assembling mechanism during epitaxy of lattice-mismatched materials, high-density quantum dots were created, and they exhibited excellent optical properties, particularly high quantum efficiency, up to room temperature. The mechanism is also called *self-organization* or *self-formation*. Both thermodynamic and kinetic ordering together create unique three-dimensional patterns of islands within a matrix for many different material system. The most popular self-assembling process is the Stranski-Krastanov (SK) mode, which produces growth islands accompanied by a thin wetting layer to release the strain energy accumulated by a large lattice mismatch. The SK growth technique has been successfully applied to Si [23], SiGe [24], InAs [25, 26], InGaAs [27 - 30], InP [31], GaSb [32], InSb [33], CdSe [34], and GaN [35].

The impact is that self-assembled quantum dots is one ultimate production of lattice-mismatched heteroepitaxy. Lattice-mismatched III-V semiconductor heterosystems are indispensable in present and future semiconductor device technology. Strained InGaAsP/InP quantum wells are now used as active layers in semiconductor lasers for fiber-optic telecommunication system. GaN structures used for light emitting diodes (LEDs) and visible lasers in the blue spectrum region are grown on sapphire or SiC substrates under highly mismatched conditions. Therefore, self-assembled semiconductor nanocrystals are compatible with present optoelectronic device technology.

The purpose of this thesis is to (1) present a unique growth technique of self-assembled quantum dots emitting at 1.3 μm, (2) describe basic optical characterization of carriers in the zero dimensional structure, and (3) demonstrate a successful application of quantum dots in semiconductor lasers. At the beginning of work on this thesis, self-assembled quantum dot structures had not yet been discovered. Up to now, lasing performances of devices with self-assembled quantum dots have been advancing close to that of quantum well lasers. The author has contributed to several significant progresses in this field. During a study on the effect of lattice mismatches on InGaAsP nanostructures, the author developed a unique growth method to obtain self-assembled InGaAs/GaAs dots. The emission wavelength of the dots covers the application wavelength of 1.3 and 1.5 μm, which cannot be obtained by ordinary InGaAs/GaAs SK dots. The uniformity of the developed dots is higher than that of SK dots. Discrete higher-ordered sublevels were first observed by optical diagnostics in highly uniform self-assembled dots. The author experimentally investigated the phonon

bottleneck effect, which is the slowdown of carrier relaxation rates among discrete sublevels in quantum dots due to a lack of phonons to satisfy the energy conservation rule. With a new model to describe the carrier relaxation process among dot sublevels, carrier relaxation rates were analyzed quantitatively. The author enabled operation of a quantum dot laser with a mili-ampere-order threshold current, and achieved the first 1.3-μm continuous wave (CW) quantum dot lasing at room temperature.

This thesis is organized as follows:

Chapter 2 describes the effect of lattice mismatches on nano-scale InGaAsP semiconductor structures. First, the author discusses how a lattice mismatch induced by interdiffusion affects the interface of InGaAsP/InP quantum wells. Then, the structural stability of strained InGaAs/InP quantum wells is investigated: dynamics of stress relaxation during growth are analyzed as functions of time, temperature, and magnitude of lattice distortions. Finally, the discovery of self-assembled InGaAs/GaAs quantum dots during a trial to grow highly lattice-mismatched quantum wells is briefly described. One of the most striking properties of the dots is their 1.3-μm emission.

Chapter 3 is focused on the growth of the 1.3-μm-emission dots described in Chapter 2. The dots were grown using an alternate supply of source materials in MOVPE, and named *ALS dots*. A basic characterization of ALS dots is presented here. In particular, how the dots vary with an alternate supply cycle, growth temperature, and composition of buffer layers on which the dots are grown is illustrated. Finally, the author describes the finding that the temperature sensitivity of interband emission energy was suppressed significantly by an InGaAs overgrowth on the self-assembled dots.

Chapter 4 deals with optical characterization of self-assembled quantum dots. Here, the first observation of discrete energy levels in self-assembled dots is presented using macro- and micro-photoluminescence measurements. Advantages of ALS dots compared with those of SK dots are discussed in addition to long-wavelength emissions and high uniformity. The controllability of quantum confinement in ALS dots is demonstrated using magnet-optical diagnostic techniques, and ALS dots are shown to have high radiative efficiency.

In Chapter 5, carrier dynamics in self-assembled quantum dots are demonstrated. The author here proposes a model to describe the process of carrier relaxation in quantum dot system having multiple sublevels. ALS dots have a high crystal quality, featuring narrow spectrum broadening and high quantum efficiency, that enables pursuit of the so-called

phonon bottleneck problem. Electroluminescence and time-resolved photoluminescence data are analyzed to provide a quantitative discussion. Experiments on annealed samples are also explained to demonstrate the effect of retarded carrier relaxation in ALS dots on emission spectra.

In Chapter 6, the high performance of quantum dot lasers fabricated with self-assembled dots is described. Mili-ampere-order threshold current operation of quantum dot lasers with the CW condition was attained at room temperature by improving the uniformity, density, and emission efficiency of quantum dots. A key point was the transfer of the growth technique of ALS dots to SK-dot growth by MBE. The first 1.3-μm CW lasing of quantum dots at room temperature is also described. Details on the laser performance are discussed to show the future prospects of quantum dot lasers.

Finally, the conclusions of the work are presented in Chapter 7.

References

[1] L. Esaki and R. Tsu, IBM J. Res. Develop. 14, 61 (1970).

[2] L. L. Chang, L. Esaki, and R. Tsu, Appl. Phys. Lett. 24, 593 (1974).

[3] R. Dingle, Festkörperprobleme 15, 21 (1975).

[4] T. Mimura, S. Hiyamizu, T. Fujii, and K. Nanbu, Jpn. J. Appl. Phys. 19, L225 (1980).

[5] J. P. van der Ziel, R. Dingle, R. C. Miller, W. Wiegmann, and A. Nordland Jr.. Appl. Phys. Lett. 26, 463 (1975).

[6] W. T. Tsang, Appl. Phys. Lett. 39, 786 (1981).

[7] L. Brus, IEEE J. Quantum Electron 22, 1909 (1986).

[8] D. S. Chemla and D. A. B. Miller, Opt. Lett. 11, 522 (1986).

[9] Y. Arakawa and H. Sakaki, Appl. Phys. Lett. 40, 939 (1982).

[10] M. Asada, Y. Miyamoto and Y. Suematsu, IEEE J. Quantum Electron. QE-22, 1915 (1986).

[11] M. P. Rocksby, J. Soc. Glass Technol. 16, 171 (1932).

[12] M. A. Olshavsky, A. N. Goldstein, and A. P. Alivisatos, J. Am. Chem. Soc. 112, 9438 (1990).

[13] A. A. Guzelian, J. E. B. Katari, A. V. Kadavanich, U. Banin, K. Hamad, E. Juban, A. P. Alivisatos, R. H. Wolters, C. C. Arnold, and J. R. Heath, J. Phys. Chem. 100, 7212 (1996).

[14] A. A. Guzelian, U. Banin, A. V. Kadavanich, X. Peng, and A. P. Alivisatos, Appl. Phys. Lett. 69, 1432 (1996).

[15] J. Ralston, A. L. Moretti, R. K. Jain, and F. A. Chambers, Appl. Phys. Lett. 50, 1817 (1987).

[16] H. Lipsanen, M. Sopanen, and J. Ahopelto, Phys. Rev. B 51, 13868 (1995).

[17] J. Christen, and D. Bimberg, Phys. Rev. B 42, 7213 (1990).

[18] A. Forchel, H. Leier, B. E. Maile, and R. Germann, Festkörperprobleme (Advances in Solid State Physics) 28, 99 (1988).

[19] S. P. Beaumount, in *Low-Dimensional Structures in Semiconductors* (Plenum Press, New York, 1991) p. 109.

[20] K. Kash, A. Scherer, J. M. Worlock, H. G. Craighead and M. C. Tamargo, Appl. Phys. Lett. 49, 1043 (1986).

[21] T. Fukui, S. Ando, Y. Tokura and T. Toriyama, Appl. Phys. Lett. 58, 2018 (1991).

[22] H. Hirayama, K. Matsunaga, M. Asada, and Y. Suematsu, Electron. Lett. 30, 142 (1994).

[23] H. Takagi, H. Ogawa, Y. Yamazaki, A. Ishizaki, and T. Nakagiri, Appl, Phys. Lett. 56, 2379 (1990).

[24] R. Apetz, L. Vescan, A. Hartmann, C. Dieker, and H. Lüth, Appl. Phys. Lett. 66, 445 (1995).

[25] M. Tabuchi, S. Noda and A. Sasaki, in *Science and Technology of Mesoscopic Structures*, edited by S. Namba, C. Hamaguchi and T. Ando (Springer, Tokyo, 1992) p. 379.

[26] J. M. Moison, F. Houzay, F. Barthe, L. Lepeince, E. Andre, and O. Vatel, Appl. Phys. Lett. 64, 196 (1994).

[27] D. Leonard, M. Kishnamurthy, C. M. Reaves, S. P. Denbaars, and P. M. Petroff, Appl. Phys. Lett. 63, 3203 (1993).

[28] R. Nötzel, J. Temmyo, H. Kamada, T. Furuta, and T. Tamamura, Appl. Phys. Lett. 65, 457 (1994).

[29] J. Oshinowo, M. Nishioka, S. Ishida, and Y. Arakawa, Appl. Phys. Lett. 65, 1421 (1994).

[30] K. Mukai, N. Ohtsuka, M. Sugawara, and S. Yamazaki, Jpn. J. Appl. Phys., 33, L1710 (1994).

[31] A. Moritz, R. Wirth, A. Hangleiter, A. Kurtenbach, and K. Eberl, Appl. Phys. Lett. 69, 212 (1996).

[32] F. Hatami, N. N. Ledentsov, M. Grundmann, J. Böhrer, F. Heinrichsdorff, M. Beer, D. Bimberg, S. S. Ruvimov, P. Werner, U. Gösele, J. Heydenreich, S. V. Ivanov, B. Ya. Meltser, P. S. Kop'ev, and Zh. I. Alferov, Appl. Phys. Lett. 67, 656 (1995).

[33] E. R. Glaser, B. R. Benett, B. V. Shanabrook, and R. Magno, Appl. Phys. Lett. 68, 3614 (1996).

[34] H. C. Ko, D. C. Park, Y. Kawakami, S. Fujita, and S. Fujita, Appl. Phys. Lett. 70, 3278 (1997).

[35] S. Tanaka, S. Iwai, and Y. Aoyagi, Appl. Phys. Lett., 69, 4096 (1996).

Chapter 2

Effect of lattice mismatch on InGaAsP nanostructures

2-1 Introduction

Lattice mismatch to substrates greatly affects the crystallographic characteristics of nano-scale semiconductor structures. The subject of this chapter is the effect on three types of nanostructures: lattice-matched InGaAsP/InP quantum wells (2-2), strained InGaAs/InP quantum wells (2-3), and self-assembled InGaAs/GaAs quantum dots (2-4).

Even in the lattice-matched quantum wells, lattice mismatch is introduced during interdiffusion. The author found that the composition at the quantum-well interface is discontinuous even after interdiffusion when strain energy is introduced. The author proposes a novel formula to describe the interdiffusion profile of quantum wells, and analyze the interdiffusion process in $In_xGa_{1-x}As_yP_{1-y}$ and $Al_xGa_{1-x}As$ quantum wells. The mechanism of interdiffusion is also discussed.

In strained epitaxial layers, a dislocation glides when the strain is over the elastic limit. The dislocation multiplication dynamics are functions of the time, temperature, and magnitude of a lattice mismatch. The author investigated the glide process in $In_xGa_{1-x}As/InP$ quantum wells based on an empirical model. Dislocation multiplication was found to start when the layer thickness is much thinner than the commonly believed critical thickness, and the stress relaxation process in the growth of strained quantum wells is calculated with experimentally obtained parameters.

A self-assembly of three-dimensional structure occurs on the growth surface if a lattice mismatch is much larger than the crystal elastic limit of a monolayer structure. In 1994, the author discovered a way to grow 1.3-μm-emission self-assembled quantum dots during a trial to grow 1.3-μm-emitting highly-strained $In_{0.5}Ga_{0.5}As/GaAs$ quantum wells,

using the atomic layer epitaxy (ALE) technique. The discovery is briefly described in this chapter, and details of the growth are presented in Chapter 3.

2-2 Interdiffusion in lattice-mismatched InGaAsP/InP quantum wells

The interdiffusion process in nanostructures of III-V compound semiconductors cannot be directly measured due to the small size, although interdiffusion is a significant phenomenon in electronic and optoelectronic device applications. The profiles of quantum wells after interdiffusion are not necessarily the same as those measured directly in wide heterostructures. Since quantum well layers are thin, interdiffusion penetrates alternate barrier layers, which complicates interdiffusion profiles. In addition, interdiffusion causes lattice strain in III-V compound semiconductors, and the lattice strain, in turn, affects the interdiffusion process. Lattice strain in heterostructure layers wider than the critical thickness generates dislocations and defects.

The interdiffusion in GaAs/AlGaAs quantum wells has been extensively examined because of its importance in practical applications and the simplicity of the analysis. Group-III atoms are the only possible interdiffusion species, and no lattice distortion occurs due to the interdiffusion. The interdiffusion in GaAs/AlGaAs quantum wells is known to begin above 800°C, and GaAs/AlGaAs quantum wells are thermally stabler than InGaAs/InP quantum wells. The effect of implanting active impurities [1-7] and lattice defects [8-11] on interdiffusion has been examined using transmission electron microscopy and by measuring quantum energy shifts. The interdiffused compositional profiles of these materials were first reported by Chang and Koma [12] for 150-nm-wide GaAs/AlAs double heterostructures measured by Auger electron spectroscopy (Fig. 2-1). The profiles were error-functional and symmetrical. The calculations include two assumptions: 1) the interdiffusion coefficient is constant in both the GaAs and AlAs layers, and 2) the interface is smooth. Considering that the strain in interdiffused AlGaAs layers is negligible, several other researchers used Chang's profiles to explain how quantum energy shifts in GaAs/AlGaAs quantum wells relate to interdiffusion [11,13,14]. These researchers did not, however, directly examine or further confirm the interdiffusion profiles of the quantum wells.

After GaAs/AlGaAs quantum wells, the next most studied structure is InGaAsP/InP

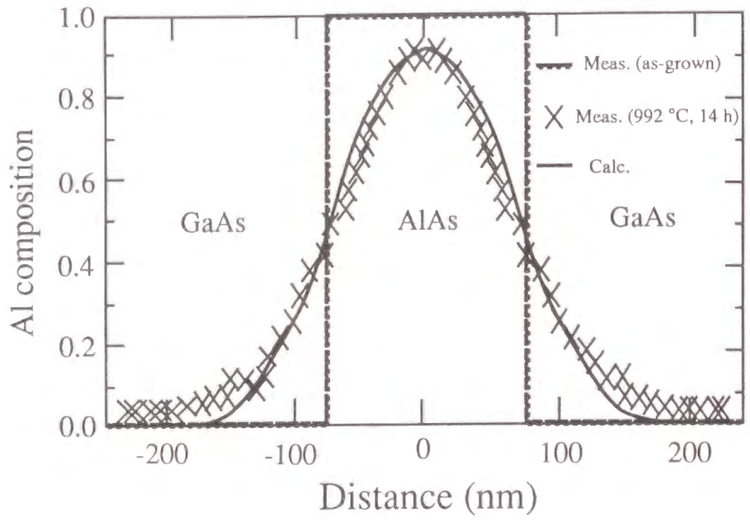

Figure 2-1 Interdiffusion profile in GaAs/AlAs systems measured by Chang and Koma using Auger electron spectroscopy [12]. Dashed lines indicate the initial Al composition, x's show the data after 14 hours of annealing, and solid lines indicates the Al composition calculated using the simple error function.

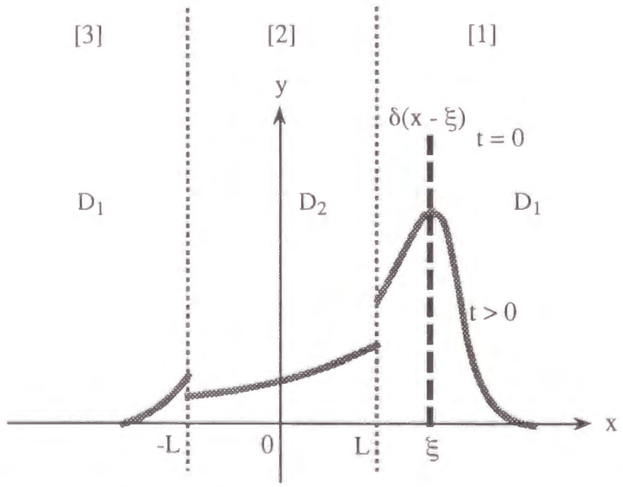

Figure 2-2 Schematic of our model. The author solved diffusion equations as a three-body system. Three conditions were imposed in solving the diffusion equations:

1) the interdiffusion coefficients differ depending on the structural region,
2) the composition of diffused species is discontinuous at the interface,
3) diffusion from one barrier layer penetrates to the next barrier layer.

quantum wells, which are the main components of 1-μm-region optoelectronic devices. This system has two possible interdiffusion species, group-III atoms and group-V atoms. The interdiffusion of group-III atoms and that of group-V atoms must be considered separately since the atoms do not mix because of their polarities. Group-V atoms reportedly interdiffuse more easily than group-III atoms [15]. Arsenic and phosphorus atoms begin to interdiffuse at about 500°C [16]. The effect of impurities and defects on interdiffusion properties has been examined [17-23], but the interdiffusion profile in InGaAsP/InP quantum wells is not yet well understood. The interdiffusion profile cannot be estimated by direct observation of wide heterostructures since the lattice constant of InGaAsP materials depends on the composition, and the induced lattice strain affects the interdiffusion process. Some researchers have pointed out the difference between the interdiffusion profiles of $In_{0.53}Ga_{0.47}As$/InP quantum wells and those of GaAs/AlGaAs systems using indirect methods. Nakashima et al. [15] used X-ray analysis and the Fleming model [24] to show that arsenic composition in an $In_{0.53}Ga_{0.47}As$ well layer decreases uniformly and that interdiffused arsenic atoms accumulate near the interface on the InP barrier layer side. Fujii et al. [16] reported that a large compositional discontinuity of group-V atoms must be at the interface, even after interdiffusion, by roughly estimating the dependence of quantum energy shifts on well-layer width.

The purpose of this section is to present the interdiffusion process in III-V compound quantum wells and quantum dots. The author first shows a formula that comprehensively describes interdiffusion profiles in quantum wells, and then evaluates the interdiffusion process of group-V atoms in lattice-matched InGaAsP/InP and that of group-III atoms in GaAs/AlGaAs quantum wells using that formula [25, 26]. The formula was derived by analytically solving diffusion equations for a stacked three-layer system, taking into account the different interdiffusion coefficients between layers and the compositional discontinuity of diffused species at interfaces. The author relates the formula to the dependence of quantum energy shifts on annealing time and annealing temperature for various well layer widths. The dependence of quantum energy shifts is shown to be very different between InGaAsP/InP and GaAs/AlGaAs quantum wells, and the formula explains the difference. Then, the author demonstrates how to enhance the thermal stability of InGaAs/InP quantum wells and discusses the interdiffusion mechanism, examining the growth-condition dependence of interdiffusion coefficients using the formula [27].

2-2-1. Model of interdiffusion profile

Linear diffusion equations are solved for a stacked three-layer structure. In the mathematical model, outside layers extend infinitely in the -x and +x directions (Fig. 2-2). The origin of the x axis is defined as the center of the middle layer. Two boundaries are at x = -L and x = L. First, linear diffusion equations are solved assuming a momentary plane source at x = ξ. The solution is then integrated using an initial composition profile to fit the actual structure. In the actual structure, diffusion species in the two outside layers can mix via the middle layer, which is equivalent to a single quantum well. To derive a solution, the author makes two generalizing assumptions [28]. First, the diffusion coefficients of the outside layers are assumed to be the same but different from that of the middle layer. Second, the author assumes a certain distribution ratio for diffused species at the interface [29], so the composition of diffused species can be discontinuous there. Two more assumptions are made to eliminate difficulties in solving the diffusion equations: 1) both the interdiffusion coefficient in each layer and the distribution ratio at the interface are constant during interdiffusion, 2) the Smigelskas-Kirkendall effect, where unbalanced interdiffusion velocity causes the interface to move, is ignored. Practical results are shown to be consistent with these assumptions. In addition, if the thicknesses of layers are less than 3 nm, a gradient correction term should be considered [30]. In this work, the correction term is disregarded.

The formula is derived as shown below. The three linear diffusion equations are

$$\frac{\partial C_1(x,t)}{\partial t} = D_1 \frac{\partial^2 C_1(x,t)}{\partial x^2} \qquad t \geq 0,\ x \geq L, \tag{2. 1}$$

$$\frac{\partial C_2(x,t)}{\partial t} = D_2 \frac{\partial^2 C_2(x,t)}{\partial x^2} \qquad t \geq 0,\ |x| < L, \tag{2. 2}$$

and

$$\frac{\partial C_3(x,t)}{\partial t} = D_1 \frac{\partial^2 C_3(x,t)}{\partial x^2} \qquad t \geq 0,\ x \leq -L\,. \tag{2. 3}$$

The boundary conditions are

$$C_1(x,t) = kC_2(x,t) \qquad \text{for } x \to L, \tag{2. 4}$$

$$C_3(x,t) = kC_2(x,t) \qquad \text{for } x \to -L, \tag{2. 5}$$

$$D_1 \frac{\partial C_1(x,t)}{\partial x} = D_2 \frac{\partial C_2(x,t)}{\partial x} \qquad \text{for } x \to L, \tag{2. 6}$$

$$D_1 \frac{\partial C_3(x,t)}{\partial x} = D_2 \frac{\partial C_2(x,t)}{\partial x} \qquad \text{for } x \to -L, \tag{2. 7}$$

and the initial conditions are

$$C_1(x, t) = \delta(x - \xi), \quad C_2(x, t) = C_3(x, t) = 0 \qquad \text{for } t \to 0. \tag{2. 8}$$

Here, C_i (i = 1, 3) is the concentration of diffusion species in the outside layers, and C_2 is the concentration in the middle layer. D_i (i = 1, 2) is the diffusion coefficient in the outside layers and the middle layer, respectively. The interfacial distribution ratio of concentration is $k = C_i/C_2$ (i = 1, 3). Equations (2. 4) and (2. 5) model the discontinuous concentration at interfaces, and Eqs. (2. 6) and (2. 7) express flux continuity. $\delta(x - \xi)$ is a delta function.

These diffusion equations are solved to obtain Eqs. (2. 24), (2. 25), and (2. 26). Details of the solution are as follows. The author rearranges Eqs. (2. 4) to (2. 7) to obtain the conventional solution. C_2 can be expressed by a Maclaurin expression using the value at x = L:

$$C_2(x',t) = C_2(x',t)\big|_0 + x' \frac{\partial C_2(x',t)}{\partial x'}\Big|_0 + \frac{x'^2}{2!} \frac{\partial^2 C_2(x',t)}{\partial x'^2}\Big|_0 + \cdots = \sum_{n=0}^{\infty} \frac{x'^n}{n!} \frac{\partial^n C_2(x',t)}{\partial x'^n}\Big|_0, \tag{2. 9}$$

where x' = x - L. From Eqs. (2. 1) and (2. 2), the following equations are given:

$$\frac{\partial^n C_1(x',t)}{\partial t^n} = D_1^n \frac{\partial^{2n} C_1(x',t)}{\partial x'^{2n}}, \tag{2. 10}$$

$$\frac{\partial^n C_2(x',t)}{\partial t^n} = D_2^n \frac{\partial^{2n} C_2(x',t)}{\partial x'^{2n}}. \tag{2. 11}$$

The author differentiates Eqs. (2. 4) and (2. 6) by t, substitutes them into Eq. (2. 10) and gets

$$D_1^n \left.\frac{\partial^{2n} C_1(x',t)}{\partial x'^{2n}}\right|_0 = kD_2^n \left.\frac{\partial^{2n} C_2(x',t)}{\partial x'^{2n}}\right|_0 , \tag{2. 12}$$

$$D_1^{n+1} \left.\frac{\partial^{2n+1} C_1(x',t)}{\partial x'^{2n+1}}\right|_0 = kD_2^{n+1} \left.\frac{\partial^{2n+1} C_2(x',t)}{\partial x'^{2n+1}}\right|_0 . \tag{2. 13}$$

Equations (2. 10) to (2. 13) are substituted into Eq. (2. 9):

$$C_2(x',t) = \frac{1}{2}\left(\frac{1}{k} + a\right)\sum_{n=0}^{\infty} \frac{1}{n!}(ax')^n \left.\frac{\partial^n C_1(x',t)}{\partial x'^n}\right|_0 + \frac{1}{2}\left(\frac{1}{k} - a\right)\sum_{n=0}^{\infty} \frac{1}{n!}(-ax')^n \left.\frac{\partial^n C_1(x',t)}{\partial x'^n}\right|_0, \tag{2. 14}$$

where $a = \sqrt{D_1/D_2}$. Then, a new condition is given :

$$C_2(x - L,t) = \frac{1}{2}\left(\frac{1}{k} + a\right) C_1(a(x - L,t)) + \frac{1}{2}\left(\frac{1}{k} - a\right) C_1(-a(x - L,t)). \tag{2. 15}$$

Using the same solution as above obtains

$$C_1(x - L,t) = \frac{1}{2}\left(k + \frac{1}{a}\right) C_2\left(\frac{1}{a}(x - L,t)\right) + \frac{1}{2}\left(k - \frac{1}{a}\right) C_2\left(-\frac{1}{a}(x - L,t)\right). \tag{2. 16}$$

At x = -L, using the same process as for $C_1(x, t)$ and $C_2(x, t)$ above obtains

$$C_2(x + L,t) = \frac{1}{2}\left(\frac{1}{k} + a\right) C_3(a(x + L,t)) + \frac{1}{2}\left(\frac{1}{k} - a\right) C_3(-a(x + L,t)) \tag{2. 17}$$

and

$$C_3(x + L,t) = \frac{1}{2}\left(k + \frac{1}{a}\right) C_2\left(\frac{1}{a}(x + L,t)\right) + \frac{1}{2}\left(k - \frac{1}{a}\right) C_2\left(-\frac{1}{a}(x + L,t)\right). \tag{2. 18}$$

Note that Eqs. (2. 15) to (2. 18) are sufficient conditions for Eqs. (2. 4) to (2. 7).

The solution must satisfy diffusion equations (2. 1) to (2. 3), boundary conditions (2. 15) to (2. 18), and the initial condition (2. 8). If only two layers separated by the boundary at x = L are considered, the solutions are [28]

i) $x \geq L$

$$C_1(x,t) = \frac{1}{2\sqrt{\pi D_1 t}}\left\{\exp\left(-\frac{(x - \xi)^2}{4D_1 t}\right) - \frac{1 - ak}{1 + ak}\exp\left(-\frac{(x - 2L + \xi)^2}{4D_1 t}\right)\right\}, \tag{2. 19}$$

ii) $|x| < L$

$$C_2(x,t) = \frac{1}{2\sqrt{\pi D_1 t}}\frac{2a}{1 + ak}\exp\left(-\frac{\left(x - L + \frac{L}{a} - \frac{\xi}{a}\right)^2}{4D_2 t}\right). \tag{2. 20}$$

These are normalized. Considering the boundary at x = -L [Eqs. (2. 17), (2. 18)] and the initial condition [Eq. (2. 8)], Eq. (2. 20) must be transformed to

ii) $|x| < L$

$$C_2(x,t) = \frac{1}{2\sqrt{\pi D_1 t}}\left\{\frac{2a}{1 + ak}\exp\left(-\frac{\left(x - L + \frac{L}{a} - \frac{\xi}{a}\right)^2}{4D_2 t}\right) + \frac{2a(1 - ak)}{(1 + ak)^2}\exp\left(-\frac{\left(x + 3L - \frac{L}{a} + \frac{\xi}{a}\right)^2}{4D_2 t}\right)\right\}, \tag{2. 21}$$

and then

iii) $x \leq -L$

$$C_3(x,t) = \frac{1}{2\sqrt{\pi D_1 t}}\frac{4ak}{(1 + ak)^2}\exp\left(-\frac{(x + 2L - 2aL - \xi)^2}{4D_1 t}\right). \tag{2. 22}$$

Because of the added second term of Eq. (2. 21), Eq. (2. 19) must be transformed to

i) $x \geq L$

$$C_1(x,t) = \frac{1}{2\sqrt{\pi D_1 t}}\left\{\exp\left(-\frac{(x - \xi)^2}{4D_1 t}\right) - \frac{1 - ak}{1 + ak}\exp\left(-\frac{(x - 2L + \xi)^2}{4D_1 t}\right) + \frac{1 - ak}{1 + ak}\exp\left(-\frac{(x - 2L + 4aL + \xi)^2}{4D_1 t}\right) - \left(\frac{1 - ak}{1 + ak}\right)^2 \exp\left(-\frac{(x - 4aL - \xi)^2}{4D_1 t}\right)\right\}. \tag{2. 23}$$

Equation (2. 23) satisfies the diffusion equations and boundary conditions, but not the initial conditions. The last term of Eq. (2. 23) shows a diffusion source at x = 4aL + x, which contradicts the single source in Eq. (2. 8). To cancel this last term, the author introduces a negative source at x = 4aL + x, which has the same absolute value as the last term of Eq. (2. 23). This imaginary source requires additional terms in regions $x \geq L$, $|x| < L$, and $x \leq -L$ to satisfy the boundary conditions (2. 15) to (2. 18). However, this also produces a diffusion source in $x \geq L$. The author finally found solutions that satisfy all conditions are infinite

series.

i) $x \geq L$

$$C_1(x,t) = \frac{1}{2\sqrt{\pi D_1 t}}\left[\exp\left\{-\frac{(x-\xi)^2}{4D_1 t}\right\} - \frac{1-ak}{1+ak}\exp\left\{-\frac{(x-2L+\xi)^2}{4D_1 t}\right\} + \frac{4ak}{(1+ak)^2}\sum_{n=1}^{\infty}\left(\frac{1-ak}{1+ak}\right)^{2n-1}\exp\left\{-\frac{(x-2L+4aL+\xi)^2}{4D_1 t}\right\}\right] \quad (2.\ 24)$$

ii) $|x| < L$

$$C_2(x,t) = \frac{1}{2\sqrt{\pi D_1 t}}\frac{2a}{1+ak}\sum_{n=1}^{\infty}\left(\frac{1-ak}{1+ak}\right)^{2(n-1)}\left(\exp\left[-\frac{\left\{x+\frac{L}{a}-(4n-3)L-\frac{\xi}{a}\right\}^2}{4D_2 t}\right] + \frac{1-ak}{1+ak}\exp\left[-\frac{\left\{x-\frac{L}{a}-(4n-1)L+\frac{\xi}{a}\right\}^2}{4D_2 t}\right]\right) \quad (2.\ 25)$$

iii) $x \leq -L$

$$C_3(x,t) = \frac{1}{2\sqrt{\pi D_1 t}}\frac{4ak}{(1+ak)^2}\sum_{n=1}^{\infty}\left(\frac{1-ak}{1+ak}\right)^{2(n-1)}\exp\left[-\frac{\{x+2L-(4n-2)aL-\xi\}^2}{4D_1 t}\right] \quad (2.\ 26)$$

Next, Eqs. (2. 24) to (2. 26) are integrated using the initial composition profile. The initial conditions are

$$F(x,0) = F_0 \qquad |x| \geq L, \quad (2.\ 27)$$

$$F(x,0) = 0 \qquad |x| < L, \quad (2.\ 28)$$

and the calculated equations are

i) $x \geq L$

$$F(x,t) = F_0\left[\int_L^{\infty} C_1(x,t)\,d\xi + \int_{-\infty}^{-L} C_3(-x,t)\,d\xi\right], \quad (2.\ 29)$$

ii) $|x| < L$

$$F(x,t) = F_0\left[\int_L^{\infty} C_2(x,t)\,d\xi + \int_{-\infty}^{-L} C_2(-x,t)\,d\xi\right], \quad (2.\ 30)$$

iii) $x \leq -L$

$$F(x,t) = F_0\left[\int_L^{\infty} C_3(x,t)\,d\xi + \int_{-\infty}^{-L} C_1(-x,t)\,d\xi\right]. \quad (2.\ 31)$$

Then, the following formulae are derived:

i) $|x| \geq L$

$$F(x,t) = \frac{F_0}{2}\left(1 + \mathrm{erf}\left(\frac{|x|-L}{2\sqrt{D_1 t}}\right) - \frac{1-ak}{1+ak}\left\{1 - \mathrm{erf}\left(\frac{|x|-L}{2\sqrt{D_1 t}}\right)\right\} + \frac{4ak}{(1+ak)^2}\sum_{n=1}^{\infty}\left(\frac{1-ak}{1+ak}\right)^{2(n-1)}\left[1 - \mathrm{erf}\left(\frac{|x|-L+(4n-2)aL}{2\sqrt{D_1 t}}\right) + \frac{1-ak}{1+ak}\left\{1 - \mathrm{erf}\left(\frac{|x|-L+4naL}{2\sqrt{D_1 t}}\right)\right\}\right]\right), \quad (2.\ 32)$$

ii) $|x| < L$

$$F(x,t) = \frac{F_0 a}{1+ak}\sum_{n=1}^{\infty}\left(\frac{1-ak}{1+ak}\right)^{2(n-1)}\left[2 + \mathrm{erf}\left(\frac{x-(4n-3)L}{2\sqrt{D_2 t}}\right) - \mathrm{erf}\left(\frac{x+(4n-3)L}{2\sqrt{D_2 t}}\right) + \frac{1-ak}{1+ak}\left\{2 - \mathrm{erf}\left(\frac{x+(4n-1)L}{2\sqrt{D_2 t}}\right) + \mathrm{erf}\left(\frac{x-(4n-1)L}{2\sqrt{D_2 t}}\right)\right\}\right]. \quad (2.\ 33)$$

Equations (2. 32) and (2. 33) generally give the concentrations of diffused species; these equations describe the interdiffusion profile if F(x, t) is regarded as the composition of layers.

In a practical analysis of interdiffusion in quantum wells, three unknown material-specific parameters, D_1 (in the barrier layer), D_2 (in the well layer) and k, are determined in this formula.

2-2-2. Calculation of quantum energy shift

The three unknown parameters, interdiffusion coefficients, and the ratio of interfacial discontinuity are determined by fitting quantum energy shifts calculated with the formula to measured shifts. The author used a numerical method to calculate quantum energies because the effective mass equation [31] cannot be solved analytically in these cases.

The effective mass equation is

$$\left(-\frac{\hbar^2}{2m_i}\frac{\partial^2}{\partial x^2} + V_i(x) + S_i(x)\right)\varphi_i(x) = E_i\varphi_i(x), \qquad i = e, hh, lh, \quad (2.\ 34)$$

where $V_i(x)$ is the potential energy, $S_i(x)$ is the strain energy, E_i is the eigenenergy, and $\varphi_i(x)$ is the envelope wave function. Subscripts i = 'e', 'hh', and 'lh' mean 'electron', 'heavy hole', and 'light hole', respectively. The potential energy, $V_i(x)$, is calculated from the composition,

which is shown as a function of x in the formula. The strain energy, $S_i(x)$, is

$$S_c(x) = 2a_c \frac{C_{11}-C_{12}}{C_{11}} \varepsilon(x) \qquad (2.35)$$

and

$$S_v(x) = \{2a_v \frac{C_{11}-C_{12}}{C_{11}} \pm b \frac{C_{11}+2C_{12}}{C_{11}}\}\varepsilon(x) \quad , \qquad (2.36)$$

where a_c and a_v are hydrostatic deformation potentials, and b is the shear deformation potential [32-34]. C_{11} and C_{12} are elastic stiffness. $\varepsilon(x)$ is misfit strain. Upper and lower signs correspond to the light-hole band and heavy-hole band, respectively.

The author used the Runge-Kutta method suggested by Sakurai [35] to solve the effective mass equations. The author computed the envelope function numerically with the boundary conditions that both $\varphi_i(x)$ and $1/m_i \cdot \partial\varphi_i(x)/\partial x$ are continuous at the interface, and determined eigenenergies for both the conduction band and valence band. The author calculated total energy shifts as the sum of energy shifts in the two bands.

The following parameters were used to calculate the quantum energy levels in $In_xGa_{1-x}As_yP_{1-y}$/InP quantum wells: effective mass, $m_e = 0.041m_0$, $m_{hh} = 0.50m_0$, and $m_{lh} = 0.052m_0$ in an $In_{0.53}Ga_{0.47}As$ well layer, $m_e = 0.08m_0$ and $m_{hh} = 0.56m_0$ in an InP barrier layer, $m_e = 0.044m_0$ and $m_{hh} = 0.49m_0$ in an $In_{0.70}Ga_{0.30}As_{0.61}P_{0.39}$ barrier layer; elastic stiffness, $C_{11} = 1.016 \times 10^{11}$ dyn/cm^2 and $C_{12} = 0.509 \times 10^{11}$ dyn/cm^2 [36]; and the distribution ratio of conduction band offset, $\Delta E_c = 0.4 \bullet \Delta E_g$ [37]. The author used the hydrostatic deformation potentials, $a_c = a_v = -3.94$ eV, and the shear deformation potential, b = -1.75 eV [38]. The author assumed that the hydrostatic deformation potential was distributed evenly between the conduction and valence bands, and disregarded the compositional dependence of these three deformation potentials. Since the compositional dependence of the energy gap at 4.2 K has not been reported, to our knowledge, the compositional dependence at 295 K was used [39]:

$$E_g^{295K}(x,y) = 1.35 + 0.672x - 1.091y + 0.758\,x^2 + 0.101y^2 + 0.111xy - 0.580\,x^2y - 0.159xy^2 + 0.268x^2y^2 \quad . \qquad (2.37)$$

The author believes this is a good approximation when calculating shifts of quantum energies since band offset does not depend on temperature.

The following material parameters were used when calculating quantum energy levels

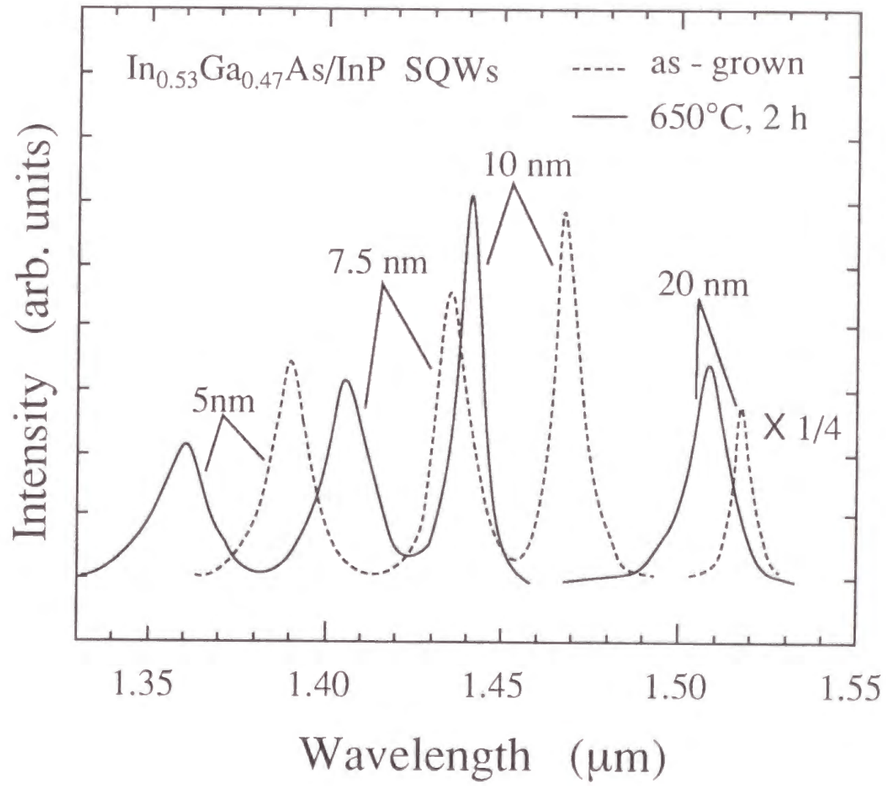

Figure 2-3 Photoluminescence spectra of as-grown and annealed samples of $In_{0.53}Ga_{0.47}As$/InP quantum wells 5, 7.5, 10, and 20 nm wide at 4.2 K. Annealing was performed at 650°C for 2 hours.

in GaAs/$Al_xGa_{1-x}As$ quantum wells: effective mass, $m_e = 0.067m_0$ and $m_{hh} = 0.42m_0$ in a GaAs well layer, $m_e = 0.088m_0$ and $m_{hh} = 0.53m_0$ in an $Al_{0.25}Ga_{0.75}As$ barrier layer; and the distribution ratio of conduction band offset, $\Delta E_c = 0.65 \bullet \Delta E_g$ [14]. Strain energy is negligible in this material. For the same reason as in an $In_xGa_{1-x}As_yP_{1-y}$ system, the compositional dependence of the energy gap of $Al_xGa_{1-x}As$ at 300 K was used [40],

$$E_g^{300K}(x) = 1.424 + 1.247x \quad (2.38)$$

and shifts of quantum energies were calculated.

2-2-3. Interdiffusion process in InGaAsP/InP quantum wells

Experimental samples were grown by metalorganic vapor-phase epitaxy (MOVPE). The samples were undoped $In_{0.53}Ga_{0.47}As/InP$ and $In_{0.53}Ga_{0.47}As/In_{0.70}Ga_{0.30}As_{0.61}P_{0.39}$ single quantum wells (SQWs) on (001)-InP substrates grown at 570°C. Each sample had a cap layer, quantum well layers, and a buffer layer on the substrate. Quantum well layers were composed of four well layers with different thicknesses to give enough data to find the three unknown material-specific parameters. The well layers of $In_{0.53}Ga_{0.47}As/InP$ SQWs were 20, 10, 7.5, and 5 nm in width, separated by 50-nm-wide barrier layers. The well layers of $In_{0.53}Ga_{0.47}As$ /$In_{0.70}Ga_{0.30}As_{0.61}P_{0.39}$ SQWs were 20, 15, 10, and 5 nm in width, separated by 30-nm-wide barrier layers. Cap and buffer layers were 200 nm wide in all samples. Width and composition were controlled via the growth conditions, which were checked by X-ray diffraction and transmission electron microscopy (TEM).

The author annealed samples in a reactor tube of a liquid-phase epitaxy system. During annealing, an InP plate was placed on $In_xGa_{1-x}As_yP_{1-y}$ samples, and pure H_2 gas was introduced. The author believes that the InP plate raises the phosphorous vapor pressure during annealing.

Photoluminescence spectra of these samples were measured at 4.2 K before and after annealing by immersing the samples in liquid helium. Luminescence was excited by the 647.1 nm line of a Kr^+ ion laser and detected by a PbS detector. Figure 2-3 is an example of the measured photoluminescence spectra of $In_{0.53}Ga_{0.47}As/InP$ SQWs. The four peaks correspond to four quantum wells of different widths, and all of them shifted to shorter

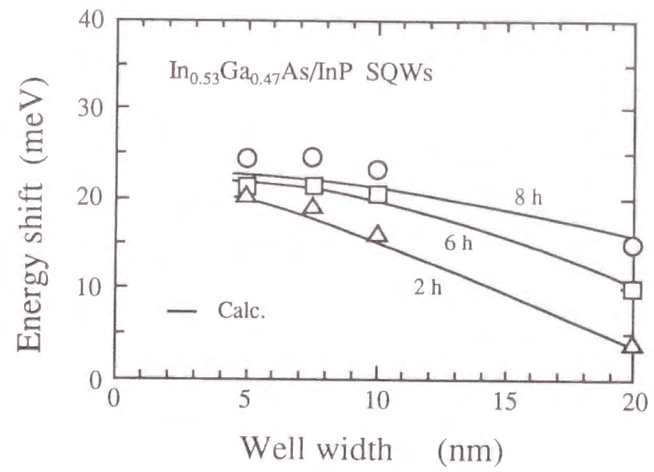

Figure 2-4 Quantum energy shifts as a function of well width: $In_{0.53}Ga_{0.47}As/InP$ quantum wells after annealing at 650°C for 2, 6, and 8 hours. Symbols show measured results and solid lines indicate calculated results.

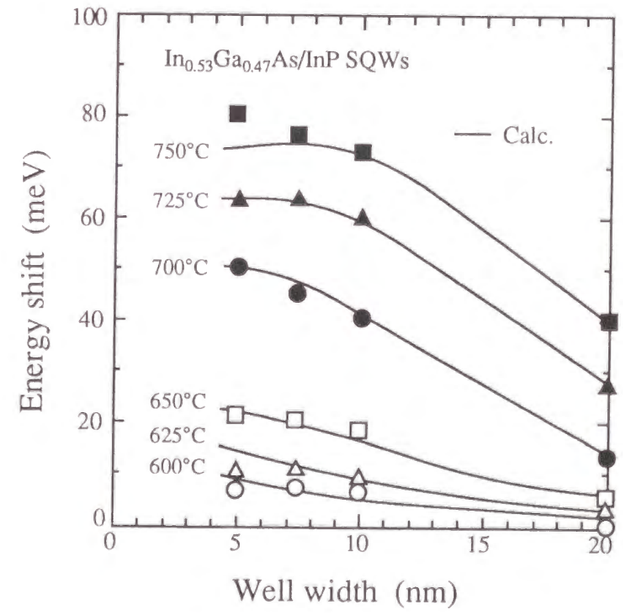

Figure 2-5 Quantum energy shifts as a function of well width: $In_{0.53}Ga_{0.47}As/InP$ quantum wells after annealing at between 600 and 750°C for 2 hours. Symbols show measured results and solid lines indicate calculated results.

wavelengths after annealing. These peak shifts are caused by changes of quantum energy levels, which are sensitive to compositional profiles.

The author compared the measured and calculated dependence of quantum energy shifts on well layer width for various annealing times in $In_{0.53}Ga_{0.47}As/InP$ (Fig. 2-4). Solid lines indicate shifts calculated using the formula. The measured shifts closely agree with those shifts. The energy shift increased gradually in 20-nm-wide well layers; and in narrower well layers, the shift increased rapidly for up to 2 hours and then became saturated. The formula explains each of these characteristics using a set of parameters, that is, interdiffusion coefficients in each layer and the interfacial distribution ratio. This result is consistent with the fundamental assumption that the three parameters can be regarded as constant during interdiffusion. Note that this assumption for the interdiffusion coefficient is equivalent to the assumption that the coefficient depends negligibly on the composition of group-V atoms. The result suggests that the assumption is valid, at least under these experimental conditions.

The author measured the dependence of quantum energy shifts on well layer width at several annealing temperatures for $In_{0.53}Ga_{0.47}As/InP$ quantum wells (Fig. 2-5) and $In_{0.53}Ga_{0.47}As/In_{0.70}Ga_{0.30}As_{0.61}P_{0.39}$ quantum wells (Fig. 2-6). The solid lines indicate the calculated shifts, which agree well with the measured shifts. Table 2-I lists calculated interdiffusion coefficients and distribution ratios for $In_xGa_{1-x}As_yP_{1-y}/InP$ quantum wells. Interdiffusion coefficients in $In_{0.53}Ga_{0.47}As$ layers were found to be common to quantum wells having different barrier layers. The distribution ratio, k, decreased as annealing temperature increased in $In_{0.53}Ga_{0.47}As/InP$ quantum wells.

Arrhenius plots of interdiffusion coefficients are shown in Fig. 2-7. The solid lines are for an Arrhenius expression with a single activation energy. The author found that activation energy was 0.5 eV in an $In_{0.53}Ga_{0.47}As$ layer, 2.0 eV in an $In_{0.70}Ga_{0.30}As_{0.61}P_{0.39}$ layer, and 8.4 eV in an InP layer. The activation energy in InP was larger than the energy of self-diffusion of phosphorus atoms in InP, which has been measured to be 5.65 eV [41]. One possible reason for this discrepancy is lattice distortion, which adds excess energy to the activation energy. The activation energies in $In_{0.53}Ga_{0.47}As$ and $In_{0.70}Ga_{0.30}As_{0.61}P_{0.39}$ layers cannot be compared with other values due to the lack of reported data.

The author concluded the following concerning the characteristics of the interdiffusion of group-V atoms in $In_xGa_{1-x}As_yP_{1-y}$ materials.

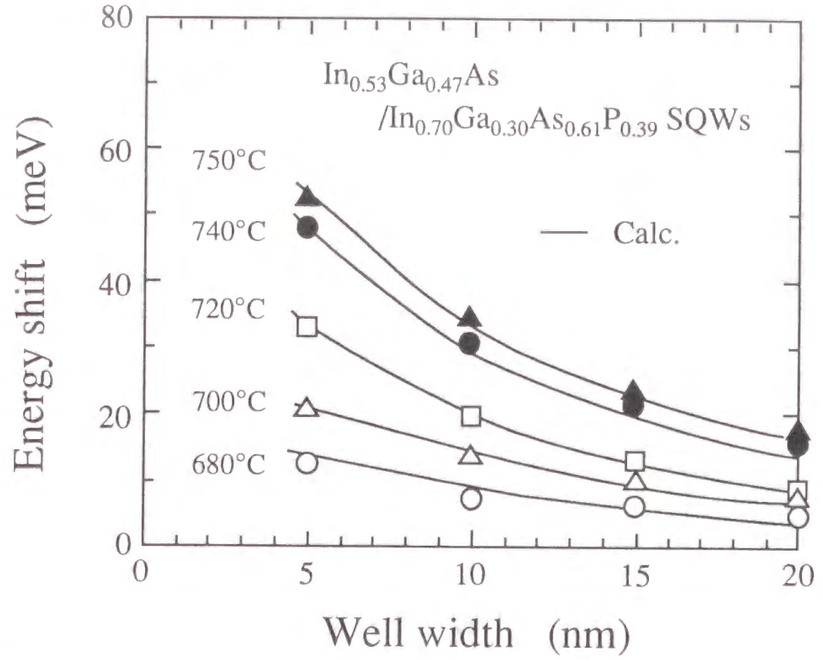

Figure 2-6 Quantum energy shifts as a function of well width : $In_{0.53}Ga_{0.47}As$ $/In_{0.70}Ga_{0.30}As_{0.61}P_{0.39}$ quantum wells after annealing at between 680 and 750°C for 2 hours. Symbols show measured results and solid lines indicate calculated results.

Table 2-I Interdiffusion coefficients and distribution ratios of $In_{0.53}Ga_{0.47}As/InP$ and $In_{0.53}Ga_{0.47}As/In_{0.70}Ga_{0.30}As_{0.61}P_{0.39}$ quantum wells.

	$In_{0.53}Ga_{0.47}As/InP$			$In_{0.53}Ga_{0.47}As/In_{0.70}Ga_{0.30}As_{0.61}P_{0.39}$		
T (°C)	D_{InGaAs} (cm^2/s)	D_{InP} (cm^2/s)	k	D_{InGaAs} (cm^2/s)	$D_{InGaAsP}$ (cm^2/s)	k
600	1.7 E-17	4.3 E-21	40			
625	2.0 E-17	2.0 E-20	35			
650	2.1 E-17	2.1 E-19	30	2.6 E-17	5.1 E-20	2
700	2.8 E-17	5.6 E-17	17	2.8 E-17	1.4 E-19	2
720				3.5 E-17	2.3 E-19	1
725	3.8 E-17	3.8 E-15	13			
740				3,5 E-17	4.3 E-19	1
750	4.7 E-17	4.7 E-14	11	3.9 E-17	5.5 E-19	1

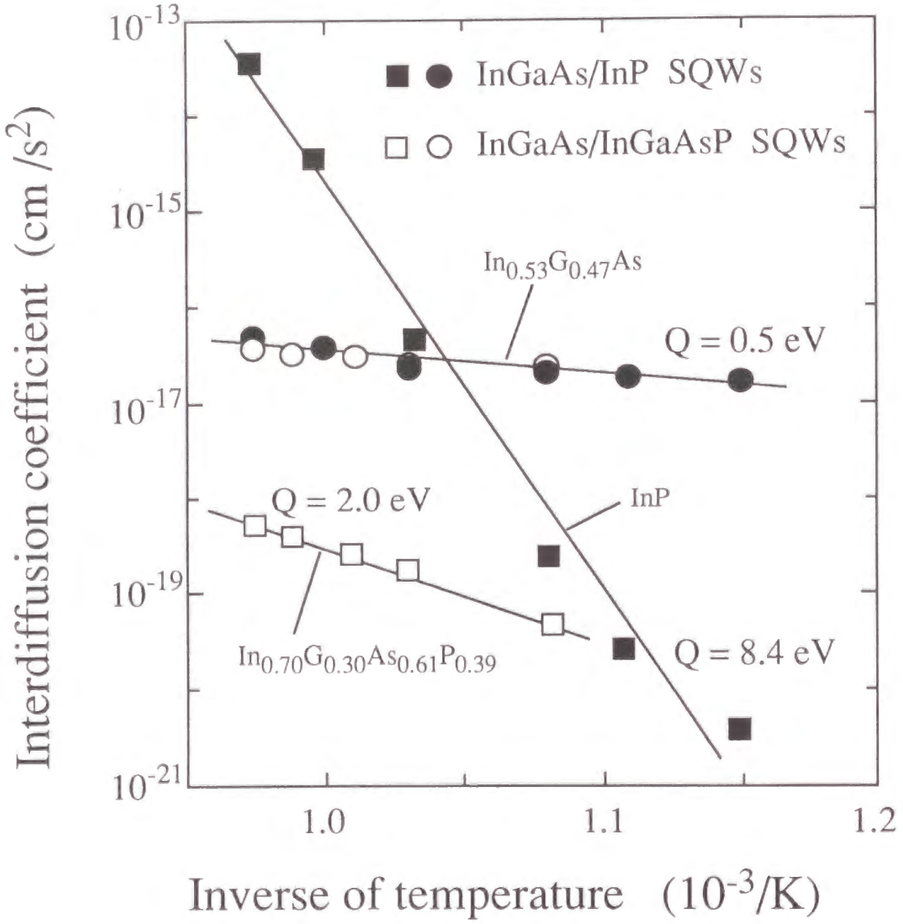

Figure 2-7 Interdiffusion coefficients in $In_xGa_{1-x}As_yP_{1-y}$ quantum wells as a function of the inverse of annealing temperature.

The author assumes that interfacial compositional discontinuity is related to lattice distortion, which is first induced at an interface during interdiffusion. If there is no interfacial discontinuity, then the greater the difference in the initial composition of group-V atoms between well and barrier layers, the greater the lattice distortion produced by interdiffusion will be. In Table 2-I, distribution ratios of $In_{0.53}Ga_{0.47}As/InP$ quantum wells are larger than those of $In_{0.53}Ga_{0.47}As/In_{0.70}Ga_{0.30}As_{0.61}P_{0.39}$ quantum wells. The ratio in GaAs/AlGaAs quantum wells is regarded to be one (shown in Fig. 2-1 and in detail in Table 2-II). This shows that the distribution ratio is larger at the interface where the greater lattice distortion was expected. Table 2-I also shows that the distribution ratio decreased as annealing temperature increased. These results support the assumption that compositional discontinuity starts due to a thermodynamic potential barrier related to lattice distortion. Yu et al. reported that a lattice mismatch was prevented when both group-III atoms and group-V atoms interdiffused [42]. They speculated that this was because the interdiffusion that produces lattice distortion requires excess energy. Considering that strain energy follows compositional profiles in layers, ratio k is expected to vary versus time. The author supposes that the annealing time in the experiment is too short to observe the effect on ratio k in this work.

Even though the author ignored the Smigelskas-Kirkendall effect, the model accurately explains quantum energy shifts due to interdiffusion. This suggests that the Smigelskas-Kirkendall effect was negligible in the samples. The author assumes that this result is also related to the lattice distortion that adds excess energy to the interdiffusion activation energy. If group-III atoms do not move, as in the experiment, the motion of the interface of group-V atoms must produce a large lattice distortion between the stable interface of group-III atoms and the moved interface of group-V atoms.

2-2-4. Interdiffusion process in GaAs/AlGaAs quantum wells

Experimental samples were grown by MOVPE. The samples were undoped $GaAs/Al_{0.25}Ga_{0.75}As$ SQWs on (001)-GaAs substrates grown at 720°C. Each sample had a cap layer, SQWs, and a buffer layer on the substrate. The well layers of $GaAs/Al_{0.25}Ga_{0.75}As$ SQWs were 20, 15, 10, and 5 nm in width, separated by 50-nm-wide barrier layers. Cap and buffer layers were 200 nm wide. Samples were annealed in a reactor tube of a liquid-phase epitaxy system. During annealing, a GaAs plate was placed on $Al_xGa_{1-x}As$ samples and pure

Table 2-II Interdiffusion coefficients and distribution ratios of GaAs/$Al_{0.25}Ga_{0.75}As$ quantum wells. Interdiffusion coefficients of GaAs and $Al_{0.25}Ga_{0.75}As$ layers were equal.

GaAs/$Al_{0.25}Ga_{0.75}As$		
T (°C)	D (cm^2/s)	k
800	2.2 E-19	1
825	6.9 E-19	1
850	1.1 E-18	1
875	2.3 E-18	1
900	4.0 E-18	1

Table 2-III Interfacial phosphorous composition ratios of samples at various annealing temperatures. The error is about 10%. The sample II value for 680°C was not determined because it showed no energy shift.

Sample	680	700	720	740
I	100	35	25	20
II	---	35	25	20
III	100	35	30	20

H_2 gas was introduced.

The dependence of quantum energy shifts on the well width in GaAs/AlGaAs SQWs differed greatly from those in InGaAsP/InP SQWs. Figure 2-8 shows the dependence of quantum energy shifts on well-layer width for various annealing times. The energy in the 20-nm-wide well layer was almost constant; and in narrower well layers, the energy shift increased but did not saturate. The formula explains each of these characteristics. Figure 2-9 shows the quantum energy shifts for several annealing temperatures. The same tendency of energy shifts in Fig. 2-8 is seen, and this tendency differs greatly from that in $In_{0.53}Ga_{0.47}As$/InP quantum wells (see Fig. 2-5).

Table 2-II lists calculated interdiffusion coefficients and distribution ratios for GaAs/$Al_{0.25}Ga_{0.75}As$ quantum wells. The parameters in Tables 2-I and 2-II give an indication of why the tendency in Fig. 2-6 is between those in Fig. 2-5 and Fig. 2-9. Interdiffusion coefficients of $In_{0.53}Ga_{0.47}As/In_{0.70}Ga_{0.30}As_{0.61}P_{0.39}$ quantum wells are different between layers, which is a characteristic of $In_{0.53}Ga_{0.47}As$/InP, and interfacial discontinuity is small, which is a characteristic of GaAs/$Al_{0.25}Ga_{0.75}As$. The parameters in Table 2-II suggest that Chang's model is applicable to GaAs/$Al_xGa_{1-x}As$ quantum wells. It was confirmed that interdiffusion coefficients were common to both layers and that distribution ratios were 1 at all the annealing temperatures adopted for GaAs/$Al_{0.25}Ga_{0.75}As$ quantum wells.

The author compared the interdiffusion profiles of $In_{0.53}Ga_{0.47}As$/InP and GaAs/$Al_{0.25}Ga_{0.75}As$ quantum wells. Figure 2-10(a) explains the results found by Nakashima et al. [15] and Fujii et al. [16] (arsenic composition in an $In_{0.53}Ga_{0.47}As$ well layer decreased uniformly, interdiffused arsenic atoms stagnated near the interface on an InP barrier layer side, and a large compositional discontinuity of group-V atoms existed at the interface even after interdiffusion). These profiles also help me understand the characteristics of energy shift in two types of quantum well. In $In_{0.53}Ga_{0.47}As$/InP quantum wells, there is a large interfacial discontinuity that starts as the distribution ratio. The distribution ratio limits the increase of phosphorus composition in the well layer. Because of this compositional limitation, the shift of quantum energy saturates. At high velocities (see Table 2-I), interdiffusion easily advances to the center of the well layer. Quantum energies therefore shift, even in a wide well layer. Distribution ratios were independent of well-layer width, so

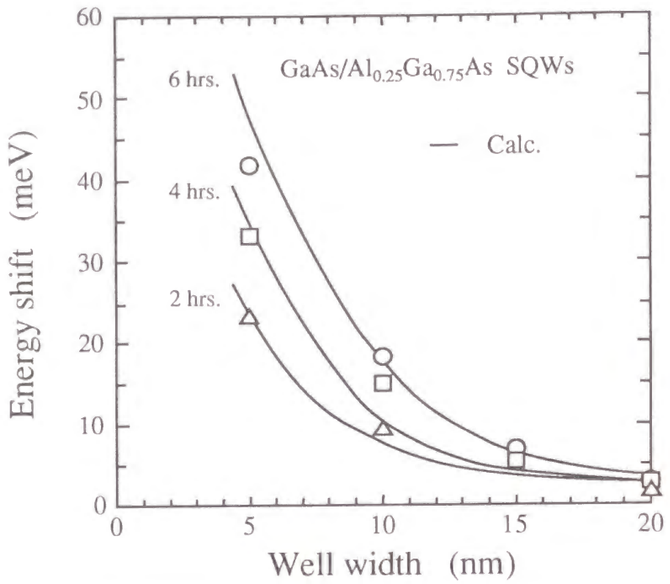

Figure 2-8 Quantum energy shifts as a function of well width: $GaAs/Al_{0.25}Ga_{0.75}As$ quantum wells after annealing at 825°C for 2, 4, and 6 hours. Symbols show measured results and solid lines indicate calculated results.

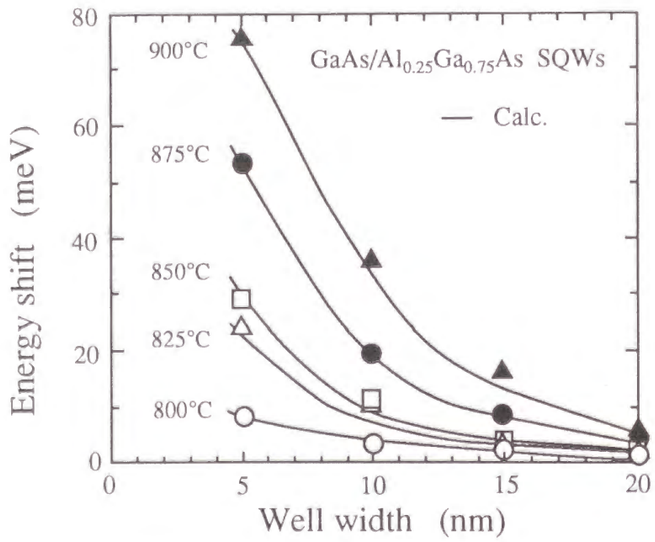

Figure 2-9 Quantum energy shifts as a function of well width: $GaAs/Al_{0.25}Ga_{0.75}As$ quantum wells after annealing at between 800 and 900°C for 2 hours. Symbols show measured results and solid lines indicate calculated results.

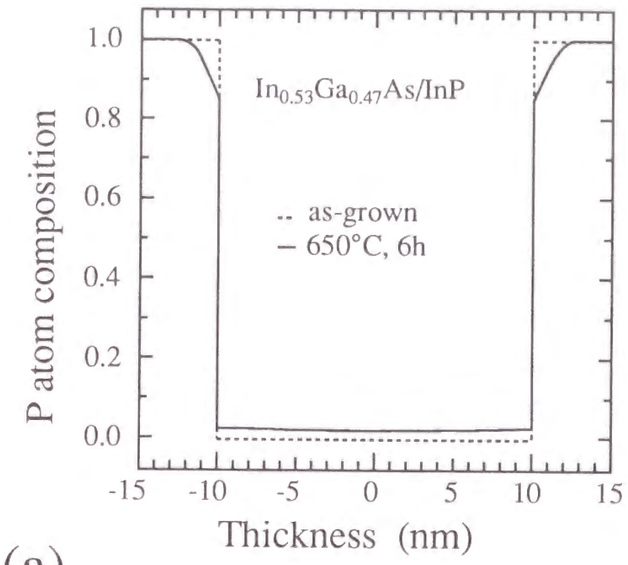

(a)

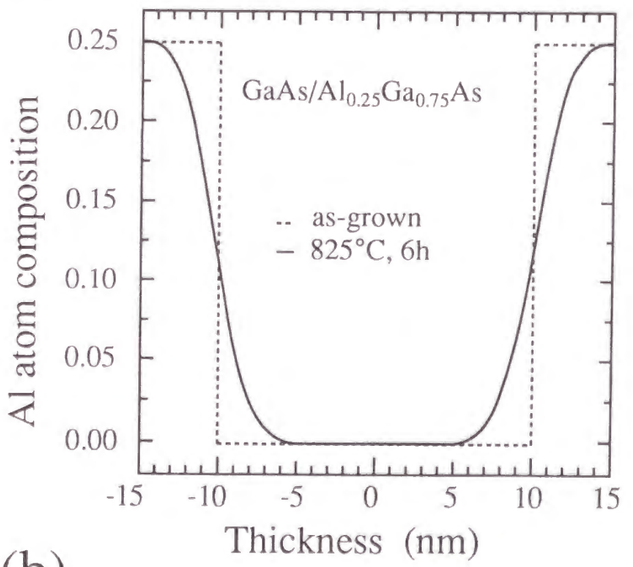

(b)

Figure 2-10 Calculated composition profiles: (a) phosphorus composition profile in an $In_{0.53}Ga_{0.47}As/InP$ quantum well 20 nm wide after annealing at 650°C for 6 hours, and (b) aluminum composition profile in a $GaAs/Al_{0.25}Ga_{0.75}As$ quantum well 20 nm wide after annealing at 825°C for 6 hours.

saturation and shifts occur earlier in narrower well layers. In GaAs/$Al_{0.25}Ga_{0.75}As$ quantum wells (Fig. 2-10(b)), the distribution ratio was 1, so energy shifts increased gradually and did not saturate.

Arrhenius plots of interdiffusion coefficients in GaAs/$Al_xGa_{1-x}As$ quantum wells are shown in Fig. 2-11. The solid lines represent an Arrhenius expression with a single activation energy. An interdiffusion activation energy of 2.8 eV was found in GaAs/$Al_{0.25}Ga_{0.75}As$ quantum wells. Previously reported data were superimposed in Fig. 2-11. The author believes that the discrepancy between the values in this work and others is caused by a difference in crystal quality. Chang and Koma found an interdiffusion activation energy of 4.1 eV in $Al_{0.25}Ga_{0.75}As$ [12]. They speculated that the disagreement between their activation energy and the Ga vacancy, which was 2.1 eV [43], was due to As vacancies via the formation of divacancies [44]. Our activation energy was closer to the Ga vacancy than Chang and Koma's, so our samples possibly had fewer As vacancies than their sample. This would also explain why our interdiffusion coefficients were lower than Chang and Koma's. Guido et al. examined the effect of vacancy concentration on interdiffusion [11]. The smallest activation energy among their samples was 3.4 eV. The results from Guido et al. are very similar to ours, although their activation energy is different.

2-2-5. Growth-condition dependence of parameters

The effect of growth temperature and buffer-layer thickness on a set of parameters (i.e., interdiffusion coefficients and interfacial distribution ratio) of $In_{0.53}Ga_{0.47}As$/InP quantum wells is described in the following. Three samples of undoped $In_{0.53}Ga_{0.47}As$/InP single quantum wells were grown on (100)-oriented InP substrates using MOVPE. Each sample consisted of a 100-nm InP cap layer, SQWs, and an InP buffer layer. The SQWs consisted of 20-, 10-, 7.5-, and 5-nm $In_{0.53}Ga_{0.47}As$ well layers separated by 50-nm InP barrier layers. Growth temperatures and buffer layer thicknesses varied among the samples. Sample I was grown at 615°C with a 1-μm buffer layer. Sample II was grown at 570°C with a 1-μm buffer layer. Sample III was grown at 615°C with a 0.1-μm buffer layer. After etching away the epitaxial layers to expose the buffer layers, etch pits that originated from substrate dislocations were observed. Etch pit density (EPD) was about 12,000/cm^2 on a 0.1-μm buffer

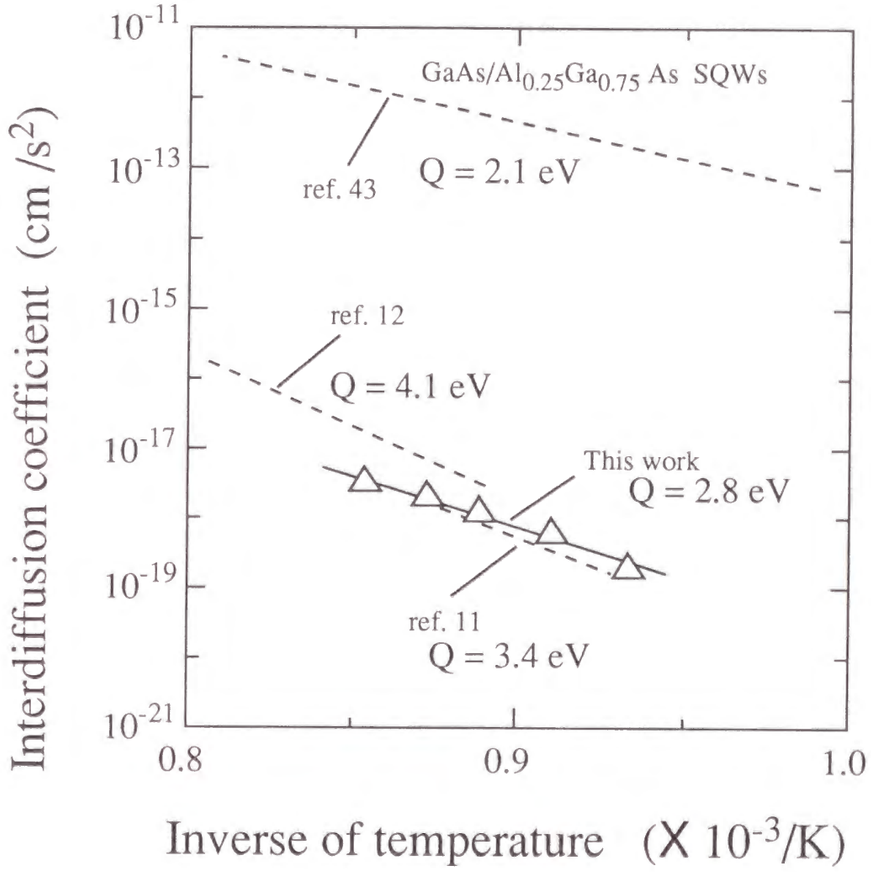

Figure 2-11 Interdiffusion coefficients in GaAs/$Al_{0.25}Ga_{0.75}As$ quantum wells as a function of the inverse of annealing temperature. Results of previous research are shown for reference.

layer and about 6,000/cm^2 on a 1-μm buffer layer. The EPD of the substrate was below 5,000/cm^2. Samples were annealed at between 680°C and 740°C for 2 hours.

The 4.2-K photoluminescence spectra were measured before and after annealing. Figure 2-12 shows the measured and calculated energy shifts as a function of well width after annealing at 700°C. The lower the growth temperature and the thicker the buffer layer, the stabler the peak energy. This tendency is consistent for annealing between 680°C and 740°C. The results suggest that the interdiffusion parameters varied among these samples. The calculated energy shifts agree very well with measured shifts, and interdiffusion coefficients and interfacial distribution ratios of each sample were determined for temperatures between 680°C and 740°C.

Table 2-III shows the interfacial phosphorous composition ratios k. The ratios were constant for any given temperature. This means that the ratios are independent of growth temperature and buffer layer thickness.

Figure 2-13 shows the interdiffusion coefficients of samples I, II, and III as functions of temperature. In the InP layer, the interdiffusion coefficients for the sample grown at 615°C (sample I) are about 20 times that for the sample grown at 570°C (sample II). The diffusion coefficients for the sample with a 0.1-μm buffer (sample III) are also about 20 times that for the sample with a 1-μm buffer (sample I). All samples have a common interdiffusion activation energy of 8.4 eV. In $In_{0.53}Ga_{0.47}As$ layers, the interdiffusion coefficients are almost independent of growth temperature and buffer layer thickness, and they show an activation energy of 0.5 eV.

It is remarkable that the activation energies are the same in layers having the same composition under all experimental conditions. Even the values in Fig. 2-13 are equal to those in Fig. 2-9. The author infers that the difference in the activation energy between layers indicates a difference in the interdiffusion mechanism. In general, defect-dependent diffusion can be categorized based on the effective defects: vacancy, dislocation, and interstitial (Fig. 2-14). Diffusion activation energies are specified according to the defect types. The activation energy of vacancy or dislocation diffusion is several electron volts, and the energy of interstitial diffusion is under one electron volt [45]. Based on these findings, it is concluded that interdiffusion in the InP layer occurs due to vacancy and/or dislocation defects, and that interdiffusion in the $In_{0.53}Ga_{0.47}As$ layer is related to interstitial phenomena. The growth-condition dependence of the interdiffusion coefficient supports this idea if the following is

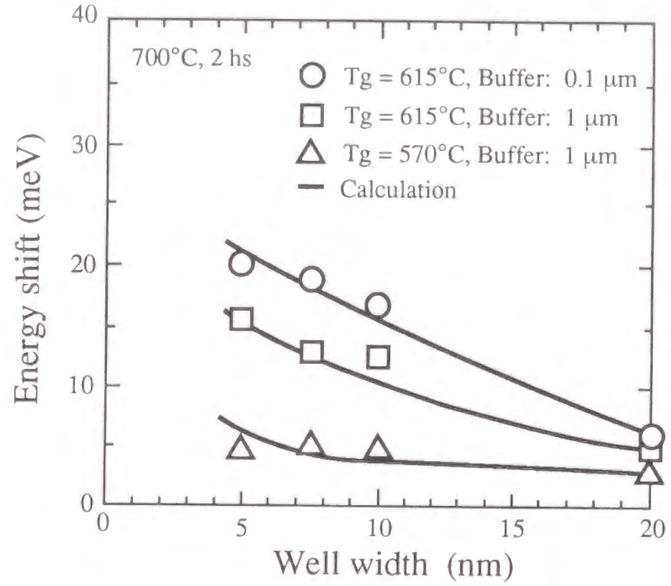

Figure 2-12 Quantum energy shift in InGaAs/InP quantum well grown under various conditions. Annealing was performed at 700°C for 2 hours.

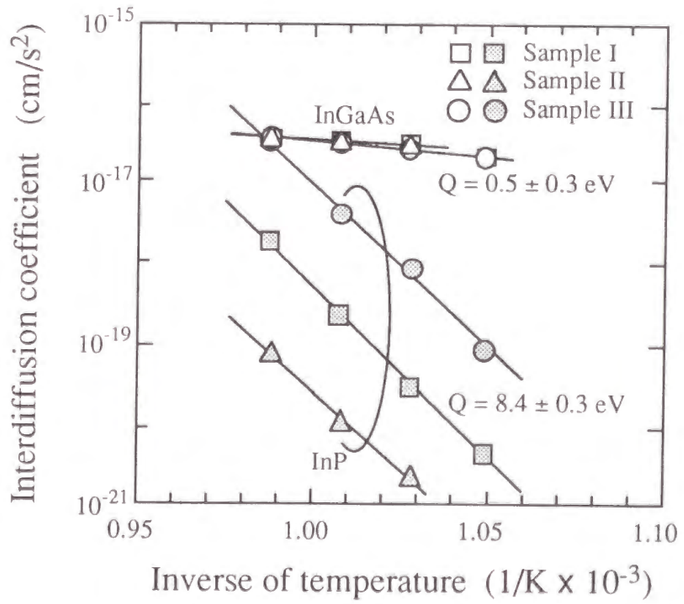

Figure 2-13 Interdiffusion coefficient in each layer of $In_{0.53}Ga_{0.43}As$/InP quantum wells as a function of temperature. Open symbols represent interdiffusion coefficients in the well layers and solid marks show coefficients in the barrier layers.

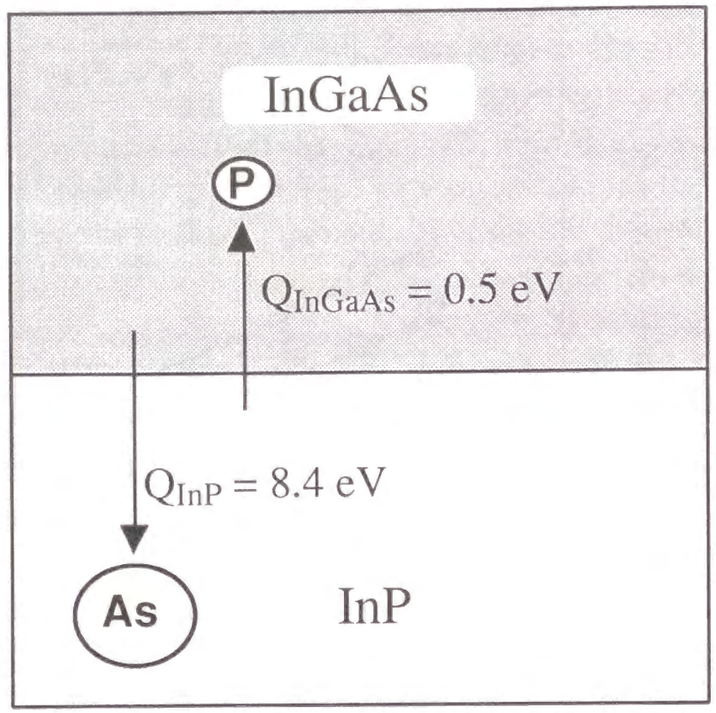

T = 600 ~ 750°C

- Vacancy-related diffusion:

  5.6 eV (P in InP), 3.9 eV (In in InP)

- Dislocation-related diffusion:

  3.7 eV (P in Si), 2.8 eV (In in Ge)

- Interstitial-site-related diffusion:

  0.51 eV (Li in Ge), 0.38 eV (Au in Si)

Figure 2-14 Defect-dependent diffusion is divided into three types and the obtained diffusion coefficient in each layer suggests the diffusion mechanism.

assumed. At increasingly higher temperatures, more vacancies are generated. If this trend is retained after quenching, vacancy-assisted interdiffusion is enhanced in the high-temperature-grown sample. Remember that EPD was twice as large in the 0.1-μm buffer layer than in the 1-μm buffer layer. If the number of dislocation paths follows the EPD trends, dislocation-assisted interdiffusion is enhanced in layers on a high-EPD buffer layer. Measurements of the InP layer matched these trends. Note that we cannot distinguish these two mechanism since the number of vacancies and number of dislocation paths may correlate to each other. On the other hand, it is reasonable that interdiffusion in the $In_{0.53}Ga_{0.47}As$ layer was not affected by the growth temperature or buffer-layer thickness if the interdiffusion is mainly due to the interstitial effects. The author considers that the interdiffusion in the $In_{0.53}Ga_{0.47}As$ layer resembles the Zn diffusion in GaAs [46]. Comparatively small phosphorous atoms are expected to be able to enter an interstitial path in the $In_{0.53}Ga_{0.47}As$ layer and extend the effective interdiffusion length.

Quantum energy shifts are shown in Fig. 2-15 as a function of the interdiffusion coefficient in the InP layer for 7.5-nm $In_{0.53}Ga_{0.47}As$ well layers after annealing at 680°C and 700°C. No energy shift was attained from the 1-μm buffer layer sample grown at 570°C and annealed at 680°C. This region is represented by a dashed line because D_b was extrapolated for the case when no energy shift was observed. The thermal stability of samples was enhanced by improving the crystal quality of the barrier InP layer, which was realized by reducing the growth temperature and making the buffer layer thicker.

The author has demonstrated that thermal stability is related to crystal quality, and also that lattice strain plays an important role in the interdiffusion process. The study enables a basic understanding of the interdiffusion process in III-V semiconductor quantum wells, providing an aid in their application to devices.

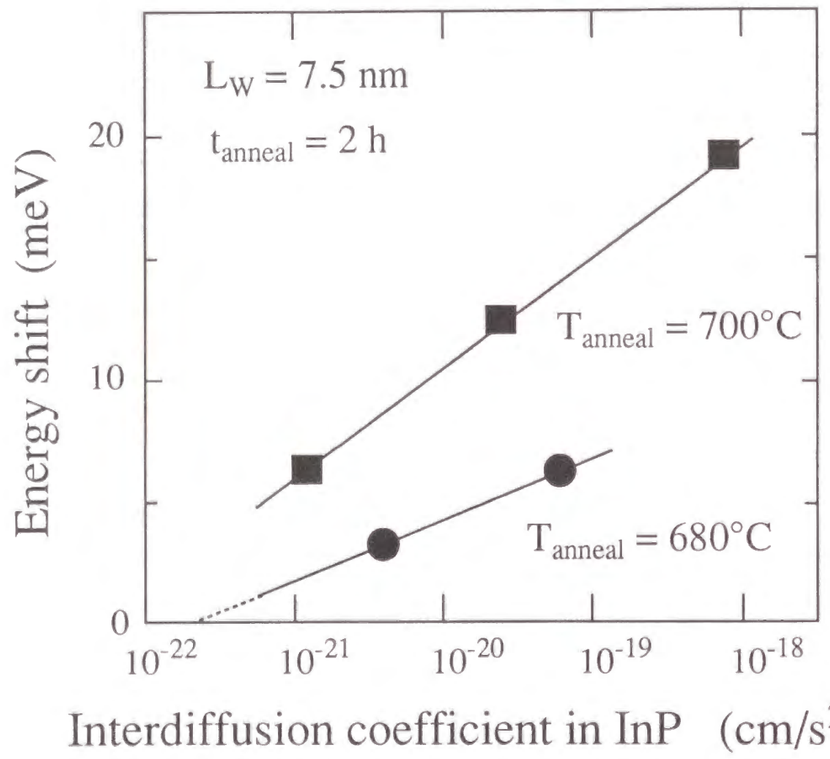

Figure 2-15 Quantum energy shift in a single 7.5-nm-wide quantum well as a function of the interdiffusion coefficient in the InP layer, after annealing at 680 and 700°C for 2 hours.

2-3 Dislocation multiplication in lattice-mismatched InGaAs/InP quantum wells

Biaxially strained $In_xGa_{1-x}As$/InP quantum wells are now commercially important for usage in semiconductor laser diodes for high-speed and large-capacity fiber telecommunications [47 - 50]. By intentionally introducing compressive or tensile stress into the well layer, we can control semiconductor band structure [51, 52], and hence improve the electronic and optical properties for device applications [53-60]. The elastic limit of lattice distortion is one of the most significant research subjects in the field of crystal growth, and this research makes good use of the strain effect.

Dodson and Tsao proposed an empirical model for the dislocation multiplication process in a SiGe bulk crystal [61, 62]. They pointed out that we can grow the layers in a metastable region [63, 64], where the dislocation density is so small that device performances do not deteriorate. Since dislocation multiplication requires a finite time and its velocity depends on temperature [65], the dislocation density is affected by growth and structural conditions. Following Dodson and Tsao's kinetic model, stress relaxation processes in thick InGaAs/GaAs heteroepitaxial layers have been examined when the relaxation is much higher (greater than 10^{-4}), high enough to detect it by the shift of an X-ray rocking curve [66] or reflection high-energy electron diffraction (RHEED) pattern [63].

In this section, the author investigates the dependence of dislocation multiplication in metastable $In_xGa_{1-x}As$/InP quantum wells on time, temperature, and stress distribution. To detect the small strain relaxation near the border between metastable and stable regions, dislocation lines are directly observed using x-ray topography. The author applies Dodson and Tsao's model to quantum wells, assuming that dislocation multiplication is governed by the net strain of a layer. The dislocation density in as-grown single quantum well and its increase due to annealing are measured and analyzed by the expanded model. Dislocation glide activation energy and a material-specific proportionality constant at InGaAs/InP interface are precisely determined. Using the parameters, the author describes the dislocation multiplication process during the growth of quantum wells. The results successfully explain quantitatively how the dislocation density in multiple strained quantum wells is practically suppressed in compressively strained well layers with tensilely strained barrier layers.

2-3-1 Model of dislocation glide process

Stress relaxation is empirically described as a function of time, temperature, and stress. Following Dodson and Tsao's model, the time dependence of a stress relaxation $\gamma(t)$ can be described by a single nonlinear differential equation:

$$\frac{d\gamma(t)}{dt} = \Gamma \cdot v \cdot \left(\frac{\sigma(\gamma)}{\mu}\right)^2 \cdot \gamma(t), \qquad (2.39)$$

where Γ is the phenomenological dislocation multiplication parameter, v is the dislocation velocity, $\sigma(\gamma)$ is the effective stress propagating the dislocation, and μ is the shear modulus. The stress relaxation $\gamma(t)$ is proportional to the misfit dislocation density r(t),

$$\gamma(t) = br(t), \qquad (2.40)$$

where b is the magnitude of the Burgers vector. Dodson and Tsao showed that the glide activation energy depends on the applied stress and that the dislocation velocity is

$$v = C_{gl}\exp\left[-\frac{E^0_{gl}\left(1-\frac{\sigma(\gamma)}{\tau_0}\right)}{kT}\right] + C_{cl}\exp\left(-\frac{E_{cl}}{kT}\right), \qquad (2.41)$$

where C_{gl} and C_{cl} are the kinetic prefactors determining the relative importance of the glide (gl) and climb (cl) processes, respectively, $E^0_{gl}(1-\sigma(\gamma)/\tau_0)$ and E_{cl} are the activation energies for dislocation glide and climb, respectively, τ_0 is the zero-temperature flow stress (which is about 0.1μ), and T is the temperature. Dislocation climb contributes to stress relaxation by constructing grain boundaries where dislocations gather.

Dodson and Tsao defined excess stress using Matthews' force balance model [55]. They compared average strain force with the line-tension force of an initial dislocation line to evaluate driving force for strain relief (see Fig. 2-16). Their excess stress for a single-kink mechanism is

$$\sigma^{SK}_{exc}(z) = \left|2\mu\left(\frac{1+\nu}{1-\nu}\right)e^{SK}_{equ}\right| - \frac{\mu}{2\pi}\left(\frac{1-\nu\cos^2\beta}{1-\nu}\right)\frac{\ln(4z/b)}{z/b}, \qquad (2.42)$$

and that for a double-kink mechanism is

$$\sigma^{DK}_{exc}(z) = \left|2\mu\left(\frac{1+\nu}{1-\nu}\right)e^{DK}_{equ}\right| - \frac{\mu}{\pi}\left(\frac{1-\nu\cos^2\beta}{1-\nu}\right)\frac{\ln(4h/b)}{h/b}, \qquad (2.43)$$

Single kink

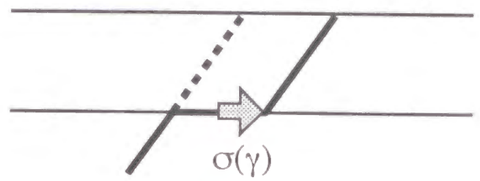

Double kink

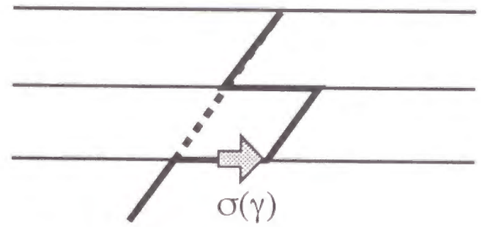

Figure 2-16 Schematic of single kink dislocation glide and double kink dislocation glide in Dodson and Tsao's model.

Single layer

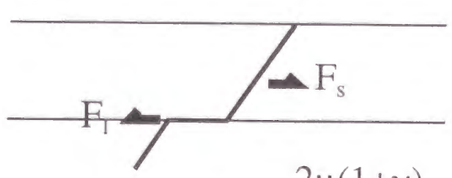

$$\sigma = F_s - F_l = \frac{2\mu(1+\nu)}{1-\nu}[\varepsilon - \gamma - r(z)\gamma]$$

Multiple layers

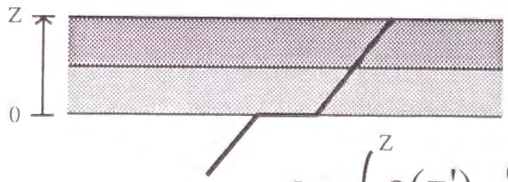

$$\varepsilon \Rightarrow \int_0^Z \varepsilon(z')\frac{dz'}{z}$$

Figure 2-17 Definition of excess stress in single layer (Dadson and Tsao) and that in multiple layers (in this study). Multiple layers are considered as a single layer having uniform strain as large as the average of the multiple layers.

where ν is the Poisson ratio, μ is the share module, b is the length of Burger's vector, β is the angle of Burger's vector to a strained-layer/unstrained-layer interface, z is depth from the surface to an interface, h is the width between kinks, and e^{SK}_{equ} and e^{DK}_{equ} are equivalent strains, which are

$$e^{SK}_{equ} = \int_0^Z e(z') \frac{dz'}{Z} \qquad (2.\ 44)$$

and

$$e^{DK}_{equ} = \int_{Z-h}^Z e(z') \frac{dz'}{h}, \qquad (2.\ 45)$$

where e(z') is the strain in the overlayer, and z' is depth from the surface. The first term of Eq. (2. 42) and (2. 43) shows misfit-strain force, and the second term shows line-tension force. In most cases, the equivalent strain of a double-kink mechanism is larger than that of a single-kink mechanism, and strain is expected to be relieved by the single-kink mechanism.

To expand this model to multiple layers, the author assumes that the effective stress in multiple layers can be described as the net stress of a layer (see Fig. 2-17). The author uses an effective stress,

$$\sigma(\gamma) = 2\mu \left(\frac{1+\nu}{1-\nu}\right) \left(\left| \int_0^z e(z') \frac{dz'}{z} \right| - \gamma(t) - r(z) \right), \qquad (2.\ 46)$$

where e(z') is the in-plane strain in the overlayer, z is the overlayer thickness, and r(z) is the critical strain predicted by Matthews and Blakeslee's model [67]. The effective stress is reduced in direct proportion to the misfit dislocation density. By defining the effective stress shown in Eq. (2. 46), the author discusses dislocation multiplication during the growth of quantum wells.

2-3-2 Dislocation glide in InGaAs/InP quantum wells

The author determined two material-specific parameters in $In_xGa_{1-x}As/InP$ quantum wells, ΓC_{gl} and E^0_{gl}, that describe the stress relaxation process with Eqs. (2. 39) to (2. 46). At low dislocation densities, the glide mechanism dominates stress relaxation. Hence, in this section, the author disregards the climb terms in (2. 41). Samples were undoped $In_{0.77}Ga_{0.23}As/InP$ single quantum wells grown by low-pressure MOVPE. The growth

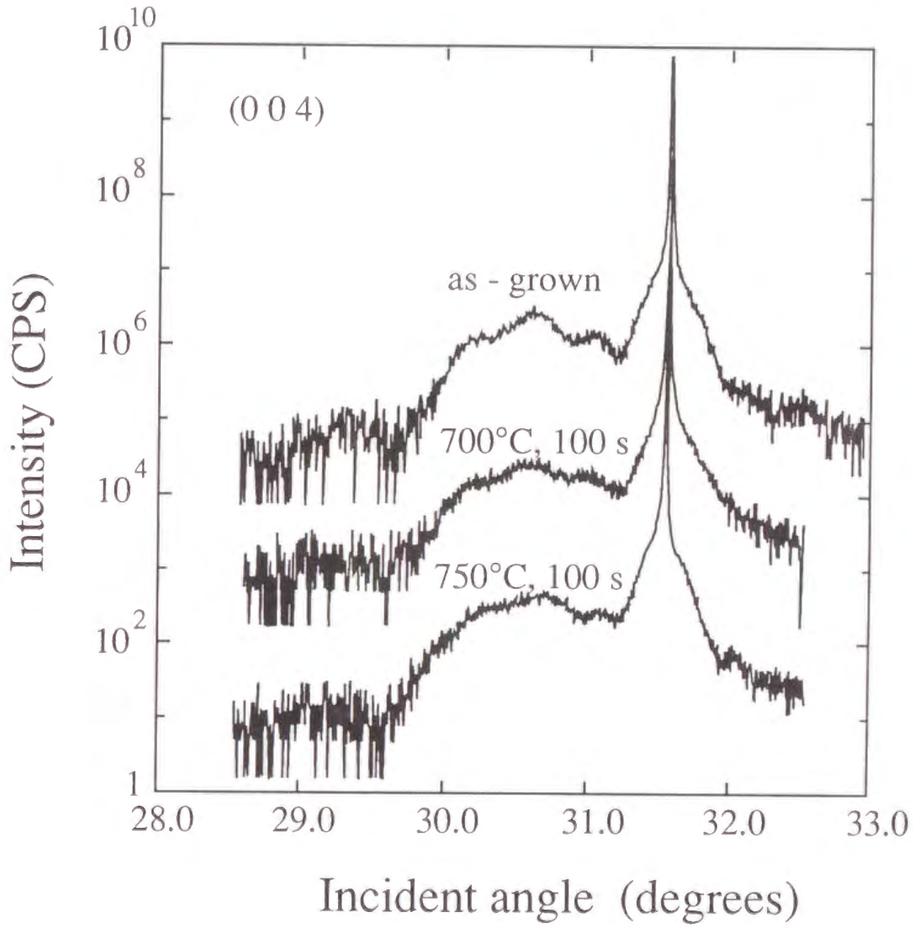

Figure 2-18 Rocking curves of samples as-grown, annealed at 700°C, and annealed at 750°C measured by four-crystal X-ray diffraction meter. No significant change, such as peak shift was not detected by these evaluation.

temperatures were 550°C and 570°C. Each sample consisted of a 10-nm wide InP cap layer, single well layer, and 500-nm wide InP buffer layer on (001) InP substrates. Etch pit densities (EPD) of substrates were below 5,000/cm^2. The well layers were strained under compression, and their thicknesses were 5 and 6 nm, which are close to the critical thickness predicted by Matthews and Blakeslee's model. The growth rates were 4 Å/s for $In_{0.77}Ga_{0.23}As$ and 2 Å/s for InP. Thicknesses and compositions of these samples were determined by growth conditions and ascertained by high resolution x-ray diffractmetory.

Samples were annealed at 600, 650, 700, and 750°C under an InP plate for a period ranging from 40 to 300 seconds. During annealing, pure N_2 gas was passed through the chamber. The author could not find any significant differences between the (004) rocking curves of samples measured before and after annealing. As an example, the rocking curves of 6-nm wide single quantum wells are shown in Fig. 2-18. The X-ray diffraction patterns of θ-2θ scan were measured using (044)Ge four-crystal monochrometer. On the left side of the substrate peak, a broad diffraction peak corresponding to the strained well layer and fringes corresponding to the cap layer can be seen. Rocking curves are slightly different from each other, but no peak shifts indicating stress relaxation in the well layer can be observed.

Dislocation lines in samples were observed by X-ray topography. The incident beam was Cu-Kα line. The distortion field in the thin layer was so small that the penetrating X-ray beam was not available to detect the strain field. The author therefore used a reflected X-ray beam. Conventional X-ray films were used as detecting plates, resolution of which was about 20 μm. In X-ray topographies, only dislocation lines perpendicular to the incident beam are observed due to the small strain field. (224) and (2$\bar{2}$4) planes were measured to evaluate dislocation density of (0$\bar{1}$1)- and (011)-directions, respectively. Dislocation density was defined to be the length of the dislocation line per area and converted to stress relaxation using Eq. (2. 40).

From the X-ray topography measurements, dislocation multiplication due to annealing was found in the samples. The dependence of dislocation multiplication on annealing temperature and annealing time is plotted in Fig. 2-19. The author found that the effective stress of these samples is negative if the critical strain r(z) predicted by Matthews and Blakeslee's model is used. This suggests that the actual critical strain is smaller [68, 69]. When the author used a 55 to 60% scale factor for Matthews and Blakeslee's model, the calculated increase of stress relaxation could be fitted to the measured one. This scale factor

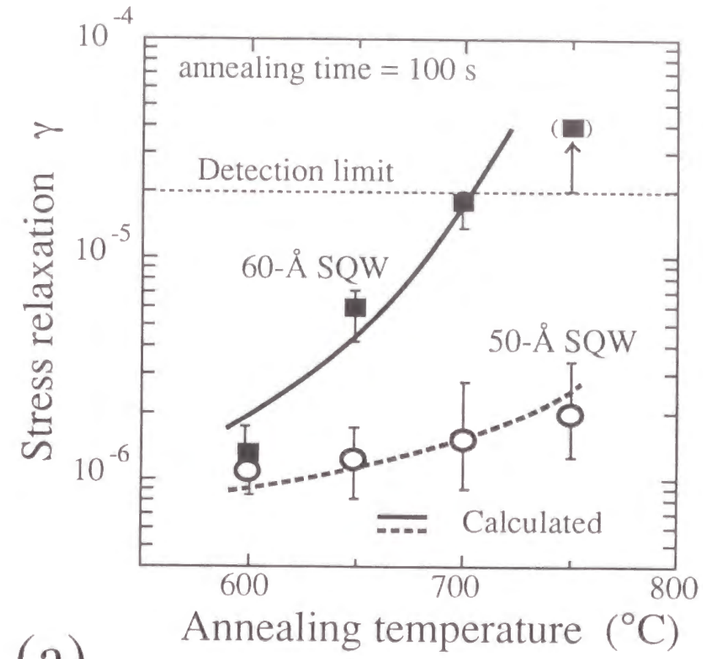

Figure 2-19 Dependence of stress relaxation in single quantum wells on (a) annealing temperature and (b) annealing time. Lines represent the fitting results.

agrees with Whaley's report [68]. From the calculations, E^0_{gl} = 1.1 ± 0.1 eV and ΓC_{gl} = 5 X 10^7 to 1 X 10^8. The error was due to the uncertainty of critical strain r(z). The activation energy is close to that for undoped GaAs crystal, which was reported to be 1.00 eV (α-dislocation) and 1.35 eV (β-dislocation) by Choi [70], and 1.00 eV (α-dislocation) and about 1.7 eV (β-dislocation) by Maeda [71]. Our values are close to those for undoped GaAs. For SiGe crystal, Dodson and Tsao reported that E^0_{gl} = 1.03 eV and ΓC_{gl} = 2 X 10^{10}. Our results suggest that strained InGaAsP crystals take longer to relax than strained SiGe crystals.

2-3-3. Stress relaxation process during growth

The author calculated the stress relaxation process during growth of quantum wells using the obtained parameters. In the calculation, layers were assumed to grow step-by-step every second, which agrees well with the growth condition that the growth rates of the samples were one to two monolayers per second.

Four types of $In_xGa_{1-x}As$/InP strained quantum-well samples were prepared to confirm whether the above model can practically describe dislocation density. Sample A was composed of a 500-nm InP buffer layer, twice multiplied (6-nm $In_{0.77}Ga_{0.23}As$)/(6-nm $In_{0.40}Ga_{0.60}As$) quantum wells, and a 6-nm InP cap layer. The opposite sign of strain reduced net strain in the structure. A lattice mismatch in the $In_{0.77}Ga_{0.23}As$ layer was 1.6 %, and that in $In_{0.40}Ga_{0.60}As$ layer was -0.9 %. Sample B was composed of a 500-nm InP buffer layer, twice multiplied (6-nm $In_{0.77}Ga_{0.23}As$)/(6-nm $In_{0.53}Ga_{0.47}As$) quantum wells, and a 6-nm InP cap layer. Type C samples were single quantum wells. There were five samples of type C having well layers of different widths. The samples were composed of a 500-nm InP buffer layer, 1.2-, 5-, 6-, 10-, and 15-nm $In_{0.77}Ga_{0.23}As$ well layers, and a 10-nm InP layer. Sample D and E were multiple quantum wells on InP substrates; the former had $In_{0.40}Ga_{0.60}As$ barrier layers under tension, and the latter had unstrained $In_{0.53}Ga_{0.47}As$ barrier layers. The composition of well layers in both samples was $In_{0.77}Ga_{0.23}As$, the same as that of the above single quantum wells. Growth rates were 0.2 nm/s in the $In_xGa_{1-x}As$ layer and 0.4 nm/s in the InP layer in all samples.

Figure 2-20 shows the calculated transition of excess stress during growth of samples

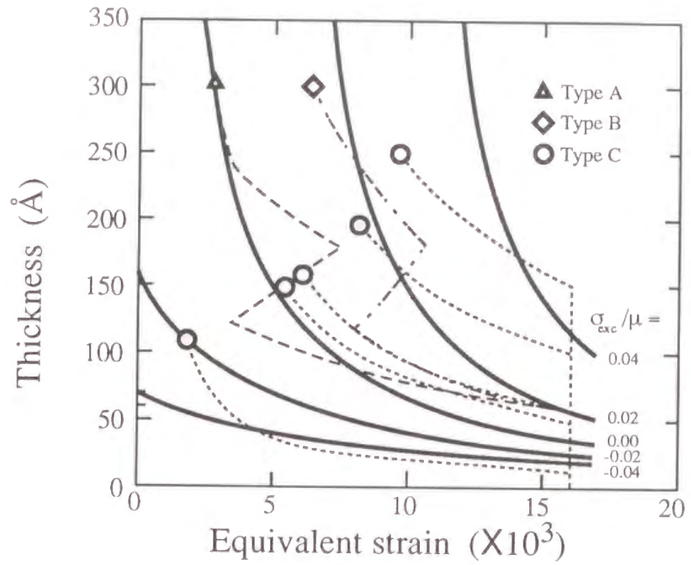

Figure 2-20 Transition of excess stress during growth on a thickness/equivalent-strain plot. Solid lines show excess stress contours.

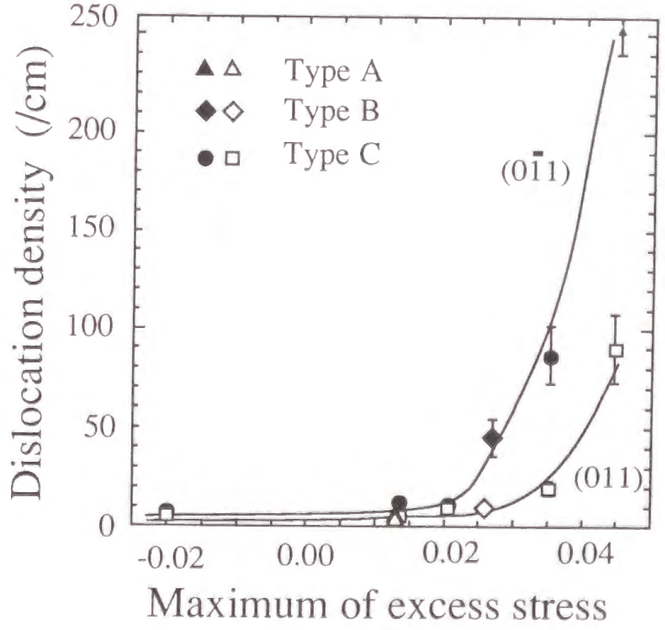

Figure 2-21 Dislocation density of (01̄1)- and (011)- direction as a function of maximum excess stress during growth.

on a thickness/equivalent-strain plot. Equivalent strain for a single-kink mechanism is also plotted with dashed lines. Here, strain due to the difference of thermal expansion parameters between layers is disregarded since it is much smaller than intentional strain [72]. By comparing dashed lines of sample A with those of sample B, the tensilely strained barrier layer can be seen to reduce excess stress during growth. Assuming dislocation glides fast enough, dislocation density is evaluated by the maximum excess stress during growth.

Figure 2-21 shows dislocation densities of (011)- and (0$\bar{1}$1)-directions as a function of maximum excess stress in the growth. In both directions, dislocation density is well fitted by single lines. Dislocation density of the (0$\bar{1}$1)-direction was about twice that of the (011)-direction, which agrees with previous reports [73, 74]. Note that dislocation density differed between multiple quantum wells having common 60-Å $In_{0.77}Ga_{0.23}As$ well layers. Dislocation density of sample A having tensilely-strained barrier layers was lower than that of sample B. Also, dislocation density was found to increase critically above $\sigma_{exc}/\mu = 0.015 \sim 0.025$. The critical excess stress is similar to that of $\sigma_{exc}/\mu = 0.026$ for SiGe reported by Tsao et al. [75].

Figure 2-22 shows the 4.2-K photoluminescence spectra of samples A to C, which have a common 6-nm $In_{0.77}Ga_{0.23}As$ well layer. In the measurements, samples were immersed in liquid helium, and luminescence was excited by 647.1-nm line of a Kr^+ laser and detected by a PbS detector. The spectrum of sample C was twice as wide and half as weak as that of sample A (consequently, integrated intensity is almost equal). By comparing type A and B, the author saw that optical property of quantum wells was improved, which may be due to the tensilely-strained barrier layer. Figure 2-23 shows the full width at half maximum (FWHM) of photoluminescence spectra at 4.2 K as a function of maximum excess stress during growth. Since carrier energy distribution is quite small at 4.2 K, the spectra width suggests uniformity of the band edge structure. Partial strain relaxation in real space causes broadening of emission spectra. The FWHM increased critically above $\sigma_{exc}/\mu = 0.005 \sim 0.010$. The figure suggests that the excess stress can be a good index for designing high-quality quantum wells. The critical excess stress of FWHM is close to that of dislocation density, suggesting the accuracy of the evaluation. Slight differences may be due to the resolution of X-ray topography.

Using the parameters, the author calculated the stress relaxation during growth. The

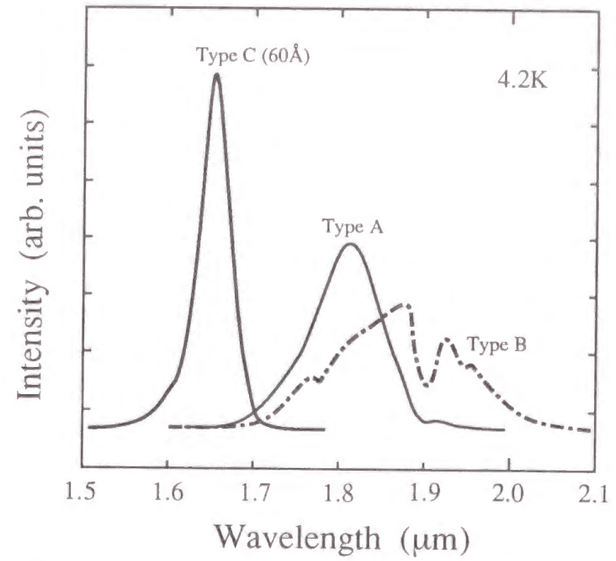

Figure 2-22 Photoluminescence spectra of three samples at 4.2 K. Uniformity of structure and radiation efficiency are compared among samples from this figure.

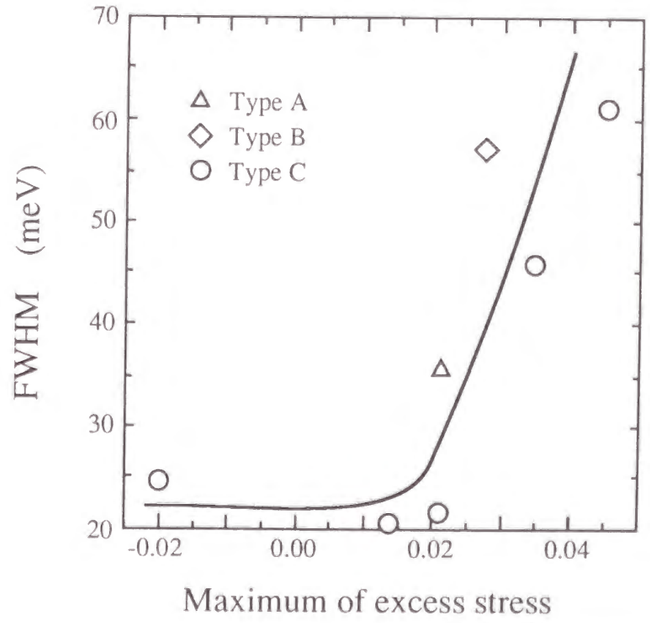

Figure 2-23 Full width half maximum of 4.2-K photoluminescence spectra as a function of maximum excess stress during growth.

results suggest that the velocity of stress relaxation in $In_xGa_{1-x}As/InP$ is slow enough for control by varying the growth rate and growth temperature.

Figure 2-24 shows the calculation of stress relaxation for sample C having a 6-nm wide single quantum well. After 65 seconds of growth, the calculated stress relaxation is close to the value measured in as-grown quantum well when using $\gamma_0 = 10^{-7}$. The figure indicates that almost all stress relaxation occurs during InP growth although only the $In_{0.77}Ga_{0.23}As$ layer is strained. This is understood after determining the effective stress during the growth. The stress relaxation occurs while the effective stress is of the order of 10^{-2} s/m. The time span for which that effective stress is of the order of 10^{-2} s/m is longer during InP growth than during $In_{0.77}Ga_{0.23}As$ growth. The stress relaxation process will be modified by changing the growth rate of each layer.

The dependence of the stress relaxation process on the growth rate is calculated for sample C having a 6-nm wide well (Fig. 2-25). If the growth rate of InP is 0.4 nm/s (II), the stress relaxation during InP growth decreases, and the resulting dislocation density is less than one-third of that in the experimental case (I). If the growth rate of $In_{0.77}Ga_{0.23}As$ layer is 0.2 nm/s (III), the stress relaxation during $In_{0.77}Ga_{0.23}As$ growth is twice that of the experimental case. The results suggest that the growth rate of the overlayer is a significant factor in controlling the dislocation density in strained quantum wells.

Growth temperature also governs the magnitude of stress relaxation during growth. Figure 2-26 shows the measured dislocation density and calculated stress relaxation during growth of 6-nm wide $In_{0.77}Ga_{0.23}As/InP$ single quantum wells at several temperatures. The dislocation density in quantum wells grown at 570°C was about twice that of quantum wells grown at 550°C. The calculated values after 65 seconds of growth agree well with the measured values. The figure suggests that the growth temperature is also a significant factor in controlling the dislocation density in strained quantum wells. For instance, reducing the growth temperature from 600°C to 500°C decreases stress relaxation by about one order of magnitude. The temperature sensitivity of stress relaxation is mainly due to the magnitude of activation energy, E^0_{gl}.

The stress relaxation during growth of multiple quantum wells, sample D and E, is shown in Fig. 2-27. After 90 seconds of growth, the relaxation in the sample with strained

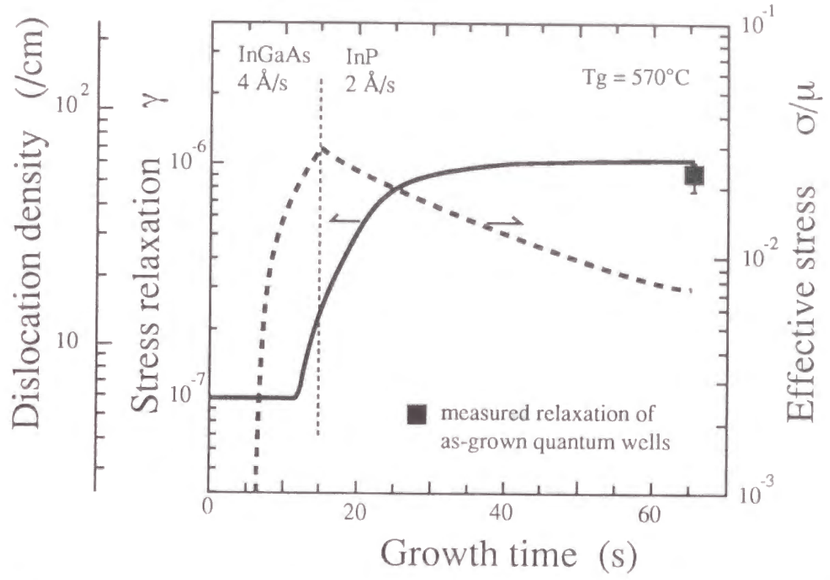

Figure 2-24 Strain relaxation and effective stress during growth of 60-Å single quantum well calculated with $E^0_{gl} = 1.2$ eV and $\Gamma C_{gl} = 7 \times 10^7$.

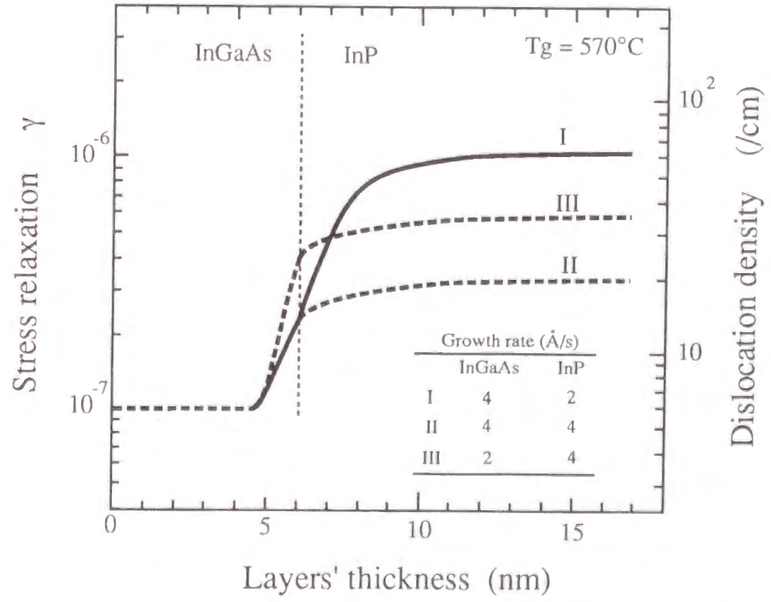

Figure 2-25 Calculated stress relaxation process during growth of single quantum well with three sets of growth rate.

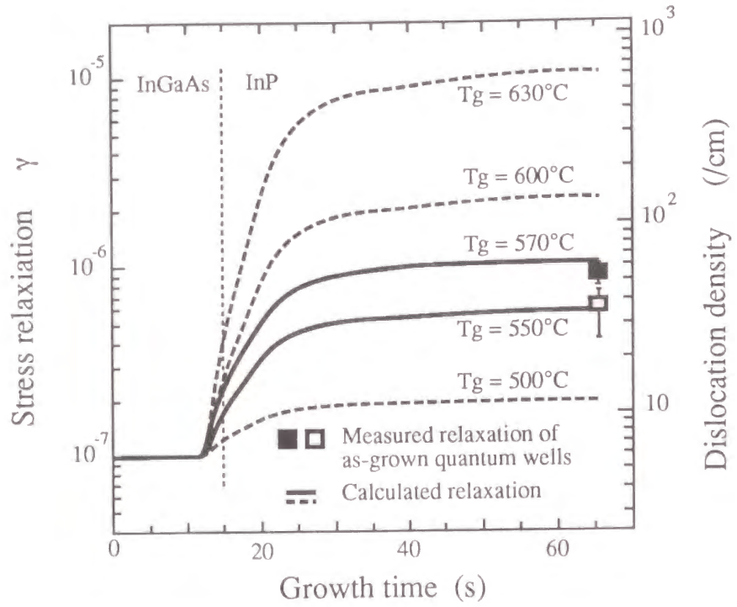

Figure 2-26 Measured dislocation density and calculated stress relaxation during growth of 60-Å wide $In_{0.77}Ga_{0.23}As$/InP single quantum wells at several temperatures.

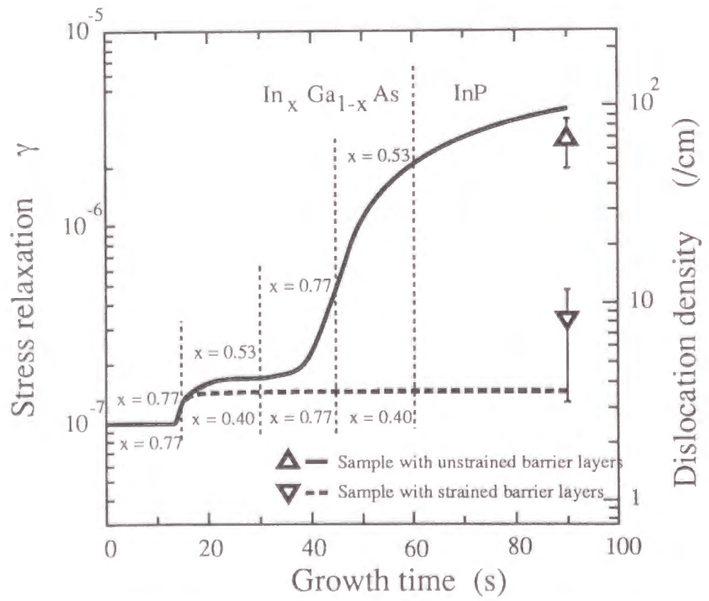

Figure 2-27 Strain relaxation during growth of multiple quantum wells with different barrier layers calculated with $E^0_{gl} = 1.2$ eV and $\Gamma C_{gl} = 6 \times 10^7$.

barrier layers under tension (sample E) was an order of magnitude lower than that in the sample with unstrained barrier layers (sample D). The calculation well explains the measured result. Stress relaxation did not occur during the growth of sample E since the inversely-strained barrier layers decreased the effective stress to less than 10^{-2} s/m. The figure indicates that reducing the net strain of the layers is a practical and effective way to prevent stress relaxation, and that the effect can be understood by using the kinetic model described in this section.

2-4 Self-assembly of InGaAs/GaAs quantum dots

By expecting that lasers on GaAs substrates would have high temperature stability since high-potential barriers like AlGaAs and AlGaInP can prevent carrier leakage from the active region, the author and co-workers engaged to realize materials that emit at 1.3 μm on GaAs substrates using the atomic layer epitaxy (ALE) technique. To realize 1.3-μm emission by III-V compound semiconductor quantum wells on GaAs, highly lattice-mismatched epitaxial growth is required. The required well thickness is larger than the critical thickness of the crystal. The large lattice mismatch causes the generation of misfit dislocations during the growth, severely damaging crystal quality, as shown in section 2-3. We believed that short-period superlattices can break through the limit set by the critical thickness to reach a highly efficient 1.3-μm emission. Actually, Roan and Cheng have already succeeded in growing $(GaAs)_1/(InAs)_1$ short-period superlattices on GaAs substrates by MBE to show 1.3-μm emission at room temperature [76].

This section briefly describes the growth of $In_{0.5}Ga_{0.5}As$/GaAs quantum dots that emit at 1.3 μm at room temperature. The dots are found to be self-assembled during alternate supplies of InAs and GaAs monolayers on GaAs substrates using ALE technique.

2-4-1 Discovery of 1.3-μm emitting nanostructures

The ALE growth system is schematically shown in Fig. 2-28. The growth system was designed for pulse jet epitaxy (PJE) in which source gases are supplied in a fast, pulsed stream [77 - 80]. The reactor was designed through a simulation to realize smooth gas flow

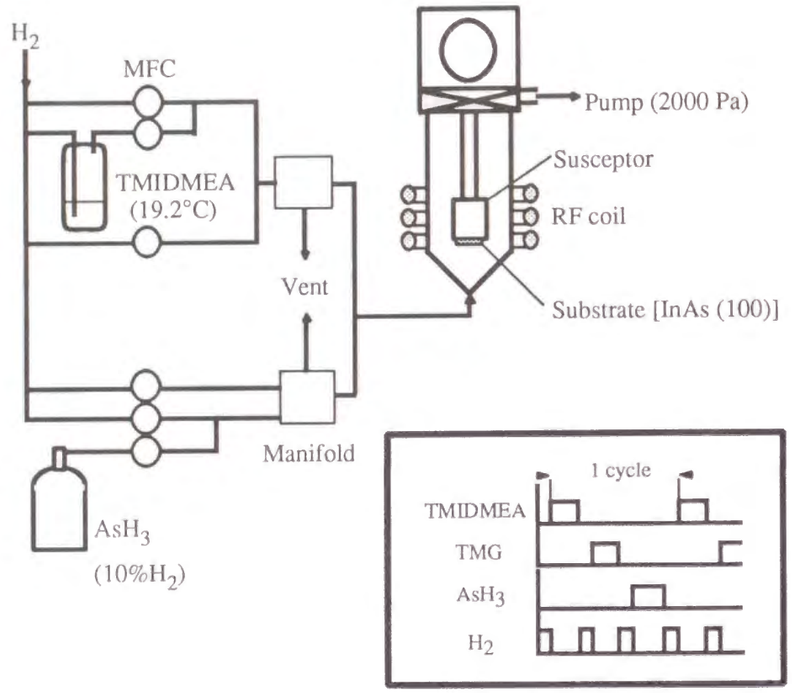

Figure 2-28 Growth system for pulse-jet epitaxy with a chimney reactor, in which precursors are supplied in a fast, pulsed stream and self-limited III-V compounds can be grown under a wide range of conditions.

streamlines without vortices. The author adopted the use of a low pressure atmosphere so that precursors decompose only on the heated substrate surface. The substrate was positioned in the fast gas stream emitted from a jet nozzle to prevent thermally decomposed source molecules from building up in stagnant layers. Source materials were trimethylindium-dimethylethylamine adduct (TMIDMEA) for InAs ALE, trimethylgallium (TMGa) for GaAs ALE, and arsine (AsH_3). A growth temperature of 460°C gives distinct self-limiting growth by both TMIDMEA and TMGa. The 12 cycles of $(InAs)_1/(GaAs)_1$ short-period growth were performed on a 250-nm-wide GaAs buffer layer on a (001)GaAs substrate and followed by the growth of a 25-nm-wide GaAs cap layer.

Plane-view and cross-sectional TEM showed that the alternated monolayer epitaxy formed microstructures. A plane-view image shows uniform dark circles of about 20 nm in diameter (Fig. 2-29(a)). The standard deviation of the diameter was 2.9 nm. Practical standard deviation was probably smaller than shown since contrast across the TEM image varied. Areal coverage of the circle was 5 to 10%. A cross-sectional image indicates that dark flat spheres were formed within the short-period-grown layer (Fig. 2-29(b)). Spheres were about 10 nm in height. No dislocations can be seen around the spheres in these figures. Two borders can be seen, indicating interfaces between the GaAs layer and the layer grown by alternately supplying InAs and GaAs monolayers (short-period-grown layer). It is remarkable that even though the short-period-grown layer was far from a short-period structure, the width of the layer was the same as the width of 12-cycle $(InAs)_1/(GaAs)_1$ at 7 nm. The author looked at a high-resolution TEM image around the dot in a cross-sectional sample and did not find any dislocations or defects in the lattice image (Fig. 2-30). A weak contrast at the border of the dots suggests that composition and lattice distortion do not abruptly change around the dot.

Figure 2-31 shows the spatial composition distribution of a sample cross section evaluated by energy dispersive X-ray microanalysis (EDX) with an excitation electron beam focused to a diameter of about 1 nm. The sample was thinned down to 10 nm, less than the in-plane diameter of the dots, to obtain a signal from only the dots. Signal intensity was calibrated to estimate a precise indium composition using the signal intensity of a lattice-matched $In_{0.53}Ga_{0.47}As$ layer grown on an InP substrate as a reference. The indium composition was 0.5 at the center of the dots (i.e., $In_{0.5}Ga_{0.5}As$) and 0.1 in the quantum-well layer surrounding the dots (i.e., $In_{0.1}Ga_{0.9}As$).

Figure 2-32 shows the photoluminescence spectrum of the sample at room

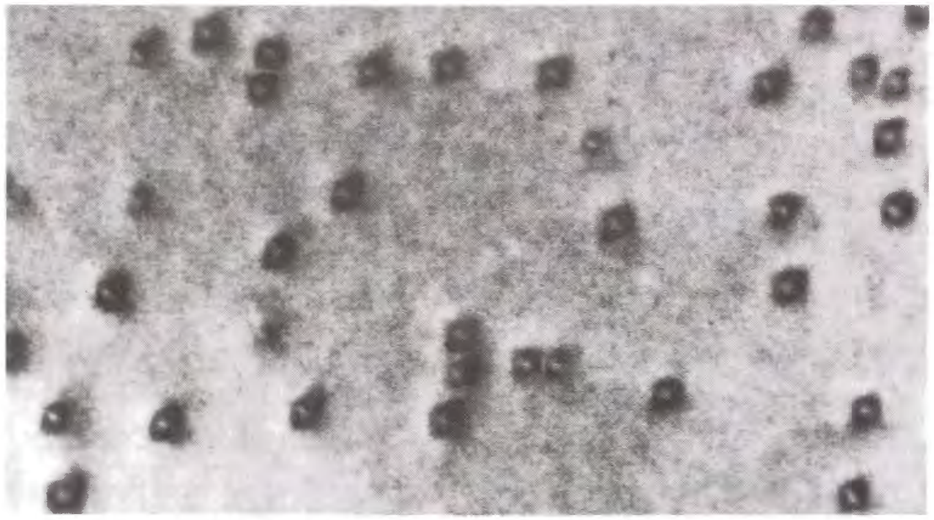

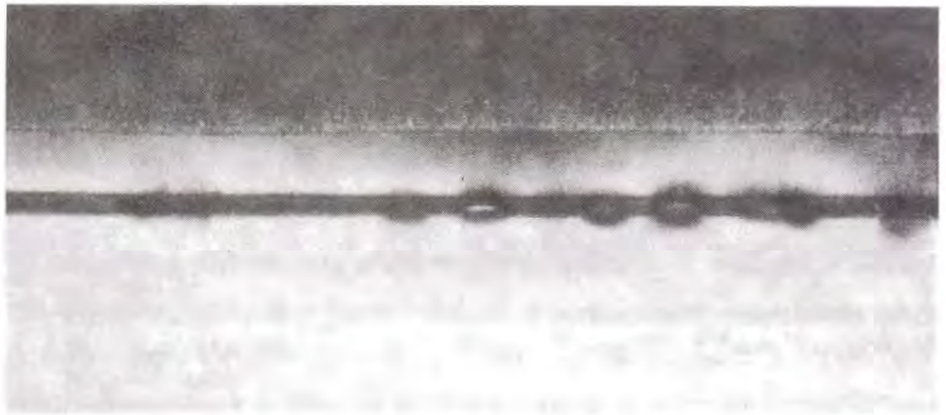

Figures 2-29 (a) Plane-view and (b) cross-sectional dark-field TEM images of ALS dots, grown by 12 cycles of $(InAs)_1/(GaAs)_1$ periodic supply on a 250-nm GaAs buffer layer on a (001)-GaAs substrate and covered by a 30-nm-thick GaAs cap layer.

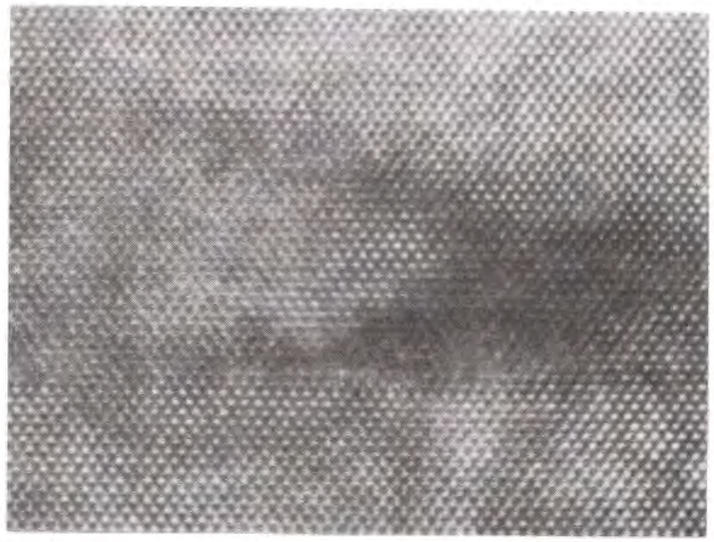

Figure 2-30 High-resolution TEM image around the dot in a cross-sectional sample. No dislocation or defects are found in the lattice image.

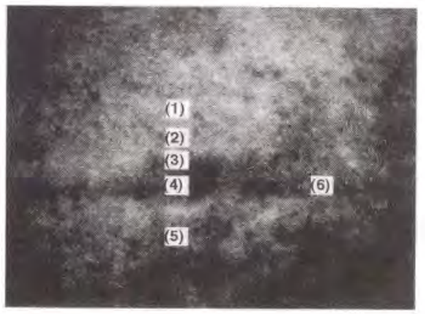

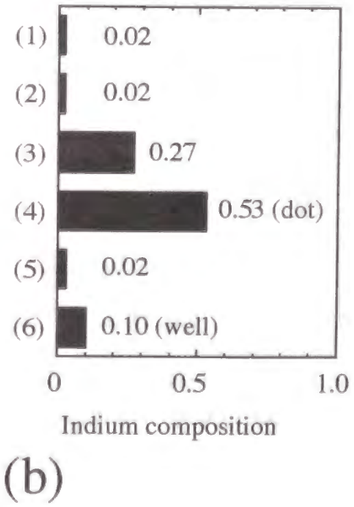

Figure 2-31 Spatial indium composition distribution of quantum-dot cross sections evaluated by energy dispersive X-ray microanalysis (EDX) with an excitation electron beam focused to a diameter of about 1 nm.

temperature. The figure suggests that a 1.3-μm emission was successfully realized [81]. However, the grown structure was not short-period superlattices but bizarre structures, as shown in Fig. 2-29, where spherical dark regions are buried in the quantum wells. Having done various diagnostic examinations of the materials (see Chapter 4), the author finally concluded that the structures are quantum dots. The full width at half maximum of the spectra is 30 meV, which suggests inhomogeneity of the quantum dots. The author named these type of dots *ALS dots* based on the unique growth method: alternate supply of source materials (see Chapter 3).

2-4-2 Unique dot structure

ALS dots have unique surface flatness, which gives a hint about their growth mechanism. A cross-sectional TEM image shows that sample surfaces were flat, even on the dots, although the cap layer thickness was only 25 nm (Fig. 2-29(b)). It also shows that a clear upper border exists between the quantum-dot layer and overlayer. These results suggest that ALS dots were not formed via ordinary Stranski-Krastanov islanding growth but via a type of two-dimensional growth; that is, the dots were formed as a result of compositional nonuniformities on (or near) the growth surface. ALE is better for layer-by-layer growth than usual MOVPE and MBE. Our growth temperature (460°C) and growth rate (1 monolayer per 10 seconds) are significantly smaller than those of other three-dimensional structures (e.g., Nötzel et. al. [82] and Oshinowo et. al. [83]). The lower the growth temperature and growth rate, the longer the surface-migration length, and consequently, the more the two-dimensional growth is enhanced [84]. Additionally, the amount of the group-III precursor at one cycle of ALE is for only single-layer coverage. Therefore, even if three-dimensional metal islands of group-III atoms were constructed on the surface, the islands deformed to a two-dimensional structure when arsine was supplied to the surface [85]. If the group-III metal islands do not form, the Stranski-Krastanov mode is prevented from occurring since an indium-stabilized surface is very reactive and arsenic atoms reaching the surface are immediately incorporated into the two-dimensional structure [86, 87]. Detailed discussion of the growth mechanism is presented in Chapter 3, based on the results of investigation on the effect of several growth conditions on the dot structure.

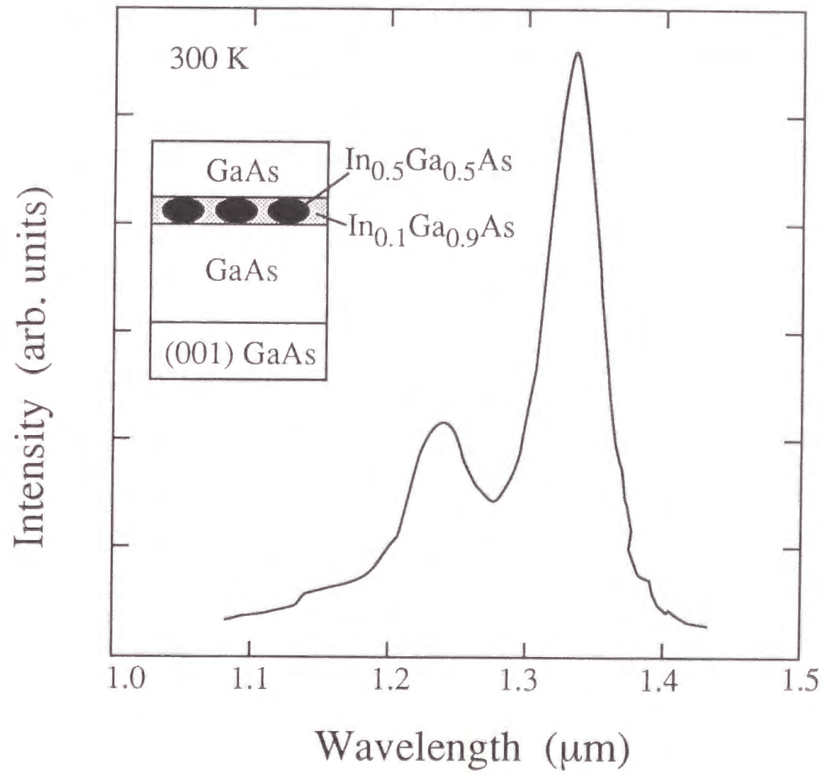

Figure 2-32 Photoluminescence spectra of the dots at 300 K measured using a Kr^+ laser. Sample structure is shown as an inset. We see the first peak at 1.33 μm, the second peak at 1.4 μm and the week third emission at 1.25 μm.

2-5 Summary

In this chapter, the author discussed the investigation of various phenomena occurring in InGaAsP nano-scale crystal while introducing a lattice mismatch.

In Section 2-2, the author showed that interfacial discontinuity in the composition of interdiffused species is generated in lattice-matched InGaAsP/InP quantum wells, probably due to interdiffusion-induced lattice distortion. The author proposed a formula that describes interdiffusion profiles of quantum wells, looked at the interdiffusion process in quantum wells composed of $In_xGa_{1-x}As_yP_{1-y}$ and $Al_xGa_{1-x}As$ alloy semiconductors, and demonstrated the accuracy of the formula. The formula was derived by solving diffusion equations assuming that interdiffusion coefficients differ between layers. The formula was applied to analysis of the dependence of quantum energy shifts on annealing time, annealing temperature, and well layer widths in lattice-matched $In_xGa_{1-x}As_yP_{1-y}$/InP and GaAs/$Al_xGa_{1-x}As$ quantum wells; and it correctly explained the dependence and clarified the differences between interdiffusion processes in these two materials.

In Section 2-3, the author examined the dislocation multiplication process in strained $In_xGa_{1-x}As$/InP quantum wells using Dodson and Tsao's kinetic model. The dependence of the stress relaxation in $In_xGa_{1-x}As$/InP quantum wells on time, temperature and effective stress was examined. The author measured the dislocation density in annealed strained quantum wells by X-ray topography, and determined the dislocation glide activation energy and the material-specific proportionality constant of $In_xGa_{1-x}As$/InP quantum wells. Consequently, the dislocation density of as-grown single and multiple quantum wells was explained. How the stress relaxation proceeds depending on growth rate and growth temperature during the growth of strained quantum well was shown. Also, how the combination of strained barrier layers under tension and strained well layers under compression effectively suppresses dislocation multiplication during growth was shown.

In Section 2-4, the discovery of self-assembled InGaAs/GaAs quantum dots emitting at 1.3 μm at 300 K was described. The dots were found during a trial to fabricate highly-strained quantum wells composed of $(GaAs)_1/(InAs)_1$ short-period superlattices on GaAs substrates, using the ALE technique. The author named the type of dots ALS dots based on

their unique growth sequence. Detailed descriptions of growth, structural and optical characterization, and application to semiconductor lasers is given in the following chapters. Here, the author has briefly discussed the unique structure of ALS dots that differs from that of Stranski-Krastanov dots.

References

[1] W. D. Laidig, N. Holonyak, Jr., M. D. Camras, K. Hess, J. J. Coleman, P. D. Dapkus, and J. Bardeen, Appl. Phys. Lett. 38, 776 (1981).

[2] M. Kawabe, N. Matsuura, N. Shimizu, F. Hasegawa, and Y. Nannichi, Jpn. J. Appl. Phys. 23, L623 (1984).

[3] K. Meehan, N. Holonyak, Jr., J. M. Brown, M. A. Nixon, and P. Gavrilovic, Appl. Phys. Lett. 45, 549 (1984).

[4] E. V. K. Rao, H. Thibiergr, F. Brillouet, F. Alexandre, and R. Azoulay, Appl. Phys. Lett. 46, 867 (1985).

[5] R. L. Thornton, R. D. Burnham, T. L. Paoli, N. Holonyak, Jr., and D. G. Deppe, Appl. Phys. Lett. 48, 7 (1986).

[6] R. L. Thornton, R. D. Burnham, T. L. Paoli, N. Holonyak, Jr., and D. G. Deppe, Appl. Phys. Lett. 47, 1239 (1985).

[7] T. Fukuzawa, S. Semura, H. Saito, T. Ohta, Y. Uchida, and H. Nakashima, Appl. Phys. Lett. 45, 1 (1984).

[8] J. Cibert, P. M. Petroff, D. J. Werder, S. J. Pearton, A. C. Gossard, and J. H. English, Appl. Phys. Lett. 49, 223 (1986).

[9] D. G. Deppe, L. J. Guido, N. Holonyak, Jr., K. C. Hsieh, R. D. Burnham, R. L. Thornton, and T. L. Paoli, Appl. Phys. Lett. 49, 510 (1986).

[10] J. Cibert, P. M. Petroff, G. J. Dolan, S. J. Pearton, A. C. Gossard, and J. H. English, Appl. Phys. Lett. 49, 1275 (1986).

[11] L. J. Guido, N. Holonyak, Jr., K. C. Hsieh, R. W. Kaliski, W. E. Plano, R. D. Burnham, R. L. Thornton, J. E. Epler, and T. L. Paoli, J. Appl. Phys. 61, 1372 (1987).

[12] L. L. Chang and Koma, Appl. Phys. Lett. 29, 138 (1976).

[13] M. D. Camras, T. L. Paoli, and C. Lindstrom, J. Appl. Phys. 54, 5637 (1983).

[14] H. Leier, H. Rothfritz, and Forchel, J. Appl. Phys. 95, 277 (1989).

[15] K. Nakashima, Y. Kawaguchi, Y. Kawamura, H. Asahi, and Y. Imamura, Jpn. J. Appl. Phys. 26, L1620 (1987).

[16] T. Fujii, N. Sugawara, S. Yamazaki, and K. Nakajima, J. Cryst. Growth, 105, 348 (1990).

[17] B. Tell, B. C. Johnson, J. L. Zyskind, J. M. Brown, J. W. Sulhoff, K. F. Brown-Goebeler, B. I. Miller, and U. Koren, Appl. Phys. Lett. 52, 1428 (1988).

[18] M. Razeghi, O. Acher, and F. Launay, Semicond. Sci. Technol. 2, 793 (1987).

[19] K. Nakashima, Y. Kawaguchi, Y. Kawamura, and Y. Imamura Appl. Phys. Lett. 52, 1383 (1988).

[20] S. A. Schwarz, P. Mei, T. Venkatesan, R. Bhat, D. M. Hwang, C. L. Schwartz, M. Koza, L. Nazar, and B. J. Skromme, Appl. Phys. Lett. 53, 1051 (1988).

[21] H. Sumida, H. Asahi, S. J. Yu, K. Asami, and S. Gonda, Appl. Phys. Lett. 54, 520 (1989).

[22] H. Ribot, K. W. Lee, R. J. Simes, R. H. Yan, and L. A. Coldren, Appl. Phys. Lett. 55, 672 (1989).

[23] E. S. Koteles, A. N. M. M. Choudhury, A. Levy, B. Elman, P. Melman, M. A. Koza, and R. Bhat, 'Materials Research Society Symposium Proceedings', 240, 171, (1991).

[24] R. M. Flemming, D. B. McWhan, A. C. Gossard, W. Wiegmann, and R. A. Logan, J. Appl. Phys. 51, 357 (1980).

[25] K. Mukai, M. Sugawara, and S. Yamazaki, J. Crystal Growth 115, 433 (1991).

[26] K. Mukai, M. Sugawara, and S. Yamazaki, Phys. Rev. B 50, 2273 (1994).

[27] K. Mukai, M. Sugawara, and S. Yamazaki, J. Crystal Growth 137, 388 (1994).

[28] W. Jost, 'Diffusion' (Academic Press, New York, 1960) p. 68.

[29] R. Smoluchowski, Phys. Rev. 62, 539 (1942).

[30] H. E. Cook and J. E. Hilliard, J. Appl. Phys. 40, 2191 (1969)

[31] H. Haken, 'Quantenfeldtheorie des Festkorpers' (B. G. Teubner, Stuttgart, 1973).

[32] G. E. Pikus and G. L. Bir, Sov. Phys. Solid State 1, 136 (1959).

[33] G. E. Pikus and G. L. Bir, Sov. Phys. Solid State 1, 1502 (1960).

[34] A. Gavini and M. Cardona, Phys. Rev. B 1, 672 (1970).

[35] K. Sakurai, 'Introduction to Quantum Mechanics by Personal Computer' (in Japanese, Shokabo, Tokyo, 1989).

[36] M. C. Joncour, J. L. Benchimol, J. Burgeat, and M. Quillec, J. Phys. (Paris) C5, 3 (1982).

[37] S. R. Forest, P. H. Schmidt, R. B. Wilson, and M. L. Kaplan, Appl. Phys. Lett. 45, 1199 (1984).

[38] C. P. Kuo, S. K. Vong, R. M. Cohen, and G. B. Stringfellow, J. Appl. Phys. 57, 5428 (1985).

[39] Y. Suematsu, 'Semiconductor Laser and OEIC' (Ohm Inc., Tokyo, 1984) p. 70 (in Japanese).

[40] H. C. Casey, Jr., J. Appl. Phys. 49, 3684 (1978).

[41] B. Goldstein, Phys. Rev. 121, 1305 (1961).

[42] S. J. Yu, H. Asahi, S. Emura, S. Gonda, and K. Nakashima, J. Appl. Phys. 70, 204 (1991).

[43] S. Y. Chiang and G. L. Pearson, J. Appl. Phys. 46, 2986 (1975).

[44] D. L. Kendal, in 'Semiconductors and Semimetals' (Academic Press, New York, 1968), Vol. 4, p. 163.

[45] For example, D. Shaw, 'Atomic Diffusion in Semiconductors' (Plenum Press, London and New York, 1973).

[46] C. H. Ting and G. L. Pearson, J. Electrochem. Soc., 118, 1454 (1971).

[47] U. Koren, M. Oron, M. G. Young, B. I. Miller, J. L. de Miguel, G. Raybon, and M. Chien, Electron Lett. 26, 465 (1990).

[48] P. J. A. Thijs and T. van Dongen, Extended Abstracts of the 22nd International Conference on Solid State Devices and Materials, (The Japan Society of Applied Physics, Sendai, 1990), paper D-4-1, p. 541.

[49] I. Suemune, L. A. Coldren, M. Yamanishi, and Y. Kan, Appl. Phys. Lett. 53, 1378 (1988)

[50] T. Ohtoshi and N. Chinone, IEEE photon Tech. Lett. 1, 117 (1989).

[51] E. Yablonovitch and E. O. Kane, IEEE J. Lightwave Technol. LT-4 (1986) 504.

[52] E. Yablonovitch and E. O. Kane, IEEE J. Lightwave Technol. 6 (1988) 1292.

[53] M. Sugawara, Appl. Phys. Lett., 60 (1992) 1842.

[54] T. E. Zipperian, L. R. Dawson, T. J. Drummond, J. E. Schirber, and I. J. Fritz, Appl. Phys. Lett. 52, 975 (1988).

[55] E. P. O'Reilly, K. C. Heasman, A. R. Adams, and G. P. Witchlow, Superlattices and

Microstructures 3, 99 (1987).

[56] I. Suemune, L. A. Coldren, M. Yamanishi, and Y. Kan, Appl. Phys. Lett. 53, 1378 (1988).

[57] T. Ohtoshi and N. Chinone, IEEE Photon. Tech. Lett. 1, 117 (1989).

[58] H. K. Choi and C. A. Wang, Appl. Phys. Lett. 57, 321 (1990).

[59] U. Koren, M. Oron, M. G. Young, B. I. Miller, J. L. de Miguel, G. Raybon, and M. Chien, Electron Lett. 26, 465 (1990).

[60] P. J. A. Thijs and T. van Dongen, Ext. Abs. 22nd Int. Conf. Solid State Dev. and Mater., (Japan Soc. of Appl. Phys., Sendai, 1990), paper D-4-1, P. 541.

[61] B. W. Dodson and J. Y. Tsao, Appl. Phys. Lett., 51, 1325 (1987).

[62] B. W. Dodson and J. Y. Tsao, Phys. Rev. B, 38, 12383 (1988).

[63] G. J. Whaley, and P. I. Cohen, Appl. Phys. Lett., 57, 144 (1990).

[64] B. W. Dodson and J. Y. Tsao, Appl. Phys. Lett., 55, 1345 (1989).

[65] H. Alexander and P. Haasen, in Solid State Physics (Academic, New York, 1968), vol. 22.

[66] C. R. Wie, J. Appl. Phys. 65, 2267 (1989).

[67] J. W. Matthews, and A. E. Blakeslee, J. Vac. Sci. Technol. B6 (1976) 1285.

[68] G. J. Whaley and P. I. Cohen, Appl. Phys. Lett., 57 (1990) 144.

[69] G. L. Price, Appl. Phys. Lett., 53 (1988) 1288.

[70] S. K. Choi, M. Mihara, and T. Ninomiya, Jpn. J. Appl. Phys., 16 (1977) 737.

[71] K. Maeda, M. Sato, A. Kubo, and S. Takeuchi, J. Appl. Phys., 54 (1983) 161.

[72] R. Bisaro, P. Merenda, and T. P. Pearsall, Appl. Phys. Lett. 34 (1979) 100

[73] M. Grundmann, U. Lienert, D. Bimberg, A. Fischer-Colbrie and J. N. Miller, Appl. Phys. Lett. 55 (1989) 1765

[74]13B. R. Bennett and J. A. D. Alemo, J. Electro. Materials 20 (1991) 1075

[75] J. Y. Tsao, B. W. Dodson, S. T. Picraux, and D. M. Cornelison, Phys. Rev. Lett., 59, 2455 (1987)

[76] E. J. Roan, and Cheng, K. Y. (1991). Appl. Phys. Lett. 59, 2688.

[77] Ozeki, M., Mochizuki, K. , Ohtsuka, N., and Kodama, K. (1988). Appl. Phys. Lett. 53, 1509.

[78] Ozeki, M., Mochizuki, K. , Ohtsuka, N., and Kodama, K. (1989). Thin Solid Films 174, 63.

[79] Ozeki, M., i, Ohtsuka, N., Sakuma, Y., and Kodama, K. (1991). J. Cryst. Growth 107, 102.

[80] Sakuma, Y., Kodama, K., and Ozeki, M. (1988). Japan. J. Appl. Phys. Lett. 27, L2189.

[81] K. Mukai, N. Ohtsuka, M. Sugawara and S. Yamazaki, jpn. J. Appl. Phys., 33, L1710 (1994).

[82] R. Notzel, J. Temmyo and T. Tamamura: Nature 369 (1994) 131

[83] J. Oshinowo, M. Nishioka, S. Ishida and Y. Arakawa: Appl. Phys. Lett., 65 (1421) 1994.

[84] N. Grandjean and J. Massies: J. Cryst. Growth 134 (1993) 51.

[85] J. Osaka, N. Inoue, Y. Mada, K. Yamada and K. Wada: J. Cryst. Growth 99 (1990) 120.

[86] E. Tournié, and K. H. Ploog, Appl., Phys., Lett., 62, 858 (1993).

[87] A. Trampert, E. Tournié, and K. H. Ploog, J. of Cryst. Growth, 146, 368 (1995).

Chapter 3

Growth of Self-Assembled InGaAs/GaAs Quantum Dots Emitting at 1.3 μm

3-1 Introduction

Island formation on an initially flat surface was first reported by Stranski and Krastanow (SK) for the growth of ionic crystals [1]. The formation of defect-free islands as a result of SK growth at strained hetero interfaces is now systematically exploited for the fabrication of semiconductor quantum dots. The idea was a breakthrough in this field. Typical InGaAs self-assembled SK islands have a flat shape with a base length of 20 - 50 nm and a height of several nanometers. Since the exciton Bohr radius is about 20 nm in an InAs - GaAs system, some SK islands are small enough for the three-dimensional quantum confinement effect to be observed (i.e., the islands work as quantum dots). After a number of early observations [2 - 4], good structural and optical qualities were reported about the self-assembled coherent islands [5 - 9], suggesting that the microcrystals can be applied to practical devices. InGaAs SK islands typically emit at 0.9 - 1.2 μm at room temperature. 1.3-μm-emission InGaAs quantum dots were first reported by the author [10 - 12].

The growth of 1.3-μm-emission self-assembled InGaAs/GaAs quantum dots is described in this chapter. The growth sequence is unique in that the group-III and group-V precursors are supplied alternately with an amount corresponding to one or less than one monolayer during metalorganic vapor phase epitaxy (MOVPE). The technique is based on atomic layer epitaxy (ALE). The original materials were named *ALS quantum dots* (*ALS dots*) for alternate supply. These new quantum dots were found during a trial to fabricate $(GaAs)_1/(InAs)_1$ short-period superlattices on GaAs substrates by ALE, as explained in Chapter 2. 1.3-μm-emission dots had an impact because the emission wavelength is the zero-

dispersive wavelength of silica optical fiber used in practical optical data transmission systems. Quantum dot lasers have the fundamental advantages over quantum well lasers (see Chapter 6), and especially for InGaAs/GaAs dots, the dot active regions are very attractive since the cladding layer on GaAs substrates have a high energy barrier that reduces carrier leakage and enables a high characteristic temperature of threshold current. The active regions are also attractive to 1.3-μm-emission vertical cavity surface-emitting lasers (VCSELs) since high-reflectivity distributed Bragg reflector mirrors for 1.3 μm can be easily fabricated on GaAs substrates. In addition to a 1.3-μm emission, ALS dots have a very narrow emission spectrum linewidth. The minimum full width at half maximum (FWHM) is 28 meV, much smaller than the 80 - 120 meV for SK growth islands. Narrow spectrum linewidth will cause high optical gain in lasers. Thus, ALS dots with 1.3-μm emission and narrow spectrum linewidth are very advantageous over SK dots.

In this chapter, the author presents two kinds of growth sequences for ALS quantum dots: (1) an [In $\rightarrow$ As $\rightarrow$ Ga $\rightarrow$ As] sequence based on the concept of making monolayer superlattices by ALE, and (2) a subsequently developed [In $\rightarrow$ Ga $\rightarrow$ As] sequence. As stated in Chapter 2, the original purpose was to grow short-period superlattices using the ALE technique. After the grown material was found to be quantum dots, growth conditions were refined to improve crystal quality. To obtain high emission efficiency, the growth sequence was changed from (1) to (2). Quantum dots are characterized by their shape, size, composition, and emission wavelength. In particular, the author illustrates how the dots vary with an alternate supply cycle, growth temperature, and composition of buffer layers on which the dots are grown on the surface. Finally, the author describes a remarkable finding that temperature sensitivity of interband emission energy was significantly suppressed by an InGaAs overgrowth on the ALS dots.

3-2 Alternate supply growth by In-As-Ga-As sequence

In this section, the author explains the growth of ALS dots by an [In $\rightarrow$ As $\rightarrow$ Ga $\rightarrow$ As] (hereafter, In-As-Ga-As) alternate supply using a reactor for pulse jet epitaxy (PJE) in a MOVPE chamber. Each supply was separated by H_2 purging pulses (Fig. 2-28). Since the original purpose was to grow $(InAs)_1/(GaAs)_1$ short-period superlattices using the ALE

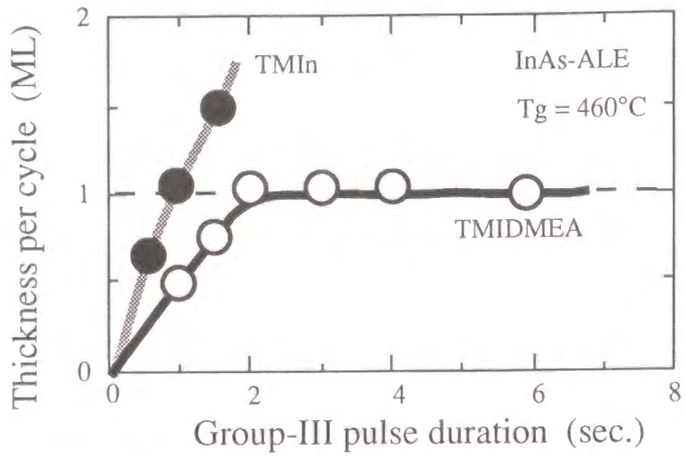

Figure 3-1 InAs thickness per cycle of ALE growth as a function of indium-source pulse duration at 460°C. When TMIn is used, the thickness per cycle increases with the TMIn pulse duration. When TMIDMEA is used, complete self-limiting growth can be achieved; that is, the growth thickness per cycle is saturated at one monolayer of InAs.

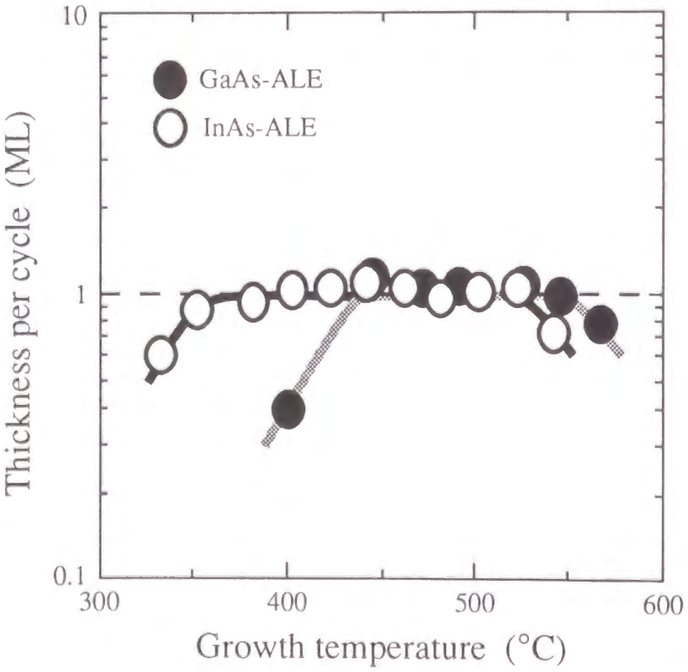

Figure 3-2 InAs and GaAs thickness per cycle of ALE growth as a function of growth temperature. InAs and GaAs were grown with self-limiting mechanism in the common temperature region. This makes it possible to grow InAs/GaAs heterostructures at a constant temperature.

technique, this section starts with a brief description of ALE growth.

3-2-1 Short periodic growth of InAs and GaAs

Source materials used for GaAs ALE, InAs ALE, and the growth of $(InAs)_1/(GaAs)_1$ short-period superlattices were trimethylindium-dimethylethylamine adduct (TMIDMEA), trimethylgallium (TMGa), and arsine (AsH_3) diluted with hydrogen (H_2). Experiments on self-limiting ALE growth were done on GaAs substrates for GaAs growth and on InAs substrates for InAs growth. A new indium source of TMIDMEA was used to solve the problem for InAs/GaAs ALE, where the temperature range for self-limiting growth was different for the two binary compounds --- 450 to 550°C for GaAs using TMGa and 300 to 400°C for InAs using trimethylindium (TMIn) [13]. The ALE growth of InAs using TMIDMEA and TMIn for indium sources is shown in Fig. 3-1, where the relationship between the group-III pulse duration and the growth thickness per cycle at 460°C is plotted. When TMIn was used, the thickness per cycle increased monotonously with the TMIn pulse duration, that is, a self-limiting mechanism did not work at this high temperature. When TMIDMEA was used, complete self-limiting growth could be achieved. The temperature dependence of the growth rate is shown in Fig. 3-2. Self-limiting growth of InAs using TMIDMEA was observed over a temperature range of 350 to 520°C. The upper limit of this temperature region is 100°C higher than that using TMIn. Between 450 and 520°C, InAs/GaAs heterostructures can be grown using a self-limiting mechanism at a constant growth temperature.

With the ALE technique, the author and co-workers tried to grow $(InAs)_1/(GaAs)_1$ superlattices on GaAs substrates. The sample was planned to consist of a 500-nm-thick undoped GaAs buffer layer, a 12-period $(InAs)_1/(GaAs)_1$ layer, and a 30-nm-thick undoped GaAs cap layer. The growth temperature was 460°C, which is preferable to self-limiting growth for both InAs and GaAs. Both buffer and cap layers were grown by conventional MOVPE using triethylgallium (TEGa). Growth pressure was 15 Torr. The room-temperature photoluminescence spectrum is shown in Fig. 3-3. An emission peak was observed at 1.34 μm with a full width at half maximum (FWHM) of 28 meV. The FWHM indicates inhomogeneity in a dot ensemble in terms of dot size, strain, and composition as long as the inhomogeneity is very larger than the homogeneous broadening of single-dot emission spectra. A spectrum of the

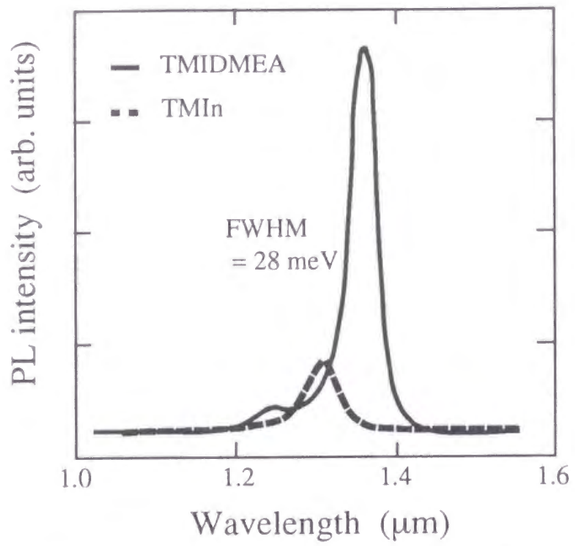

Figure 3-3 Room temperature photoluminescence spectra of $(InAs)_1/(GaAs)_1$ superlattices on (100) GaAs substrates. The spectrum of the sample grown using TMIDMEA shows a peak at 1.34 μm with a FWHM of 28 meV. The emission intensity is much stronger than that of the sample grown using TMIn.

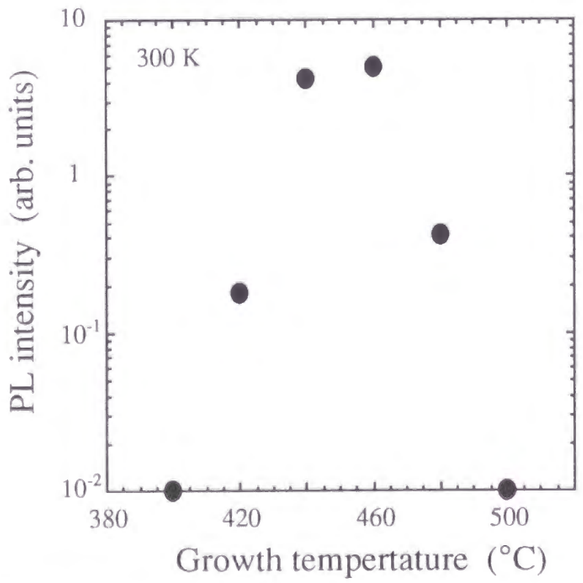

Figure 3-4 Photoluminescence intensity of ALS dots at 300 K as a function of growth temperature. The ALS dots were grown by 12 cycles of $(InAs)_1/(GaAs)_1$ alternate supply. Note that this figure is semi-log plot.

sample grown using TMIn as a substitute source material for TMIDMEA is shown as a reference. We can see that the use of TMIDMEA is better to obtain a high emission intensity.

Using TEM observation, the author found quantum dots in the alternately supplied layer instead of $(InAs)_1/(GaAs)_1$ superlattices. A plan-view image shows uniform dot-like microstructures of about 20 nm in diameter and covering an area of 5 - 10% (Fig. 2-29(a)). A cross-sectional dark field image, which is more sensitive to composition than a bright field image, indicates that spherical dots were self-assembled within an InAs/GaAs alternately supplied layer sandwiched by GaAs (Fig. 2-29(b)). The dots were about 10 nm in height and surrounded laterally by a quantum-well layer having almost the same thickness as that of the dots. The thickness of the quantum-well layer is definitely greater than that of the so-called wetting layer of SK islands [14 - 17]. Two clear upper and lower borders can be observed between the GaAs sandwiching layers and the dot layer. These characteristics suggest that the dots were not self-assembled by the conventional SK mode. According to EDX measurements, the composition at the center of the dots is $In_{0.5}Ga_{0.5}As$ and that in the quantum-well layer surrounding the dots is $In_{0.1}Ga_{0.9}As$.(Fig. 2-31).

3-2-2 Optimization of growth condition

In order to improve quantum dot crystal quality, various growth conditions, such as temperature, source supply amount, supply cycle number, and buffer layer composition, were optimized by checking the photoluminescence emission efficiency. Figure 3-4 shows the photoluminescence intensity versus growth temperature for dots grown at 12 cycles of $(InAs)_1/(GaAs)_1$. Growth temperature was critical. Above and below the optimized temperature, emission intensities rapidly decreased. The optimized source supply amount was less than one monolayer.

Changing the cycle of short-period growth and the indium composition of the $In_XGa_{1-X}As$ buffer layer gave the ALS quantum dots a wide-range wavelength tunability of between 1.2 and 1.5 μm via 1.3 μm. Figure 3-3 shows that emission from the ground level of ALS dots grown by 12 cycles of $(InAs)_1/(GaAs)_1$ was 1.34 μm, and that from the excited allowed level was 1.24 μm. Figure 3-5 shows photoluminescence wavelength as a function of the number of cycles. The buffer layer was $In_{0.05}Ga_{0.95}As$. When the alternate growth cycle number was

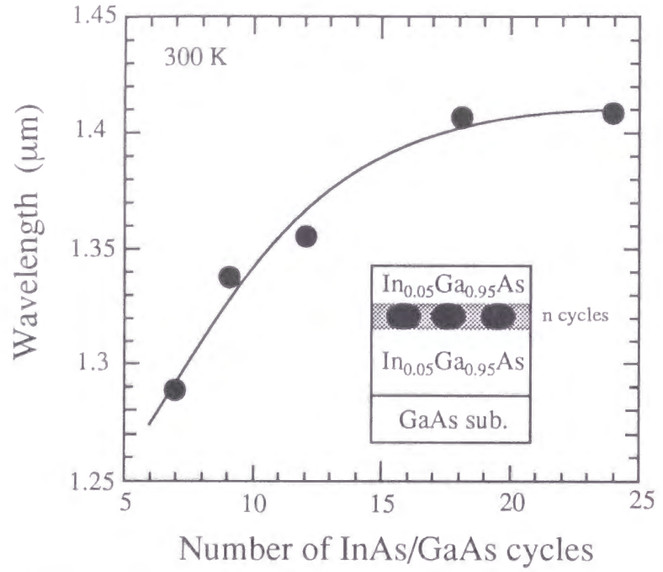

Figure 3-5 Photoluminescence wavelength at 300 K as a function of the number of cycles. The wavelength variation is due to changes in dot size.

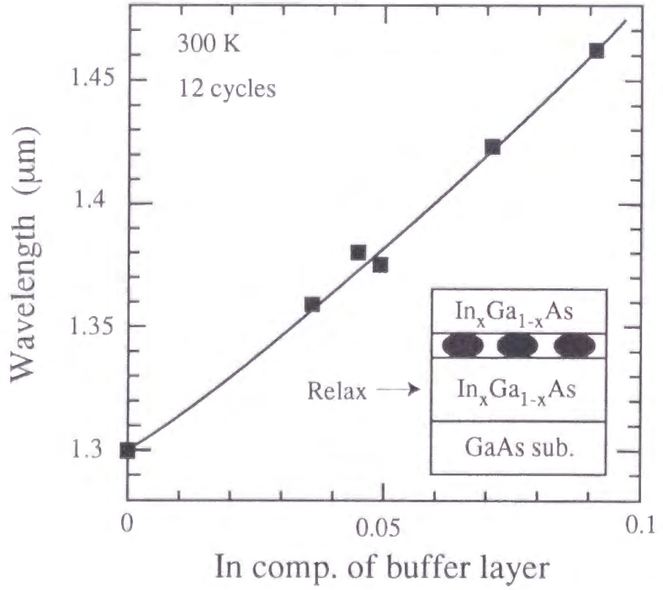

Figure 3-6 Photoluminescence wavelength at 300 K as a function of indium composition of the $In_xGa_{1-x}As$ buffer layer. With 12 cycles of alternate supply, the emission wavelength increased from 1.3 to 1.46 μm as x increased from 0 to 0.09. The reciprocal lattice mapping by X-ray diffraction indicated that an increase in x caused an increase in strain relaxation.

increased from 7 to 24, the emission peak wavelength increased from 1.29 to 1.41 μm. Figure 3-6 shows the photoluminescence wavelength as a function of the buffer-layer indium composition. When the indium composition of the buffer layer was increased from 0 (GaAs) to 0.09 ($In_{0.09}Ga_{0.91}As$), the emission peak wavelength increased from 1.3 to 1.46 μm at 12 cycles of InAs/GaAs. Since there was no distinct differences among the indium composition in dots measured by energy dispersive x-ray analysis (EDX), the author concluded that wavelength variations are caused by changes in dot size. After combining the above results concerning the number of supply cycles and indium composition of the buffer layer, the emission wavelength was continuously controlled from 1.2 to 1.5 μm. Quantum confinement in these samples are investigated in Chapter 4.

During the optimization of growth conditions, other growth sequences such as [In → Ga → As], [Ga → In → As], and [(In + Ga) → As] were tested, and the sequence [In → Ga → As] (hereafter, In-Ga-As) was found to be most effective to improve emission efficiency. In this sequence, the total group-III source amount (In and Ga) in a single cycle was set to less than one monolayer. With the In-Ga-As sequence, the concept of ALE was not adequate for growth of ALS dots, but the alternate supply of source materials is still unique for growth of 1.3-μm-emission dots.

Using the ALS dots grown under In-Ga-As optimized conditions, stripe lasers were fabricated (see Chapter 6). However, lasing was done at a higher-order excited level and at a low temperature because of insufficient optical gain due to the low sheet density of the ALS dots. In addition, since the PJE system was not equipped with gas supply lines sufficient to fabricate laser devices, a laser structure other than the quantum-dot active region had to be grown by other growth systems via an air-transfer process. This process possibly damaged the crystal severely.

3-3 Alternate supply growth by In-Ga-As sequence

In this section, the growth conditions of ALS quantum dots are further explored using the In-Ga-As sequence in a state-of-the-art MOVPE system, where two types of ALS quantum dots are obtained by changing the growth temperature and the alternate supply cycle.

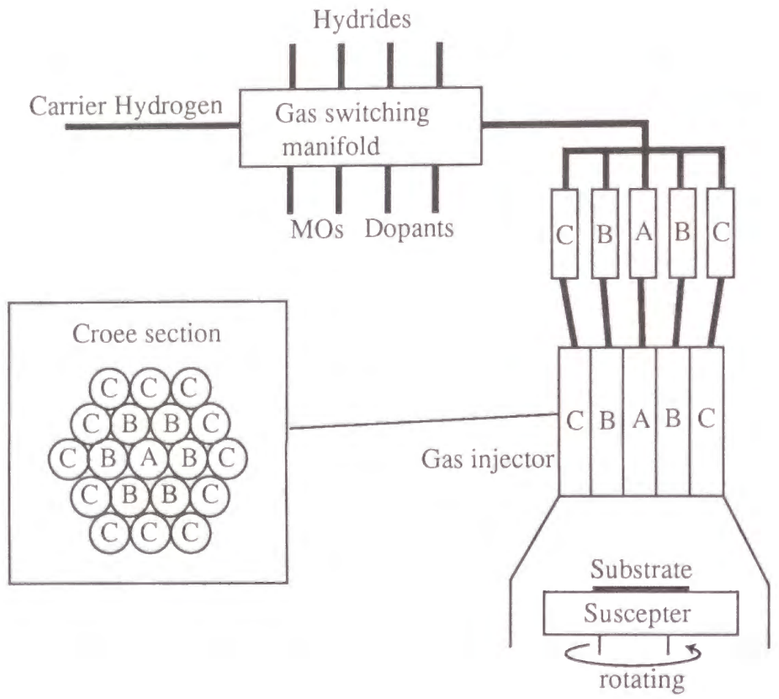

Figure 3-7 Schematic of MOVPE reactor. The inset shows the cross section of the multiple gas injector. Injectors are classified into three groups; A, B, and C, according to their radial location.

3-3-1 State-of-the-art metalorganic vapor phase epitaxy system

The state-of-the-art MOVPE system is a standard type designed by Fujitsu Laboratories to produce commercial optical semiconductor devices. Figure 3-7 is a schematic of the reactor, which has a vertical configuration with a wide-area inlet consisting of multiple gas injectors [18]. The injectors are arranged in a threefold honeycomb configuration so that inlet gas impinges perpendicularly in the entire area of the substrate. Organometallics, hydrides, and dopants are mixed with the main hydrogen carrier gas in a compact gas-switching manifold, then divided into subflows and introduced to the injectors. The flow rate of each injector is controlled by a mass flow controller that is designed to operate under low differential pressure. For the gas-handling system, a pressure-balanced vent-and-run configuration was used. The injectors are classified into three groups according to their radial rotation: A, B, and C. By fixing the flow rate of injectors at the same radial location, and changing the flow rate ratio for injectors at different radial locations, a wide area and axis-symmetric flow with a variety of radial flow velocity distributions was obtained, including a radially uniform velocity flow.

Self-limiting growth was again observed for InAs and GaAs at common temperatures with TMIDMEA and TMGa in the new MOVPE system. Note that the growth temperature indicated in this section does not agree with the temperature of the PJE reactor in Section 3-2. In comparing temperatures for self-limiting growth in each reactor, a growth temperature of 460°C for the PJE reactor in Section 3-2 corresponds to 520°C for the MOVPE reactor in this section. For the growth sequence of In-Ga-As, optimized source supply amounts were 2.0 seconds for TMIDMEA and 0.3 seconds for TMGa, corresponding to 0.5-monolayer indium and 0.1-monolayer gallium. The duration of the AsH_3 supply was fixed at 7 seconds. The H_2 purge was inserted after the TMGa and AsH_3 supply for 3 seconds and 0.5 seconds, respectively. TMIDMEA, TMGa, and AsH_3 sources had supply rates of 0.04, 4.6, and 40 cc per minute, respectively. A single cycle time of 12.8 seconds provided a very low growth rate of about 0.04 ML per second.

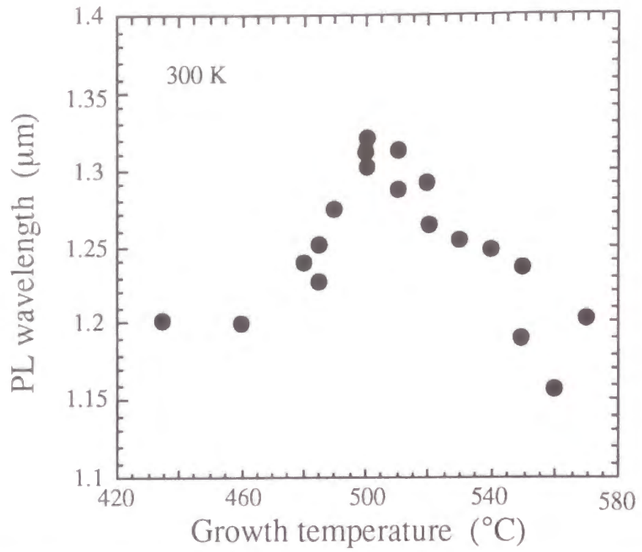

Figure 3-8 Wavelength of photoluminescence spectrum peak as a function of growth temperature for the 18 cycle of In-Ga-As sequence. The emission wavelength varied considerably between 1.2 and 1.3 μm, depending upon the growth temperature, with a 1.3 μm emission at around 500°C.

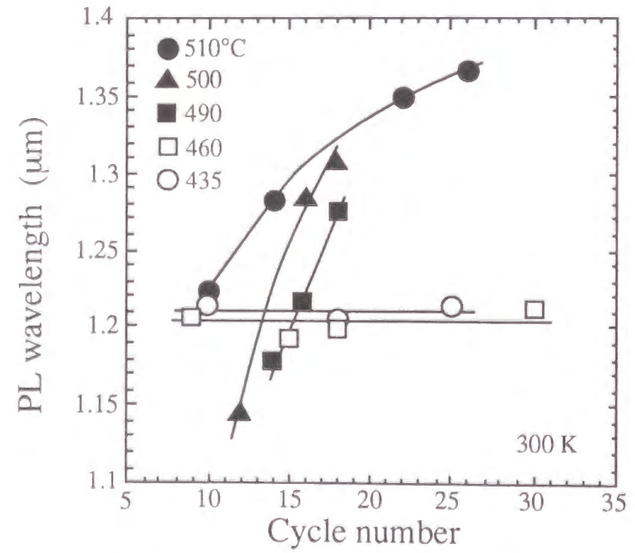

Figure 3-9 Peak wavelength of photoluminescence spectra as a function of the In - Ga- As cycle number grown at various temperatures. The relationship between the cycle number and the emission wavelength varies considerably between the two temperature ranges.

Samples were prepared as follows. First, a 0.25-μm GaAs buffer layer was grown on a (100)-GaAs substrate at 630°C. The growth was then interrupted for 10 minutes, and the substrate temperature was lowered to, for example, 520°C under an AsH_3 atmosphere. After an additional 0.05-μm GaAs buffer layer growth, the In-Ga-As layer was grown by the alternate source supply, followed by a growth of a 30-nm GaAs cap layer. The GaAs buffer and cap layers were grown by conventional MOVPE using TEGa and AsH_3. The growth pressure was 15 Torr throughout the growth of the structure.

Figure 3-8 shows the wavelength of a photoluminescence spectrum peak as a function of growth temperature for an 18-cycle In-Ga-As supply. The emission wavelength varied considerably between 1.2 and 1.3 μm depending on the growth temperature, with a 1.3-μm emission at around 500°C. Figure 3-9 shows the photoluminescence peak as a function of the cycle number at various growth temperatures. Variations in the relationship between the cycle number and the emission wavelength were found, depending on the temperature ranges (i.e., the dots grown at 435 and 460°C showed almost constant emission wavelength, but the emission wavelength of dots grown at 490 - 510°C increased as the cycle number increased.) This suggests that there are at least two types of ALS dots grown according to growth temperature.

Figures 3-10 and 3-11 are cross-sectional TEM images and photoluminescence spectra for two types of ALS dots. Both dots were grown at 520°C. Dots in Fig. 3-10(a) emit at 1.2 μm, and have a diameter of 15 nm and a height of 5 nm. Dots in Fig. 3-10(b) emit at 1.3 μm, and their diameter and height are 25 nm and 8 nm, respectively. The indium composition detected by EDX for type-A dots was almost the same as that for type-B dots, indicating that the longer photoluminescence wavelength is due to larger dot sizes. (Obtained indium atomic percentages were 15% for type-A dots and 12% for type-B dots. These values were not calibrated using the standard sample.) The quantum well layer surrounding quantum dots became thinner, like the wetting layer of the SK mode in the In-Ga-As sequence. This is because the supply of group-III source gases has been reduced to less than one monolayer. The photoluminescence intensity of 1.2-μm-emission dots is weaker than that of 1.3-μm-emission dots. The photoluminescence linewidth for the 1.3-μm-emission dots is narrow, typically with an FWHM of 30 - 50 meV, while the linewidth for type-A quantum dots is broad, typically

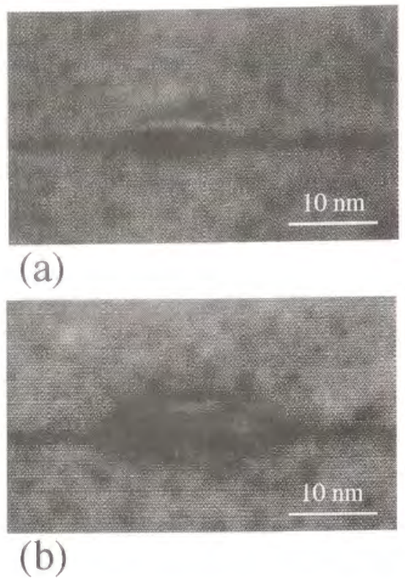

Figure 3-10 Cross-sectional TEM images of quantum dots: (a) 1.2-μm emission dots grown at 520°C with 14 cycles, (b) 1.3-μm emission dots grown at 520°C with 18 cycles.

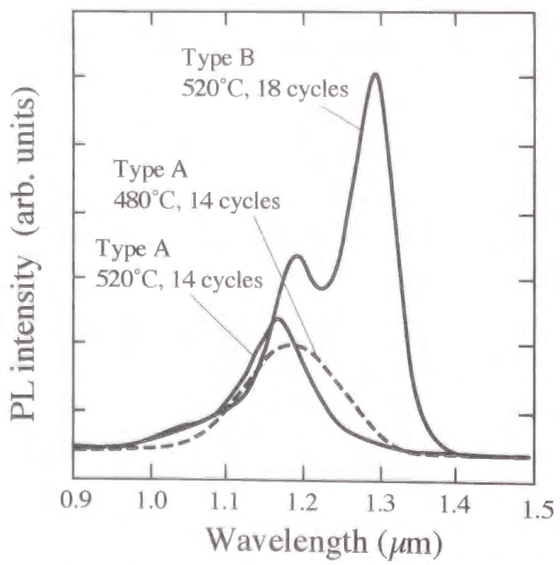

Figure 3-11 Photoluminescence spectra of type-A ALS dots and type-B ALS dots. Intensity of type-A dots is weaker than that of type-B dots. FWHM of photoluminescence for type-B dots is 40 meV, while that for type-A dots is 90 meV.

with a FWHM of 80 - 120 meV. A shorter wavelength peak in the spectra of 1.3-μm emission dots was assigned to be the second sublevel emission because, as excitation laser power increases, several peaks appear in the higher energy regime of the second peak (see Chapter 4).

The growth temperature and the supply cycle number govern the formation of 1.2-μm-emission and 1.3-μm-emission ALS dots. The author found that the 1.2-μm-emission dots grown with various growth temperatures and supply cycle numbers share common structural and spectral characteristics [12]. In this chapter, the author therefore calls the 1.2-μm-emission dots (i.e., grown at 435 - 460°C) 'type-A dots', and the 1.3-μm-emission dots (i.e., grown at 490 - 510°C) 'type-B dots'. Type-A ALS dots are similar to SK dots in that the emission wavelength is independent of the source supply amount.

3-3-3 Stacking of quantum dot layer

The author shows how vertical stacking proceeds in type-A and type-B quantum dots in the following. Vertically stacked quantum dot layers result in high optical gain in a laser cavity as long as quantum efficiency in the dots is not seriously damaged. Tersoff et al. demonstrated that the sizes and in-plane spacings of the dots become more uniform with the growth of successive layers [19] by using a simple model showing that new quantum dots tend to nucleate above buried quantum dots in a stacked structure. Because of these importance and interest, the stacking of quantum dot layers is a well-founded research subject [20 - 24].

The examined samples were triple-layered structures of type-A and type-B ALS dots with GaAs intermediate layers whose thicknesses varied from 10 nm to 30 nm. The growth temperature for both samples was set at 520°C. The cycle number of alternate supply was set to 14 and 18 for type-A and type-B, respectively. Figure 3-12 shows cross-sectional TEM images of the samples. TEM images of a single-layer structure are also shown for comparison. In both types, the vertical alignment of multistacked quantum dots occurred by thinning the GaAs intermediate layer, originated by a crystal lattice distortion induced by buried quantum dots. The vertical alignment occurs with a 15-nm intermediate layer for type B but not for type A because the lattice distortion is larger in type B due to a larger quantum dot volume. Vertically aligned quantum dots became larger toward the upper layers in triple-layered type-A dots with 10-nm intermediate layers, a phenomenon also observed in SK islands. The diameter of the dots at the top layer was about 35 nm, while the diameter of those at the bottom layer was about 25 nm.

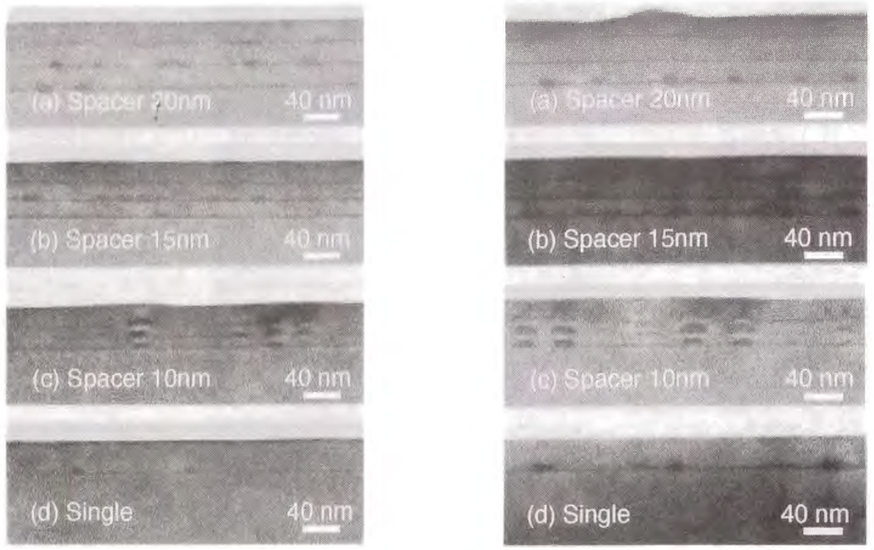

Figure 3-12 Cross-sectional TEM images of triple-layered structures of (A) type-A quantum dots grown with 14 cycles and (B) type-B quantum dots grown with 18 cycles. Growth temperature for both was 520°C. The GaAs spacers are 20 nm, 15 nm, and 10 nm. Single-layered structures are shown in (d).

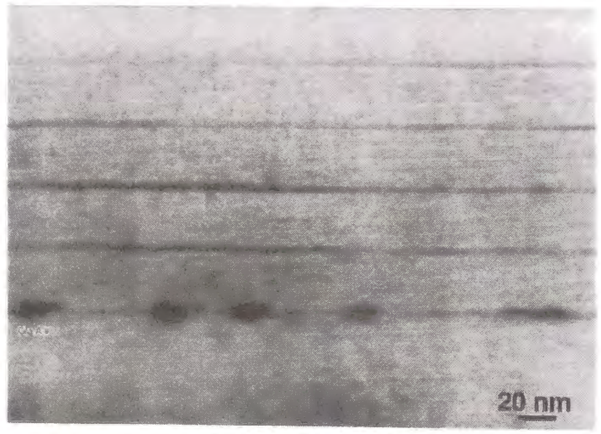

Figure 3-13 Cross-sectional TEM image of stacked ALS dots grown by PJE reactor. The composition of intermediate layer, buffer layer, and cap layer was GaAs. Thickness of the intermediate layer was 40 nm and the number of multiple-layer growth was five.

A unique phenomenon was found in the stacking of type-B quantum dots if the dots were separated with a thick GaAs intermediate layer. In the case of a 20-nm GaAs spacer, few dots were formed on the upper layers. For type-A quantum dots, a drastic decrease in density did not occur and similar structures were simply repeated. Similar multiple stacking behavior was observed in ALS dots grown via the In-As-Ga-As sequence in a PJE reactor (Fig. 3-13). The ALS dots were self-assembled only in the first grown layer. At the present stage, it is not known why the two types of dots display different multiple stacking behavior.

In the closing of this section, the author would like to demonstrate that the unique structure of ALS dots grown in a PJE reactor can be reproduced in a state-of-art MOVPE system. The dots were surrounded by quantum wells having the same thickness as the dots. To reproduce the structure, one method uses the In-As-Ga-As sequence again, and the other uses an InGaAs overgrowth layer to cover the island shape. TEM images of Figs. 3-14 and 3-15 shows the results of the two methods. In Fig. 3-14, the upper and lower borders of the quantum well are not flat since growth conditions had not yet been optimized, but the dots emit at 1.3 μm. The merit of the method presented in Fig. 3-15 is that we can intentionally determine the composition of the overgrowth quantum well layer (an $In_{0.2}Ga_{0.8}As$ layer was used here), and also, a 1.3-μm emission can be achieved. Using the overgrowth method, the author achieved the first 1.3-μm continuous wave (CW) lasing of quantum dot lasers at room temperature (see Chapter 6). In addition, the author found that the temperature sensitivity of emission wavelengths of quantum dots can be controlled with the method. Details are presented in Section 3-5. The experiments suggest that quantum dot lasers might achieve a high stability of lasing wavelength against ambient temperature variations in the 1.3-μm wavelength region.

3-4. Growth process of dots

So far in this chapter, ALS dots have been shown to be very different from SK islands. (An exception is type-A ALS dots, which have many common characteristics with SK dots. The author, therefore, assigns type-A quantum dots as a kind of SK islands.) The main reason why ALS dots emit at a wavelength of 1.3 μm or longer is probably their structure that is thicker than that of SK islands. The FWHM of the emission spectra of ALS dots is 30 - 50

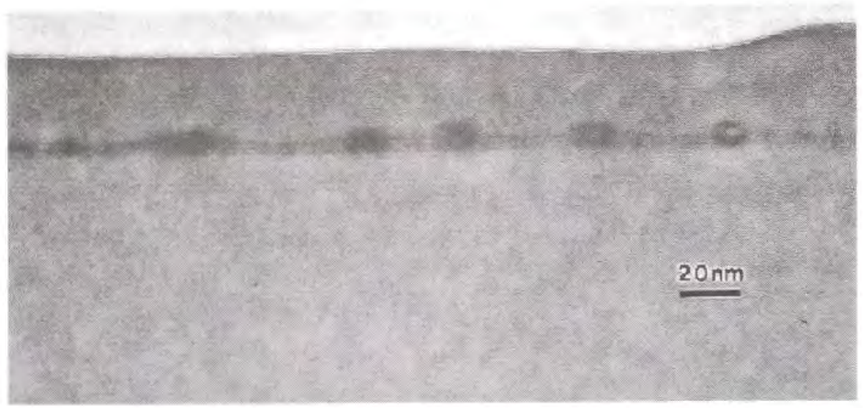

Figure 3-14 TEM image of ALS dots grown by an In-As-Ga-As sequence in the state-of-the-art MOVPE system. Thick quantum well is observed around the quantum dots.

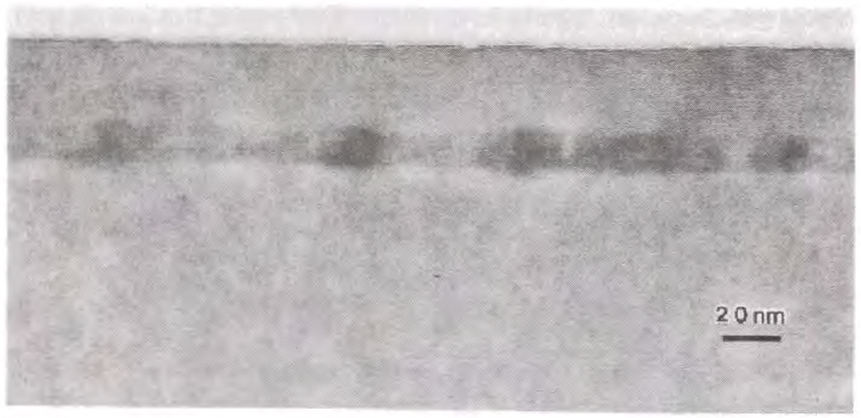

Figure 3-15 TEM image of ALS dots grown by an In-Ga-As sequence embedded by an $In_{0.2}Ga_{0.8}As$ overgrowth layer. The structure is similar to the ALS dots grown in PJE system.

meV, which is much smaller than the 80 - 120 meV of SK islands. ALS dots are buried in a quantum well with clear upper and lower borders against the GaAs. The thickness of the quantum well decreases and becomes like that of a wetting layer in SK-mode growth as the supply amount of group-III sources is reduced. The area coverage of the dots is 5 - 10%, which is definitely smaller than the 20 - 40% of SK islands. As the alternate supply cycle increases, dot emission wavelength increases, whereas SK islands are almost insensitive to the supply amount of InAs.

As the supply cycle increases, three-dimensional structures become large in the growth of ALS dots. The process gives us a hint to identify the growth mechanism of the ALS dots. Primal nuclei islands are self-assembled probably by the thermodynamical balance between strain energy and surface energy. If only indium is supplied after primal islands form, dot size hardly changes, as in the case of usual SK growth, since the islands have already reached an equilibrium point. A supply of gallium to the islands decreases the total strain energy, making it possible to add further indium to the islands and thus increases dot size in a direction perpendicular to the growth surface. This process repeats itself until the dots reach another equilibrium point.

The author believes that the growth process of ALS dots is not exactly the same for the supply sequences of In-As-Ga-As and In-Ga-As, although both sequences provide a unique 1.3-μm emission. The plan-view TEM images in Fig. 3-16 and 3-17 indicate how the indium source gas contents in a supply cycle affect the structure of the ALS dots with the two growth sequences. For the In-Ga-As sequence, surface density increases but the diameter does not change after the increase of source gas contents (Fig. 3-16). For the In-As-Ga-As sequence, surface density does not change but the dot size becomes large after the increase of source gas contents (Fig. 3-17). During the In-As-Ga-As sequence, the supply of AsH_3 fixes metal islands on the growth surface by forming a semiconductor. The author suppose that the metal island constitution at AsH_3 supply is the origin of the difference between the figures. In the In-As-Ga-As sequence, only In or Ga metal islands exist on the surface, but in the In-Ga-As sequence, both In and Ga metal islands exist. Therefore, in the In-As-Ga-As sequence, InAs and GaAs are piled up step-by-step. However, in the In-Ga-As sequence, InAs and GaAs are crystallized in one layer. If the indium source gas content is raised, the number of In metal islands increases on the surface, and the island size does not change if other particles such as the Ga metal islands do not interfere with In metal island formation.

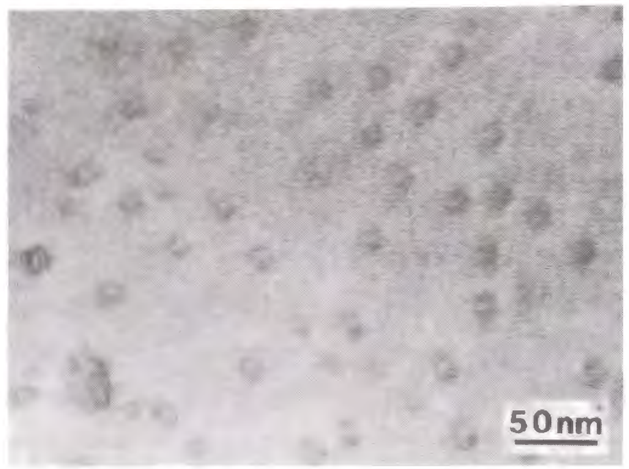

(a)

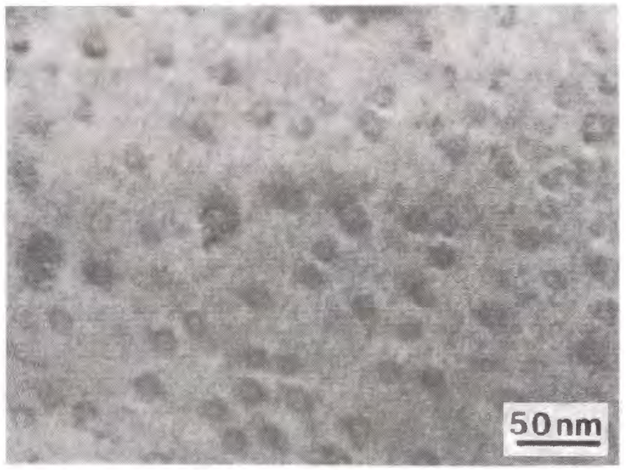

(b)

Figure 3-16 Plan-view TEM images of the ALS dots grown by 18 cycle of the In-Ga-As supply sequence: (a) the standard case and (b) the case when indium source gas content in a supply cycle was raised by 20%.

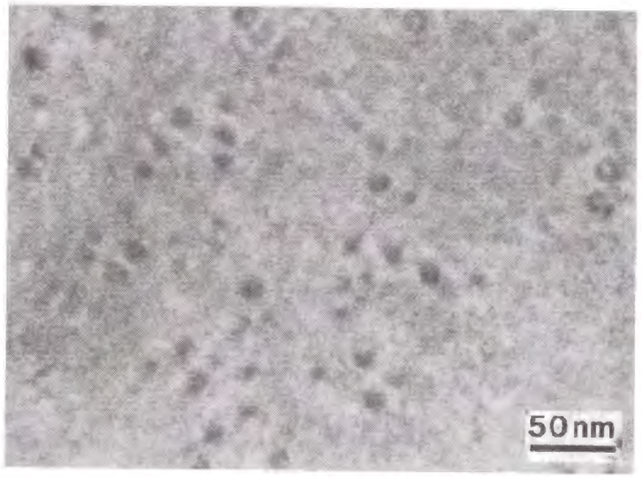

(a)

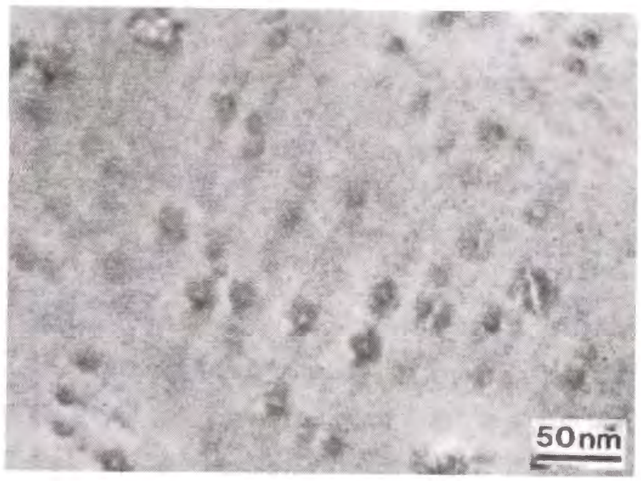

(b)

Figure 3-17 Plan-view TEM images of the ALS dots grown by 12 cycle of the In-As-Ga-As supply sequence: (a) the standard case and (b) the case when indium source gas content in a supply cycle was raised by 100%.

The problem of low surface density in ALS dots probably arises from a low source supply amount at primal nuclei formation. Therefore, the problem can be solved by raising the number of the nuclei. If high-density SK islands are formed on the surface and an alternate supply is then started, sources will gather at the islands, resulting in high ALS dot densities. Figure 3-18 shows a trial of the above, a plan-view TEM image of a sample grown by 10 cycles of the In-Ga-As sequence after a supply of 2 monolayer InAs. The figure indicates the formation of quantum dots with a diameter of about 20 nm, and the increase of the surface density (see Fig. 2-29 (a)). Figure 3-19 shows photoluminescence spectra of the sample at room temperature. A 1.3-μm emission with good emission efficiency was obtained by this hybrid (SK + ALS) growth method, suggesting that the method can solve the dot density problems. The author expects that the hybrid method will rectify the incapable stacking of ALS dots because SK dots can be stacked well.

3-5 Suppression of temperature sensitivity of interband emission energy

As briefly premised in Section 3-3, the temperature sensitivity of a band gap in ALS dots was greatly suppressed by the InGaAs-layer overgrowth, and that is the subject of this section.

Lasing wavelengths of semiconductor lasers change greatly as a function of ambient temperature, primarily due to temperature-induced changes in the band gap energy of the active region. This phenomenon is a serious problem for lasers that work in fiber optics data transition systems, such as wavelength division multiplexing (WDM) systems, where the lasing wavelength should be strictly controlled. To solve the problem in the device itself, development of new materials whose band gap is constant against temperature variations is required. TlInGaP [25] and GaInAsBi [26], which are alloys of semiconductors and semimetals, were proposed for this purpose. These materials can be lattice-matched to InP and InAs substrates, respectively, and the weak dependence of their band gap energy on temperature has been experimentally demonstrated thereafter [27 - 29]. However, high-quality epitaxial growth of these materials is still under investigation, and a practical laser structure has not yet been provided with these materials.

Figure 3-18 Plan-view TEM image of a sample grown by 10 cycles of an In-Ga-As sequence after supply of 2-monolayer In and As. Quantum dots having an in-plane diameter of 20 nm were observed.

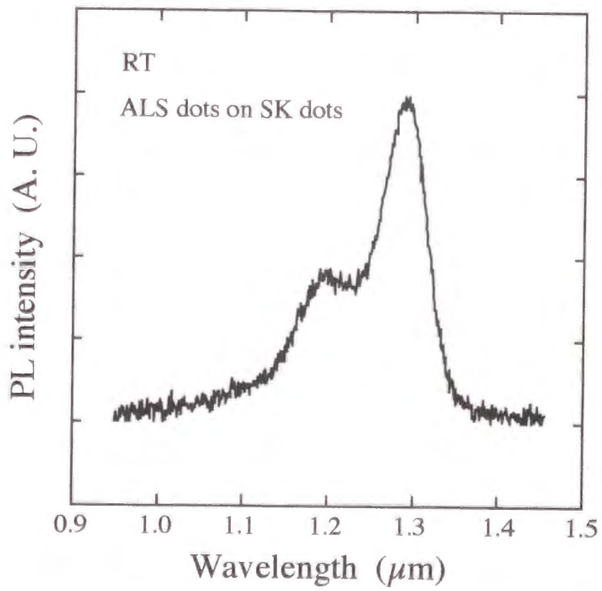

Figure 3-19 Photoluminescence spectrum of a sample grown by 10 cycles of the In-Ga-As sequence after supply of 2-monolayer In and As. A 1.3-μm emission was obtained at room temperature.

A stable threshold current against temperature variations is generally a tradeoff with stable lasing wavelength. In quantum-well lasers operating at a uniform carrier density, the lasing wavelength will be greatly shifted according to any band gap changes since the maximum gain is obtained off their band edge at almost the same energy. In quantum dot lasers where state density is similar to the delta-function, this situation is very severe. Lasing wavelengths of quantum dot lasers must follow the band gap changes exactly. Therefore, the insensitivity of band gap to ambient temperatures is especially significant for quantum dots in aiming laser application.

The author found that an overgrowth of an InGaAs layer on self-assembled InGaAs/GaAs quantum dots drastically modified the strain distribution around the dots, and that the interband emission energy became less responsive to temperature under the modified strain field [30]. The findings open up an optimistic future where quantum dot lasers achieve high stability in both threshold current and lasing wavelength against ambient temperature variations since quantum dot lasers have already the potential of achieving temperature-insensitive threshold current.

3-5-1 Embedded dot structure

Growth was performed in a state-of-the-art MOVPE system, as in Section 3-3. The growth temperature was 520°C. Self-assembled quantum dots were grown by 18 cycles of alternate supply of (TMIDMEA)-(TMGa)-(AsH_3) on a GaAs substrate (type-B ALS dots). The dots were buried in a 10-nm-thick compressively-strained $In_XGa_{1-X}As$ ($0 \le x \le 0.3$) layer and capped by a 30-nm GaAs layer.

Cross-sectional TEM images of samples are shown in Fig. 3-20. Dot structure without an InGaAs overgrowth (i.e., x = 0) consists of a two-dimensional layer and three-dimensional islands on it (Fig. 3-20(b)). With the InGaAs overgrowth, a dark contrast expands from the top of dot in the overgrowth layer (Fig. 3-20(a)). Spacial distribution of the indium composition in cross-sectional samples was evaluated by EDX (Fig. 3-21). The electron beam was focused to a diameter of 1 nm, and signals were calibrated using four reference samples, 20-nm-thick strained $In_XGa_{1-X}As$ (x = 0.1, 0.2, 0.25, 0.3) single quantum wells grown on a GaAs substrate. The calibrated indium composition was 0.5 at the center of a dot and 0.3 at the overgrowth layer beside the dot. Remarkably, the composition was also 0.3 on the dot in the

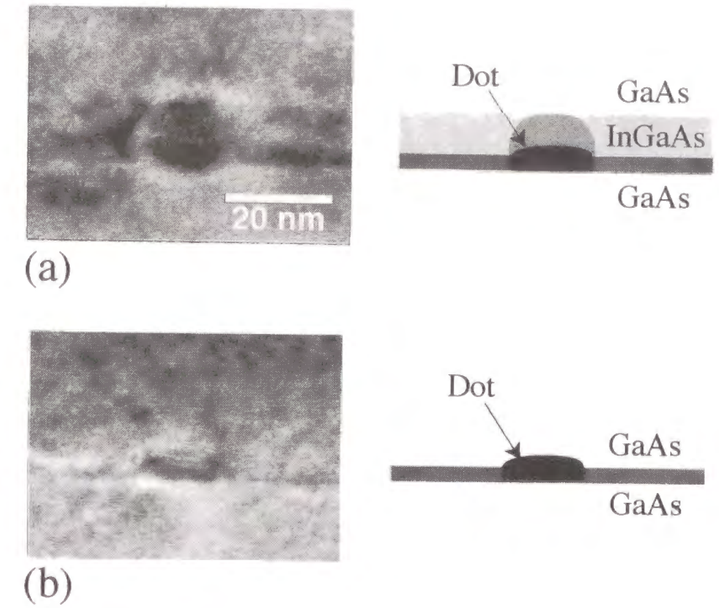

Figure 3-20 Closs-sectional TEM images of ALS dots: (a) buried in a 10-nm-thick strained $In_{0.3}Ga_{0.7}As$ overgrowth layer followed by a GaAs layer, and (b) covered with only a GaAs layer. Structures are illustrates in right-hand figures.

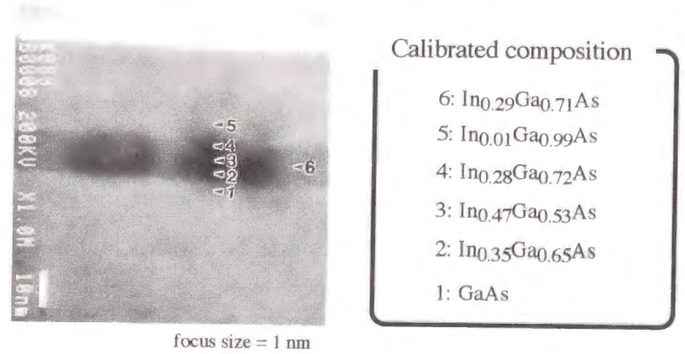

Figure 3-21 Energy dispersive X-ray (EDX) analysis of cross-sectioin sample. Data were calibrated using four reference samples composed of a 20-nm-thick strained InxGa1-xAs (x = 0.1, 0.2, 0.25, 0.3) layer grown on a GaAs substrate.

overgrowth layer where the dark contrast expands. The result suggests that the indium composition in the overgrowth layer was uniform, but additional lattice distortion is generated on the dots. The author compared cross-sectional TEM images of samples having various indium compositions in the overgrowth layer, and found that the dark contrast on dots got strong as x rose. The result suggests that lattice distortions in the overgrowth layer on the dots enlarged as x rose.

3-5-2 Photoluminescence characteristics

Photoluminescence spectra of the samples were measured at between 4.2 K and 300 K. For the measurements, samples were set in a temperature-controlled cryostat for the measurements at over 20 K, and immersed in liquid helium for 4.2-K measurements. A 514.5-nm Ar^+ laser beam was focused on the sample surface, and luminescence was monochromed by a 50-cm monochrometer and detected by an InGaAs photo-multiplier detector cooled at -80°C. Emission wavelength was found to got longer as the indium composition of the overgrowth layer increases (Fig. 3-22) [31]. This is probably because the in-plane potential barrier height was reduced by the overgrowth layer, and also because the generated strain field on dots enlarged the actual dot size.

Figure 3-23 shows the photoluminescence spectra of dots with an $In_{0.3}Ga_{0.7}As$ overgrowth layer at between 20 and 200 K. Intensity has been normalized. Ground and second sublevel peaks were observed up to 200 K. Since the peak intensity of the ground level was drastically reduced at over 200 K, the relative intensity of peaks below 1.3 μm appeared strong at 200 K. Emission energy of the ground level showed a gradual shift in the 1.3-μm region during a temperature increase. Since the shape and width of ground-level peaks were almost uniform at these temperatures, the author supposes that the dot structure worked as a quantum dot up to 200 K.

Figure 3-24 compares the emission energy shift of the ground level among samples as a function of temperature. The shift of bulk GaAs is superimposed as a reference [32]. The results varied depending on x. Emission energy at x = 0, 0.1, and 0.2 decreased monotonously with temperature increases, and the shifts are almost uniform and similar to that of bulk GaAs. The results at x = 0.25 and 0.3 were remarkable. At x = 0.25, energy shifts stopped above 150 K. At x = 0.3, the shift between 4.2 K and 200 K was less than half that of bulk GaAs. The

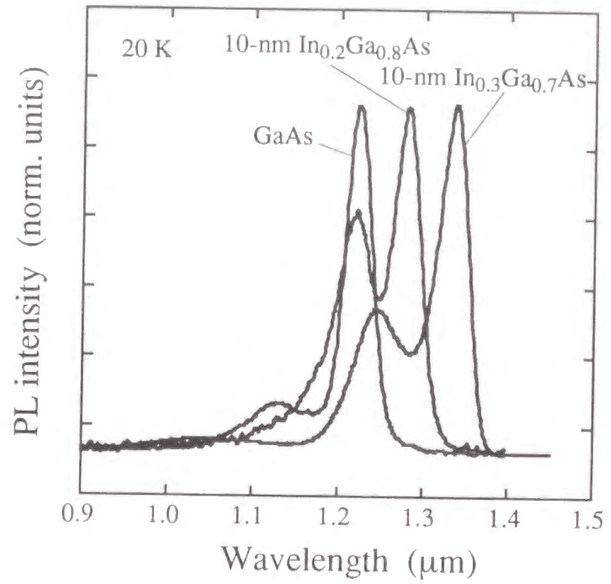

Figure 3-22 Photoluminescence spectra of samples where dots are buried in overgrowth layer having various composition. As the indium composition of the overgrowth layer increased, emission wavelength got longer.

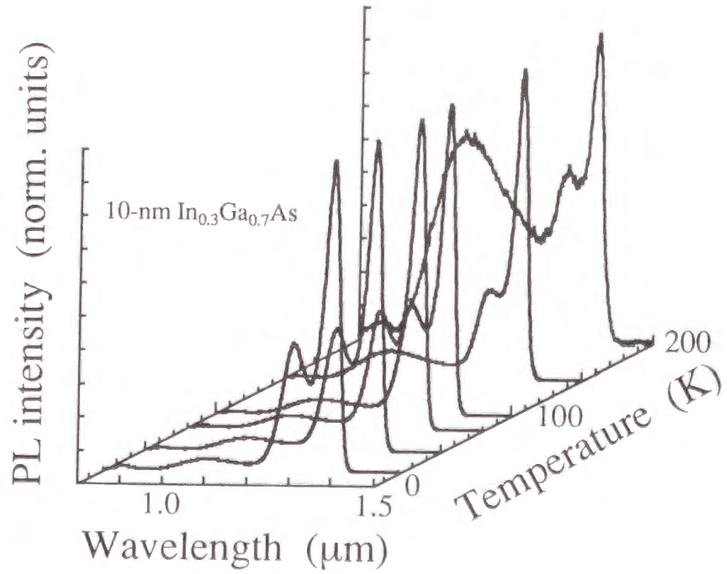

Figure 3-23 PL spectra of dots buried in a 10-nm-thick In0.3Ga0.7As overgrowth layer at between 20 and 200 K. Intensity has been normalized.

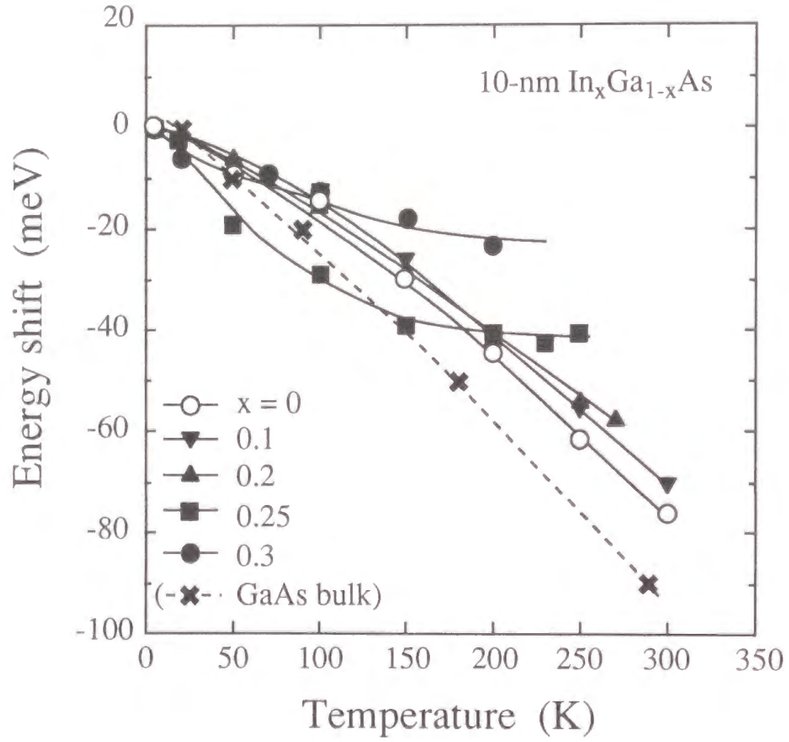

Figure 3-24 Emission energy shift of dots buried in a 10-nm-thick $In_xGa_{1-x}As$ ($0 \le x \le 0.3$) overgrowth layer as a function of temperature. Energy shift of bulk GaAs is indicated as a reference.

results suggest that the temperature sensitivity of emission energy is controlled by the overgrowth layer.

In addition to the ground-level emission wavelength, the author found that level separation was also non-linear to temperature at x = 0.3. In Fig. 3-25, we can see that energy separation between the ground and the second level decreased linearly during temperature increases without an overgrowth layer but not with an $In_{0.3}Ga_{0.7}As$ overgrowth layer.

3-5-3 Discussion on mechanism

Let me consider a mechanism for the temperature insensitive emission energy of InGaAs-covered dots. A major cause of semiconductor band gap shrinkage with temperature increases is thermal expansion of the material lattice constant, which is an essential phenomenon. In quantum wells, band filling in **k** space causes a shift of emission energy, but it cannot be expected in quantum dots having the delta-functionlike state density. Carrier distribution among dots having non-uniform energy may be related to the emission peak shift. However, the distribution is determined by a carrier capture process that is random and independent of temperature unless dot-potential depth is shallow enough for carriers to be thermally excited out of dots, or unless dot-to-dot distance in real space is small enough for carriers to tunnel via phonon scattering (neither condition was satisfied in the samples). The author then considered that a lattice-constant variation itself provides the most likely explanation for the temperature insensitive emission energy. The author supposes that a three-dimensional strain distribution peculiar to the dot structure is a key issue.

A simple model for the InGaAs-buried quantum dot structure helps us to consider what is the point in the mechanism. Figure 3-26 illustrates the model. Here, cylindrical $In_{0.5}Ga_{0.5}As$ dots are sandwiched by GaAs and surrounded by an $In_vGa_{1-v}As$ ($0.5 > v \ge 0$) layer. The band gap energy shift of dots with a temperature increase is given by $\Delta E = \Delta E_{bulk} + \Delta E_{strain} + \Delta E_{offset}$, where ΔE_{bulk} represents the shift due to a change of bulk band gap, ΔE_{strain} represents the shift due to a change of lattice strain, and ΔE_{offset} represents the shift due to a change of band offset. ΔE_{offset} is secondary and negligible compared with the other two shifts. The lattice constant of InGaAs material expands simply as temperature increases, and thus, $\Delta E_{bulk} < 0$. Let me check the temperature dependence of ΔE_{strain}. Thermal lattice expansion in

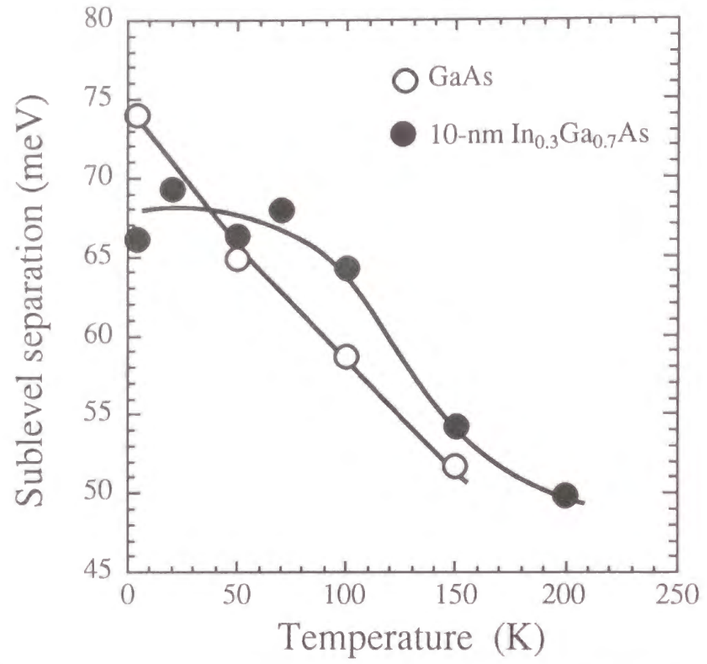

Figure 3-25 Energy separation between the ground and the second sublevel as a function of temperature for sample with or without a 10-nm-thick $In_{0.3}Ga_{0.7}As$ overgrowth layer.

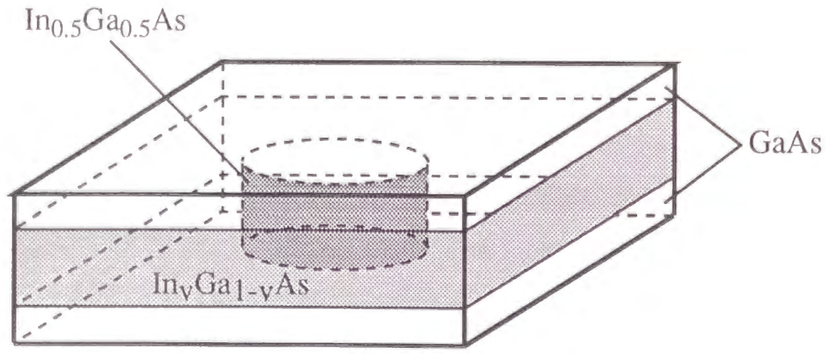

Figure 3-26 Schematic of the very simple model for InGaAs-buried quantum-dot structure. Cylindrical $In_{0.5}Ga_{0.5}As$ dot is surrounded by $In_yGa_{1-y}As$ layer and sandwiched by GaAs layers.

the structure governs ΔE_{strain}. Since the thermal line expansion coefficient for GaAs (6.4×10^{-6} K^{-1}) is larger than that for InAs (5.2×10^{-6} K^{-1}) [33], thermal lattice expansion is larger in GaAs than in InGaAs. Assuming that the in-plane lattice match is complete, the perpendicular lattice distortion of the InGaAs layer reduces as temperature increases. Here, the strain in the dots is compressive, $\Delta E_{strain} < 0$. Since ΔE_{strain} has the same sign as ΔE_{bulk}, small $|\Delta E_{strain}|$ reveals a small emission energy shift. As the indium composition of the InGaAs layer increases, the emission shift due to $|\Delta E_{strain}|$ increases. However, the dots are compressively strained not only in-plane but also perpendicularly. Therefore, in quantum dots, the value of $|\Delta E_{strain}|$ due to perpendicular lattice distortion decreases as the indium composition of the surrounding InGaAs layer gets closer to that of the dots.

However, temperature-insensitive energy shifts over 150 K in Fig. 3-24 cannot be explained by the simple model above since ΔE_{strain} cannot cancel ΔE_{bulk}. The problem in the model may be that the strain field in the dot structure was oversimplified. Although a practical dot structure is too complex to understand completely, a strain field modified by an overgrowth layer is known to not be cylindrically symmetrical but multi-axial. It is not surprising that multi-axial asymmetrical lattice distortion does not change linearly with temperature [34, 35]. Also, we know that the line expansion coefficient is not linear to temperature variations [37].

The author calculated the strain field and resulting wave function of embedded dot structures using the finite element method. Figure 3-27 shows the division of voxel for the finite element method and calculated displacement of lattice plane at the positions indicated by arrows. The author calculated in the quarter area because of symmetry of the system. The author here assumed a pyramid-shaped SK dot structure [36] in which the indium composition (= x) of both dots and wetting layer was 0.5. The x of the overgrowth layer was set to be 0.22. Dot size was assumed to be 160 Å on x- and y-axes, and 112.5 Å on the z-axis. The thickness of wetting layer was assumed to be 7.5 Å and that of the overgrowth layer to be 105 Å. An interesting result is that the contour of the displacement of lattice plane is far from a pyramid shape. Plane (b) is very hollow just under the dot, and more remarkably, plane (c) is also hollow in the center of quantum dot. Conversely, the overgrowth layer swells everywhere near the dot. By solving the Shrödinger equation under the model in three dimensions, we can calculate sublevel energy in the buried dot structure. Figure 3-28 shows an example: heavy-hole wave function for the ground and the second levels at plane (d). The second level is

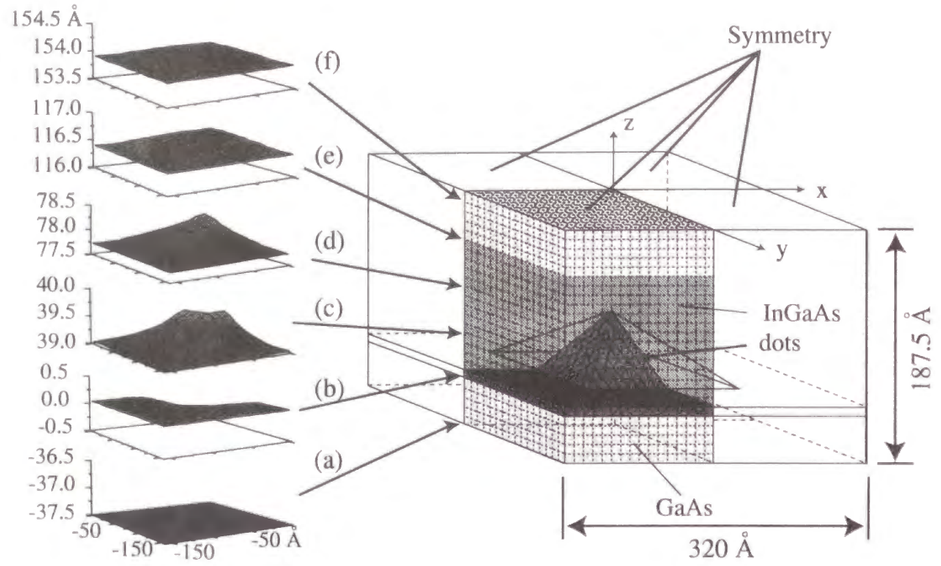

Figure 3-27 The division of voxel for the finite element method and calculated displacement of lattice plane at the position (a) - (f) indicated by arrows. The author calculated in the quarter area because of symmetry of the system, assuming the pyramid-shaped SK dot structure. The indium composition of dot, wetting layer, and overgrowth layer is 0.5, 0.5, and 0.22. Dot size is 160 Å in x- and y-axis, and 112.5 Å in z-axis. Thickness of wetting layer is 7.5 Å and that of overgrowth layer is 105 Å.

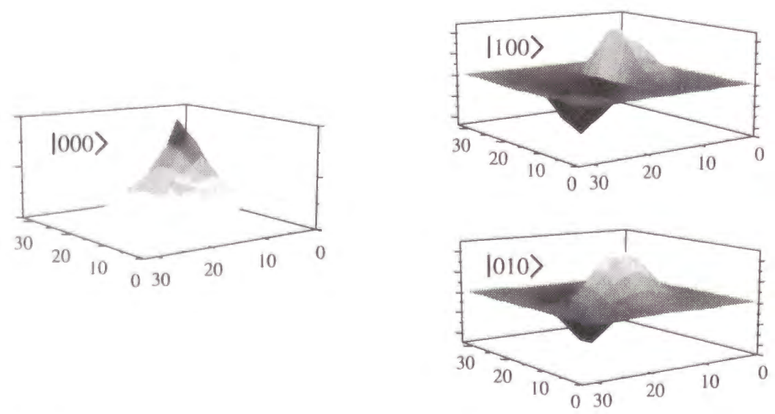

Figure 3-28 Heavy-hole wave function for the ground and the second level at the plane (d). The second level is degenerated with the symmetric dot structure.

degenerated with the symmetrical dot structure. If non-linear dependence of the line expansion coefficient to temperature is taken into account in the calculation, the mechanism of temperature insensitivity of emission energy will be understood in the future [37].

3-6 Summary

This chapter reviewed the growth of ALS quantum dots that are produced by an alternate supply of source materials in an amount of one monolayer or less. In Section 3-2, ALS dots grown with a sequence of In-As-Ga-As in a PJE reactor were described. The dots have a 1.3-μm emission and narrow spectrum linewidth of 28 meV. The quantum dots also acquire great controllability in emission wavelength by an adjustment in the cycle number and the composition of buffer layers on which the dots are grown. In Section 3-3, ALS dots grown with a sequence of In-Ga-As in a state-of-the-art MOVPE system were described. The dots grown at various growth temperatures and by various supply cycle numbers were categorized into two types by photoluminescence characteristics. Difficulty in multiple-layer growth of ALS dots were presented. In Section 3-4, a possible picture of the growth process of ALS dots is discussed. Based on the discussion, the author showed that the surface density of the ALS dots can be raised with hybrid growth in an SK and ALS mode. In Section 3-5, suppression of the temperature sensitivity of interband emission energy from dots using an InGaAs-layer overgrowth layer is presented, and this offers the possibility that quantum dot lasers will achieve high stability in both threshold current and lasing wavelength against ambient temperature variations.

References

[1] I. N. Stranski and L. Krastanow, Akad. Wiss. Wien Math.-Natur., IIb 146, 797 (1937).

[2] D. J. Eaglesham, and M. Cerullo, Phys. Rev. Lett. 64, 1943 (1990).

[3] S. Guha, A. Madhukar, and K. C. Rajkumar, Appl. Phys. Lett. 57, 2110 (1990).

[4] C. W. Snyder, B. G. Orr, D. Kessler, and L. M. Sander, Phys. Rev. Lett. 66,3032 (1991).

[5] M. Tabuchi, S. Noda,. and A. Sasaki, in Science and Technology of Mesoscopic Structures, Edited by S. Namba, C. Hamaguchi, and T. Ando (Springer, Tokyo) p. 379, 1992.

[6] D. Leonard, M. Krishnamurthy, C. M. Reaves, S. P. DenBaars, and P. M. Petroff, Appl. Phys. Lett. 63, 3203 (1993).

[7] D. Bimberg, QUEST Workshop on Quantum Structures, Colloquium Abstracts, Santa Barbara, p.15, 1994.

[8] A. Madhukar, Q. Xie, P.Chen, and Konkar, Appl. Phys. Lett. 64, 2727, (1994).

[9] J. M. Moison, F. Houzay, F. Barthe, L. Leprince, E. André, and O. Vatel, Appl. Phys. Lett. 64, 196 (1994).

[10] K. Mukai, N. Ohtsuka, M. Sugawara, and S. Yamazaki, Jpn. J. Appl. Phys., 33, L1710 (1994).

[11] K. Mukai, N. Ohtsuka, H. Shoji, and M. Sugawara, Appl. Surface Science, 112, 102 (1997).

[12] K. Mukai, M. Egawa, M. Sugawara, and N. Ohtsuka, Semicond. and Semimetals, vol. 60, chap. 3, 1999 (Academic Press Inc. NewYork).

[13] K. Mori, and S. Usui, Appl. Phys. Lett., 60, 1717 (1992).

[14] A. Krost, F. Heinrichsdorff, D. Bimberg, A. Darhuber, and G. Bauer, Appl. Phys. Lett. 68, 785 (1996).

[15] R.T. Ramachandran, R. Heitz, P. Chen, and A. Madhukar, Appl. Phys. Lett. 70, 640 (1997).

[16] R.T. Ramachandran, R. Heitz, P.N. Kobayashi, A. Kalburge, W. Yu, P. Chen, and A. Madhukar, J. Cryst. Growth 175/176, 216 (1997).

[17] M. Kitamura, M. Nishioka, R. Schur, and Y. Arakawa, J. Cryst. Growth 170, 563 (1997).

[18] M. Kondo, A. Kuramata, T. Fujii, C. Anayama, J. Okazaki, H. Sekiguchi, T. Tanahashi, S. Yamazaki, and K. Nakajima, J. Cryst. Growth, 124, 265 (1992).

[19] J. Tersoff, C. Teichert, and G. M. Lagally, Phys. Rev. Lett. 76, 1675 (1996).

[20] S.T. Kuan, and S.S. Iyer, Appl. Phys. Lett. 59, 2242 (1991).

[21] Y.J. Yao, G.T. Andersson, and L.G. Dunlop, J. Appl. Phys. 69, 2224 (1991).

[22] Q. Xie, A. Madhukar, P. Chen, and P.N. Kobayashi, Phys. Rev. Lett. 75, 2542 (1995).

[23] S.G. Solomon, A.J. Trezza, F.A. Marshall, and S.J. Harris, Jr., Phys. Rev. Lett. 76, 952 (1996).

[24] N.N. Ledentsov, J. Bohrer, D. Bimberg, V.I. Kochnev, V.M Maximov, S.P. Kop'ev,, I.Zh. Alferov, O.A. Kosogov, S.S. Ruvimov, P. Werner, and U. Gosele, Appl. Phys. Lett. 69, 1095 (1996).

[25] H. Asahi, K. Yamamoto, K. Iwata, S. Gonda, and K. Oe, jpn. J. Appl. Phys., 35, L876 (1996).

[26] H. Okamoto, and K. Oe, jpn. J. Appl. Phys., 37, 1608 (1998).

[27] K. Koh, H. Asahi, M. Fushida, K. Yamamoto, K. Takenaka, K. Asami, S. Gonda, and K. Oe, J. of Cryst. Growth, 188, 107 (1998).

[28] H. Okamoto and K. Oe, proc. InP and Related Materials '98 pp. 60.

[29] K. Oe and H. Okamoto, proc. PD paper in InP and Related Materials '98, FB3-3.

[30] K. Mukai, and M. Sugawara, Appl. Phys. Lett., 74, 3963 (1999).

[31] K. Nishi, H. Saito, and S. Sugou, Appl. Phys. Lett., 74, 1111 (1999).

[32] K. P. O'Donnel and X. Chen, Appl. Phys. Lett., 28, 2924 (1991).

[33] for instance, "III-V Mixed Crystals", edited by H. Nagai, S. Adachi, and T. Fukui (Corona, Tokyo, 1988, in Japanese), p. 52.

[34] S-J. Kim, H. Asahi, K. Asami, M. Takemoto, M. Fudeta, and S. Gonda, jpn. J. Appl. Phys., 37, 1540 (1998).

[35] D. E. Wohlert, S. T. Chou, A. C. Chen, K. Y. Cheng, and K. C. Hsieh, Appl. Phys. Lett., 68, 2386 (1996).

[36] S. Noda, T. Abe, and M. Tamura, Phys. Rev. B58, 7181 (1998).

[37] S. I. Novikova, "Physics of III-V Compounds", Semicond. & Semimetals (Academic, NY, 1966), vol. 2, chap. 2.

Chapter 4

Optical Characterization of Quantum Dots

4-1. Introduction

Optical evaluation is particularly well suited to revealing unique properties of semiconductor nanostructures. By probing photons that interact with electrons in nanostructures, and by analyzing the optical spectra in time and wavelength regimes, we can obtain wide-ranging information on the electronic states of nanostructures (e.g., level energy, state density, band structure, wave function) as well as their carrier dynamics (e.g., carrier capture, relaxation, recombination). Also, in the fabrication of optical devices, information on the strength and resonant wavelengths of the photon-electron interaction process itself, such as spontaneous emission, stimulated emission, optical absorption and a variety of optical nonlinear interactions, is required. over the past two decades of quantum-well research, many useful optical evaluation techniques have been established. Photoluminescence is one of the most conventional and useful techniques. It provides information on not only energy levels but also crystal quality. Other optical methods are photoluminescence excitation spectroscopy, time-resolved photoluminescence, microprobe optical spectroscopy performed with a microscope or sharpened optical fiber, and magneto-optical measurements.

The discovery of self-assembled semiconductor microcrystals caused an explosive rise in the population of researchers in the field of quantum dots. It was a great breakthrough. Microcrystals have a uniform and small size, high emission efficiencies, and high numerical densities, which are not possible with artificially fabricated structures. Various types of self-assembled microcrystals have been reported. The most popular microcrystals are Stranski-Krastanov (SK) dots [1, 2]. They are dome- or pyramid-shaped islands on highly lattice-mismatched growth surfaces [3]. Disk-shaped dots [4] and dash-shaped dots [5] have also been

(a) Stranski-Krastanow (SK) dot

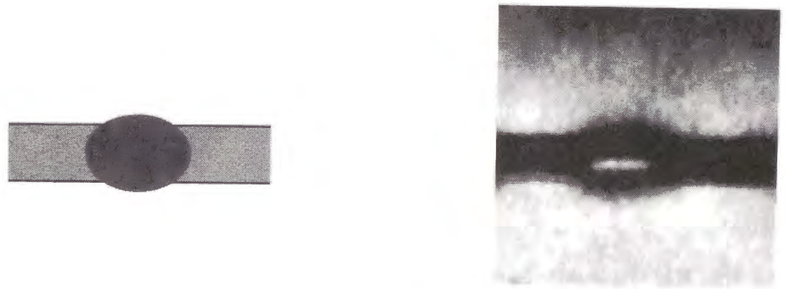

(b) ALS dot

Figure 4-1 Schematic and TEM images of two types of self-assembled dots in cross-section. The InGaAs SK dots are grown by MBE or MOVPE via Stranski-Krastanow (SK) mode under highly strained epitaxy. The InGaAs ALS dots are grown by alternatively supplying InAs and GaAs precursors with one or fewer-than-one monolayer. While SK dots are dome- (or pyramid-) shaped islands on a growth surface, ALS dots are spherical and surrounded laterally by a quantum-well layer having almost same thickness as the dots.

reported. The author discovered 1.3-μm emitting sphere-shaped dots (ALS dots) [6] (see Chapter 2). Figure 4-1 compares transmission electron microscope (TEM) photographs of ALS and SK dots. While SK dots are dome-shaped islands on a monolayer-thick wetting layer, ALS dots are spherical and surrounded laterally by a quantum-well layer having almost the same thickness as that of the dots. It should be noted that some self-assembled microcrystals are obviously too large. At the least, the size of quantum dots (observed by TEM, AFM, etc.) should be smaller than the exciton Bohr radius.

Unique optical characteristics originated by a delta-functionlike state density are expected in quantum dots, and therefore, the characteristics can be the criteria of optical characteristics as quantum dots. Multiple discrete sublevels appear in emission spectra of quantum dots. Widths of the emission peaks do not depend on temperature as long as the width are determined by dot inhomogeneity since thermal carrier distribution does not exist in quantum dots. Ultra-narrow emission is observable from a single quantum dot. Emission energy is insensitive to a magnetic field application since excitons are initially localized in the dots. Carrier recombination lifetimes are independent of temperature since carrier energy does not have thermal distribution in a quantum dot.

This chapter deals with the optical characterization of quantum dots, focusing on the original ALS quantum dots introduced in Chapter 3. Unique properties of ALS dots will be demonstrated, such as long emission wavelengths, emission spectra with multiple peaks from discrete energy levels, the harmonic-oscillator-type confinement potential, a large wavelength tunability between 1.2 and 1.5 μm by size control, and carrier lifetimes through radiative and nonradiative recombinations. These properties indicate the advantages of the alternate supply growth method. ALS dots are shown to satisfy the criteria of optical characteristics as quantum dots.

4-2. Light emission from discrete energy levels

4-2-1 Emission spectra

Photoluminescence spectra of ALS and SK dots at 300 K are compared in Fig. 4-2 [7]. Differences between the two are remarkable. The spectrum peak wavelength of the ALS dots is

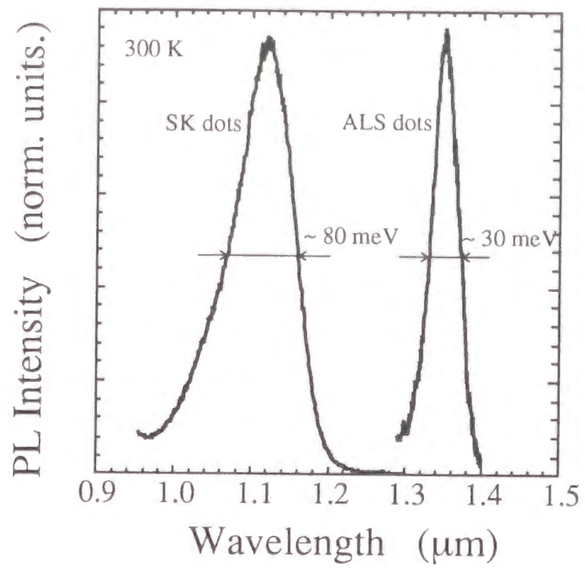

Figure 4-2 Photoluminescence spectra at 300 K of the ALS dots and the SK dots, measured with a Kr^+ laser at a low excitation power of 60 W/cm^2. The emission wavelength of ALS dots was above 1.35 μm, longer than that of the SK dots. The full width at half maximum of the spectrum is 30 meV in the ALS dots, showing high uniformity.

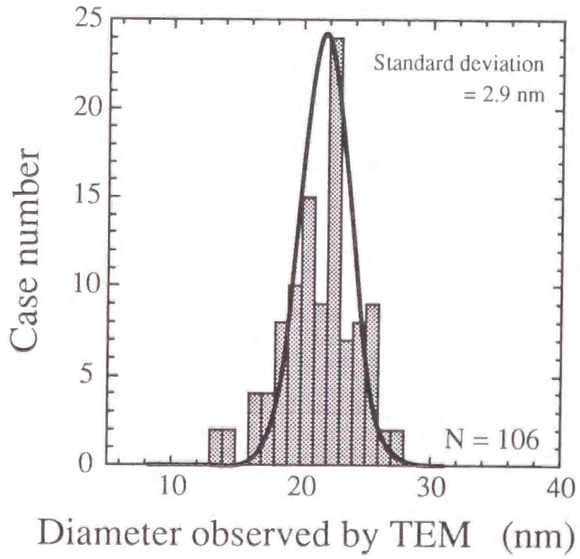

Figure 4-3 Diameter of ALS dots observed in a plan-view TEM image. The distribution follows a Gaussian curve with a standard deviation of 2.9 nm.

about 1.35 μm, which is longer than the 1.12 μm of the SK dots. Spectrum broadening in the ALS dots is less than half that of the SK dots. Figure 4-3 shows the size fluctuation of ALS dots evaluated by plan-view TEM images. The diameter distribution follows a Gaussian curve and is comparable to or smaller than that of SK dots [2, 8]. Since a spectrum consists of an ensemble of one emission line per quantum dot, the narrower spectrum in ALS dots indicates higher uniformity of dot emission energies and thus higher uniformity of dot size, composition, and strain.

Figure 4-4 shows the full width at half maximum (FWHM) of the emission spectra of ALS dots as a function of temperature between 60 and 300 K. Spectra at 4.2, 77 and 300 K are shown in the inset. The temperature-independent spectrum width indicates that broadening is dominated neither by the thermal carrier distribution nor by homogeneous broadening from phonon scattering, but by structural inhomogeneity. The homogeneous broadening of a single SK dot has been shown by microprobe photoluminescence to be less than 0.1 meV at low temperatures, much smaller than the measured spectrum width in the figure [9]. Theoretically, the homogeneous broadening of a single quantum dot is determined by the spontaneous emission rate and carrier scattering rate. It is yet to be investigated how large the homogeneous broadening of a single dot becomes at room temperature and when there are numerous carriers both inside and outside the dots, as is the case with lasing operations. Note that, in quantum wells, photoluminescence spectra broaden toward high energies as temperature increases, primarily due to the thermal distribution of carriers over continuous energy levels. The temperature-independent spectrum width in Fig. 4-4 is one proof that photoluminescence is caused by interband transitions between discrete levels in the conduction band and valence band.

The first sign of excited-level photo emission from self-assembled dots was observed in ALS dots [6, 10]. The inset of Fig. 4-4 shows additional shoulders at the peak wavelength regime of the spectra. Multiple peak emissions from discrete levels can be detected because of a narrower spectrum linewidth than that of interlevel separation. Figure 4-5 shows the excitation power dependence of the photoluminescence spectra of ALS dots at 77 K. As the excitation power increased, the second peak appeared and its intensity increased to exceed that of the first peak. At the highest power of 306 W/cm^2, a shoulder appeared. Figure 4-6 compares the photoluminescence spectrum at a rather high excitation intensity of 100 W/cm^2, and the photoluminescence excitation spectrum, monitored at the energy of 1.0 eV (the energy of first

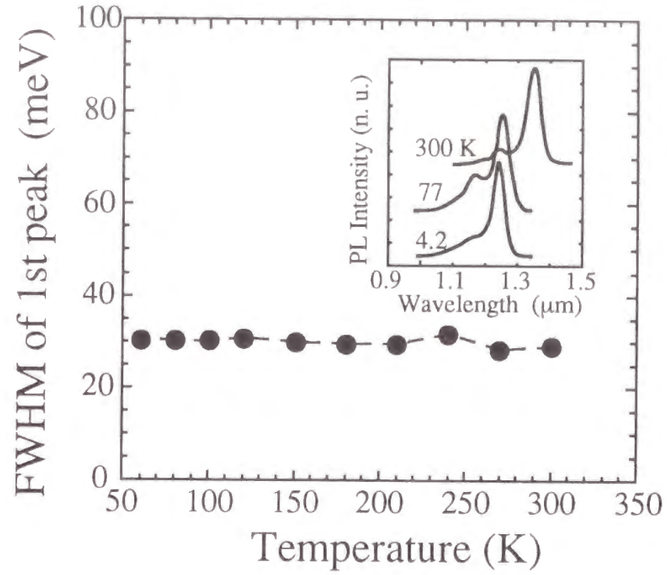

Figure 4-4 Photoluminescence spectrum width (FWHM) of the ALS dots as a function of temperature. The dots were grown using 12 cycles of the In-As-Ga-As alternate supply on an $In_{0.05}Ga_{0.95}As$ buffer and capped with an $In_{0.05}Ga_{0.95}As$ layer. Photoluminescence spectra at 4.2, 77 and 300 K are shown. The width of 30 meV is independent of temperature.

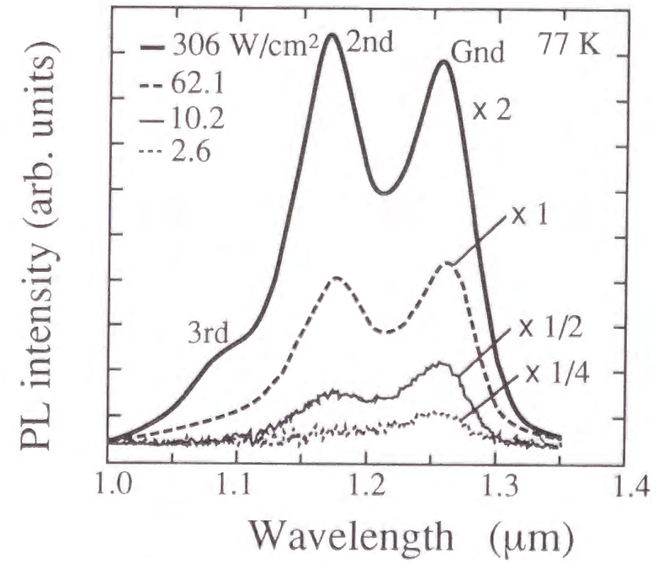

Figure 4-5 Excitation power dependence of photoluminescence spectra of ALS dots grown using 9 cycles of alternate supply. The sample was excited by a 647.1-nm Kr^+-ion laser. As the excitation power increased, the second peak appeared and its intensity increased to exceed the first peak. At the highest power, a shoulder assigned to the third peak appeared.

peak emission). It was possible to detect two clear resonances exactly at the same energy as those in the photoluminescence spectra. This represents direct proof that multiple peaks in photoluminescence spectra are due to the discrete levels under the three-dimensional quantum confinement. Let us call the first peak in the photoluminescence spectra the ground-level emission and the second peak the first excited-level emission.

Figure 4-7 shows the electroluminescence spectra of ALS dots at 77 K. The electrode size was 20 x 900 μm^2. Since electric carrier injection can provide many more carriers into dots than optical excitation, up to the 5 peaks appeared at the current injection of 400 mA. As the injected current increased, the emission intensity of the first and the second peaks were almost saturated. Since the emission rate is given by N/τ_{sp}, where N is the carrier number occupying the level and τ_{sp} is the spontaneous emission lifetime, saturation of the emission intensity is due to saturation of the carrier number in the corresponding energy level. As levels become fully occupied by carriers, the relaxation rate into the levels decreases due to Pauli blocking, and the emission starts to rise from higher energy levels.

However, Pauli blocking cannot completely explain the excitation intensity dependence of emission spectra in Fig. 4-7. Note that, at 10 mA, the second and third emissions appeared although the first emission intensity was less than its maximum. The carrier number, N, of each level, governing the emission intensity, is determined by the balance between rates of different kind processes, such as spontaneous emission at the level, relaxation into the level, and thermal emission from the level. In ALS dots with an energy separation of 50 to 80 meV --- much higher than the thermal energy at 77 K --- the thermal emission rate is negligible, and the experimental emission spectrum with multiple peaks even at low excitation indicates that the relaxation rate is comparable to the spontaneous emission rate. This is a phonon bottleneck (discussed in detail in Chapter 5). The emission spectrum at 10 mA in the figure cannot be reproduced by a calculation that simply combines the Fermi-Dirac distribution at 77 K and the state density of quantum dots.

Three other features of the emission spectra of ALS dots are observed in Fig. 4-7. First, the higher the peak order, the larger the maximum peak intensity. Second, peak energies were constant during increases of injected current, supporting the belief that the observed peaks correspond to sublevels in the dots. Third, the peak intervals between the neighboring emission lines are almost common --- a characteristic of harmonic-oscillator-type quantum confinement. The confinement potential is determined by the magneto-optical measurements described in

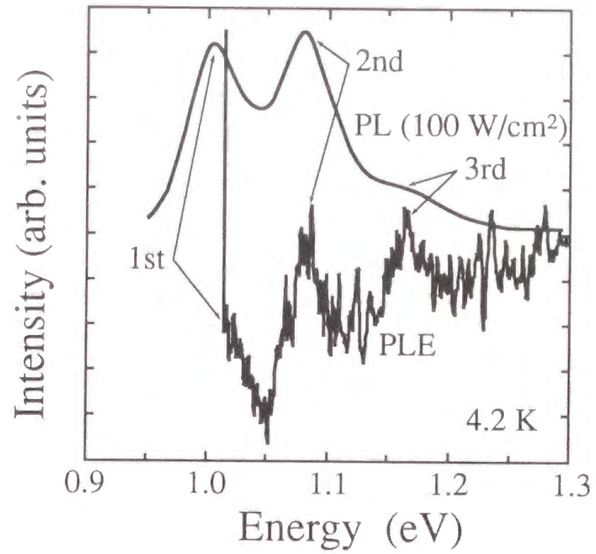

Figure 4-6 Photoluminescence excitation spectrum at 4.2 K of the sample grown by 18 cycles of In-Ga-As supply. The sample was excited by the monochromated light of a Halogen lamp, and a Ge detector was used to detect luminescence from the sample surface at the energy of 1.0 eV, that is, the lowest-energy first emission. Two clear resonances could be detected exactly at the same energy as that in the photoluminescence spectra.

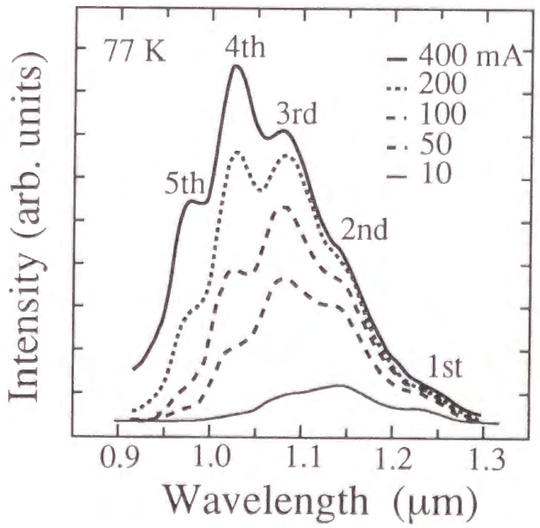

Figure 4-7 Electroluminescence spectra of ALS dots grown by 18 cycles of In-Ga-As alternate supply. The luminescence parallel to the surface was dispersed and detected by an InGaAs photo-multi detector quenched to -70°C using a conventional lock-in technique. Electrode size was 20 x 900 μm^2. Up to the 5th emission peaks appeared as the injected current increased.

4-2-2 Wafer mapping

Microprobe photoluminescence maps of an ALS quantum-dot wafer at room temperature are shown in Fig. 4-8: (a) energy separation between the ground-level (first) and the first excited-level (second) emission peaks; (b) the ground-level emission energy; and (c) FWHM of the ground-level emission spectrum. The correction of luminescence from the sample surface was restricted in an area measuring $2 \times 2\ \mu m^2$ using a crossing slit. The sample was grown by 14 cycles of an In-Ga-As supply on a 2-inch (100)-GaAs wafer in a state-of-the-art MOVPE system (see Chapter 3 for details on growth). During growth, the wafer was rotated at the rate of 30 rpm, which caused the distribution of the three diagnostic items to have a rough rotational symmetry around the wafer center.

By comparing the three maps, we can deduce what caused the observed patterns. The energy separation of Fig. 4-8(a) is in the 85- to 95-meV range and is almost uniform except at the wafer edge. The ground-level emission energy in Fig. 4-8(b) is greatest at about 1 inch from the wafer center. The FWHM in Fig. 4-8(c) has a distribution similar to that of the ground-level emission energy of (b) --- the higher the ground-level energy, the narrower the spectrum width. To understand the patterns, the author notes two factors causing the observed distributions: the dot size and indium composition of dots. As the quantum-dot size decreases, all three items of Fig. 4-8 --- the energy separation, ground-level emission energy, and spectrum width --- increase. As the indium composition decreases, the ground-level emission energy increases but the energy separation hardly increases.

The observed maps are explained as follows. First, energy separation in Fig. 4-8(a) suggests good uniformity in dot size across all wafer sizes. Second, the high-energy region off the wafer center in Fig. 4-8(b) has the smallest indium composition but does not have the smallest dot size. Third, the narrowest spectrum broadening off the wafer center in Fig. 4-8(c) is due to the uniform indium composition. This indicates that the spectrum broadening is caused not only by size fluctuation but also by compositional fluctuation of indium in each quantum dot.

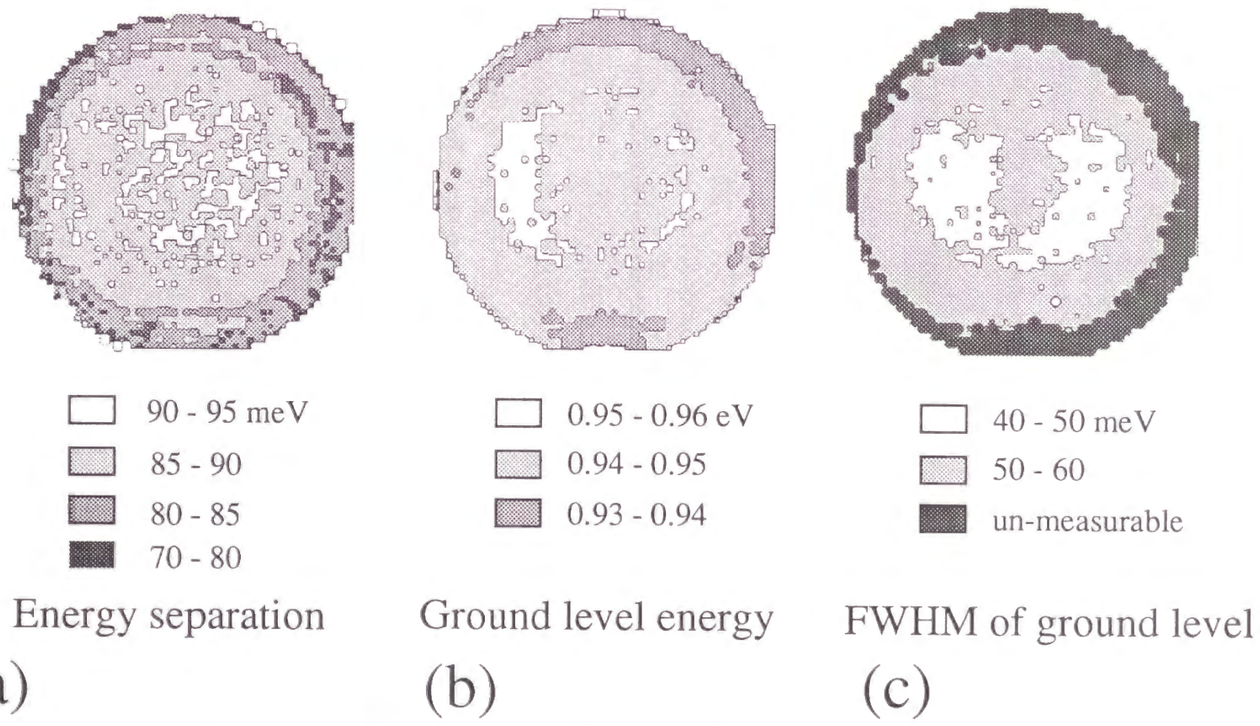

Figure 4-8 Area mapping of photoluminescence of an ALS quantum-dot wafer at room temperature: (a) energy separation between the ground-state (first) and the first excited-state (second) emission peaks; (b) the ground-state emission energy; and (c) FWHM of the ground-state emission spectrum. The probe size was 2 μm. The Scan step was 2 mm in both x and y directions. The sample was excited by an Ar+ laser at 514.5 nm, and luminescence from the sample surface was monochromed by a 50-cm monochrometer and detected by a multichannel photo detector.

4-2-3 Microprobe photoluminescence

Raising the spatial resolution of the optical probe is a major target in the development of optical diagnostic techniques. It enables us to understand the optical properties of a small number of dots [11]. Microscope photoluminescence that focuses the excitation laser beam via an objective lens to about a 1-μm diameter on a sample surface is already a popular technique, and its experimental setup is commercially available. Higher spatial resolutions are obtained via simple sample processing that opens a window in a metal mask covering the surface through which the photoluminescence can be measured. Sharp emission lines caused by a single or a small number of dots can be detected, and the linewidth --- homogeneous broadening of a single-dot emission line --- has been evaluated by several researchers [9, 12].

The other approach to microprobe spectroscopy is near-field optical microscopy (fiber probe microscopy) [13, 14], which involves collecting near-field light. Its advantage is that spatial resolution is not limited by the wavelength of the excitation laser; its drawback is weak signal intensity. With the shear-force feedback technique, high resolution optical imaging can be obtained by tracing the surface structure of samples [15-18].

The author performed microprobe photoluminescence spectroscopy of ALS dots using the near-field scanning optical microscopy system (NSOM). The equipment in the experiment is illustrated in Fig. 4-9. The excitation beam of a wavelength of 633 nm from the laser diode went through an optical fiber to the sample surface, and luminescence from the surface was collected by a fiber probe. The luminescence was monochromed by a monochrometer with a resolution of 1 nm. The tip was kept in close proximity to the sample (~10 nm) by applying the shear-force feedback technique [19]. The fiber probe resolution was restricted to ~ 1 μm because of a tradeoff between spatial resolution and detection sensitivity [20]. The number of the dots was estimated to be about 200 in a 1-μm spot.

Figure 4-10 shows the luminescence spectrum of ALS dots using the NSOM system with an excitation power of 90 W/cm^2 [21]. Spectra of macroscopic photoluminescence with a 300 μm$^{\phi}$ excitation laser spot are superimposed by a dashed line. Two sets of emission spectra with fine structures are denoted as S_1 and S_2 corresponding to the ground level and the first-excited level, respectively. Note that S_1 and S_2 are well separated and that almost no emission

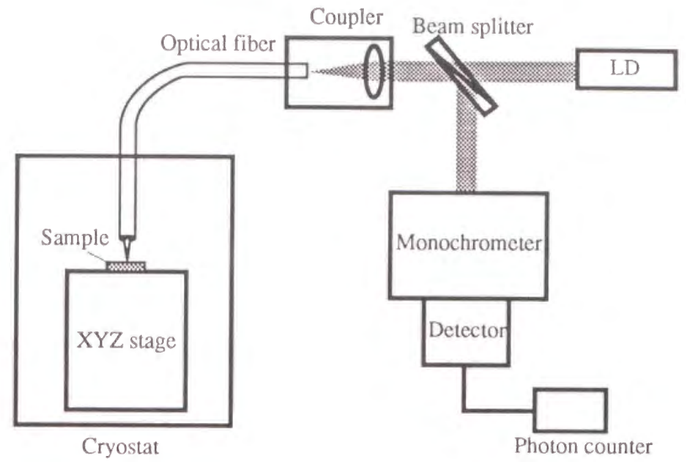

Figure 4-9 Near-field optical microscope. Samples were set in the cryostat and cooled to 5 K. The excitation beam of a wavelength of 633 nm from laser diode went thorough a sharpened optical fiber to the sample surface. Luminescence from the surface was collected by the fiber probe. The tip was controlled in close proximity to the sample by the shear-force feedback technique. The luminescence was dispersed by a monochrometer and the photon signal was counted with an InGaAs photo-multi detector kept at -80°C.

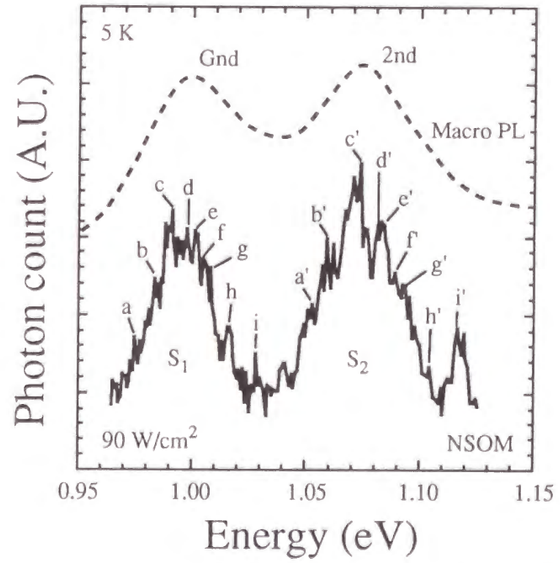

Figure 4-10 Photoluminescence spectra of the ALS dots by the near-field optical microscope. The excitation power was estimated to be 90 W/cm^2. The spectra of macro-photoluminescence is shown by a dashed line. The two sets of multiple emission peaks in the NSOM spectra correspond to the ground-state (S_1) and the first excited-state (S_2) emission.

was observed in between. This is because the smaller probing area reduced the inhomogeneous spectrum broadening. However, the emission spectrum of S_1 and S_2 did not become as narrow as expected, indicating that inhomogeneity of the dots had already occurred in an area smaller than 1 μm. Inhomogeneity in such a small area cannot be caused by non-uniformity in growth conditions, such as wafer temperature distribution and source gas streamline. The fine structures on S_1 and S_2 are reproduced by repeated measurements and can be attributed to emission from one or a few dots, so the sharp peaks denoted by a common letter with/without an apostrophe might be the ground-level and excited-level emissions of the same dots. Differing from SK dots, ALS dots have a closely spherical symmetric structure, and therefore, fine degeneracy can be expected at higher sublevels.

Figure 4-11 shows the excitation-power dependence of the NSOM spectra. After comparing that with the macroscopic photoluminescence spectra of Fig. 4-5, the emission from each level is found to be sharper, and emissions up to the seventh emission are resolved, due to the higher spatial resolution. It was found that the higher the sublevel order, the wider the peak width, and thus, higher-order peaks were not well isolated. Possible explanations are that the sublevel-energy interval was not uniform in dot ensembles in the area (i.e., non-uniform interval enhances peak broadening at excited sublevels), and that the degeneracy of higher levels was slightly split. Another reason might be that an additional emission appeared at the lower-energy side in each peak. The spectrum around the ground-level emission is magnified in Fig. 4-12. As the excitation power was increased from 90 W/cm^2 to 9 kW/cm^2, the peak emission intensity of the ground level decreased, and the lower-energy emission rose. This red shift of emission might be due to the many-body effect in quantum dots [22].

4-3. Controllability of quantum confinement

Energy band structures of quantum nanostructures can be artificially controlled. In quantum wells, well width and strain are designed to match target devices using the well-established $\mathbf{k}\cdot\mathbf{p}$ band calculation methods [23], and the designed structures are precisely actualized in the atomic scale using state-of-the-art epitaxial growth techniques like MOVPE and molecular beam epitaxy (MBE). The ability to control quantum-dot structures is not yet as

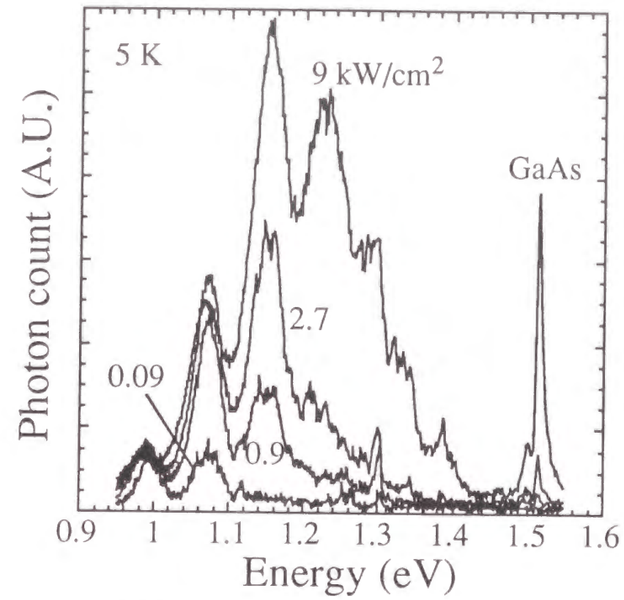

Figure 4-11 Photoluminescence spectra of the ALS dots by a near-field optical microscope at various excitation-power densities. As the excitation power increased, a higher-energy emission peak was clearly discernable.

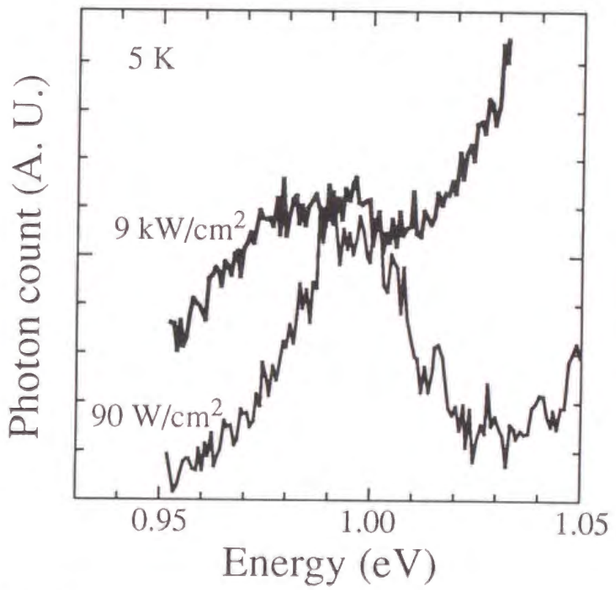

Figure 4-12 NSOM spectra around the ground-state emission. An additional emission appeared at the lower-energy side of the peak at high excitation.

strong as it can be in spite of its significance for practical device applications. In self-assembled InAs SK dots on GaAs substrates, the size and emission wavelength can be controlled only within a narrow range by changing the growth temperature. Changing the supply amount of sources has a negligible effect because the self-assembly process is driven toward a thermodynamic equilibrium point.

In this section, the author describes two methods of controlling the size and emission wavelength of InGaAs ALS quantum dots over a wide range of 1.2 to 1.5 μm, that is followed by an explanation of the quantum-dot confinement potential evaluated by magneto-optical measurements.

4-3-1 Two methods of controlling quantized energies

The first method of controlling the emission wavelength of ALS dots is to change the number of supply cycles in the alternate supply growth (see Chapter 3 for the ALS growth sequence). Figure 4-13 shows the 4.2-K photoluminescence spectra of ALS quantum dots at several cycle numbers of the In-As-Ga-As supply. At cycle 7, the dots were self-assembled to release the strain energy accumulated by a lattice mismatch between InAs and GaAs. As the number of cycles increased from 7 to 30, the peak wavelength shifted from 1.17 to 1.3 μm. Weak peaks or shoulders (indicated by arrows) that had higher emission energies than the first peaks were observed. In the 7-cycle sample, a second peak was barely observable, probably due to low optical quality. As the number of cycles increased, the second peak moved towards the first peak; and in the 30-cycle sample, the two merged. Plan-view TEM images of the samples in Fig. 4-14 show that, as the supply cycle increased, the diameter of the dots increased. As summarized in Fig. 4-15, the cycle increase enlarges the diameter and reduces the emission energy and energy separation between the two peaks. If the first peak is assigned to the ground-level emission and the second peak to the excited-level emission, as in section 4-2-1, the results in Fig. 4-15 go along well with the quantum-confinement concept of energy increase due to confinement. The maximum emission intensity and narrowest spectrum width were achieved at the same time at 9 cycles, showing that the alternate supply method controls not only size but also crystal quality.

The second way to control emission wavelength is to change the lattice constant of the layer on which dots are grown. This method is based on the ideas that formation of self-

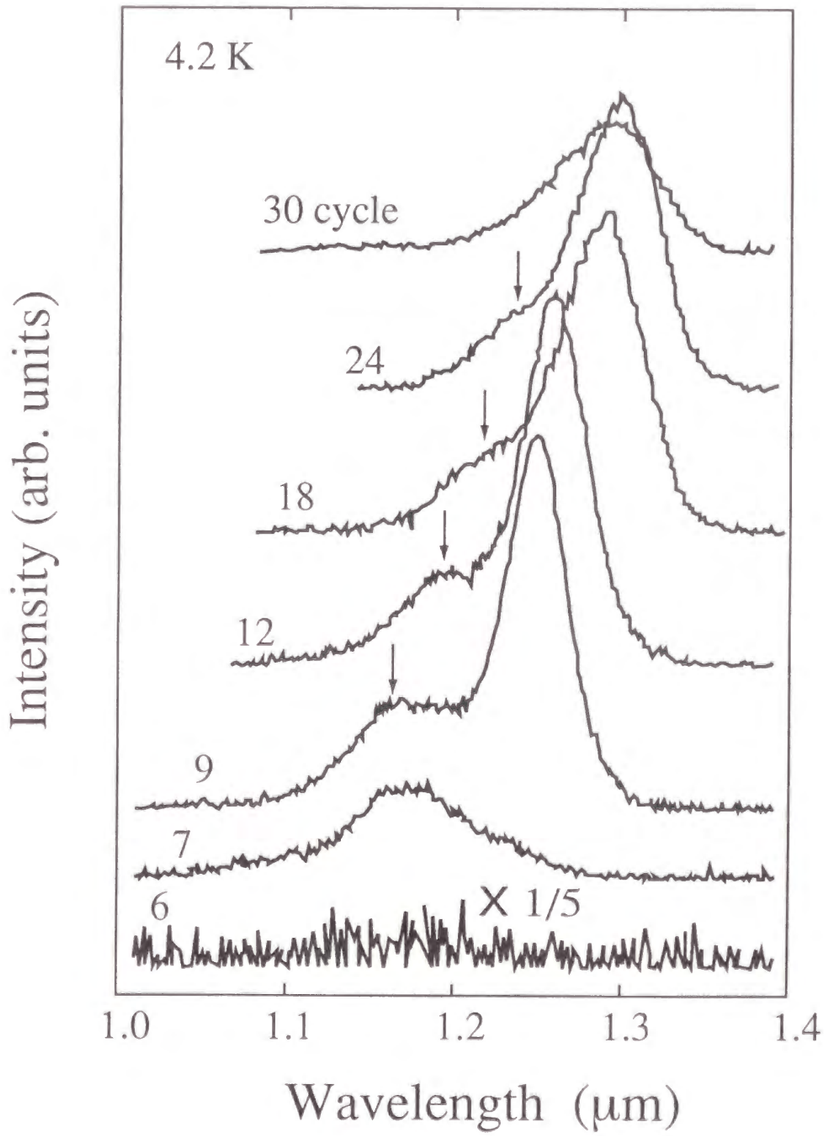

Figure 4-13 Photoluminescence spectra of the ALS dots grown by various cycles of In-As-Ga-As alternate supply. As the number of cycles increased, the peak wavelength shifted from 1.17 to 1.3 μm. The second peaks were observed at the left side of the first peak. The maximum emission intensity was obtained by the sample grown by 9 cycles.

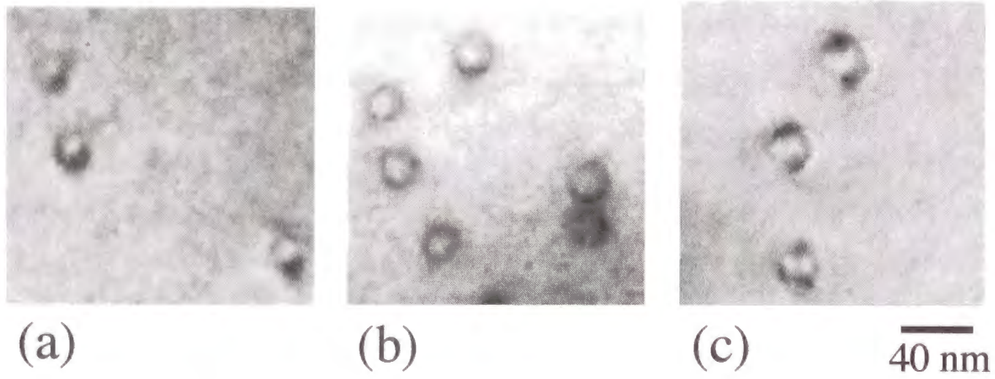

Figure 4-14 Plan-view TEM images of ALS dots grown with (a) 9 cycles, (b) 12 cycles, and (c) 24 cycles. The dot diameter increased as the number of cycles increased.

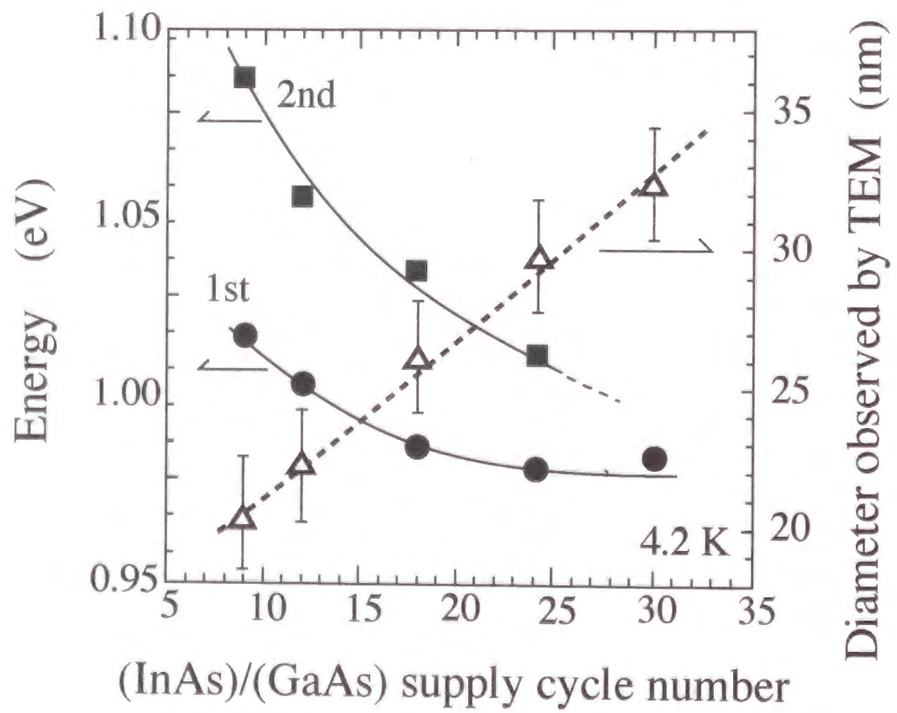

Figure 4-15 Energies of the first and second peaks in the photoluminescence spectra and dot size observed by TEM as a function of the supply cycle number during ALS quantum-dot growth.

assembled three-dimensional islands is motivated by the release of accumulated strain energy, and that the size of the islands increases as a lattice mismatch between the substrate and supplied materials decreases. 500-nm $In_XGa_{1-X}As$ buffer layers with a composition of x = 0 to 0.09 were grown on GaAs substrates. A reciprocal space map of X-ray diffraction showed that up to 50% strain relaxation occurred in the $In_XGa_{1-X}As$ buffer layer and that the lattice constant of the buffer layer increased along with increases of x due to the relaxation of strain. Figure 4-16 shows that, as the indium composition of the buffer layer increased from 0 (GaAs) to 0.09 ($In_{0.09}Ga_{0.91}As$), the emission wavelength increased from 1.3 to 1.46 μm with supply cycle of 12. TEM measurements show that the diameter of ALS dots increased from 20 nm to 35 nm as the indium composition of the buffer layer increased (Fig. 4-17). Energy dispersive X-ray microanalysis (EDX) determined that the composition of the dots was between 0.4 and 0.6 and did not obviously depend on the composition of the buffer layer.

By combining the two control methods just described, the emission wavelength of ALS dots can be controlled from 1.2 to 1.5 μm. The buffer layer can be also applied to tune the size and emission wavelength of ordinary SK dots.

4-3-2 Magneto-optical spectroscopy

Diamagnetic shifts of excitons are powerful tools for evaluating not only the reduced effective mass but also the magnitude of affecting potential. A magnetic field confines excitons in a plane perpendicular to the field and increases their energy. The magnitude of other competing confinement potentials can be determined by evaluating the diamagnetic energy shifts. In an examination of the diamagnetic shifts of luminescence from 1.3-μm-emission InGaAsP/InP quantum wells and the ALS dots, the confinement potentials were detected for localized excitons in the quantum wells and quantum dots. Magnetic fields were applied perpendicularly to the wafer using a superconducting magnet immersed in liquid helium. The sample was placed near the center of this magnet, which can generate a magnetic field of up to 14 Tesla. A multiline Ar^+ laser beam was fed to the sample through an optical fiber bundle. Photoluminescence from the sample surface was led to a 32-cm monochrometer through the optical fiber and detected by a cooled InGaAs photomultiplier using a conventional lock-in technique.

Figure 4-18 shows the diamagnetic shifts of the main peak in the photoluminescence

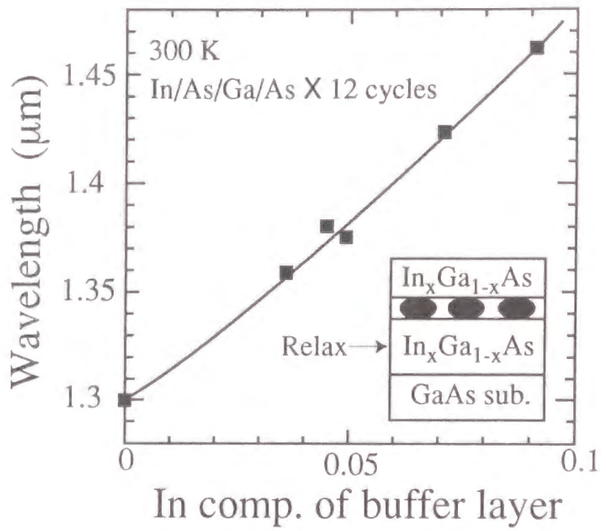

Figure 4-16 Emission wavelength as a function of the indium composition of an InGaAs buffer layer. With 12 cycles of In-As-Ga-As alternate supply, the emission wavelength increased from 1.3 to 1.46 μm as the indium composition increased from 0 (i.e., GaAs) to 0.09.

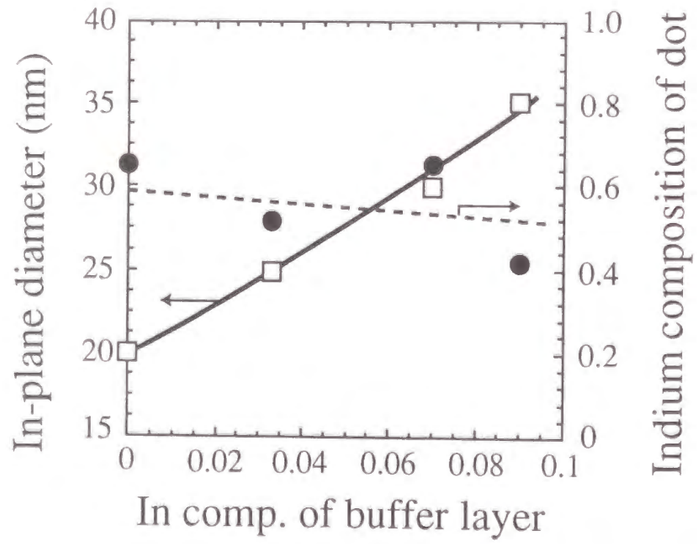

Figure 4-17 In-plane dot diameter observed by plan-view TEM and indium composition measured by EDX as a function of the indium composition of InGaAs buffer layer. Composition was determined by calibrating the signal intensity using the intensity of the lattice-matched $In_{0.53}Ga_{0.47}As/InP$ as a reference.

spectra of dot samples grown using several alternate supply cycles [24]. In the measurements, a magnetic field was applied perpendicularly to the sample surface using a superconducting magnet. A multiline Ar^+ laser beam was fed to the sample through an optical fiber bundle. Photoluminescence from the sample was detected from behind the sample through another fiber bundle. The diamagnetic shifts of 1.3-μm-emission InGaAsP/InP quantum wells are superimposed for reference. The diamagnetic shifts in dots are shown to be smaller than that of quantum wells, proving in-plane confinement potential in ALS dots. As the number of cycles decreased, the diamagnetic shift decreased. The shift was negligible in 9-cycle samples. These results indicate that the quantum confinement potential was controlled by the number of cycles.

By simulating energy shifts using the harmonic-oscillator-type confinement potential under effective mass approximation, the author evaluated the in-plane confinement potential of quantum dots. The dots were assumed to be disks, where electron coordinates are (z_e, $\mathbf{r}_e$) and hole coordinates are (z_h, $\mathbf{r}_h$). The origin of the coordinate axis was set at the center of the disk, and the z axis was perpendicular to the layer [25]. The author assumed that the quantum confinement potential in the growth direction is much greater than the Coulomb potential energy. Also, the lateral quantum confinement potential for both electrons and holes is described by harmonic-oscillator-type potentials, $m_e\omega^2 r_e^2/2$ and $m_h\omega^2 r_h^2/2$, respectively [26]. Here, m_e and m_h are the effective mass of an electron and hole, and ω is the confinement frequency. Under these assumptions the relative motion and center-of-mass motion of the exciton are exactly separated. In a magnetic field parallel to the growth direction, the effective-mass equation for the relative motion is

$$\left[-\frac{\hbar^2}{2\mu}\nabla_r^2 - \frac{e^2}{4\pi\varepsilon\rho} + \frac{1}{2}\mu\omega^2 r^2 + \frac{e^2B^2}{8\mu}r^2\right]\Psi_r = E_r^r\Psi_r , \qquad (4.1)$$

where $\hbar$ is Plank's constant divided by 2π, μ is the reduced mass described by $(m_e^{-1}+m_h^{-1})^{-1}$, $r = [r^2 + (z_e - z_h)^2]^{1/2}$, z_e and z_h are the electron and hole coordinates in the z direction (growth direction), $r = |\mathbf{r}_e - \mathbf{r}_h|$ is the in-plane electron-hole distance, and ε is the static dielectric constant. The fourth term in this Hamiltonian describes the diamagnetic shift. For the center-of-mass motion the effective-mass equation is

$$\left[-\frac{\hbar^2}{2M}\nabla_M^2 + \frac{1}{2}M\omega^2 R^2\right]\chi_{kl}(R) = E_{kl}^R\chi_{kl}(R) , \qquad (4.2)$$

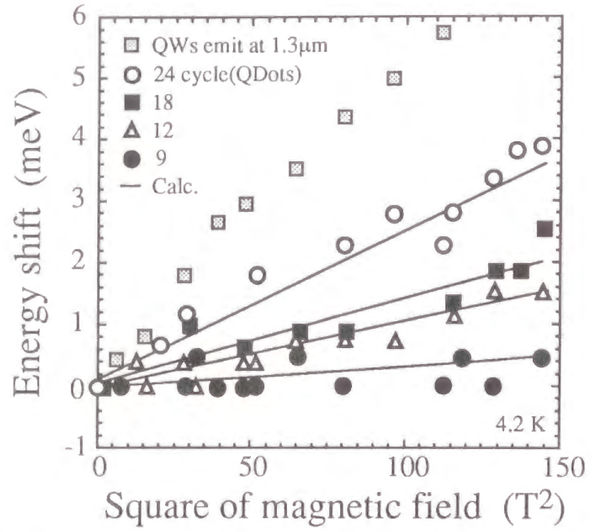

Figure 4-18 Measured and calculated magnetic-field-induced energy shifts as a function of the square of the magnetic field. Diamagnetic shifts of exciton resonance in InGaAsP quantum wells emitting at 1.3 μm are superimposed as a reference. Lateral quantum-confinement potentials were determined by fitting the calculation (solid lines) to the measured shifts.

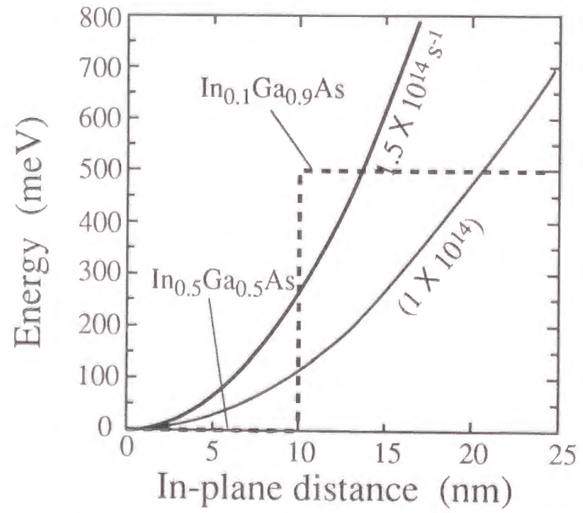

Figure 4-19 Confinement potential estimated by TEM and EDX (dashed line) and that estimated by magnet-optical evaluation (solid line) for the sample grown using 12 cycles. The origin of the x-axis was set at the center of dot. The two results agree well.

where $M = m_e + m_h$, k = 0, 1, 2, 3, ..., and l = 0, ±1, ±2, ..., ±k. Equation (4. 2) can be solved analytically, with the energy given by

$$E_{kl}^{R} = (2k - |l| + 1)\hbar\omega. \qquad (4.\ 3)$$

Note that the energy of the center-of-mass motion is described by a multiple of $\hbar\omega$, independent of magnetic fields. The diamagnetic energy shift was calculated by solving Eq. (4. 1), and fitted calculated shifts to measured ones using ω as a parameter. In the calculation, $\mu = 0.035m_0$ was used [27]. The obtained values are $\omega = 7 \times 10^{13}$, 1×10^{14}, 1.3×10^{14}, and 4×10^{14} s^{-1} for 24, 18, 12, and 9 supply cycles, respectively.

As the cycle number increases, the confinement potential spreads. Figure 4-19 compares the confinement potential estimated by TEM and EDX (dashed line) with that estimated by magneto-optical evaluation (solid line) for the sample grown using 12 cycles. The origin of the x-axis was set at the center of the dot. The two estimations agree well.

4-4. Radiative emission efficiency

Laser performances (e.g., threshold currents and external quantum efficiencies) are quite sensitive to crystal quality. This is because nonradiative centers consume carriers injected into the laser active region. Considering that the emission efficiency of these dots is greatly reduced as the temperature increases [28, 29], it is possible that non-radiative centers were produced during the self-formation phenomena, reducing device performances. We must pay attention to the quality of both inside dots and outside dots since the retarded carrier relaxation peculiar to quantum dots enhances the opportunity for carriers to be killed before they relax. Here, the author evaluates a nonradiative channel in quantum-dot crystals by measuring time-resolved photoluminescence decay and photoluminescence intensity as a function of temperature.

4-4-1 Photoluminescence lifetime and intensity

Recombination lifetimes of the discrete emission spectra from ALS dots are shown in Fig. 4-20 [30]. (See Chapter 5 for details on time-resolved photoluminescence measurements.)

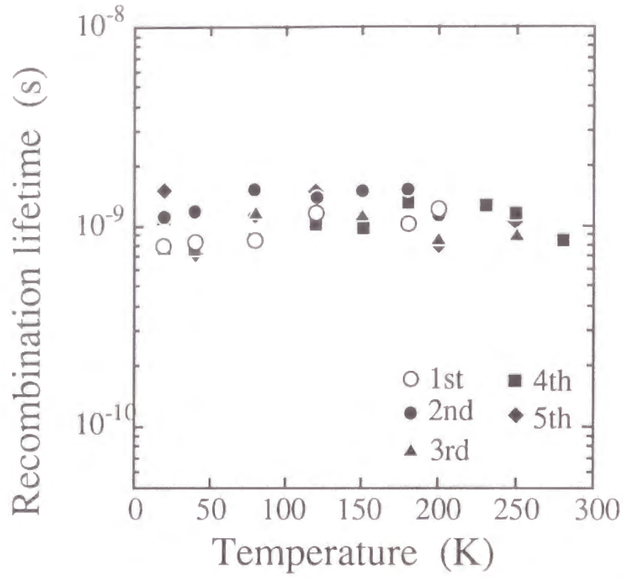

Figure 4-20 Recombination lifetimes of the five emission peaks in the ALS dots measured by time-resolved photoluminescence. The lifetimes were about one nanosecond and almost independent of temperature up to 300 K.

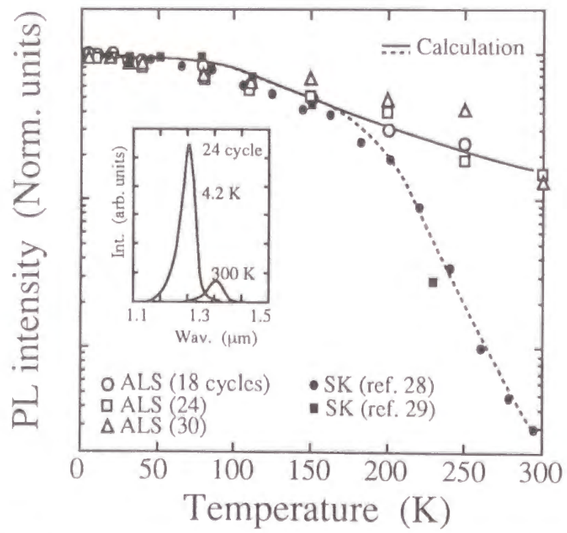

Figure 4-21 Photoluminescence intensity of the ALS dots as a function of temperature. The intensity was normalized by the value at a low temperature. Excitation was done by a 647.1-nm Kr^+ ion laser. Reported intensities of the SK dots grown by MBE are also shown as references. Solid and dashed lines indicate the results of fitting.

The measured lifetimes, τ_r, are almost independent of the emission level and are about 0.8 to 1.5 nanoseconds, which has been judged to be long enough for laser application. The measured lifetimes are almost independent of temperatures up to 300 K because of the discrete quantized levels that prevent exciton thermal distribution, which are peculiar to quantum dots [31]. Since τ_{nr} normally depends on temperature, a nonradiative process does not seem to affect the recombination lifetime.

Figure 4-21 shows the photoluminescence intensity of the ground-level emission of ALS dots as a function of temperature. The intensity was normalized by a value at 4.2 K. Reported photoluminescence intensities of SK dots grown by MBE are also shown as references. From 4.2 K to 300 K, the photoluminescence intensity of the ALS dots decreased monotonously by about one order of magnitude. The decrease is almost equal to, or even smaller than, that of the quantum wells [28]. The photoluminescence intensity of the SK dots decreased by almost three orders of magnitude. For the SK dots, there seems to be a critical temperature between 150 and 200 K, where the slope inclination changes, suggesting that there are at least two sources for the reduction in photoluminescence intensity.

4-4-2 Theoretical investigation

The temperature independence of recombination lifetimes tells us that nonradiative centers outside ALS dots degrade emission efficiency as temperature increases. Since the excitation wavelength was 647.1 nm, carriers were initially excited outside the dots and diffused into the dots to emit inside them. Assuming nonradiative centers outside the dots, the author simulated the temperature dependence of photoluminescence intensity. Radiative recombination outside the dots was disregarded, since no emission was observed from the GaAs substrate and the $In_{0.1}Ga_{0.9}As$ layer surrounding the dots. The photoluminescence intensity can thus be described using

$$I_{PL} = G\left[1 + \tau_d / \tau_{nr}^{out}(T)\right]^{-1}, \qquad (4.4)$$

where G is the carrier generation rate, and τ_d is the carrier relaxation time from outside to the ground level of the dots. Since only the emission from the ground level was observed, an intersubband carrier relaxation time was included in τ_d. The lifetime of $\tau_{nr}^{out}(T)$ is the

nonradiative recombination lifetime outside the dots and written as

$$\tau_{nr}^{out}(T)^{-1} = N \cdot \sigma^{out}(T) \cdot V(T), \qquad (4.5)$$

where N is the trap density, V(T) is the carrier thermal velocity ($\sqrt{3kT/m}$), and $\sigma^{out}(T)$ is the capture cross section. The cross section is described using the activation energy of Q as

$$\sigma^{out}(T) = \sigma \cdot \exp(-Q/kT), \qquad (4.6)$$

With two parameters, $N \cdot \sigma$ and Q, as fitting parameters, the measured emission intensity was reproduced by calculation using Eq. (4. 4). In Fig. 4-21, the result for ALS dots is shown by a solid line and that for SK dots by a dashed line. The carrier relaxation time was set at τ_d = 1 ns after time-resolved measurements (see Chapter 5). The parameter set of [$N \cdot \sigma$, Q] = [10^2 cm^{-1}, 35 meV] explains the results for ALS dots. Also, the combination of [10^2 cm^{-1}, 35 meV] and [10^8 cm^{-1}, 280 meV] describes the results for the MBE-grown dots; the former set is in common with that of ALS dots, and the latter set explains the large bending at over 150 K. If τ_d = 100 ps is used in the fitting, the values of $N \cdot \sigma$ become smaller by one order of magnitude.

Table 4-I lists the known parameters of nonradiative centers in the InGaAs system [33-36]. The parameter set obtained for the ALS dots is close to the sets in Table 4-I. Remarkably the parameter set for the MBE-grown dots is much different from the sets in Table 4-I, suggesting that ordinary defects in bulk cannot explain the large decrease of emission intensity of the MBE-grown dots. Other origins, such as a network of dislocation lines or a nonradiative center inside the dots, should be assumed for the dots.

The high emission efficiency of ALS dots can be attributed to their unique growth process. One possible reason for their better optical quality is that the quality of their interface is higher. ALS dots are surrounded laterally by a quantum-well layer, and the interface around them is ambiguous (see Fig. 4-1). This may be because atoms around the dots reconstruct the interface during growth, given that ALS dots are supposedly formed through the repetition of the equilibrium and non-equilibrium points of a thermodynamical balance between strain energy and surface energy (see Chapter 3). The interface of SK dots is abrupt since it is the border between growth islands and the overgrown layer. Another possible reason for the better optical

Table 4-I : Reported parameters of non-radiative centers in InGaAs materials. E is the activation energy for the thermal emission rate, σ is the capture cross section, Q is the activation energy for the capture cross section, and N is the trap density. VPE is a simplified character of vapor phase epitaxy.

	E (eV)	σ (cm^2)	Q (meV)	N (cm^{-3})	Growth Method
a[33]	0.82	1.6E-16	-	2.6E+13	MBE
b[33]	0.54	3.1E-16	-	1.0E+13	MBE
c[33]	0.27	5.9E-14	-	7E+12	MBE
d[33]	0.74	1.6E-13	-	2.1E+14	MBE
e[33, 34]	0.53	5E-15	-	1.4E+15	MBE, VPE
f[34, 35]	0.17	2E-12	-	3E+15	MBE, VPE
g[36]	0.83	1E-14	80	-	VPE
h[36]	0.76	1E-15	80	-	VPE
i[36]	0.68	1E-16	40	-	VPE

quality of ALS dots is that they are in-situ annealed due to the low growth rate of the alternate supply of precursors. The growth rate is about 1 monolayer per 10 seconds for the alternate supply --- significantly smaller than that of MBE. The growth temperature of ALS dots is lower than the temperature where arsenic desorption occurs [32], and some defects may have enough time to go out from the surface during the slow growth.

4-5. Summary

The optical characteristics of ALS quantum dots were investigated, and the results featured their advantages over SK dots. Self-assembled dots were shown to achieve discrete state density and unique characteristics not previously available. Multiple peak emissions from discrete levels caused by three-dimensional quantum confinement were observed using photoluminescence, electroluminescence, and photoluminescence excitation. Photoluminescence mapping of a wafer revealed the compositional fluctuation of indium among quantum dots. Microprobe photoluminescence revealed the fine structure of emissions. Quantum confinement potential was controlled by changing the number of supply cycles and the composition of the buffer layer, and the potential was evaluated by diamagnetic energy shifts. Time-resolved photoluminescence and photoluminescence intensity as a function of temperature were examined to evaluate the nonradiative recombination channel inside and outside the dots.

Besides the intrinsic interests in it, optical characterization of materials is indispensable for the development of practical devices. When ALS dots are compared with SK dots, the 1.3-μm emission wavelength is the most remarkable advantage of ALS dots since it means that they can be applied to lasers in optical telecommunication systems. Good controllability of the wavelength of ALS dots is also significant in practical device manufacturing. ALS dots achieved a spectral width of 30 meV --- less than half of that of SK dots --- and have a better emission efficiency. However, ALS dots have the drawbacks of low density and insufficient multiple stacking (see Chapter 3), making it difficult to realize high-performance lasers. Research on eliminating the drawbacks, described in Chapter 6, enabled the first 1.3-μm quantum-dot lasing to be attained.

References

[1] M. Tabuchi, S. Noda,. and A. Sasaki, in Science and Technology of Mesoscopic Structures, Edited by S. Namba, C. Hamaguchi, and T. Ando (Springer, Tokyo) p. 379, 1992.

[2] D. Leonard, M. Kishnamurthy, M. C. Reaves, P. S. Denbaars, and M. P. Petroff, Appl. Phys. Lett. 63, 3203 (1993).

[3] I. Daruka, and A-L. Barabási, Phys Rev Lett., 79, 3708 (1997).

[4] R. Nötzel, J. Temmyo, and T. Tamamura, Nature 369, 131 (1994).

[5] T. Utzmeier, P. A. Postigo, J. Tamayo, R. Garcia, and F. Briones, Appl. Phys. Lett., 69, 2674 (1996).

[6] K. Mukai, N. Ohtsuka, M. Sugawara, and S. Yamazaki, Jpn. J. Appl. Phys. 33, L1710 (1994).

[7] K. Mukai, N. Ohtsuka, H. Shoji, and M. Sugawara, Appl. Surface Science, 112, 102 (1997).

[8] M. J. Moison, F. Houzay, F. Barthe, and L. Leprince, Appl. Phys. Lett. 64, 196 (1993).

[9] Y. J. Marzin, M. J. Gérard, A. Izraël, D. Barrier, G. Bastard, Phys. Rev. Lett., 73, 716 (1994).

[10] K. Mukai, H. Shoji, N. Ohtsuka, and M. Sugawara, Appl. Phys. Lett. 68, 3013 (1996).

[11] K. Brunner, U. Bockelmann, G. Abstreiter, M. Walther, G. Böhm, G. Tränkle, and G. Weimann, Phys. Rev. Lett., 69, 3218 (1992).

[12] D. Hessman, P. Castrillo, E. M. Pistol, C. Pryor, and L. Samuelson, Appl. Phys. Lett., 69, 749 (1996).

[13] U. Dürig, W. D. Pohl, and F. Rohner, J. Appl. Phys., 59, 3318 (1986).

[14] E. Betzig, K. J. Trautman, D. T. Harris, S. J. Weiner, and L. R. Kostelak, Science, 251, 1468 (1991).

[15] E. Betzig, and J. R. Chichester, Science, 262, 1422 (1993).

[16] P. W. Ambrose, M. P. Goodwin, C. J. Martin, and A. R. Keller, Phys. Lev. Lett., 72, 160 (1994).

[17] D. R. Grober, D. T. Harris, K. J. Trautmann, E. Betzig, W. Wegscheider, L. Pfeiffer, and K. West, Appl. Phys. Lett., 64, 1421 (1994).

[18] F. H. Gaemi, B. B. Goldberg, C. Cates, D. P. Wang, M. C. Sotomayor-Torres, M. Fritze, and A. Nurmikko, Superlattices and MIcrostructures 17, 15 (1995).

[19] E. Betzig, L. P. Finn, and S. J. Weiner, Appl. Phys. Lett., 60, 2484 (1992).

[20] T. Saiki, S. Mononobe, M. Ohtsu, N. Saito, and J. Kusano, Appl. Phys. Lett., 68, 2612 (1996).

[21] K. Mukai, N. Ohtsuka, and M. Sugawara, Ext. Abs. The 58th Autumn Meeting of The Japan Society of Applied Physics, 4pS-8, p.1360, 1997 (in japanese).

[22] M. Sugawara, Jpn. J. Appl. Phys., 35, 124 (1996).

[23] for example, S. L. Chuang, "Physics of Optoelectronics Devices", (John Wiley & Sons, New York., 1995)

[24] K. Mukai, N. Ohtsuka, and M. Sugawara, Jpn. J. Appl. Phys. 35, L262 (1996).

[25] M. Sugawara: Phys. Rev. B 51, 10743 (1995).

[26] W. Que: Phys. Rev. B 45, 11036 (1992).

[27] M. Sugawara, N. Okazaki, T. Fujii and S. Yamazaki: Phys. Rev. B 48, 8102 (1993).

[28] R. P. Mirin, P. J. Ibbetson, K. Nishi, C. A. Gossard, and E. J. Bowers, Appl. Phys. Lett., 67, 3795 (1995).

[29] D. Bimberg, N. N. Ledentsov, N. Kirstaedter, O. Schmidt, M. Grundmann, M. V. Ustinov, Yu. A. Egorov, E. A. Zhukov, V. M. Maximov, S. P. Kop'ev, and I. Zh. Alferov, Extended Abstracts of the 1995 Int. Conf. on Solid State Devices and Materials, Osaka, p. 716

[30] K. Mukai, N. Ohtsuka, H. Shoji, and M. Sugawara, Phys. Rev. B, 54, R5243 (1996).

[31] M. Sugawara, Phys. Rev. B51, 10743 (1995).

[32] Y. Sakuma, M. Ozeki, and K. Nakajima, J. Cryst. Growth 130, 147 (1993).

[33] P. K. Bhattacharya, and S. Dhar, Semicond. and Semimeta. vol. 26 ch. 3.

[34] M. Ogawa, S. Hongo, Y. Watanabe, N. Sano, H. Katoh, M. Nakayama, K. Ishida, and J. Shirafuji, Sixth Record of Alloy Semicond. Phys. and Electro. Symposium, p345

[35] M. Ogura, M. Mizuta, K. Onaka, and H. Kukimoto, Jpn. J. Appl. Phys., 22, 1502 (1983).

[36] A. Mircea, A. Mitonneau, J. Hallais, and M. Jaros, Phys. Rev., B16, 3665 (1977).

Chapter 5

Carrier Relaxation in Quantum Dots

5-1. Introduction

After the prediction was made about the promise of quantum dots in future optoelectronic device applications [1 - 5], carrier dynamics among discrete sublevels in a zero dimensional semiconductor structure, have been intensively investigated. Many researchers were worried that carrier relaxation into quantum-dot discrete levels would be significantly slowed due to a lack of phonons, which satisfies the energy conservation rule (the phonon bottleneck problem) [6]. If the phonon bottleneck exists, practical application of quantum dots are extremely limited. Before a self-assembling technique was developed to produce semiconductor quantum dots, the phonon bottleneck had been a theoretical research subject. Benisty predicted that low scattering rates in a 0D system result in carrier relaxation lifetimes of nanoseconds or longer between discrete levels, and that slow relaxation rates enhance the nonradiative recombination process (Fig. 5-1) [7, 8]. Comparatively shorter lifetimes (i.e., more optimistic pictures) have been predicted with other theoretical approaches. Bockelmann stated that the lifetimes may be in the picosecond order considering electron-hole interaction [9]. Many researchers have suggested the Auger process can possibly create a fast relaxation channel with a lifetime of ten or fewer picoseconds [10 - 12]. Inoshita and Sakaki examined the LA-LO phonon process and reported that the lifetime can decrease drastically (subpicosecond order) when level spacing matches LO phonon energy [13]. Nakayama noted a large margin for the energy conservation rule due to time-energy uncertainty and predicted a relaxation time of less than one picosecond, solving the time-dependent Schrödinger equation that includes an electron-LO phonon interaction Hamiltonian [14].

In Chapter 4, the author demonstrated that excited levels appeared before the intensity of

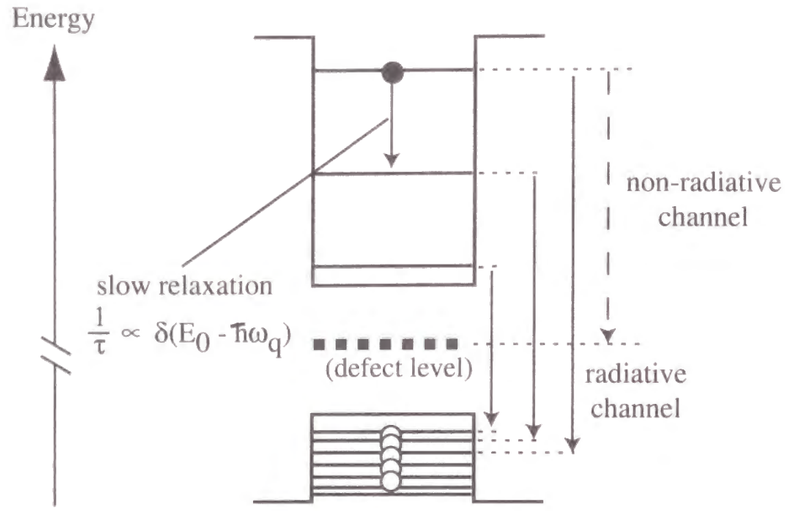

Figure 5-1 Schematic of the phonon bottleneck. Discrete sublevels in quantum dots may hinder carrier relaxation toward the ground level. In this case, carriers will recombine to emit at higher states or go to the nonradiative channel during a carrier cascade toward the ground level.

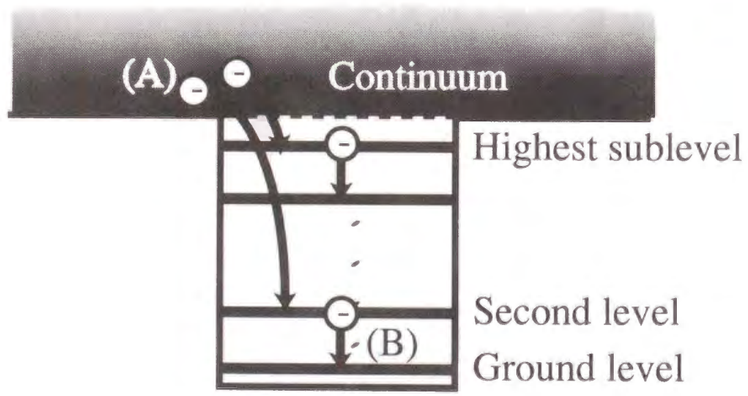

Figure 5-2 Two cases of carrier relaxation in a quantum-dot system : (A) the relaxation from continuum and (B) the relaxation between discrete sublevels. It is expected that case (A) will occur faster than case (B) since the energy conservation rule is more severe for the latter case.

the ground level was saturated in photoluminescence and electroluminescence spectra [15], suggesting slow carrier relaxation among sublevels in the system. Thus, recent discoveries of self-assembled quantum dots composed of different kinds of semiconductor materials enabled us to experimentally evaluate carrier relaxation lifetimes. Actual lifetimes have been compared with those in higher dimensional structures, which were reported to be 10^{-14} s in a GaAs bulk [16] and 10^{-13} s in a GaAs quantum well [17]. In the early stages of experiments, the author has observed the carrier relaxation lifetimes in ALS quantum dots using time-resolved photoluminescence measurements [18]. Retarded carrier relaxation with lifetimes of 10^{-11}~$^{-10}$ seconds, which are close to ours and longer than those in higher dimensional structures, have also been observed in many experiments [19, 20]. Some of the experiments for quantum dots confirmed the importance of phonon resonant excitation conditions in accelerating relaxation [21, 22]. Fast relaxation through the Auger process reportedly manifests itself during the fast rise of time-resolved photoluminescence and during the initial stage of carrier relaxation, when a large number of carriers surround quantum dots [23, 24]. Although more detailed theoretical and experimental work is required to reach precise conclusions about relaxation mechanisms, the phonon bottleneck does exist in the sense that relaxation in quantum dots is slower than in quantum wells.

The subject of this chapter is carrier dynamics in self-assembled InGaAs/GaAs quantum dots. High crystal quality of ALS dots (i.e., narrow spectrum broadening and high emission efficiency) enables us to experimentally pursue the phonon bottleneck problem. First, the author describes a proposed model of carrier relaxation processes into quantum dots, and then analyzes electroluminescence and time-resolved photoluminescence data to provide recombination and relaxation lifetimes. The model is used to explain luminescence decay and rise. Then, experiments on annealed quantum-dot samples are explained to demonstrate the effect of retarded carrier relaxation on emission spectra. After this chapter, how the phonon bottleneck effect works in quantum dots is clarified.

5-2. A model of carrier relaxation process in quantum dots

The carrier relaxation process into quantum dots generally consists of two processes

(Fig. 5-2). One is carrier relaxation from continuous energy levels into quantum-dot discrete levels, and the other is relaxation between the discrete levels inside dots. In many optical experiments as well as in quantum-dot lasers, carriers go through these two processes except when they are brought directly into the discrete levels by optical resonant excitation or through tunneling [25]. Since the energy conservation rule must be satisfied for carrier relaxation, relaxing carriers transfer a corresponding amount of energy to other particles such as phonons and other carriers. Thus, the relaxation rate strongly depends on the density of the final levels and on the number of the particles other than the transition matrix elements.

Figure 5-3 shows two representative processes from the continuum: (a) a single- or multi-phonon process, and (b) an Auger process. Usually, energy separation between the continuous level and sublevel in a dot does not exactly match the energy of a single phonon. Inoshita and Sakaki showed that two-phonon processes, including LO and LA phonons, reduce the requirements of energy conservation and drastically decrease relaxation lifetimes to the subpicosecond order [13]. Even so, this relaxation process cannot send carriers deep inside dots since the transition probability for the relaxation processes that include more than three phonons are greatly reduced. Therefore, once carriers are trapped in the upper levels of dots, they relax into lower energy levels by emitting phonons step-by-step. The Auger process of Fig. 5-3(b) works effectively if there are many carriers, since an electron can find another electron or a hole into which to transfer its energy and thus fall into the dot energy levels. This process works to further relax carriers into lower energy regions, as long as there is still a larger number of carriers outside the dots. The Auger process is more effective for carrier relaxation into deep sublevels.

Figure 5-4 shows an experimental report on the rise characteristics of photoluminescence for SK dots as a function of excitation power in Ref. 23. The rise time depends on the optical excitation density. For an excitation density between 10^{-1} and 4, the rise time stays almost constant at 90 ps. An increase in the excitation density to 10^2 W/cm^2 achieves a rise time of 40 ps. The results suggest that the rise time is dominated by the multi-phonon process while it is constant and by the Auger process while it decreases.

A large number of carriers, many more than the number of dots, are excited by a short intense laser pulse in time-resolved photoluminescence. Then, within at least half a hundred picoseconds, most carriers are captured to occupy the quantum-dot levels, primarily via the Auger process. This is followed by a carrier relaxation process in individual dots toward lower

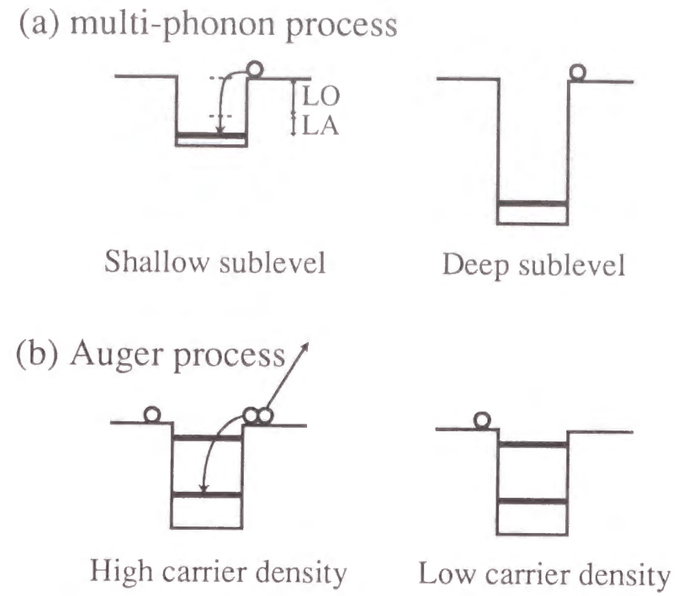

Figure 5-3 Schematic of two processes of carrier relaxation from continuous levels : (a) the multi-phonon process and (b) the Auger process. There can be a combination of LO and LA phonons during relaxation from the continuous energy level, but this is unlikely for deep sublevels. The Auger process is effective when carrier density is high.

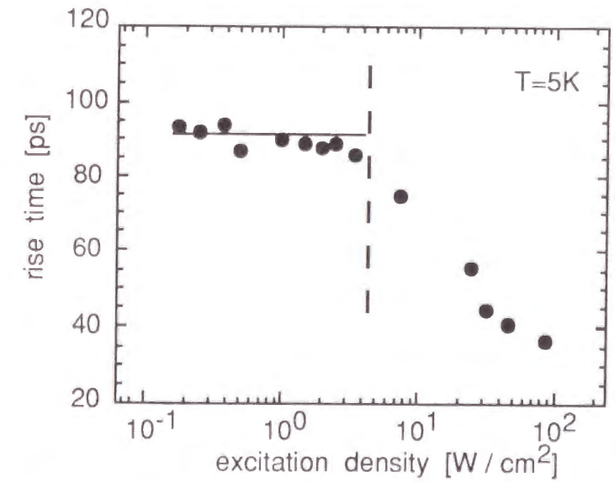

Figure 5-4 Experimental study of rising characteristics by Ohnesorge et al. (1996). The authors showed that the rising time depended on the excitation density in the SK dots. They reported that about 4 W/cm^2 was the critical excitation density for the Auger carrier relaxation process. (from Ohnesorge et al., 1996)

energy levels via phonon emission. In photoluminescence and electroluminescence, where there are fewer carriers than quantum dots, carrier injection and relaxation into dots is dominated by phonon emission. As a result, carriers are first captured by upper energy levels and then relax as though they were going down a ladder of discrete energy levels. The capture process occurs at a relatively high rate since the transition is from the continuous to discrete levels and energy conservation requirements are easily satisfied by the multi-phonon process. However, intersubband relaxation is significantly slowed as long as the energy separation closely matches the phonon energies. During laser operation at a low injection level, even at level above the threshold, carrier relaxation relies on the ladder process. As the injection level increases, the number of carriers around dots increases, making the Auger process effective for carrier relaxation.

5-3 Experiments on radiative recombination and relaxation of carriers in discrete energy levels

In this section, the injected-current dependence of the electroluminescence spectra is discussed to examine the impact of phonon bottleneck effect on carrier dynamics in ALS quantum dots. And then, the carrier relaxation and recombination lifetimes in the dots are directly measured by time-resolved photoluminescence. The emission decay curve from excited levels is found to be double exponential, but the decay from the ground level follows a single exponential curve. The decay curves are analyzed by a model that takes into account a rapid initial carrier capture process and the independence of each quantum dot. This approach enables us to obtain relaxation lifetimes as well as recombination lifetimes. The unique injected-current dependence of electroluminescence spectra is well simulated by the determined lifetimes with rate equation formulae.

5-3-1 Electroluminescence spectra

Figures 5-5 shows electroluminescence spectra for (a) 300 K and (b) 77 K. The diode structure is a 0.5-μm p-GaAs layer, 1-μm p-InGaP layer, ALS-dot layer sandwiched between 100-nm GaAs layers, 1-μm n-AlGaAs layer, and 0.5-μm n-GaAs layer grown on a (001)GaAs

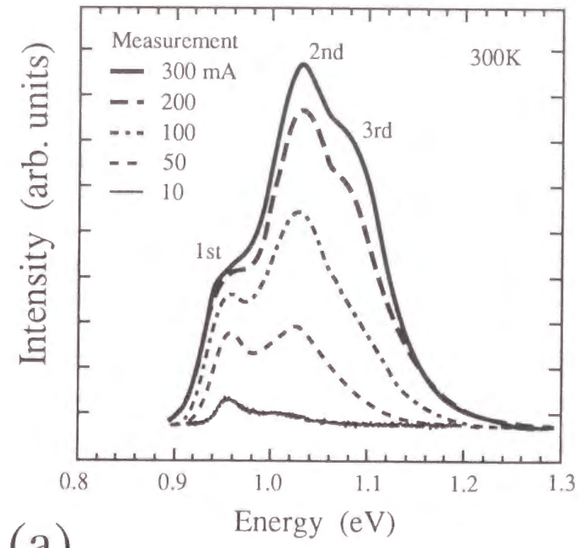

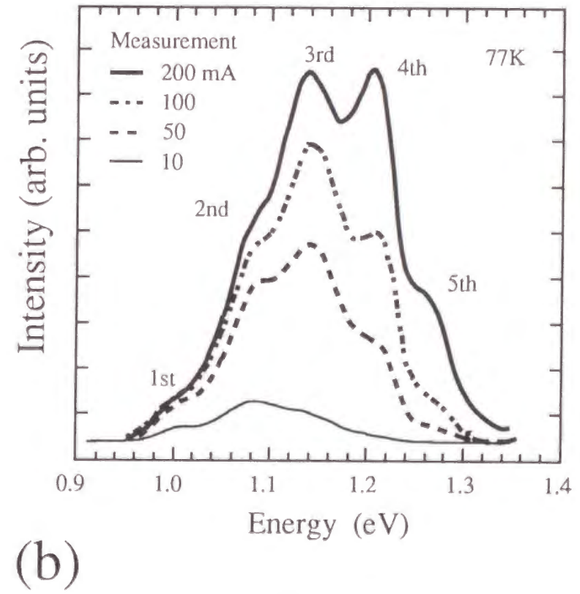

Figure 5-5 Electroluminescence spectra at (a) 300 K and (b) 77 K. As the injected current was increased, five discrete level appeared. Higher-level emissions appeared before the emission intensity of the lowest level reached its maximum value. Considering that the k_BT value is much narrower than the broadening of the spectra, these figures suggest the existence of a phonon bottleneck.

substrate. Luminescence parallel to the sample surface was dispersed and detected with a lock-in technique using an InGaAs photo-multi detector that was kept at -70°C. The electrode size was 20 x 900 μm^2. The current-injected area was estimated by the near field pattern, and according to this estimation, it was spread out over 150 to 200 x 900 μm^2 in the quantum-dot layer. Three emission peaks corresponding to the interband transition between the discrete levels of the conduction and valence bands appeared at 300 K when the injected current was increased, and five peaks appeared at 77 K. In Chapter 4, a clue to the phonon bottleneck problem was pointed out in the electroluminescence spectra at 77 K. At increasing amounts of current injection, second- and third-level emissions occur, that exceeds ground-level emission well before the emission from the ground level is saturated (at 10 mA); in other words, the carrier distribution between discrete levels in no way follows the Fermi-Dirac distribution at the measured temperature of 77 K. The most probable explanation for this is that the carrier relaxation lifetime is comparable to the carrier recombination lifetime.

Characteristics of sublevel emission varied between the two temperatures, indicating that some features of carrier dynamics depend on temperature. For example, when the emission intensity of the ground level reached half maximum, the intensity of the second level was stronger than that of the ground level at 77 K (10 mA), but the two were almost equal at 300 K (50 mA). The result suggests comparatively faster carrier relaxation at 300 K. The author directly evaluates the relaxation lifetimes in section 5-3-2.

It should be noted that random carrier capturing into the dots [26] has been proposed as an alternative interpretation of multiple emission peaks [15, 27]. The emission spectra was calculated using a Poisson distribution to count the number of carriers that were trapped in quantum dots. As a result, they claim that, even if retarded carrier relaxation is not taken into account, emissions from higher energy levels appears before lower-energy-level emissions are saturated. However, their calculation of the emission spectra cannot explain the emission spectra measured, where the third-level emission exceeded the ground-level emission before the ground-level intensity saturated. Above all, the random capture model offers no explanations of the difference in the emission spectra between 77 K and 300 K.

5-3-2 Time-resolved photoluminescence

Carrier lifetimes in ALS quantum dots were measured by time-resolved

photoluminescence. The ALS dots were grown in PJE reactor tube by 18 cycles of In-Ga-As alternate supply onto a 500-nm GaAs buffer layer on a (001)-GaAs substrate and capped by a 100-nm GaAs layer (see Chapter 2). The growth temperature was 460°C. Samples set in a temperature-controlled cryostat were excited by a mode-locked 532-nm Nd:YAG laser beam with a pulse width of 200-ps and a repetition rate of 82 MHz. Luminescence from the sample surface was dispersed by a monochrometer and time-resolved with a streak camera. Figure 5-6 shows typical experimental results of luminescence intensity decay up to the fifth emission peak at 20 and 250 K. The order of emission peaks corresponds to that in the electroluminescence spectra of Fig. 5-5 (b).

Some features appear in the decay curves. First, luminescence decays faster as the order of emission peaks gets higher. Similar results were obtained by Raymond et al. [28]. Since the spontaneous emission lifetime due to the interband transition in quantum dots is common among energy levels if a constant oscillator strength is assumed [29], the observed variation of the decay curves suggests that carrier relaxation lifetimes decrease with increasing order of levels. Second, emission decay is not exponential, which is probably because the decay is a combination of relaxation and recombination components. The decay is fast at the initial stage and becomes slow. This is in contradiction to theoretical curves, which are moderate at the beginning but become fast at the end [26, 30]. Third, the decay is faster at 250 K than at 20 K, indicating that relaxation and/or recombination lifetimes are shorter at higher temperatures.

To analyze the decay curves, the author developed a new model that describes the temporal evolution of carrier number and is based on the following two points [31]. First, assuming that carriers rapidly relax into the quantum-dot discrete levels during pulse excitation, calculations start at the point where levels inside the dots are occupied by carriers. This is reasonable because there are a large number of carriers within 10^{12} to 10^{13} cm^{-2} around the dots during short pulse excitation, and carrier-carrier scattering causes rapid carrier relaxation from the continuum into dots via the Auger process. Second, the model takes into account that the carrier capture process occurs randomly, and that the number of carriers and their distribution in discrete levels differs from dot to dot. Therefore, the author named the model the 'RIO' (random initial occupation) model.

Taking into account only the two electron levels of ground and excited for reasons of simplicity, the initial situation of carriers and levels is categorized into the four types shown in Fig. 5-7: A, both levels are filled; B, only the excited level is filled; C, only the ground level is

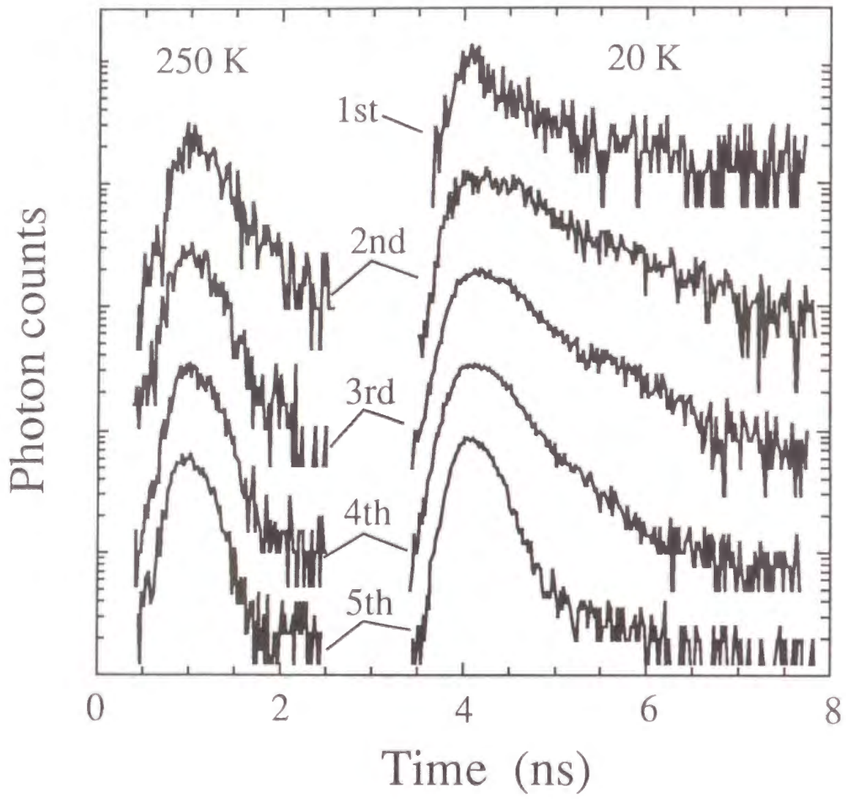

Figure 5-6 Example of luminescence decay of the five levels at 250 and 20 K. The higher the temperature, the faster progresses the decay; the lower a state, the slower the decay.

filled; and D, both levels are empty. All paths to the final situation in this system is described in the figure. When a dot is initially in case A, three paths, A_1, A_2, and A_3, are possible for reaching the final destination of D. Also, two paths, B_1 and B_2, are possible for case B, and a single path, C_1, is possible for case C. Radiative decay is allowed in both levels on the assumption that hole quantization energies are less than k_BT due to the comparatively heavy effective mass [7].

The number of carriers in the excited level is counted by evaluating the paths beginning from case A and also the paths beginning from case B. Let $N_{AA}(t)$ be the number of A at time t, and $N_{AB}(t)$ to be the number of B formed from A as a result of the recombination of only the ground-level carrier. The carrier number in the excited level in dots if the initial situation is A is described by

$$N_A(t) = N_{AA}(t) + N_{AB}(t). \qquad (5.\ 1)$$

Here, the rate equation for $N_{AA}(t)$ is

$$\frac{dN_{AA}(t)}{dt} = -\frac{2N_{AA}(t)}{\tau_r}, \qquad (5.\ 2)$$

where τ_r is the carrier recombination lifetime, which is assumed to be common between the two levels. Considering both paths A_1 and A_2, the rate equation for $N_{AB}(t)$ is given by

$$\frac{dN_{AB}(t)}{dt} = \frac{N_{AA}(t)}{\tau_r} - \frac{N_{AB}(t)}{\tau_{rel}} - \frac{N_{AB}(t)}{\tau_r}, \qquad (5.3)$$

where τ_{rel} is the carrier relaxation lifetime from the excited to ground levels. Solving Eqs. (5. 2) and (5. 3) obtains

$$N_{AA}(t) = N_{A0}e^{-\frac{2t}{\tau_r}}, \qquad (5.\ 4)$$

$$N_{AB}(t) = e^{-\left(\frac{1}{\tau_{rel}}+\frac{1}{\tau_r}\right)t}\int_0^t \frac{N_{AA}(s)}{\tau_r} e^{\left(\frac{1}{\tau_{rel}}+\frac{1}{\tau_r}\right)s} ds, \qquad (5.\ 5)$$

where N_{A0} is the initial number of case-A dots. If $\tau_{rel} << \tau_r$, $N_{AB}(t)$ becomes zero and the decay lifetime of $N_A(t)$ reduces to $\tau_r/2$. If τ_{rel} is not negligible compared with τ_r, the decay of $N_{AB}(t)$ is not negligible and the decay lifetime of $N_A(t)$ is larger than $\tau_r/2$.

For the number of carriers in the excited level if the initial situation is B, $N_B(t)$, the rate equation is

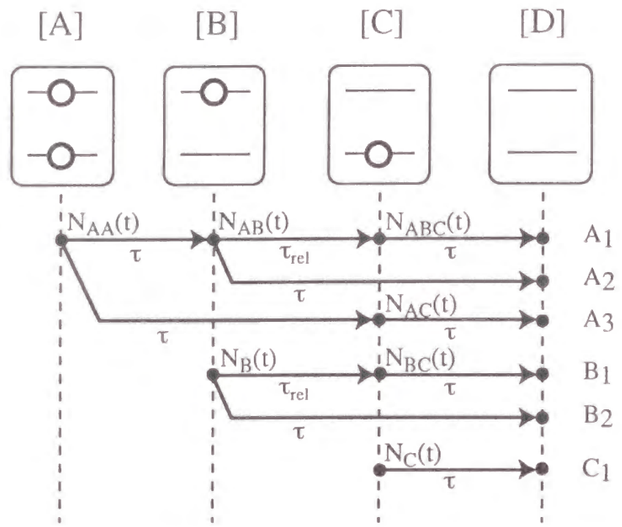

Figure 5.7 Model for the carrier dynamics between two levels in an uncoupled dot. When the carrier injection from continuous levels into sublevels is sufficiently fast, all possible initial situations can be classified as four cases, A, B, C, or D. The decay in the carrier number in the excited state is described by considering paths A_1, A_2, A_3, B_1 and B_2.

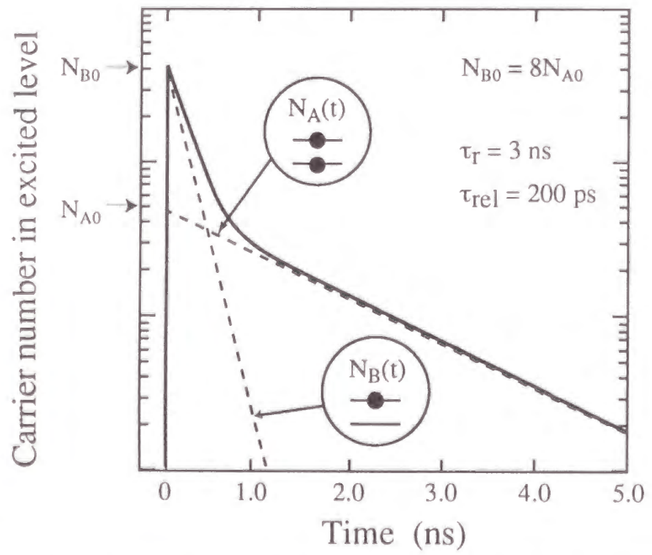

Figure 5-8 Calculated number of carriers in the excited levels as a function of time. The solid line shows N(t), the dashed lines show $N_A(t)$ and $N_B(t)$. The figure shows a double exponential decay line, which matches the measured results. The faster decay indicates a carrier process that begins at case B, and the slower decay indicates one that begins at case A.

$$\frac{dN_B(t)}{dt} = -\frac{N_B(t)}{\tau_{rel}} - \frac{N_B(t)}{\tau_r}, \qquad (5.\ 6)$$

and the result is

$$N_B(t) = N_{B0}e^{-\left(\frac{1}{\tau_{rel}}+\frac{1}{\tau_r}\right)t}, \qquad (5.\ 7)$$

where N_{B0} is the initial number of case B. The decay lifetime of $N_B(t)$ is $(\tau_{rel}^{-1} + \tau_r^{-1})^{-1}$, and it gets closer to τ_{rel} if $\tau_{rel} << \tau_r$. As a result, the total number of carriers in the excited level is given by

$$N_{ex}(t) = N_A(t) + N_B(t). \qquad (5.\ 8)$$

The emission intensity is given by $N_{ex}(t)/\tau_r$.

The measured decay curves having (more than) two components in Fig. 5-6 are reproducible by this type of calculation. Figure 5-8 shows an example. The solid curve in the figure is the number of carriers in the excited levels, as calculated by Eq. (5. 8) with $\tau_r = 3$ ns, $\tau_{rel} = 200$ ps, and $N_{A0} = N_{B0}/8$ as parameters. The resultant solid curve consists of two dashed lines: steep, reflecting the decay starting from case B ($N_B(t)$); and moderate, reflecting the decay starting from case A ($N_A(t)$). The critical point where the inclination of the line changes depends on the ratio of N_{A0} / N_{B0}, and a decay curve with fast and slow components is obtained for $N_{B0} > N_{A0}$.

The carrier number in the ground level is also calculated by considering the paths A_1, A_3, B_1, and C_1. As for the excited level, let us define the numbers of carriers as $N_{ABC}(t)$, $N_{AC}(t)$, $N_{BC}(t)$, and $N_C(t)$, as shown in Fig. 5-7. The rate equation for these are

$$\frac{dN_{ABC}(t)}{dt} = \frac{N_{AB}(t)}{\tau_{rel}} - \frac{N_{ABC}(t)}{\tau_r}, \qquad (5.\ 9)$$

$$\frac{dN_{AC}(t)}{dt} = \frac{N_{AA}(t)}{\tau_r} - \frac{N_{AC}(t)}{\tau_r}, \qquad (5.\ 10)$$

$$\frac{dN_{BC}(t)}{dt} = \frac{N_B(t)}{\tau_{rel}} - \frac{N_{BC}(t)}{\tau_r}, \qquad (5.\ 11)$$

and

$$\frac{dN_C(t)}{dt} = -\frac{N_C(t)}{\tau_r}. \qquad (5.\ 12)$$

Solving Eqs. (5. 9) through (5. 12) obtains

$$N_{ABC}(t) = e^{-\frac{t}{\tau_r}} \int_0^t \frac{N_{AB}(s)}{\tau_{rel}} e^{\frac{s}{\tau_r}} ds \quad , \qquad (5.\ 13)$$

$$N_{AC}(t) = e^{-\frac{t}{\tau_r}} \int_0^t \frac{N_{AA}(s)}{\tau_r} e^{\frac{s}{\tau_r}} ds \quad , \qquad (5.\ 14)$$

$$N_{BC}(t) = e^{-\frac{t}{\tau_r}} \int_0^t \frac{N_B(s)}{\tau_{rel}} e^{\frac{s}{\tau_r}} ds \quad , \qquad (5.\ 15)$$

and

$$N_C(t) = N_{C0} e^{-\frac{t}{\tau_r}}, \qquad (5.\ 16)$$

where N_{C0} is the initial number of carriers in case C. Finally, the total number of carriers in the ground level is given by

$$N_{gr}(t) = N_{ABC}(t) + N_{AC}(t) + N_{BC}(t) + N_C(t). \qquad (5.\ 17)$$

If $\tau_{rel} << \tau_r$, Eqs. (5. 13) through (5. 15) become zero and the decay time of $N_{gr}(t)$ reduces to τ_r. In the same case, the decay lifetime of $N_A(t)$ reduces to $\tau_r/2$. However, in Fig. 5-6, the later moderate decay in the second level is not half of the decay in the ground level. This indicates that relaxation lifetimes are not negligible compared with recombination lifetimes and/or that recombination lifetimes are not constant among the sublevels.

The measured decay curves are analyzed by the simple double-exponential formulation of

$$N(t) = N_{A0} e^{-\frac{t}{\tau_r}} + N_{B0} e^{-\frac{t}{\tau_{rel}}}, \qquad (5.\ 18)$$

after deconvoluting the decay curves from the excitation pulse. The second term of Eq. (5. 18) is, of course disregarded in considering the decay of the ground level. Here, from the estimation of the RIO model at the limit of $\tau_{rel} << \tau_r$, the author assumes the initial steep decay component to be dominated by carrier relaxation and the subsequent slow decay component by recombination. In strict treatment, the degeneracy and selection rules in relaxation for multiple sublevels must be taken into account in solving the rate equations. However, Eq. (5. 18) is a good approximation because the initial situation of dots is roughly categorized into two cases: when the lower level is empty and when the lower level is filled.

The results of the analysis are plotted in Fig. 5-9 as a function of temperature. The recombination lifetime in Fig. 5-9 (a) is independent of level order and temperature. The relaxation lifetime of Fig. 5-9 (b) varies among the levels and is temperature-dependent. The nanosecond recombination lifetimes and their temperature independence match a theory about the spontaneous emission of electron-hole pairs in quantum dots [29]. Similar experimental results were obtained for InGaAs/GaAs SK dots by Wang et al. [32] and Kamath et al. [33], and for InP/InGaP SK dots by Kurtenbach et al. [34]. As the order of levels rose from the second to the fifth, the relaxation lifetime decreased by one order of magnitude. This is probably because the state density increases with the order of levels, as seen in the electroluminescence intensity. High state density enhances the probability of carrier relaxation. The decrease in relaxation lifetimes following a temperature decrease can be attributed to the increase in the number of phonons following the Bose distribution function.

Let me check what the decay curves look like if it is assumed that carriers relax from the continuous level to the topmost fifth level and then relax step-by-step. The rate equations for this case are

$$\frac{dN_w(t)}{dt} = -N_w(t)\left(\frac{1}{\tau_w} + \frac{1}{\tau_{wr}}\right), \qquad (5.\ 19)$$

$$\frac{dN_5(t)}{dt} = \frac{N_w(t)}{\tau_w} - N_5(t)\left(\frac{1}{\tau_5} + \frac{1}{\tau_r}\right), \qquad (5.\ 20)$$

$$\frac{dN_i(t)}{dt} = \frac{N_{i+1}(t)}{\tau_{i+1}} - N_i(t)\left(\frac{1}{\tau_i} + \frac{1}{\tau_r}\right) \qquad (i = 2, 3, 4), \qquad (5.\ 21)$$

and

$$\frac{dN_1(t)}{dt} = \frac{N_2(t)}{\tau_2} - \frac{N_1(t)}{\tau_r}, \qquad (5.\ 22)$$

where τ_{wr} is the recombination lifetime in the continuous level, τ_w is the relaxation lifetime from the continuous level to the topmost fifth level, and τ_i denotes the relaxation lifetime from the i-th sublevel to the (i - 1)-th sublevel. Using the occupation factor of $f_i = N_i/D_i$ with the state density of D_i obtains

$$\tau_i^{-1} = (1 - f_{i-1})\,\tau_{i0}^{-1}, \qquad (5.\ 23)$$

where τ_{i0} is the intrinsic carrier relaxation lifetime at the i-th level. By defining the lifetimes in

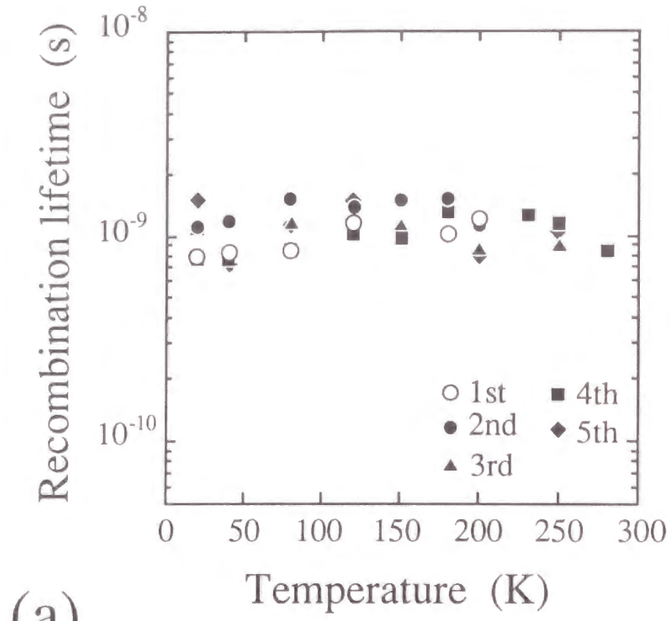

(a)

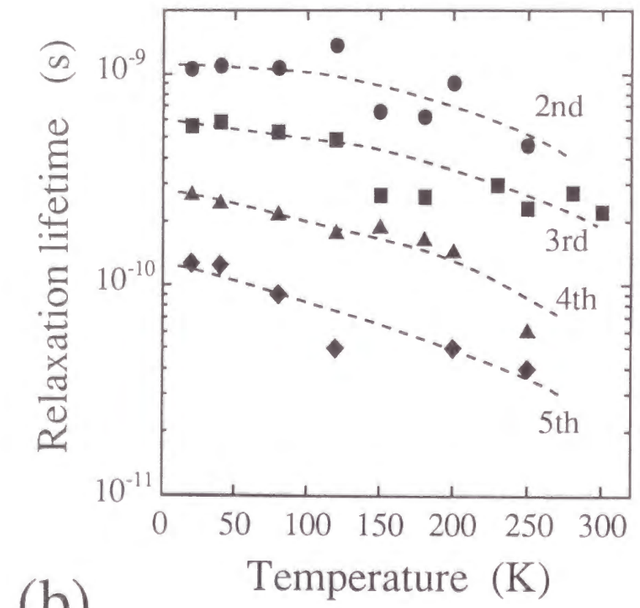

(b)

Figure 5-9 Carrier lifetimes of sublevels as a function of temperature: (a) recombination lifetime and (b) relaxation lifetime. The recombination lifetime is independent of temperature and about 1 ns in all sublevels. The higher the temperature and the higher the level order, the faster the carrier relaxation.

Fig. 5-9 as τ_{i0}, the temporal evolution of the carrier number in sublevels was calculated (Fig. 5-10). To estimate the fastest rise under step-by-step relaxation, the author assumed $f_i = 0$ in the calculation. The figure indicates that the delay of rising at lower-ordered levels cannot be ignored. The delay is about 2 ns between the fifth and the ground level, which is approximately equal to the simple sum of the relaxation lifetimes of the sublevels. Comparing the experimental results of Fig. 5-6 and the calculated results of Fig. 5-10, it is clear that the assumption of the step-by-step relaxation process cannot explain the fast rising of photoluminescence in the time-resolved measurements. The RIO model, which assumes fast carrier setup in quantum dots resulting from the Auger process and the subsequent slow step-by step relaxation inside quantum dots, successfully explains the decay curves of time-resolved photoluminescence.

5-3-3 Simulation of electroluminescence spectra

In this section, the electroluminescence spectra of Fig. 5-5 are simulated using the obtained relaxation and recombination lifetimes. Note that the carrier number around the quantum dots is estimated to be about two to three orders of magnitude smaller than that in time-resolved photoluminescence measurements. Thus, the author used the step-by-step relaxation model instead of RIO model; that is carriers first relax from the continuum into the topmost level and then relax between discrete sublevels. The thermal excitation of electrons was disregarded since the sublevel spacing is much larger than the value of k_BT.

The rate equation for the carrier number in sublevels during electroluminescence measurement is obtained from Eqs. (5. 20) through (5. 22) by assuming the differential of time is zero,

$$\frac{N_5}{\tau_5} + \frac{N_5}{\tau_r} - G = 0 \quad , \tag{5. 24}$$

$$\frac{N_i}{\tau_i} + \frac{N_i}{\tau_r} - \frac{N_{i+1}}{\tau_{i+1}} = 0 \qquad (i = 2, 3, 4), \tag{5. 25}$$

and

$$\frac{N_1}{\tau_r} - \frac{N_2}{\tau_2} = 0 \quad , \tag{5. 26}$$

where G is the carrier injection rate from the continuous level into dots. Here, the recombination lifetime, τ_r, is considered to be common to all levels, as seen in Fig. 5-9(a), and

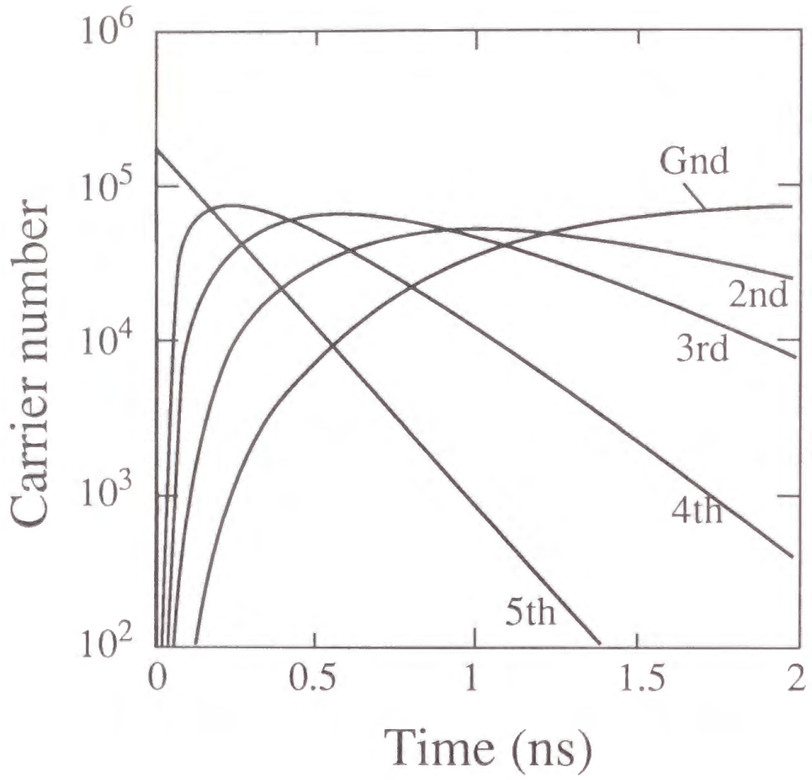

Figure 5-10 Calculated rise of the carrier number when the direct carrier relaxation from the continuous level is negligible. The rise slowed as the level order decreased. The delay is approximately equal to the simple sum of the relaxation lifetimes of sublevels.

nonradiative recombination is disregarded in high-quality samples (see Chapter 4). Assuming a Gaussian distribution for the broadening of emission spectra, the luminescence spectra were calculated by

$$I(E) = \sum_{i=1}^{5} \frac{f_i N_i}{\tau_r} \exp\left[- \frac{(E - E_i)^2}{2\Gamma^2} \right], \qquad (5.27)$$

where E is the energy of the photon, E_i is the energy at the i-th level, and Γ is an inhomogeneous broadening factor.

Figures 5-11(a) and 5-11(b) show the results of the calculations for 300 K and 77 K, respectively. During calculation, the author used an in-plane dot density of 5%, a broadening factor of 50 meV, τ_r = 1 ns, and $D_i = 2 \bullet i$ (i = 1 to 5), taking spin into consideration. The intrinsic relaxation lifetimes used were τ_{02} = 400, τ_{03} = 200, τ_{04} = 50, and τ_{05} = 20 ps for 300 K, and τ_{02} = 1000, τ_{03} = 500, τ_{04} = 200, and τ_{05} = 90 ps for 77 K. The calculations explain the measured electroluminescence spectra of Fig. 5-5. The author found that the relaxation lifetime is short enough so that the ground-level emission is dominant at lower currents. As the number of injected carriers increases, the carrier relaxation rate decreases, and emissions from higher levels occur. Since the relaxation lifetime is closer to the radiative recombination lifetime at 77 K than at 300 K, emissions from higher levels at 77 K occur for a lower current. At 77 K, the calculated current values match the measured values. At 300 K, the trend of relative peak intensities is well explained. However, the values for the current by calculation are much smaller than that using the measured values. This discrepancy grows larger as the current increases --- a tendency that can be attributed to consumption of carriers due to thermally activated nonradiative recombination outside the dots (see Chapter 4). A rise in local temperature due to the nonradiative process may lead to further acceleration of nonradiative recombination.

Figures 5-12 shows the values of f_i as a function of the current for (a) 300 K and (b) 77 K. Note that the ground, second, and third levels are not completely filled and that characteristic features depend on temperature. For example, the maximum of f_i for the ground and the second levels are about 80% at 300 K and about 60% at 77 K. For the third level, these maximum are 90% at 300 K and 80% at 77 K. Although the emission from the ground level is dominant, the maximum occupation factor at the ground level is 60% for 300 K. In quantum dot lasers, the suppression of carrier filling may limit the optical gain required for lasing at the ground level

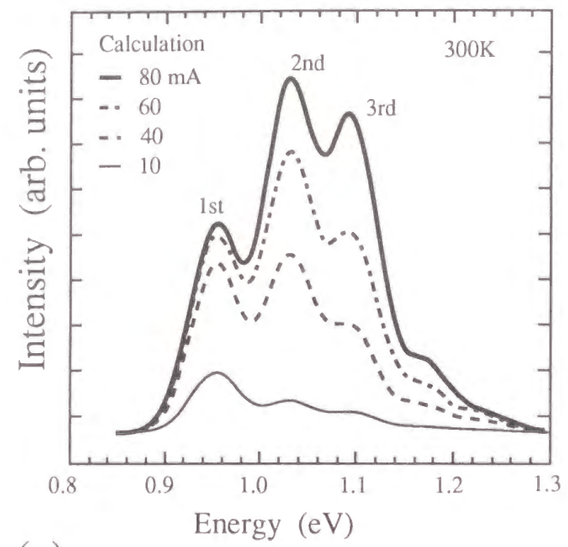

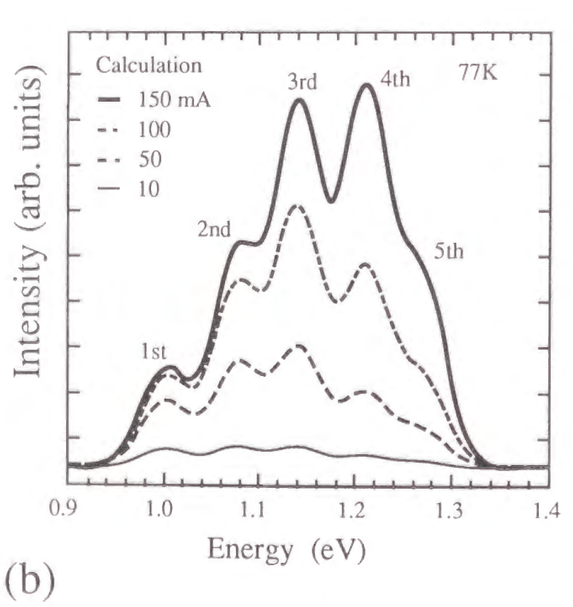

Figure 5-11 Calculated electroluminescence spectra at (a) 300 and (b) 77 K using the rate equations of the five states. The results of the calculation correlate with the measured spectra in Figs. 5-5(a) and (b).

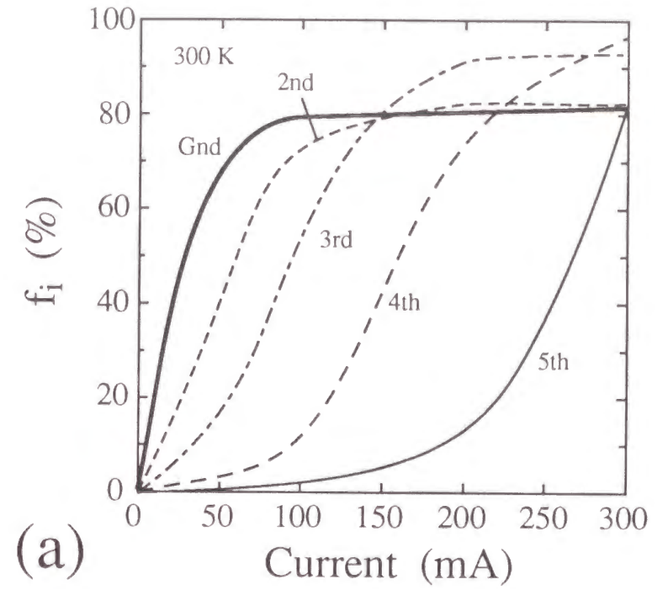

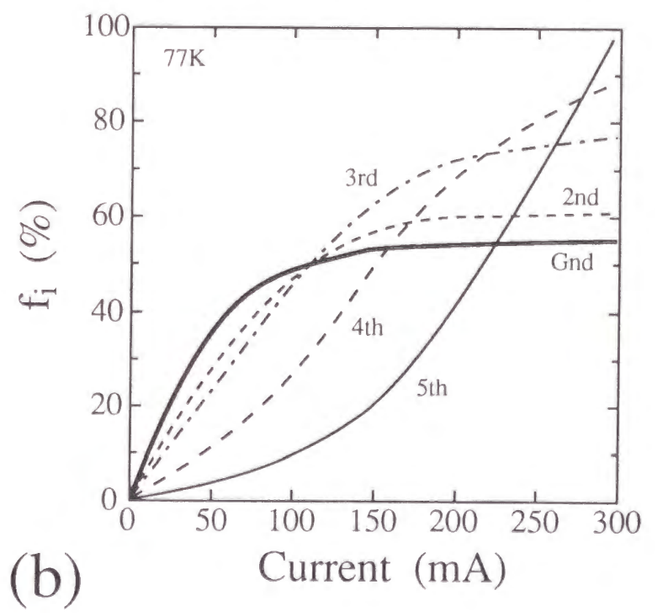

Figure 5-12 Value of f_i as a function of injected current for (a) 300 K and (b) 77 K. The ground, second and third states were not completely filled, and the maximum occupation factor of these levels depended on the temperature.

[35].

5-4. Effect of thermal treatment

A relative intensity of emission peaks in the electroluminescence spectra are dominated by the balance between carrier relaxation and recombination rates, as explained in the previous section. In this section, an interesting example of this fact in annealed quantum dots is described.

5-4-1 Change of emission spectra after annealing

Annealing of ALS-dot samples was performed in a reactor tube of a liquid-phase epitaxy system between 500°C and 680°C, in a pure N_2 gas atmosphere to protect the samples from oxidation (see Chapter 1). A GaAs plate was placed on a sample surface to raise the arsenic vapor pressure and thus prevent arsenic desorption from the sample surface. The quantum dots were originally grown at 460°C using the growth sequence of 18 cycles of In-Ga-As (see Chapter 3).

Figure 5-13 compares the photoluminescence spectrum of an as-grown sample with the spectra of samples after annealing at 615°C for 30 and 60 minutes. In the as-grown sample, three peaks were observed that are due to the interband transition between the discrete levels of the conduction and valence bands. The excitation power is very low; the emission intensity of the ground level in Fig. 5-13 is less than one-fifth of the maximum value reached at a higher excitation. Annealing greatly reduces the integrated photoluminescence intensity, broadens the spectra, and slightly moves the emission peak toward higher energies. What is most remarkable is that the relative peak intensity between the ground- and second-level emissions is greatly changed after annealing: although the ground-level emission is about three times stronger than the second-level emission in the as-grown sample, the two peaks are almost comparable in their intensity after 30 minutes of annealing. This is not due to drastic structural changes and the resultant reduction of the transition oscillator strength since the emission energy shift is only about 5 meV and the TEM image of the 30-minute-annealed samples shows no significant

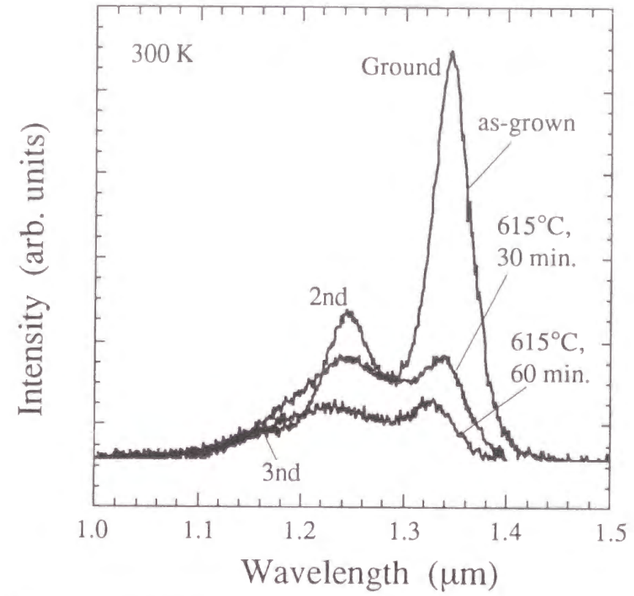

Figure 5-13 Photoluminescence spectra before and after annealing at 615°C for 30 and 60 minutes. The emission from the sublevels is observed. It is remarkable that the emission intensity of the ground level decreased several times over that of the second level.

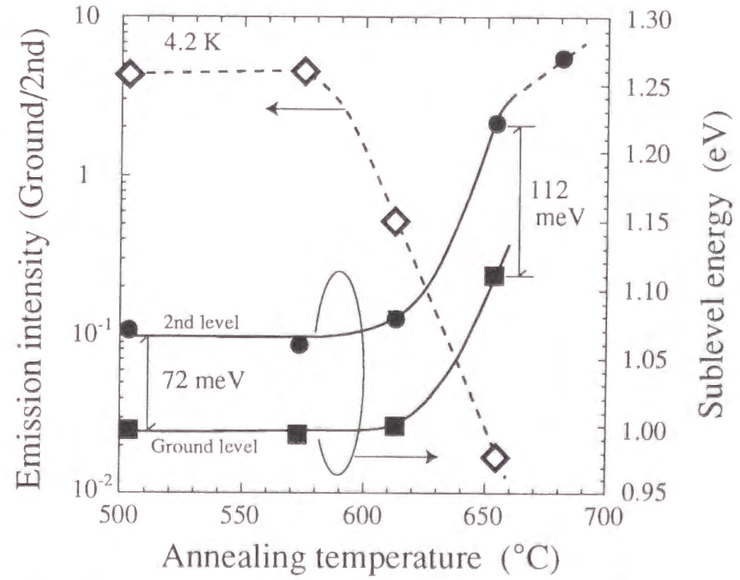

Figure 5-14 Emission intensity of the ground level divided by that of the second level (I_{ground}/I_{2nd}) and emission energy of the sublevels as a function of annealing temperature. At over 600°C, the energy shift occurred, and the relative intensity of the ground level was greatly reduced after annealing. The energy shift was larger in the second level up to 650°C.

changes in dot structure, size, and numerical density. One possible explanation for this phenomenon is that the carrier dynamic process in quantum dots is affected by the thermal treatment.

Figure 5-14 shows the energy of the ground- and second-level emission peaks, as well as the emission intensity of the ground level relative to the second level, as a function of the annealing temperature. The energy shift occurs at over 600°C because of interdiffusion, and simultaneously, the relative intensity of the ground-level emission is greatly reduced. The figure also shows that the energy shift is larger in the second peak and that the level separation is increased by annealing. This contradicts the experiences in the study of interdiffusion in quantum wells, where the level separation always decreases after interdiffusion since interdiffusion spreads the confinement potential in the growth direction. This unique feature can be attributed to structural asymmetry between the in-plane and perpendicular directions in ALS dots with a disk-like shape; because of the asymmetry, the interdiffusion in early stages occurs faster at the edge of the dot than in the central region [36]. Since this corresponds virtually to the decrease in the in-plane diameter of the dots, the energy separation increases.

5-4-2 Competition between carrier relaxation and recombination

Figure 5-15 shows examples of time-resolved photoluminescence of the ground- and second-level emissions after annealing at 615°C for 60 minutes. The decay time of the ground-level emission decreases as the temperature rises. This is in contrast to the decay times of as-grown samples, which are insensitive to temperature (Fig. 5-9(a)). The decay curves of the second level are double-exponential, a result of the competition between relaxation into the ground level and recombination at the second level, as seen in Section III. As the temperature increases, the relaxation accelerates but the recombination lifetime is not sensitive to temperature. Figure 5-16 shows (a) recombination and (b) relaxation lifetimes up to the third level before and after annealing. The solid and open symbols indicate the lifetimes of as-grown and annealed samples, respectively. The third level in the annealed sample is not clearly visible because of emission broadening. The recombination lifetimes at the ground level become temperature-dependent after annealing and decrease to a few hundred picoseconds near room temperature. This suggests that the nonradiative channel affects only the ground level. The nonradiative lifetime for the ground level is estimated to be 250 ps if the recombination lifetime

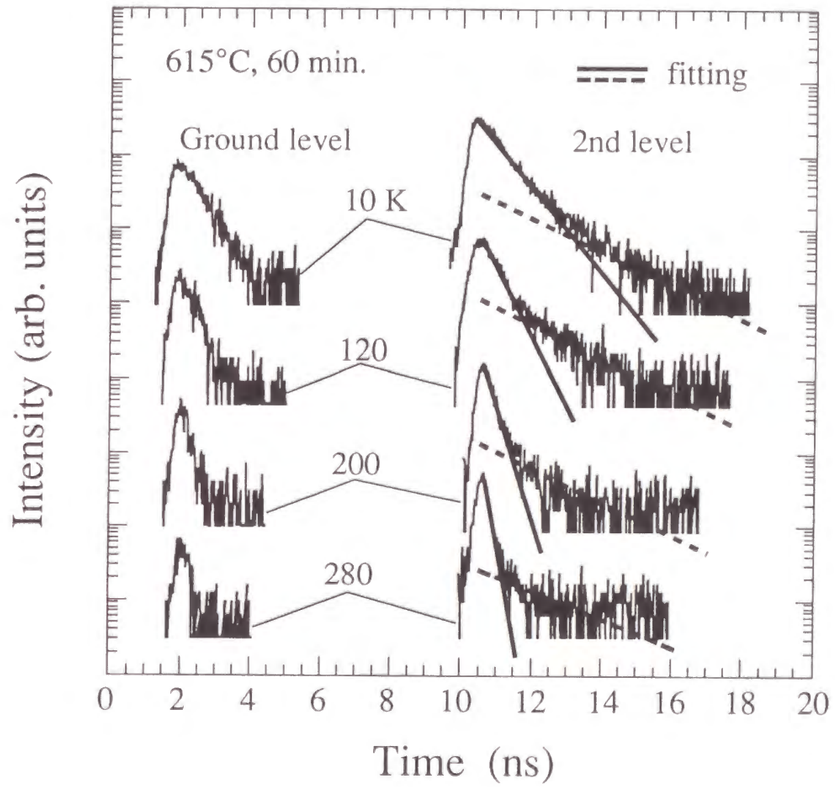

Figure 5-15 Examples of decay curves of the ground and second levels after annealing at 615 °C for 60 minutes. The decay time of the ground level decreased as the temperature rose, but was insensitive to temperature in as-grown samples. The decay curves of the second level were double-exponential.

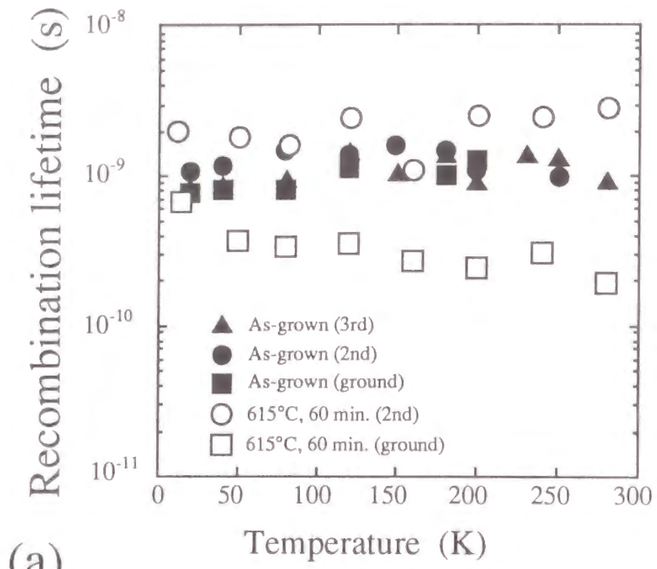

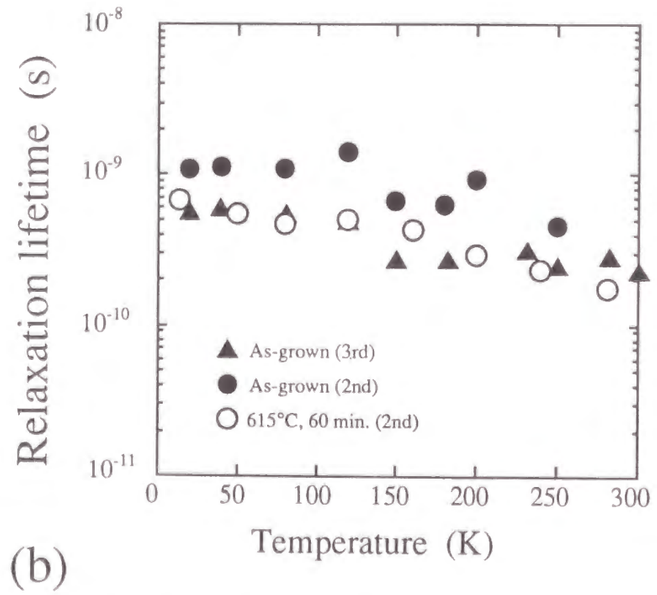

Figure 5-16 Lifetimes up to the third level as a function of temperature: (a) recombination lifetimes and (b) relaxation lifetimes. The solid and open symbols indicate lifetimes of as-grown and annealed samples, respectively. The recombination lifetimes in the ground level became temperature-dependent after annealing and decreased to a few hundred picoseconds near room temperature. The relaxation lifetimes decreased slightly after annealing.

of 200 ps and the radiative lifetime of 1 ns are used. The relaxation lifetimes decrease to about half after annealing, and it is not clear whether the decrease is significant since, following the RIO model used in the analysis, the faster decay time is not a pure carrier relaxation lifetime. However, it should be noted that nonradiative levels possibly assist carrier relaxation, which was predicted by Sercal [37].

Let me test several possibilities to explain why the nonradiative channel affects only the ground level. One is that carrier trapping may require some phonon scattering and the probability of scattering is low for higher levels. Another is that defect levels outside the dots, resonant in energy with the ground level, are the origin of the nonradiative channel (such resonant carrier trapping was reported by Tsang [38]).

The photoluminescence spectra were simulated by the same procedure as in section 5-3-3. The rate equation for the ground-level population should be changed to include the nonradiative process as

$$\frac{N_1}{\tau_{n1}} + \frac{N_1}{\tau_r} - \frac{N_2}{\tau_2} = 0 \qquad (5.28)$$

where τ_{n1} is the nonradiative lifetime at the ground level. Figure 5-17 shows the photoluminescence spectra calculated using the nonradiative lifetime as a parameter. Parameters used are a carrier injection rate of $G = 10^{-6}$ s^{-1} per individual dot, a broadening factor with a Gaussian distribution of 50 meV, $\tau_r = 1$ ns, $D_i = 2 \bullet i$ ($i = 1, 2, ..., 5$), $\tau_{02} = 200$, $\tau_{03} = 100$, $\tau_{04} = 50$, and $\tau_{05} = 20$ ps. Unknown relaxation lifetimes of τ_{03} were assumed to be half of that used in section 5-3-3, since present experiments show that the relaxation lifetimes of τ_{02} decrease by about half after annealing. The unknown relaxation lifetimes of τ_{04} and τ_{05} do not affect the results of Fig. 5-17 as long as emission from either the fourth or fifth level does not appear. The injection rate was chosen to give a low injection condition, where the fourth and fifth levels do not appear in the calculated spectrum. The occupation at the ground level, f_1, is about 8%. As the nonradiative lifetime decreases from infinity to a few hundred picoseconds, the emission intensity of the ground level decreases and becomes comparable to that of the second level. The value of the nonradiative lifetime in the simulation well matches the value estimated in Fig. 5-16.

The carrier dynamics in ALS dots are summarized in Fig. 5-18. The relative emission intensity of the ground and second levels is determined by the equilibrium between the radiative

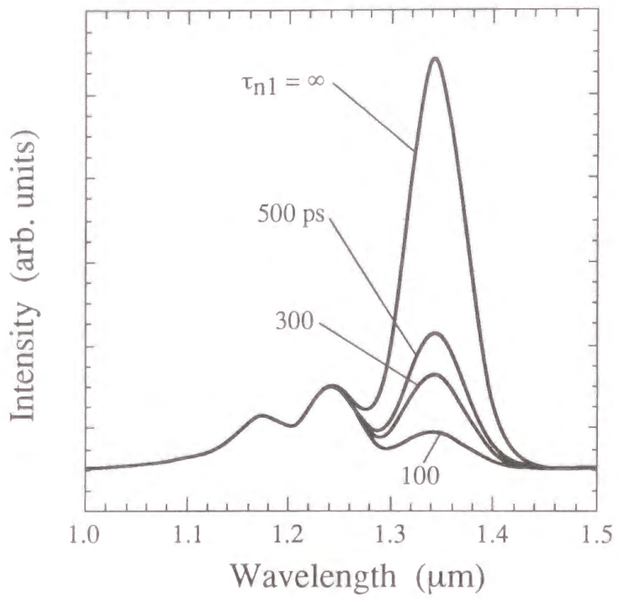

Figure 5-17 Photoluminescence spectra calculated by assuming values for the nonradiative lifetime (τ_{n1}). As the nonradiative lifetime decreased from infinity to a few hundred picoseconds, the emission intensity of the ground level decreased and becames comparable to that of the second level.

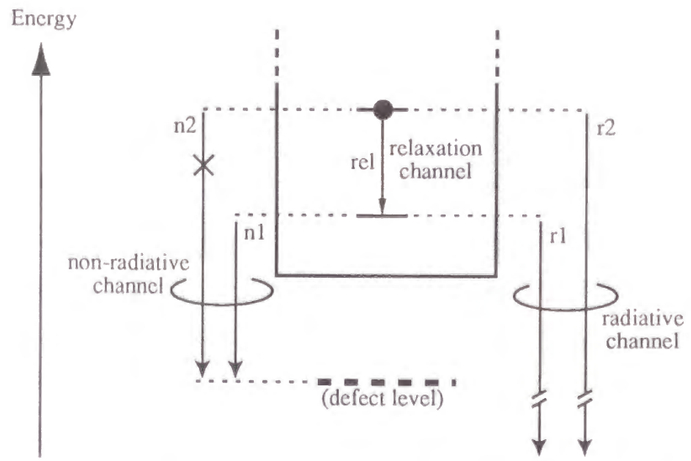

Figure 5-18 Schematic of carrier dynamics in a quantum dot before and after annealing. The relative emission intensity of the ground and second levels was determined by the equilibrium between the radiative recombination process (r1, r2), the relaxation process (rel), and the nonradiative recombination process (n1, n2). The nonradiative lifetimes, τ_{n1} and τ_{n2}, were neglectable for the as-grown sample, and after annealing, the nonradiative lifetime, τ_{n1}, became effective.

recombination process (r1, r2), the relaxation process (rel), and the nonradiative recombination process (n1, n2). In an as-grown sample, the nonradiative lifetimes are negligible, which can be expected from the temperature-independent radiative lifetimes (see section 5-3-3). After annealing, the recombination lifetime at the ground level decreases due to the nonradiative channel, while the nonradiative process of the second level is still negligible. The drastic change in relative emission intensity demonstrates that the balance of radiative and nonradiative recombination and relaxation rates determines the shape of the emission spectrum. This contradicts the experience with quantum wells whose emission spectra generally narrow toward a lower energy regime as the emission intensity decreases. In quantum wells, intersubband carrier relaxation is much faster than the recombination process.

5-5. Summary

Theoretical and experimental studies on carrier dynamics in self-assembled quantum dots were explained. Electroluminescence and time-resolved photoluminescence data were analyzed to provide recombination and relaxation lifetimes as a function of temperature. The RIO model in the analysis explained the double-exponential decay of excited levels, and using the obtained lifetimes, electroluminescence and photoluminescence spectra were successfully simulated even after annealings. Carrier relaxation between discrete energy levels was experimentally found to be very slow with a lifetime above 100 ps in ALS dots (but, it may depend on dot structure). Also, carrier-carrier scattering rapidly sends carriers deep inside the dots, as seen in the initial stage of time-resolved photoluminescence. These two findings help to clear up the confusion in this research field.

References

[1] Y. Arakawa, and H. Sakaki, Appl. Phys. Lett. 40, 939 (1982).

[2] Y. Arakawa, K. Vahala, and A. Yariv, Apple. Phys. Lett. 45, 950 (1994).

[3] L. Brus, IEEE J. Quantum Electron. 22, 1909 (1986).

[4] D. S. Chemla, and B. A. D Miller, Opt. Lett. 11, 522 (1986).

[5] M. Asada, Y. Miyamoto, and Y. Suematsu, IEEE J. Quantum Electron. QE-22, 1915 (1986).

[6] U. Bockelmann and G. Bastard, Phys. Rev. B 42, 8947 (1990).

[7] H. Benisty, C. M. Sotomayor-Torres, and C. Weisbuch, Phys. Rev. B 44, 10945 (1991).

[8] H. Benisty, Phys. Rev. B 51, 13281 (1995).

[9] U. Bockelmann, Phys. Rev. B 48, 17637 (1993).

[10] U. Bockelmann and T. Egeler, Phys. Rev. B 46, 15574 (1992).

[11] Al. L. Efros, V. A. Khachenko, and M. Rosen, Solid State Commun. 93, 281 (1995).

[12] J-M. Gërard, *Confined Electrons and Photons: New Physics and Applications*, edited by Burstein E., and Weisbuch C. (Plenum, New York, 1995) p. 357.

[13] T. Inoshita and H. Sakaki, Phys. Rev. B 46, 7260 (1992).

[14] H. Nakayama, and Y. Arakawa, 7th Int. Conf. Superlattices, Microstructures, and Microdevices, Banff, Canada (1994).

[15] K. Mukai, H. Shoji, N. Ohtsuka and M. Sugawara, Appl. Phys. Lett. 68 (1996) 3013.

[16] M. Yamada, H. Ishiguro, and H. Nagato, Jpn. J. Appl. Phys. 19, 135 (1980).

[17] M. Asada, IEEE J. Quantum Electron. 25, 2019 (1989).

[18] K. Mukai, N. Ohtsuka, S. Hajime, and M. Sugawara, Phys. Rev. B 54 (1996) R5243.

[19] H. Yu, S. Lycett, C. Roberts, and R.Murray, Appl. Phys. Lett. 69, 4087 (1996).

[20] F. Adler, M. Geiger, A. Bauknecht, F. Scholz, H. Schweizer, M. H. Pilkuhn, B. Ohnesorge, and A. Forchel, J. Appl. Phys. 80, 4019 (1996).

[21] S. Raymond, S. Fafard, S. Charbonneau, R. Leon, D. Leonard, M. P. Petroff, and L. J. Merz, Phys. Rev. B 52, 17238 (1995).

[22] M. Vollmer, J. E. Mayer, W. W. Rühle, A. Kurtenbach, and K. Eberl, Phys. Rev. B 54, R17292 (1996).

[23] B. Ohnesorge, M. Albercht, J. Oshinowo, A. Forchel, and Y. Arakawa, Phys. Rev. B 54, 11532 (1996).

[24] U. Bockelmann, W. Heller, A. Filoramo, and Ph. Roussignol, Phys. Rev. B 55, 4456 (1997).

[25] K. Kamath, D. Klotzkin, and P. Bhattacharya, Proc. Conf. IEEE Lasers and Electro-Optics Society, 1997, p. 498.

[26] M. Grundmann, and D. Bimberg, Phys. Rev. B 55, 9740 (1997).

[27] H. Lipsanen, and M. Sopanen, Phys. Rev. B 51, 13868 (1995).

[28] S. Raymond, S. Fafard, J. P. Poole, A. Wojs, P. Hawrylak, S. Charbonneau, D. Leonard, R. Leon, M. P. Petroff, and L. J. Merz, Phys. Rev. B 54, 12548 (1996).

[29] M. Sugawara, Semicond. and Semimetals, vol. 60, chap. 1, 1999 (Academic Press Inc. NewYork).

[30] S. Grosse, H. H. J. Sandmann, V. G. Plessen, J. Feldmann, H. Lipsanen, M. Sopanen, J. Tulkki, and J. Ahopelto, Phys. Rev. B 55, 4473 (1997).

[31] K. Mukai and M. Sugawara, Jpn. J. of Appl. Phys. 37, 5451 (1998).

[32] G. Wang, S. Fafard, D. Leonard, E. J. Bowers, L. J. Merz, and M. P. Petroff, Appl. Phys. Lett. 64, 2815 (1994).

[33] K. Kamath, N. Chervela, K. K. Linder, T. Sosnowski, H-T. Jiang, T. Norris, J. Singh, and P. Battacharya, Appl. Phys. Lett. 71, 927 (1997).

[34] A. Kurtenbach, W. W. Rühle, and K. Eberl, Solid State Com. 96, 265 (1995).

[35] H. Shoji, K. Mukai, N. Ohtsuka, M. Sugawara, T. Uchida, and H. Ishikawa, IEEE Photo. Tech. Lett. 7, 1385 (1995).

[36] J. M. Sallese, F. J. Carlin, M. Gaihanou, and P. Grunberg, Appl. Phys. Lett. 67, 2633 (1995).

[37] P. C. Sercel, Phys. Rev. B 51, 14532 (1995).

[38] W. T. Tsang, Appl. Phys. Lett. 33, 245 (1978).

Chapter 6

Quantum Dot Lasers

6-1 Introduction

The evolution of semiconductor lasers has been with creating population inversion in constricted energy ranges. Low threshold current densities (< 50 A/cm^2 at room temperature) were obtained using compressively strained quantum well lasers [1], and the further improvements in threshold current densities and other decisive fundamental parameters will be achieved by the introduction of a lower-dimensional structure in the active region. Semiconductor quantum dots, where electrons, holes, and excitons are confined in the zero dimension, are believed to be the promising lower-dimensional structure. Because of an atom-like state density in quantum dots and the resulting increases in material and differential gain and limited thermal carrier distribution, quantum dot lasers are expected to attain remarkable reductions in threshold current, temperature-insensitive operation, narrow spectral linewidth, and large modulation bandwidth [2 - 5].

The distinct effects of low dimensionality on lasing properties have been the motivation for extensive experimental research on quantum dot lasers. Primary experimental attempts to study the lasing properties of carriers under three-dimensional confinement were done with strong magnetic fields applied to quantum well lasers [6]. These experiments indicated a reduction in the temperature dependence of threshold current, but did not prove a reduction in threshold current (on the contrary, an increase was practically observed). More advanced quantum dot lasers used dots that were created by combining lithography and regrowth on a processed substrate [7, 8], but were still troubled by extremely high threshold current densities (e.g., 7.6 kA/cm^2 at 77 K) due to nonuniform dot size, poor interface quality, and low surface density [9]. The development of a strain-induced self-assembling technique

was a breakthrough in the fabrication of quantum dots for lasers (see Chapter 3). The most well-known self-assembled dots are growth islands formed via the Stranski-Krastanov mode (SK dots) [10, 11]. These self-assembled microcrystals have a uniform size, high numerical density, and high emission efficiency, none of which has been realized using previous artificial techniques. Fabry-Perot injection lasers based on self-assembled dots have been demonstrated since 1994 [12 - 15]. However, the predicted distinct laser performances have not yet been achieved.

To actualize the advantages of dot lasers, there are many problem to be solved. One is the traits of dot structure themselves. Peak material gains depend on spectra broadening due to dot inhomogeneity and volume density of dots. The actual spectra broadening is in the order of several tens of meV. There are about 10^6 quantum dots in the active region in a laser with typical dimensions, with quantum dot densities of several 10^{10} cm^{-2}. Improving the imperfection in self-assembly and controlling dot nucleation will increase the peak material gain. Also, there might be a carrier injection problem. The velocity of carrier capturing and relaxation among sublevels affects laser performance (see Chapter 5). Thermal carrier excitation is allowed if sublevel separation is not large enough, in the case of which optical gain at the lasing level is reduced.

Before work on this thesis began, even room-temperature lasing of quantum dots was a dream to be challenged. However, benefited by recent progress in self-assembling technology, the performance of quantum dot lasers have drastically advanced close to that of quantum well lasers. For instance, by closely stacking self-assembled dot structures in the growth direction, the threshold current of dot lasers was reduced to 5.4 mA in 1998 [16]. Also, a threshold current density of 26 A/cm^2 [17], a small-signal modulation of 8.5 GHz [18], 1.3-μm lasing, which is at a suitable wavelength for fiber-optic communication systems [19 - 21], have been achieved.

In this chapter, the author describes an achievement with and improvements in quantum dot lasers using self-assembled microcrystals. Since quantum dot lasers that have been fabricated are very similar to quantum well lasers (the noticeable difference is that the optically active region consists of quantum dots), this chapter starts without any special discussion on laser structure. Metalorganic vapor phase epitaxy (MOVPE) and molecular beam epitaxy (MBE) are used to grow the self-assembled quantum dots. Improvements in threshold current, output power, and lasing wavelength has been attained by evolving a

special growth method for 1.3-μm-emission InGaAs/GaAs dots. The first 1.3-μm-emission dots (ALS dots) were grown by alternately supplying group-III and group-V source materials under a very low growth rate in a MOVPE chamber, as described in Chapters 2 and 3. The dot structure is quite different from that of SK dots (i.e., the dots were buried in an InGaAs quantum-well layer which has the same thickness as the dots). In the beginning of this chapter, the author describes lasers using ALS dots. Low sheet density is, however, the most fatal obstacle to achieving 1.3-μm lasing of the dots. The growth methods of 1.3-μm-emission dots were inherited by molecular beam epitaxy (MBE), where the growth process is monitored in-situ and therefore highly controlled. Drastic improvements in threshold current and output power was achieved with the quantum dots grown by applying the alternate source supply technique of ALS dots to growth in MBE. The author achieved the first 1.3-μm continuous wave (CW) lasing of quantum dots. High-density 1.3-μm-emission InGaAs/GaAs dots were successfully attained in MBE, regarding the essence of ALS-dot growth: a low growth rate and a InGaAs-layer covering. Lasing properties and their temperature dependence of these quantum-dot lasers are demonstrated, indicating key points for the improvement of quantum dot lasers.

6-2 Lasers with dots prepared by alternate supply method

In this section, the fabrication and performance of ALS dot lasers are described. This is one of the significant primary achievements of quantum dot lasers. Electroluminescence and diamagnetic shifts of lasing wavelength were measured to confirm that lasing occurred at a three-dimensionally confined sublevel in quantum dots. After an investigation of the device properties, the potential and drawback of ALS dot lasers get clearer.

6-2-1 Lasing at low temperature

An active region of semiconductor lasers was made up of ALS dots grown via an In-Ga-As supply sequence in a MOVPE chamber (see Chapter 3). A broad contact laser structure was fabricated [22]. Since the pulse jet epitaxy system was not equipped with gas supply lines sufficient to fabricate laser devices, the parts of the laser structure other than the quantum-dot active region were grown using other equipment. A n-GaAs buffer layer (0.5

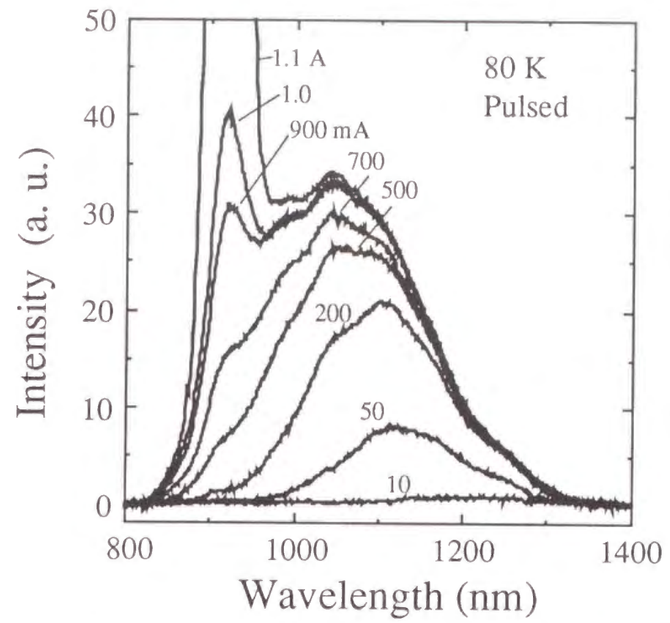

Figure 6-1 EL spectra of an ALS-dot laser for various injection currents.

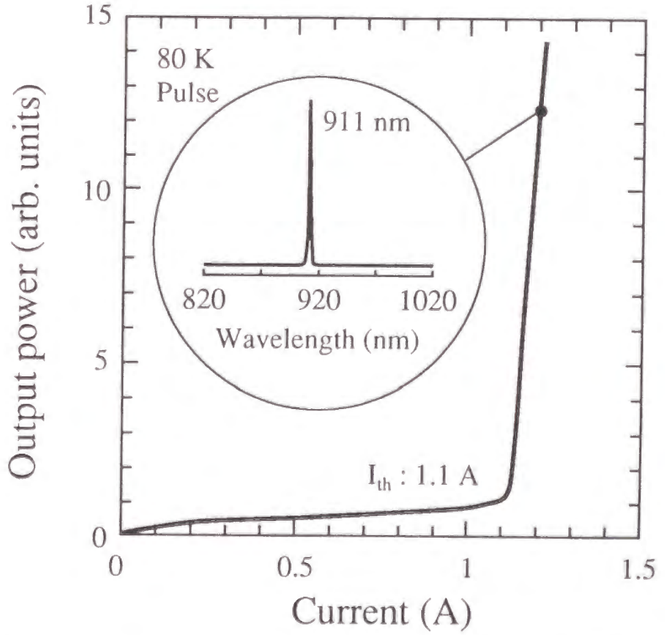

Figure 6-2 L-I characteristics of an ALS-dot laser. Lasing spectrum is shown in the inset.

μm) and a n-InGaP cladding layer (1.0 μm) were grown by a state-of-art MOVPE system. A p-AlGaAs cladding layer (1.0 μm) and a p-GaAs cap layer (0.5 μm) were grown by a solid source MBE system. The author supposes that this process severely damaged the crystal, and therefore, deteriorated lasing properties of this lasers. An active layer was one sheet of an ALS dot layer. The cavity length was 900 μm, and a high-reflective (HR) coating was applied to both facets. A 95% high reflectivity for a 1 μm region was realized by two pairs of (2050-Å SiO_2) / (840-Å Si) coating.

Figure 6-1 shows electroluminescence spectra at various injection currents. Measurements were done at 80 K by pulsed current injection (pulse width: 500 ns; repetition rate: 10 kHz). The peak wavelength of the dot ground level was 1.25 μm (see Chapter 4), and peak broadening in shorter wavelength regions was observed during a current increase owing to emission from excited sublevels. In other words, band filling with current injection was observed. Laser oscillation occurred at a threshold current of 1.1 A.

Light output versus injected current characteristics are shown in Fig. 6-2. The threshold current of 1.1 A corresponds to a threshold current density of 815 A/cm^2 since the width of the current injection area is 150 μm in the near field pattern. This current density is one-order smaller than that of lasers built using artificially fabricated dots [9]. As shown in the inset, the lasing wavelength was 911 nm. Considering that the compositional wavelength of the $In_{0.1}Ga_{0.9}As$ barrier layer at 80 K is shorter than 850 nm, the lasing level can be assigned to be a high-order sublevel of ALS dots.

Figure 6-3 shows the threshold current of ALS-dot lasers as a function of a temperature between 80 and 135 K. Observation of high-temperature lasing was limited by current source capacity. Characteristic temperature, T_0, defined by

$$I_{th} \propto \exp(T/T_0) \qquad (6.1)$$

was over 400 K for the measurements below 100 K. However, at higher temperatures, T_0 was degraded to 130 K, which is significantly smaller than the expected value for quantum dot lasers. The author supposes that the reason is related to radiative efficiency. As seen in Fig. 4-21, emission efficiency decreased in this temperature range. In addition, the laser structure was fabricated via air transfers between three kinds of growth equipment, degrading crystal quality. The decrease in radiative efficiency possibly requires an additional injection of carriers into the quantum dots, which results in a proportional increase in the threshold

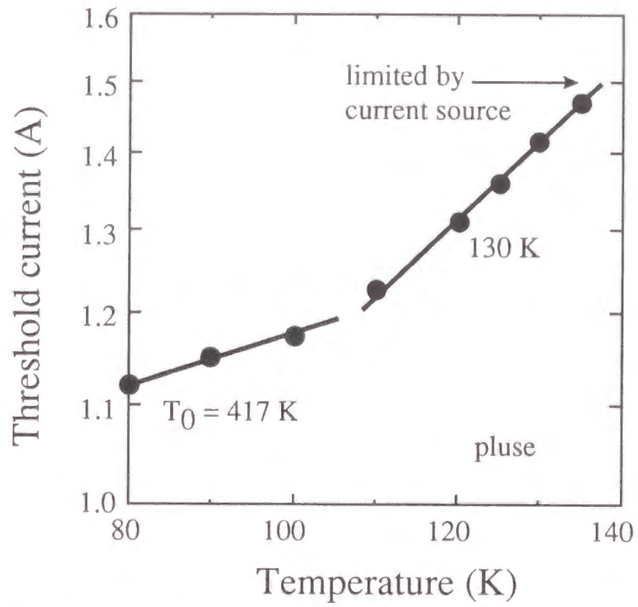

Figure 6-3 Threshold current of ALS-dot lasers as a function of temperature. Observation of lasing was limited by current source capacity. Over 400 K of characteristic temperature was obtained for the measurements below 100 K.

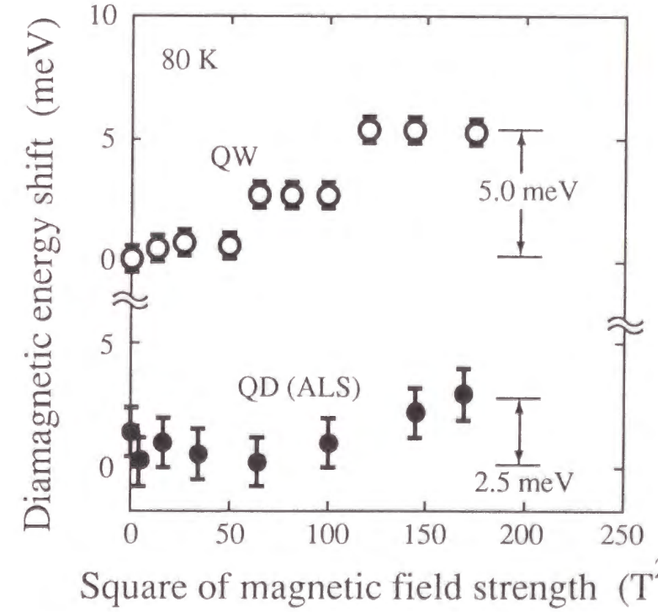

Figure 6-4 Diamagnetic energy shift of lasing wavelength for quantum-dot laser and quantum-well laser as a function of square of magnetic field strength. The amount of energy shifts in the quantum-dot laser is smaller than that of the quantum well laser.

current.

6-2-2 Diamagnetic measurement of laser emission

To confirm that the obtained laser oscillation is really from a high-order sublevel of quantum dots, diamagnetic shifts of the lasing peak at 80 K were compared with those for a quantum well laser (see Chapter 4). A 0.98-μm single-quantum-well laser was used since it operates in the same wavelength region at 80 K as a quantum dot laser. A magnetic field was applied perpendicular to the lasers up to 13 Tesla using a superconductor magnet. Light output under pulsed current injection was collected through a bundle fiber and introduced into a monochrometer. Figure 6-4 shows the results. The emission energy of the quantum dot laser is almost insensitive to the magnetic field in the weak magnetic field region, and the total amount of energy shifts was less than 2.5 meV. On the other hand, the reference quantum well laser oscillated at several modes under a strong magnetic field, and the envelope of emission shifted to a high energy region. The amount of energy shifts was about 5 meV, which was obviously larger than that of the quantum dot laser. Even though the magnetic-field dependence of higher-order sublevel energy is not theoretically supported, the experimental results prove that lasing did not occur at the two-dimensional layer but at the quantum dots, considering that the indium composition of the two-dimensional layer surrounding ALS dots was close to that of the reference quantum well laser.

Lasing at the three-dimensionally confined sublevel in ALS quantum dots has been achieved. The observed electroluminescence spectra indicate that the ground level was filled with an extremely low current injection level (below 50 mA). This suggests that ultra-low threshold current density operation can be realized in quantum dot lasers. One of the reasons why laser oscillation occurred at a high-order sublevel of ALS dots may be a small ground-level optical gain that was caused by low dot density. Sheet density is quite low, and stacking is not capable for ALS dots, so we cannot raise even the volume density (see Chapter 3). The other reason is low crystal quality due to air transfers between the three kinds of growth equipment used during the fabrication of the laser structure. Increasing dot sheet density and multiplication of the dot layers in the growth direction raises optical gain, leading to lasing at a lower sublevel. Also, it should be noted that the phonon bottleneck effect was experimentally observed in ALS dots (see Chapter 5). After these results, a new type of self-

assembled dots, described in the following, were developed based on the growth technique for ALS dots.

6-3 Lasers with columnar closely stacked dots

In this section, achievements in quantum dot lasers with a mili-ampere-order threshold current and output power of over 100 mW are described. A new type of dots were grown via alternate supply of source materials by MBE, resulting in directly stacked SK-dot structures having a columnar shape (columnar dots) [16, 23, 24]. Spectral broadening of photoluminescence is reduced by the alternate supply growth in MBE without detriment to emission efficiency. The surface density is larger than that of ALS dots. Improvements in uniformity, emission efficiency and density actually caused better performance of quantum dot lasers.

6-3-1 Growth of dots by molecular beam epitaxy

Alternate supplies of InAs and GaAs on a (001)GaAs substrate in solid source MBE succeeded in producing self-assembled dots with a high uniformity and high emission efficiency [25]. The dots are a kind of closely stacked InAs dots with a GaAs intermediate layer. The growth conditions are illustrated in Fig. 6-5 and compared with those of ordinary closely stacked dots. In the novel growth method, at first, InAs SK islands are prepared by a supply of 1.8 monolayer's (ML's) as nuclei for the following three-dimensional growth. Then, InAs of 0.71 ML and GaAs of 3 MLs are supplied repeatedly. Since GaAs of 3 MLs cannot fully cover the InAs island layer, InAs islands formed during the supply of 0.71 ML come into contact each other. In a growth of ordinary closely stacked dots (see Fig. 6-5(b)), InAs islands are completely covered by intermediate GaAs layers, and the islands do not make contact in the growth direction but are coupled electrically through thin potential barriers of intermediate layers [26 - 28]. Figure 6-6 is a cross-sectional TEM image of the dots. Because of the columnar shape of the dots, the author calls this type of dot *columnar dot*. Two columnar dots can be seen in the figure. Both the diameter and height of the dots are about 15 nm. The figure also clearly indicates multiple wetting layers produced during each InAs supply, suggesting that columnar dots are a type of closely stacked SK dots. However, clear

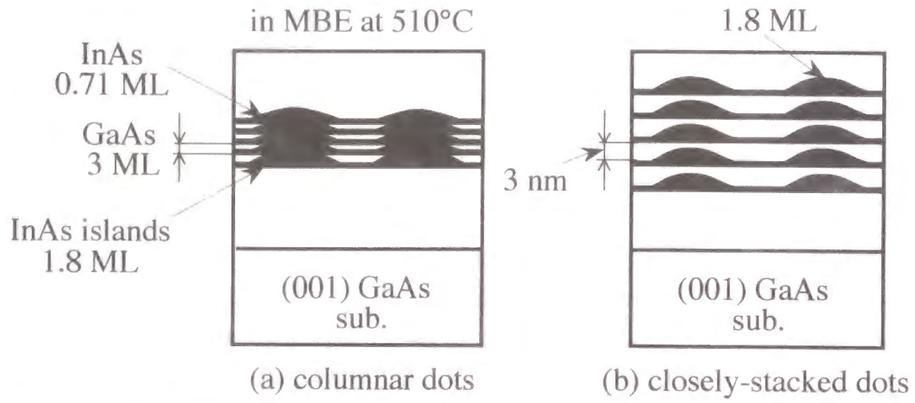

Figure 6-5 Schematics of structure in closs section of (a) columnar dots and (b) closely-stacked dots. The columnar dots are grown by MBE. In the new growth methods (a), the 8 cycles of InAs-GaAs supply were typically performed after a single 1.8-ML InAs supply. The growth temperature was 510°C. In the ordinary closely-stacked dots (b), dot does not make contact each other in growth direction but is coupled electrically through thin potential barriers of the intermediate layers.

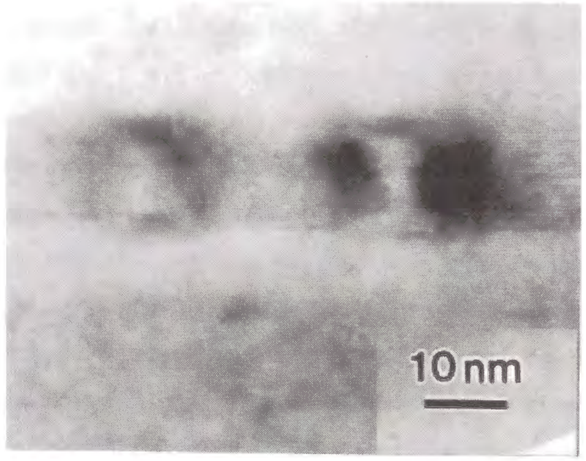

Figure 6-6 Cross-sectional TEM image of two columnar dots. Both the diameter and height of the dots were about 15 nm. InAs islands formed during 0.71 ML's InAs supply came into contact each other, and the multiple wetting layers were produced during each InAs supply.

multiple structures cannot be seen in the dots themselves, suggesting that columnar dots are stack of small islands in physical contacted with one another [29, 30]. The amount of InAs during alternate supply is critical in the new growth methods, as shown by the AFM images in Fig. 6-7.

Figure 6-8 compares the photoluminescence spectra of columnar dots, SK InAs dots, and previously reported closely stacked SK dots. The emission wavelength of the ground level of columnar dots was 1.17 μm and that of the second level was 1.1 μm. An emission peak related to multiple wetting layers was observed at 1.01 μm, which is longer than that of SK dots (0.92 μm). The author supposes that the longer emission wavelength of the wetting layers is because multiple wetting layers were coupled electrically in a columnar-dot layer.

Two points deserve special attention in Fig. 6-8. First, the emission intensity of columnar dots is equal to that of SK dots and is quite improved compared to that of previously reported closely stacked dots, which hardly emitted at room temperature. Photoluminescence intensity in the closely stacked dots at room temperature is less than one thousandth of the intensity at 77 K. The emission efficiency of columnar dots is improved by optimizing the source amount of supply. Second, columnar dots have a narrower spectrum width than SK dots. Because of the narrow spectra width, the existence of excited levels becomes observable in columnar dots. The peak width of the ground level is almost half that of SK dots: the half width at half maximum (HWHM) in the spectrum was 20 meV for the ground level and significantly smaller than 45 meV of the ordinary single SK dots (but larger than 15 meV of ALS dots). The narrower spectrum suggests that columnar dots have a better uniformity than SK dots. The author supposes that the thick dot structure of columnar dots makes the sublevel energy unresponsive to height fluctuations, compared with the case of SK dots. In addition, due to the stacking, the emission wavelength of columnar dots is longer than that of normal SK dots.

The author insists that columnar dots are very similar to ALS dots in the growth sequence and structure. In the growth sequence, source materials are alternately supplied in the growth of both types of dots. As for the structure, both dots are surrounded by a quantum well layer which has the same thickness as dots (in columnar dots, nearly multiplied wetting layers are electrically coupled). The distinct difference is just the supply amount (i.e., ALS dots formed by an alternate supply of 1-ML InAs and 1-ML GaAs while columnar dots formed by an alternate supply of 0.7-ML InAs and 3-ML GaAs). The role of alternate supply

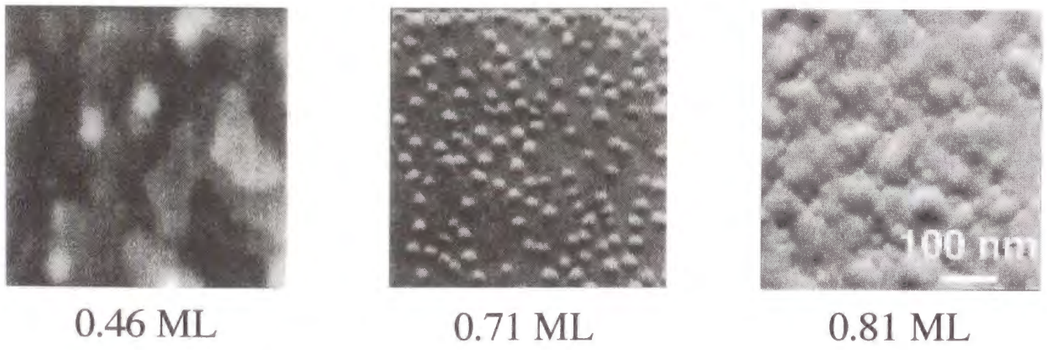

Figure 6-7 Plan-view AFM images of columnar dots at various supply amount of InAs during alternate supply: (a) 0.46 monolayer (ML), (b) 0.71 ML, and (c) 0.81 ML. We can see that the amount of InAs is critical to grow clear dot structure.

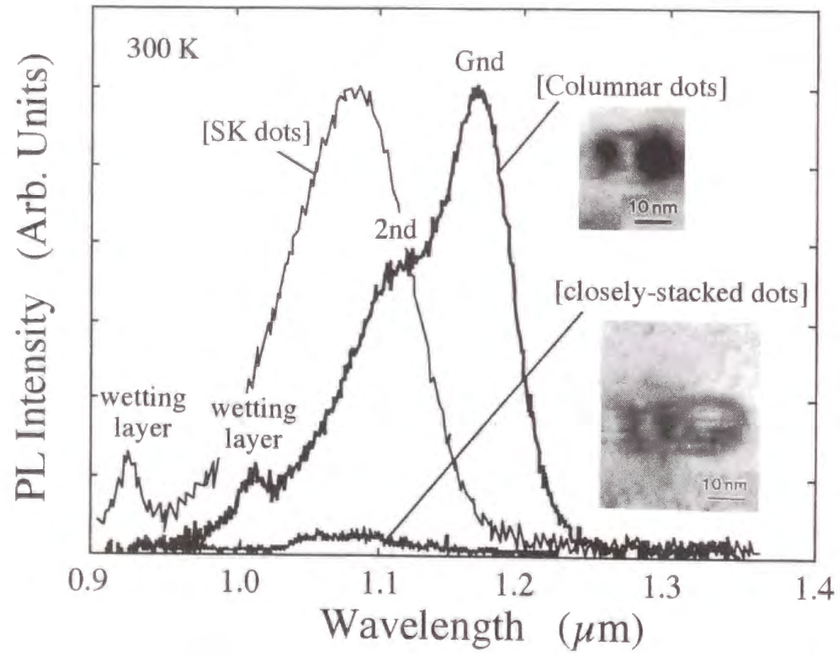

Figure 6-8 Photoluminescence spectra of the columnar dots, SK InAs dots, and closely-stacked dots grown by stacking 1.8-ML InAs dots with 3-nm GaAs intermediate layers. Improved properties of the columnar dots appear in this figure. First, the emission intensity of the columnar dots is higher than that of the closely-stacked dots. Second, the spectra width of the columnar dots is narrow. In addition, we can see that the emission wavelength of the wetting layer is quite long, which suggests the electrical coupling of wetting layer through thin intermediate layers.

in both types of quantum dots may be common (i.e., inserting gallium into the structures reduces the total strain energy and leads to higher and more uniform dots, but the growth process is not exactly the same). Multiple wetting layers are clearly observed in the columnar dot structure but not observed in the ALS dot structure. Dot surface density can be raised up to 10^{11} cm^{-1} for columnar dots, but 2 X 10^{10} cm^{-1} to the utmost for ALS dots.

6-3-2 Room temperature lasing with mili-ampere-order threshold current

Double heterostructure lasers with two columnar-dot layers (N = 2) were fabricated. A schematic of the laser structure is shown in Fig. 6-9. The structures were grown by MBE on a (001)n-GaAs substrate followed by a 1.4-μm n-$Al_{0.4}Ga_{0.6}As$ cladding layer, a quantum-dot active layer, a 1.4-μm p-$Al_{0.4}Ga_{0.6}As$ cladding layer, and a 0.4-μm p-GaAs contact layer. One or two sheets of the columnar-dot layers were used as the active layer and sandwiched between GaAs separate confinement heterostructure (SCH) layers. Two sheets of the columnar-dot layer were separated by a 30-nm GaAs layer. 3-μm-wide ridge structures were formed by chemical wet etching.

Room-temperature CW operation was achieved for a laser with L (cavity length) = 900 μm and double cleaved facets [23]. Figure 6-10 shows the light output versus current characteristic. The threshold current was 31 mA, which is more than one order of magnitude smaller than that (520 mA) of SK dot lasers having a common laser structure [14]. The lasing spectrum is shown as the inset. After the lasing wavelength is compared with the photoluminescence wavelength (Fig. 6-8), the lasing level is assigned to the second level. A high output power of 42 mW was obtained at an injected current of 150 mA. The external quantum efficiency, η_d, was 36%, which did not decrease much when the temperature was increased (η_d = 30% at 70°C). Let me estimate the internal loss, α, of the laser structure. The differential internal efficiency (η_i) has been reported as being 70% for an $In_{0.5}Ga_{0.5}As$ quantum dot laser and 81% for an $In_{0.3}Ga_{0.7}As$ quantum dot laser [13]. The external quantum efficiency is described by the differential internal efficiency and the internal loss as

$$\frac{1}{\eta_d} = \frac{1}{\eta_i}\left[\frac{\alpha_i + \frac{1}{2L}\ln\frac{1}{R_f R_b}}{\frac{1}{2L}\ln\frac{1}{R_f}}\right], \qquad (6.2)$$

where α_i is the internal loss, η_i is the internal quantum efficiency, and R_f and R_b are the

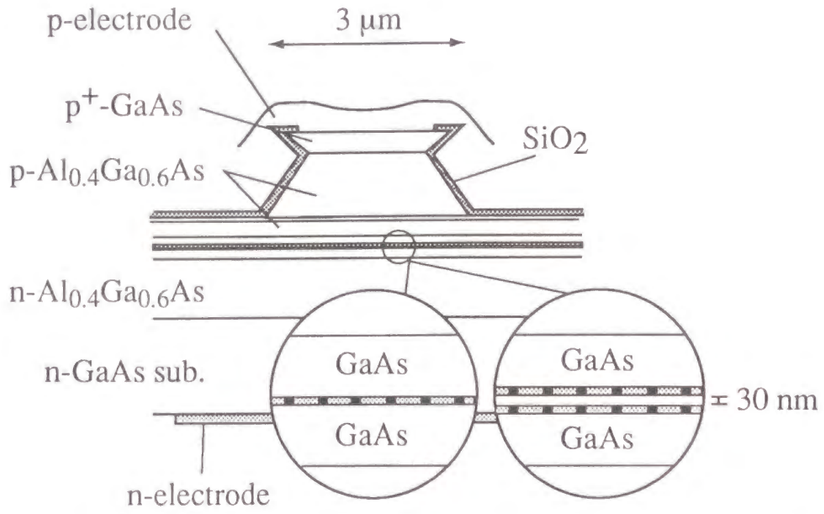

Figure 6-9 Schematic cross section of columnar-dot laser. Two sheets of the columnar-dot layer were separated by a 30-nm GaAs layer. The 3-μm-wide and 1.2-μm-high ridge structures are formed by chemical etching. The cavity length was 300 and 900 μm.

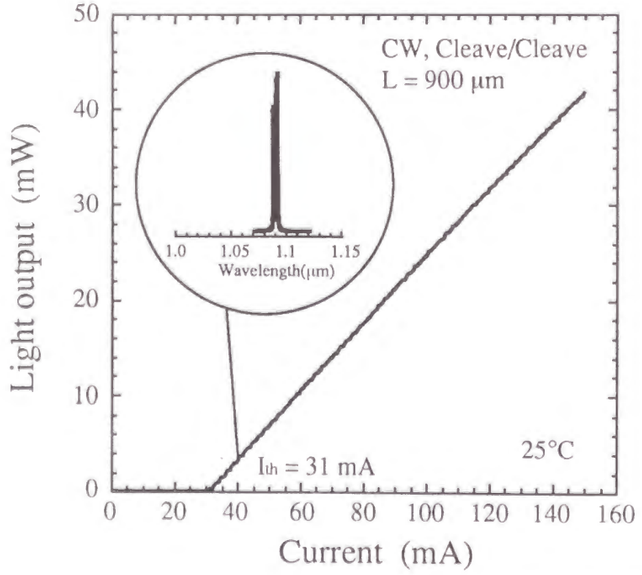

Figure 6-10 L-I characteristics of a columnar-dot laser at 25°C. Both facets were as-cleaved.

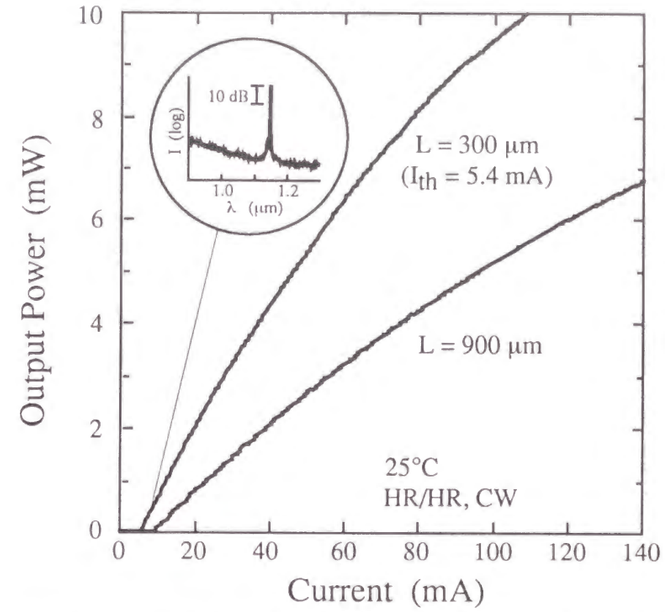

Figure 6-11 L-I characteristics of columnar-dot lasers with L = 300 and 900 μm and HR coating on both facets.

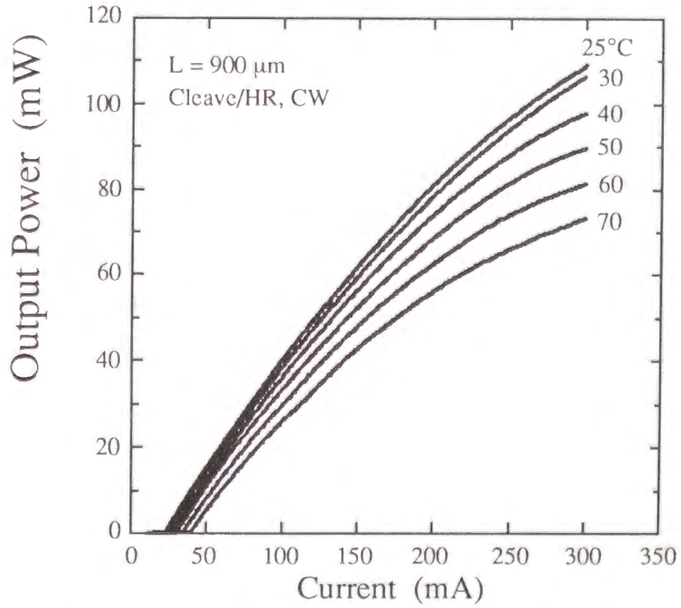

Figure 6-12 L-I characteristics of a columnar-dot laser with L = 900 μm and HR coating on one facet at temperature between 25 and 70°C.

reflectivities of the front and rear facets, respectively. Assuming $R_f = R_b = 0.3$ for the present structure, the internal loss at 25°C is calculated to be about 3.5 cm^{-1} with $\eta_i = 90\%$ and about 5.5 cm^{-1} at $\eta_i = 100\%$, indicating that a very low internal loss or a high differential internal efficiency can be expected in the columnar-dot laser.

A further lowering of threshold current and higher output power were achieved by columnar dot lasers with 95%-HR-coated facets. For a laser with L = 300 μm and HR coating on both facets, lasing oscillation occurred at a threshold current of 5.4 mA at 25°C [16] (Fig. 6-11). The low threshold current were a record for edge-emitting quantum-dot lasers at the time in 1998. The lasing wavelength of the devices was 1.15 μm. Since the ground-level peak was 1.17 μm in photoluminescence spectra, the author infers that the lasing occurred mainly at the ground level and that some gain at the second level assisted the lasing. For a laser with L = 900 μm and HR coating on one side of the facets, an output power of 110 mW was achieved (Fig. 6-12). Even at 70°C, an output power of 75 mW was obtained [24].

The author compares lasing characteristics of the columnar dot lasers having various cavity conditions. Figure 6-13 shows the L-I curves of the lasers. Under the Cleave/HR facet condition, shortening cavity length did not always reduce threshold current due to the lasing level variation. The usage of two sheets of dot layer (N = 2) had advantages in lasing level and the resulting low threshold current. From these results, the relationship between threshold gain per dot layer and lasing wavelength is summarized (Fig. 6-14). Here, the threshold gains are estimated from mirror loss and by assuming a constant internal loss of 6 cm^{-1}.This figure proves that the wavelength jumps from the second level to the ground level with lowering the threshold gain per one dot layer by the use of long cavity structure and multiple dot layers. It was apparent that the maximum gain at the ground level was higher for the columnar dot lasers than for the SK dot lasers. Figure 6-15 shows the relationship between modal gain and threshold current density. Both values are normalized for one dot layer. Differences in differential gain were found for the ground level and the second level. Since degeneracy at the second level is expected to be larger than that at the ground level, the large degeneracy leads to large differential gains. The intersection of the two straight lines agrees with the threshold gain for the wavelength jump from the second level to the ground level shown in Fig. 6-14.

Several reasons for high gains in columnar dot lasers can be considered. First, high

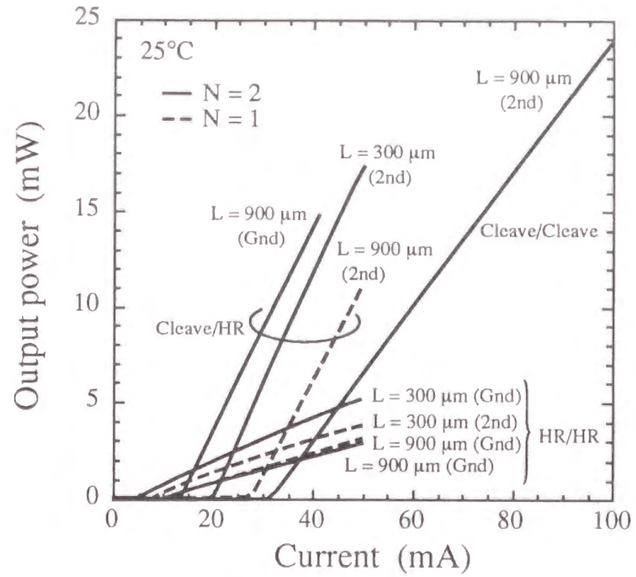

Figure 6-13 L-I curves of columnar-dot lasers having various cavity conditions. CL and HR indicate as-cleaved and HR-coated facet, respectively. Lasing level is indicated in parentheses.

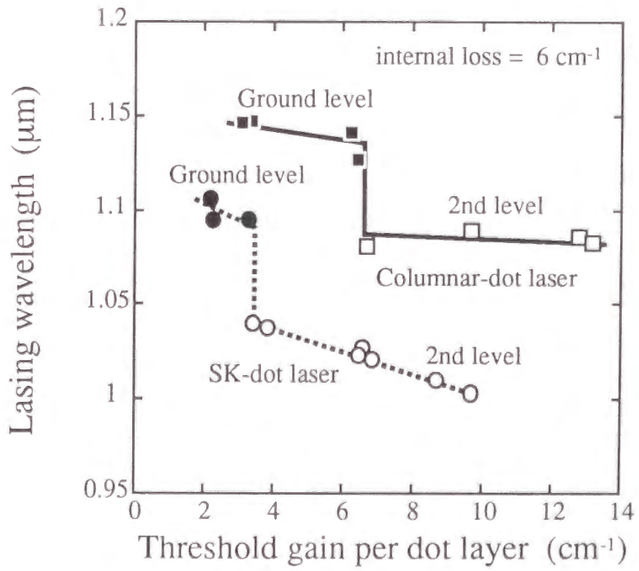

Figure 6-14 Relationship between threshold gain per dot layer and lasing wavelength. The threshold gains are estimated from mirror loss and assuming a constant internal loss of 6 cm^{-1}.

uniform energy levels and high radiative efficiency in columnar dots are expected to be decisive factors. In addition, good optical coupling is expected in the structure. Due to the multiple wetting layer, optical confinement is possibly high around columnar dots. Large height may also contribute to optical coupling. A large overlap of electron and hole wave function expected in thick dot structures possibly increases the transition probability.

Let me point out the possibility that multiple wetting layers work as a reservoir of carriers and raise the rate of carrier injection into dots (closely stacked wetting layers are electrically coupled). Carriers are possibly more easily captured by deep and wide quantum well than by a single (and therefore shallow) wetting layer of SK dots. The deeper the wetting layers, the more strongly the thermal carrier diffusion from the wetting layers to GaAs layers is restricted. Any resulting good carrier capture efficiency would contribute to the threshold current and output power.

6-3-3 Temperature characteristics

Figure 6-16 shows the threshold current of columnar dot lasers as a function of temperature between 110 and 300 K. Data for SK dot lasers are superimposed as a reference. An excellent T_0 (about 500 K) was obtained at low temperatures for both dot lasers, as in the case of ALS dot lasers (Fig. 6-3). However, T_0 was also reduced at higher temperatures. For columnar dot lasers, a small T_0 of 69 K was obtained between 180 K and 240 K, and near room temperature, T_0 was 86 K, which is about twice that of SK dot lasers.

An observed T_0 at over 180 K is still significantly smaller than the expected value for quantum dot lasers. The author assumes that there can be two factors dominating the temperature characteristics. The first one is related to radiative efficiency, as in the case of ALS dot lasers. A decrease in radiative efficiency requires additional carrier injection into the dots, resulting in a proportional increase in the threshold current. The second factor is thermal carrier diffusion to the upper sublevel. The energy separation between the ground level and the second level is 45 meV for columnar dots. As shown in Fig. 6-8, carrier distribution to the second level cannot be neglected at room temperature. The author supposes that, in order to improve the temperature characteristics of threshold current, energy separation between the sublevels of quantum dots should be optimized regarding rapid carrier injection (the phonon bottleneck problem) and reduction of thermal diffusion of carriers, as well as improvement of

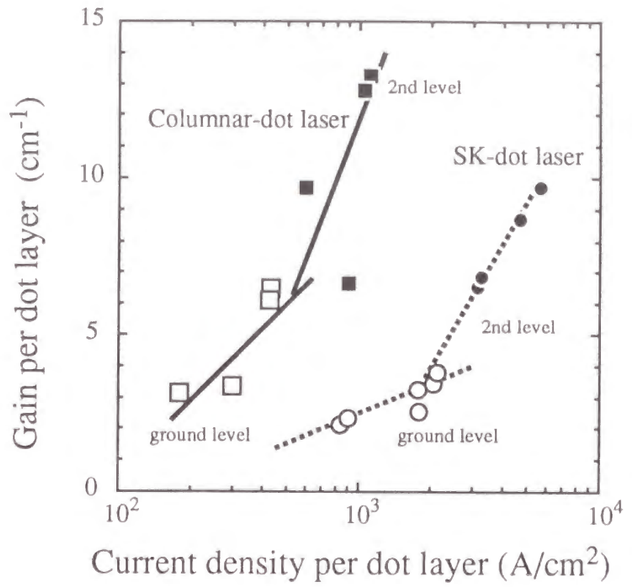

Figure 6-15 Relationship between the modal gain and the current density. Both values are normalized for one dot layer. Difference in differential gain is found for the ground level and the second level. The different differential gains can be attributed to the difference in the degeneracy at the two level.

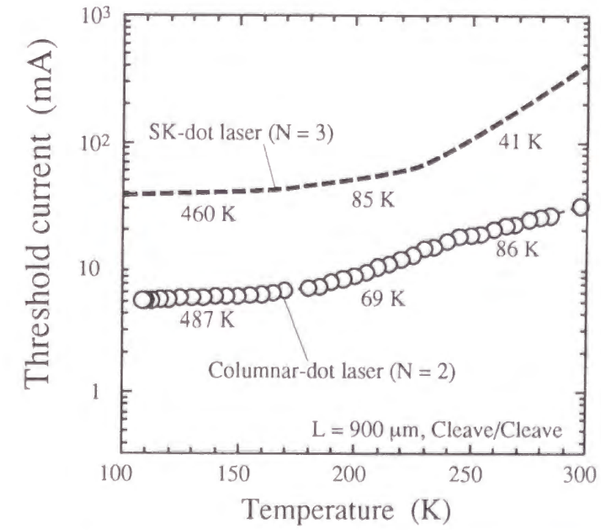

Figure 6-16 Threshold current of a columnar-dot lasers as a function of temperature. Threshold current of SK-dot lasers is superimposed as a reference.

emission efficiency.

The reason why T_0 was smallest between 180 K and 240 K for columnar dot lasers is that the lasing level shifted from the second level to the ground level and threshold current decreased in the temperature region. The point where lasing level began to move was 240 K for the columnar dot lasers, which is lower than 280 K for SK dot lasers. This is because the total ground-level gain was smaller for the columnar dot lasers due to a smaller number of dot layers (N).

Lasing-level variations are indicated in Fig. 6-17, which compares the electroluminescence spectra at 110 and 298 K at various injected currents up to lasing. Facets were as-cleaved and cavity length was 300 μm. Clear differences can be observed here. At 298 K, the threshold current is large, and the electroluminescence spectra below the threshold exhibit an asymmetric shape. The second sublevel emission was raised as the injection current was increased, resulting in asymmetric spectra. The large threshold carrier density was due to the carrier distribution in multiple levels and the thermally activated nonradiative recombination. Low threshold current at lower temperatures leads to narrower broadening of the electroluminescence spectra because of negligible emission from higher-order sublevels. This is attributed to the suppression of thermal excitation of carriers.

Lasing occurred at many wavelengths at 110 K. This is not the multi-mode oscillation observed in ordinary Fabry-Perot lasers. Various quantum dots with different sizes and compositions were simultaneously lasing, since the gains in the various dots can reach the threshold due to decreased nonradiative carrier recombination at 110 K. The wavelength span became smaller as the temperature was increased. This result gives an insight that each quantum dot is spatially separated and optically coupled. Also, it suggests the possibility that lasing operation at lower threshold currents will be enabled if the uniformity of quantum dots is greatly improved, that is, when lasing occurs in narrower wavelength ranges.

Lasing-level jumps to the higher level as temperature is raised. Figure 6-18 shows an example, which is light output versus injected current characteristics at 25 - 70°C for the columnar dot lasers of L = 300 μm and Cleave/HR facets. The inset shows lasing spectra at 25 and 70°C at the injected current of 70 mA, suggesting that the lasing-level order was the second at 25°C and higher (probably, the third) at 70°C (see Fig. 6-8). With a lasing-level shift at between 50 and 60°C, slope efficiency changed and threshold current discontinuously increased.

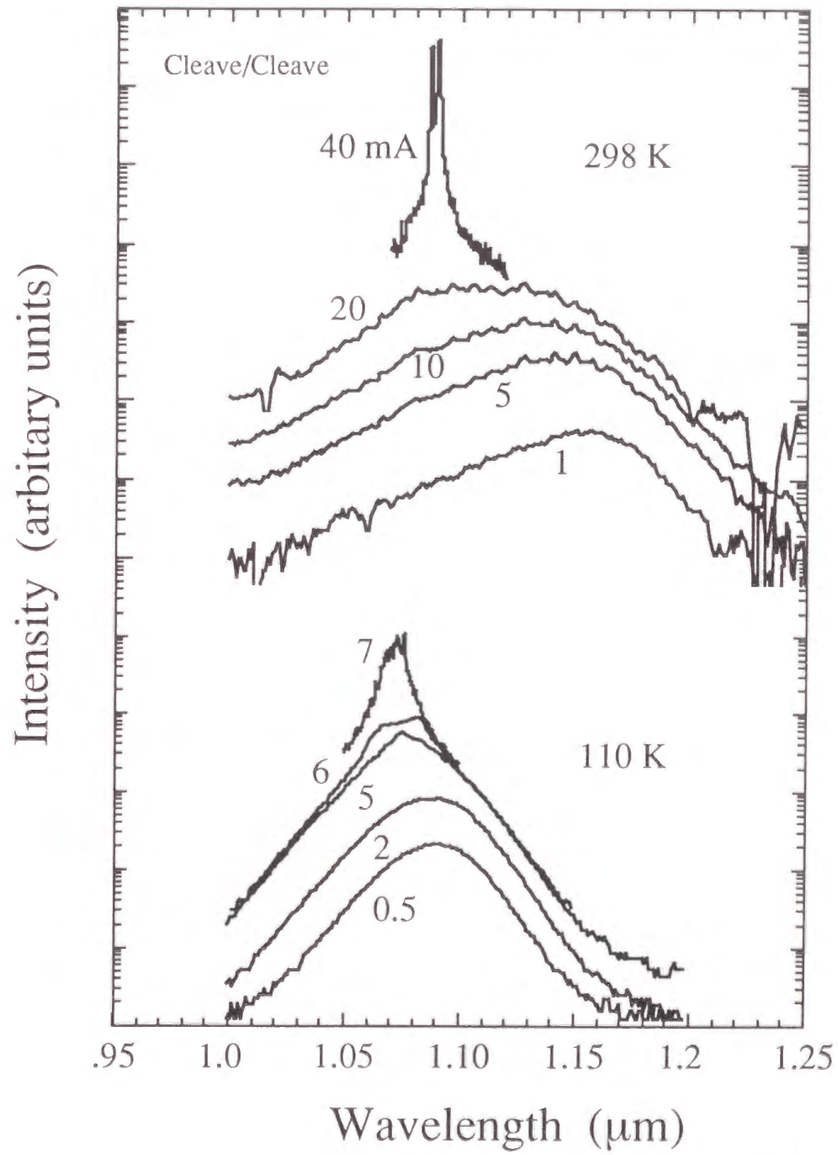

Figure 6-17 Lasing spectra and EL spectra of a columnar-dot laser at 110 K and 298 K.

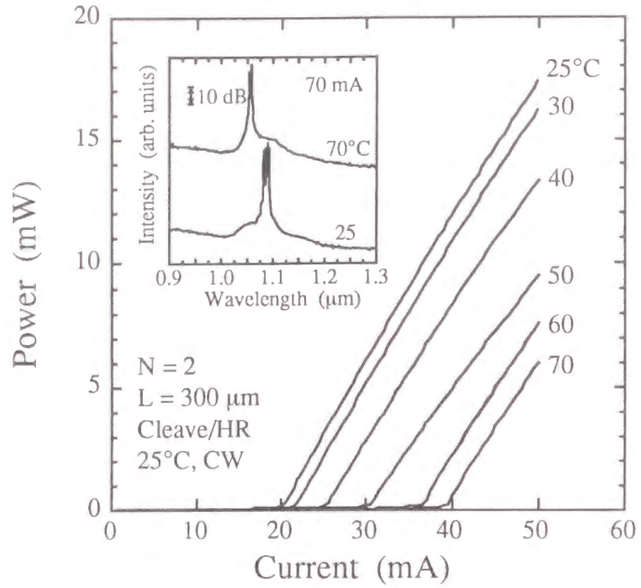

Figure 6-18 Light output versus injected current characteristics of the columnar-dot lasers at between 25 and 70 °C. Lasing level shifted at between 40 and 50 °C.

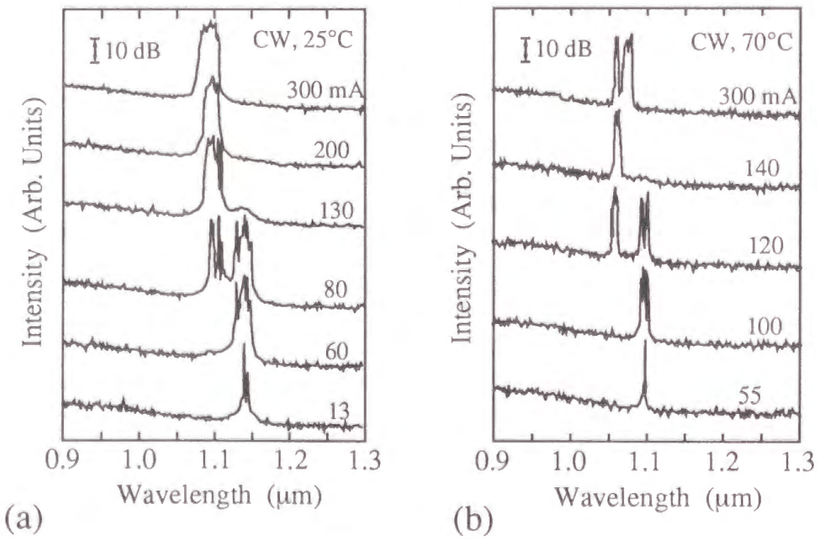

Figure 6-19 Lasing spectra at various injected current: (a) HR/HR, N = 1, L = 900 μm and (b) CL/HR, N = 1, L = 900 μm. For (a), the lasing level jumped from the ground level to the second level. For (b), the lasing level jumped from the second level to the higher (third?) level.

The author found that a distinct jumping of lasing level also occurs during an injected current increase. Figure 6-19 provides examples. In Fig. 6-19(a), the lasing level jumped from the ground level to the second level at the injected current of 80 mA. External quantum efficiency was recovered at that point. Also, in Fig. 6-19(b), the lasing level jumped from the second level to the higher level at 120 mA. Such distinct jumping has not been observed in SK dot lasers, where lasing spectra were continuously broadened even when higher levels began to lase during an increase of injected current. Higher uniformity of columnar dots enabled the observation of the distinct jumping. Figure 6-20 shows the relationship between the current density per dot layer, at which the lasing level jumped from the second level to the third level, and threshold gain for the second-level lasing per dot layer. The level jumping occurred with lower current density at 70°C rather than 25°C, clearly indicating that the jumping is dominated by thermal carrier diffusion.

From the point of view of application, lasing-level jumping during current injection is a serious drawback. Since the phenomenon depends on carrier distribution, enlarging level separation is effective in restricting the jumping. Also, it should be noted that gain saturation might be one of the root factors for the jumping. For exhaustive solution of the problem, inhomogeneous broadening of the state density of dot ensembles must be reduced. In addition, improvements in dot density, carrier capture rate by dots, carrier relaxation rate among sublevels, oscillator strength of electron-hole pair, optical confinement factor at the active region are effective in suppressing the level jumping and to make the dot lasers applicable to practical application.

High sheet density and multiplication of dot layers can be realized for columnar dots as well as SK dots since SK dots are used as nuclei of their formation, and actually provided advantages over ALS dots in the lasing properties. However, 1.3-μm emission, which is suitable for present fiber-optic communication systems, was not attained by the growth method. In order to achieve 1.3-μm lasing with good lasing performance, a new type of 1.3-μm-emission dots was developed by MBE, referring to the ALS-dot growth process again, as shown in the following section.

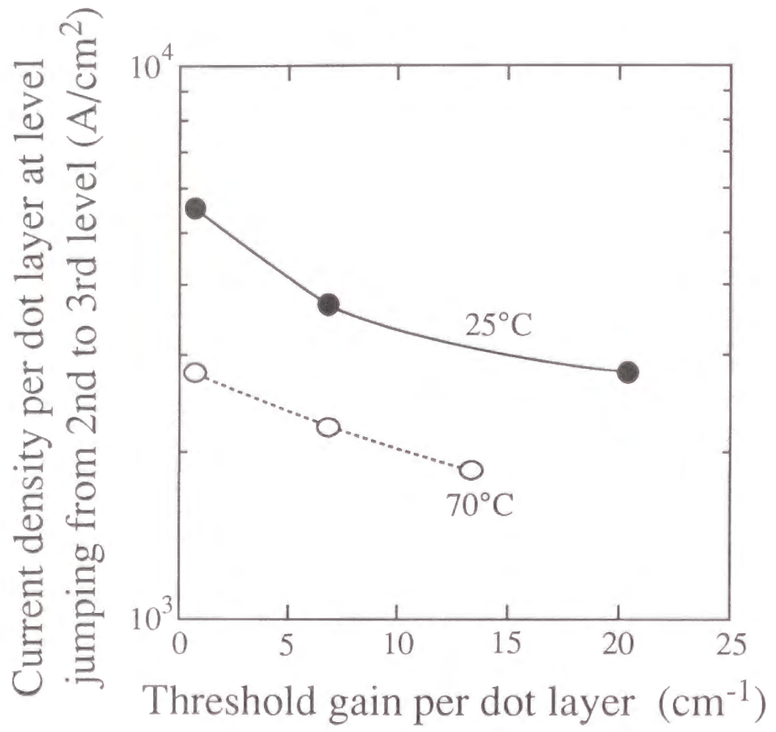

Figure 6-20 The relationship between the current density per one dot layer where the lasing level jumped from the second level to the third level, and threshold gain for the second-level lasing per dot layer. It is shown that the jumping occurred with lower current density at 70 °C than 25 °C.

6-4 1.3-μm lasing at room temperature

1.3-μm-emission self-assembled dots (ALS dots) were first formed in an early stage of research into self-assembled quantum dots, in 1994 by the author [31] (see Chapter 3). The growth method of alternate supply under quite low growth rates and the structure involved within quantum well have been taken over by MBE growth of dots [32 - 34], but lasing at 1.3 μm had not been attained, due to the low dot density, until 1998 [19]. The lasers, however, required a pulsed injection current to operate at room temperature since the low dot density was compensated by diode design: enlarging the optical confinement factor with high-refractive-index $Al_{0.7}Ga_{0.3}As$ cladding layers and reducing optical loss with a low doping concentration. In this section, the achievement of the first 1.3-μm CW lasing at room temperature of self-assembled InGaAs/GaAs quantum dots is explained. High-density 1.3-μm-emission dots were successfully formed by applying the growth method of ALS dots to MBE growth. The achievement was a milestone for creating quantum dot lasers applicable to fiber-optic communication systems. Lasing properties and temperature characteristics of the lasers are investigated, and the keys to further evolution of quantum-dot lasers are discussed.

6-4-1 Low-rate growth and InGaAs-layer overgrowth

As presented in Chapter 2, ALS dots emitting at 1.3 μm are grown with quite a low growth rate and surrounded by an InGaAs quantum well layer. To realize a similar structure by MBE and resulting long-wavelength emissions, SK dots have been grown using a low growth rate [33] and InGaAs-layer overgrowth [34]. However, low volume density did reappear in the MBE growth. Growth rate dependence of dot characteristics is shown in Fig. 6-21. By reducing the growth rate, sheet density decreases, and the dot diameter increases with an emission wavelength shift to 1.3 μm. The sheet density of 1.3-μm-emission dots was under 10^{10} cm^{-1}. Also, when stacking the 1.3-μm-emission dots with a-few-tens-nm GaAs spacer layers, the upper dot layers contained an extremely small number of dots. An InGaAs overgrowth on SK dots also reduces emission energy, but emission efficiency was simultaneously degraded (Figs. 6-22 and 6-23). Thus, each technique has an individual problem.

The author and co-workers noticed that the problem is moderate with a medium growth rate and a medium thickness of overgrowth layer, and hit the combination the growth

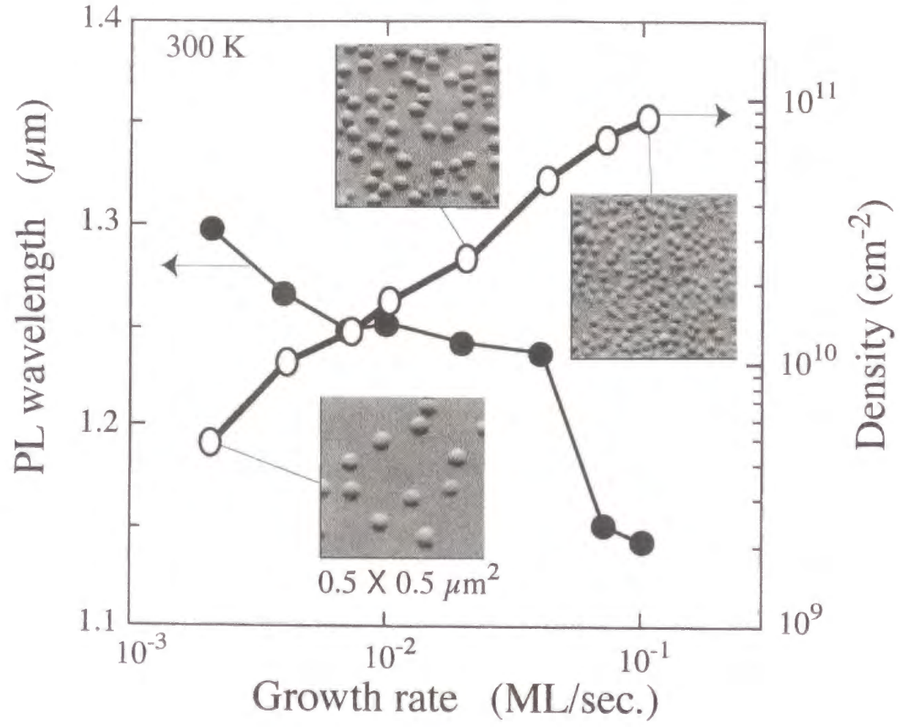

Figure 6-21 Photoluminescence wavelength and dot density as a function of gowth rate. AFM images are indicated as insets.

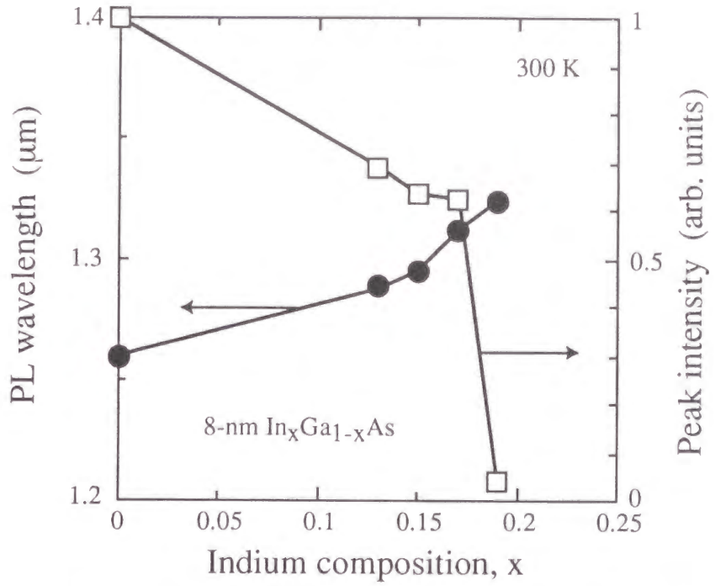

Figure 6-22 Photoluminescence wavelength and intensity as a function of indium composition of InGaAs overgrowth layer.

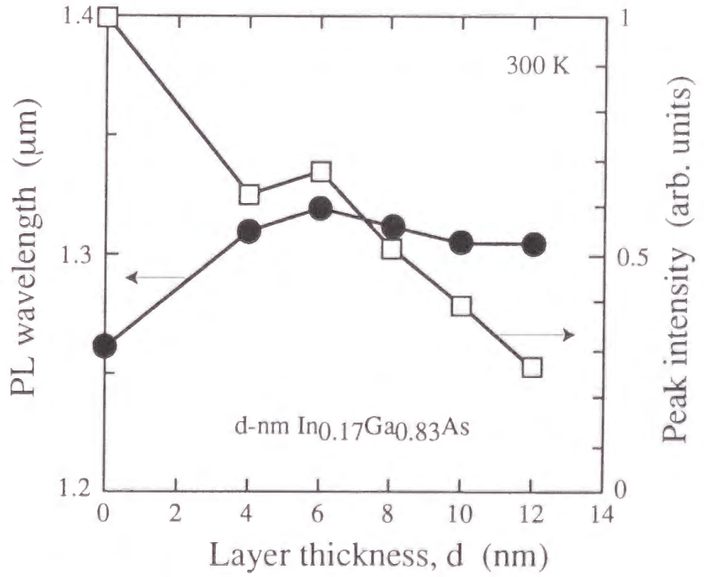

Figure 6-23 Photoluminescence wavelength and intensity as a function of thickness of InGaAs overgrowth layer.

methods, with which both dot density and emission efficiency are rather high. The new growth method is as follows. First, dots emitting in the 1.2-μm region are grown with a low growth rate. Compared with the 1.3-μm region, the dot sheet density is rather high and decreases in dot density due to stacking are restricted to some extent. Then, the dots are covered with an InGaAs layer to make the emission wavelength 1.3 μm. Consequently, high-density 1.3-μm-emission dots were successfully formed. After optimization of the growth condition [20], the growth rate was 0.007 monolayers per second and the overgrowth layer was 4-nm-thick $In_{0.17}Ga_{0.83}As$. The growth temperature was 510°C. Sheet density in an atomic-force microscope (AFM) image was 2-3 X 10^{10} cm^{-2}.

Figure 6-24 shows the cross-sectional transmission electron microscopy (TEM) images of the dot layers. Dot size was 15 - 18 nm in diameter and 9 - 12 nm in height. In this figure, we can see that the stacking was successful, that is, self-assembled quantum dots were reproduced in all layers with a similar surface density. In TEM images of lower magnification, we found that the position of the dots was weakly correlated in the growth direction and that the numerical density was slightly reduced in upper layers.

Figure 6-25 shows the photoluminescence spectra of samples having single and triple dot layers. Measurements were done at 25°C with a 647.1-nm Kr^+ ion laser as a pump. In the measurements, p-type layers were removed by chemical etching. The emission wavelength of the dot ground level was 1.31 μm and that of the second level was 1.22 μm. A shoulder at 1.16 μm indicates the third level, and an isolated weak peak at 0.98 μm may be related to the two-dimensional structure composed of a wetting layer and overgrowth layer. We see that the emission intensity of the triple-layered sample is stronger than that of the single-layer one. The result suggests that the quantum efficiency was not degraded by the stacking. Note that full width at half maximum (FWHM) of the ground level emission peak was about 40 meV in both samples, indicating that the dot-energy medium and dot inhomogeneity were reproduced during stacking. The results suggest that stacking was effective to raise the optical gain of the active region.

6-4-2 CW operation with low threshold current

Ridge-type double heterostructure lasers were fabricated with 1.3-μm-emission dots. The structures were grown on (001)n-GaAs substrate followed by growth of a 1.4-μm n-$Al_{0.4}Ga_{0.6}As$ cladding layer, an active layer, 1.4-μm p-$Al_{0.4}Ga_{0.6}As$ and 20-nm p-

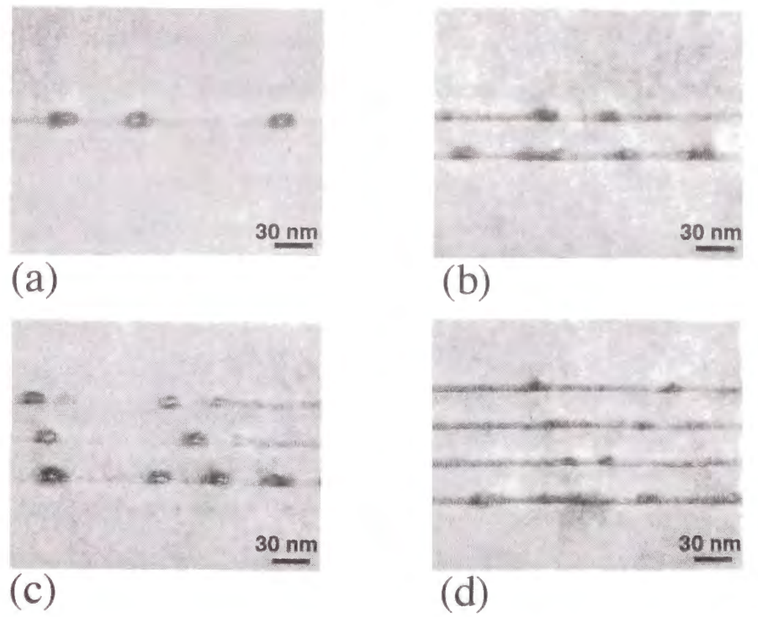

Figure 6-24 Cross-sectional transmission electron microscopy (TEM) image of InGaAs/GaAs quantum-dot layers: (a) single, (b) double, (c) triple, and (d) quadruple stacked structures. Dot layers were separated by 26-nm-thick GaAs barrier layers.

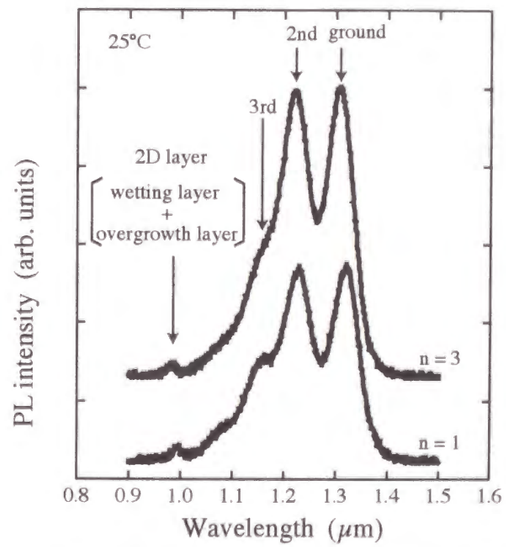

Figure 6-25 Photoluminescence spectra of samples having single and tripled quantum-dot layers at 25°C. The peaks did not broad after the stacking. Small peak at 0.98 μm corresponds to two dimensional layer composed of wetting layer and overgrowth layer.

$Al_{0.2}Ga_{0.8}As$ cladding layers, and a 0.4-μm p-GaAs contact layer. The active layer was composed of dot layer(s) and GaAs separate confinement heterostructure (SCH) layers. The number of dot layers (= N) in the active layer was varied from 1 to 4. The thickness of GaAs spacer layers separating dot layers was 26 nm in all structures. The thickness of the SCH layers was changed following the number of dot layers to obtain high optical confinement in the active layer. Cavity length (= L) was 300, 600, 900, and 1800 μm. Ridge structures were formed by chemical etching. Mesa width varied between 4.0 and 6.0 μm. A 95% HR coating was applied to both facets.

Figure 6-26 shows the electroluminescence spectra at 25°C of the laser diode where three sheets of dot layers were included (N = 3) and the cavity length was 300 μm (L = 900 μm) [21, 35]. Data were obtained using an optical spectrum analyzer (MS9710B, Anritsu). As the injection current increased, luminescence at 1.31 μm rose to begin lasing at over 7 mA. This was the first 1.3-μm CW lasing of quantum dot lasers. Comparing the spectra with the photoluminescence results in Fig. 6-25, we can see that the lasing occurred at the dot ground level. At the lasing threshold, there is no appearance of a third-level peak, and the second-level emission intensity is 10dB below the ground-level one. These results indicate that the carrier injection rate from the continuous level into the dot ground level was much faster than the carrier recombination rate. The carrier injection rate was probably enhanced by the Auger effect at the high carrier densities near the lasing threshold (see Chapter 5). The results also indicate that the optical gain reached the lasing threshold when carrier overflow into the upper sublevels was still negligible.

Figure 6-27 shows the CW light output versus injection current characteristics of the laser with N = 4 and L = 300 μm [36]. The threshold current, I_{th}, was as low as 5.4 mA at 25°C. The inset shows the lasing spectrum at an injection current of 6 mA ($\approx$ 1.1 X I_{th}), where we saw one sharp spectrum at 1.31 μm. We believe that the large gain realized by the improvements in dot density and stacking enabled low threshold 1.3-μm lasing.

From the differential quantum efficiency of various cavity lasers, the author evaluated the internal loss and internal quantum efficiency of the 1.3-μm ground-level lasing. 1.3-μm lasing was observed for n = 3 and 4 for all cavity lengths as well as for n = 2 with L = 900 and 1800 μm. Differential quantum efficiency, η_d, is described by Eq. (6. 2), and the internal loss and the internal quantum efficiency were determined from the relationship between the differential quantum efficiency and the cavity length with the assumption that the parameters

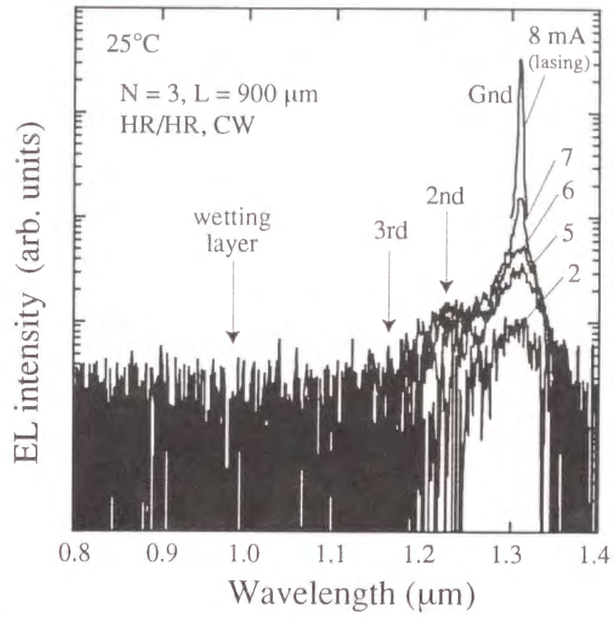

Figure 6-26 Electroluminescence spectra measured at 25°C. Lasing occurred at 1.3 μm of the ground level. There is no appearance of the third level and the upper continuous level, and the second-level emission is quite weak even in the log-scale plot.

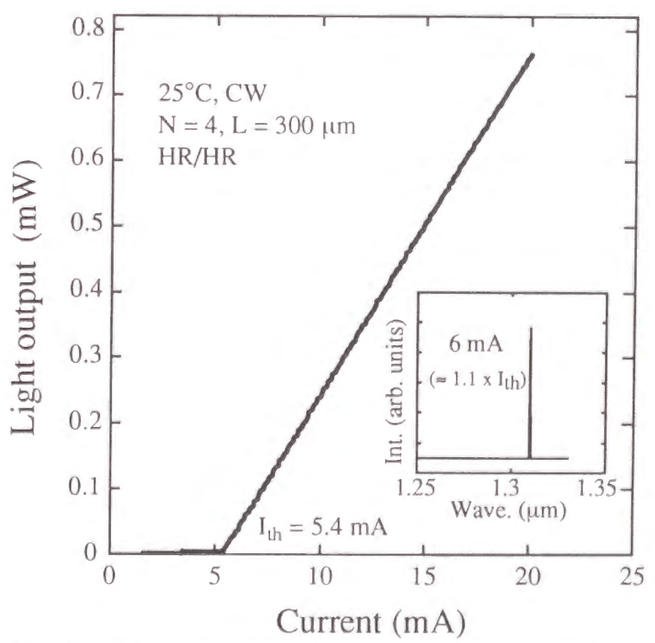

Figure 6-27 CW light output versus injected current characteristics at 25°C of quantum-dot laser. Threshold current was 5.4 mA. Inset indicates that the lasing occurred at the 1.3-μm ground level.

α_i and η_i are constant and $R_f = R_b$. In Fig. 6-28, the calculation by Eq. (6. 2) was fitted to the measured results for N = 3 and 4 using the least squares method. Since the data in Fig. 6-28 are roughly on straight lines, the author supposes that the evaluation is valid. The internal loss was determined to be 1.16 cm^{-1} for N = 3 and 1.31 cm^{-1} for N = 4. The values are one order smaller than those of 1.3-μm quantum well lasers on InP substrates. Low absorption losses in the dot active region possibly caused the small internal losses. Also, the internal loss is less than a quarter of the equivalent value for columnar dot lasers. This is probably because optical scattering is more frequent in columnar dots having multiple wetting layers. The internal quantum efficiency was simultaneously determined to be about 20%.

The author evaluated the maximum gain of the ground level of the samples. Figure 6-29 compares the lasing wavelength and threshold current density per sheet as a function of threshold gain per sheet. Here, the threshold gains were calculated from mirror loss and an internal loss of 1.2 cm^{-1}. The figure clearly indicates that the wavelength jumps from the second level to the ground level upon a lowering of the threshold gain. The level jump occurred at a gain of 1.0 cm^{-1}, which corresponds to the maximum modal gain of the ground level per sheet. The slope of the threshold current density per sheet line also changed to decrease at the gain of 1.0 cm^{-1}. This is due to the larger differential gain caused by the high degeneracy of the second level.

Let us discuss the maximum gain obtained of the ground level per sheet. The author calculated material gain taking into account both homogeneous and inhomogeneous broadening of quantum dot energy. Linear optical gain of dot sublevels can be described by [37]

$$g(E) = \frac{2\pi e^2 \hbar N_D}{c n_r \varepsilon_0 m_0^2} \sum_{c,v} \frac{\left|P_{cv}^{\sigma}\right|^2}{E_{cv}} \int_{-\infty}^{\infty} \left[f_c(E') - f_v(E') \right] B_0(E' - E_{cv}) B_{cv}(E - E') dE' \tag{6. 3}$$

where N_D is the volume density of quantum dots, c is the velocity of light, n_r is the background refractive index, ε_0 is the permittivity of a vacuum, m_0 is the electron mass, E_{cv} is the band gap energy, and f_i ($i = c, v$) is the occupation probability for the conduction and valence band, respectively. If charge neutrality is assumed, $f_c + f_v = 1$. B_0 is the normalized inhomogeneous broadening function described by a Gaussian distribution as

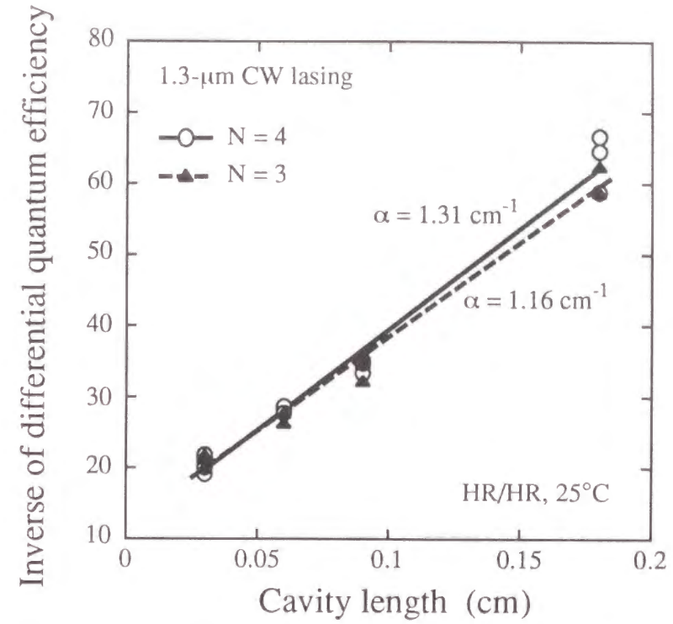

Figure 6-28 Inverse of differential quantum efficiency of 1.3-μm dot lasers with N = 3 and 4 as a function of cavity length. Internal loss was determined to be 1.16 cm^{-1} for N = 3 and 1.31 cm^{-1} for N = 4.

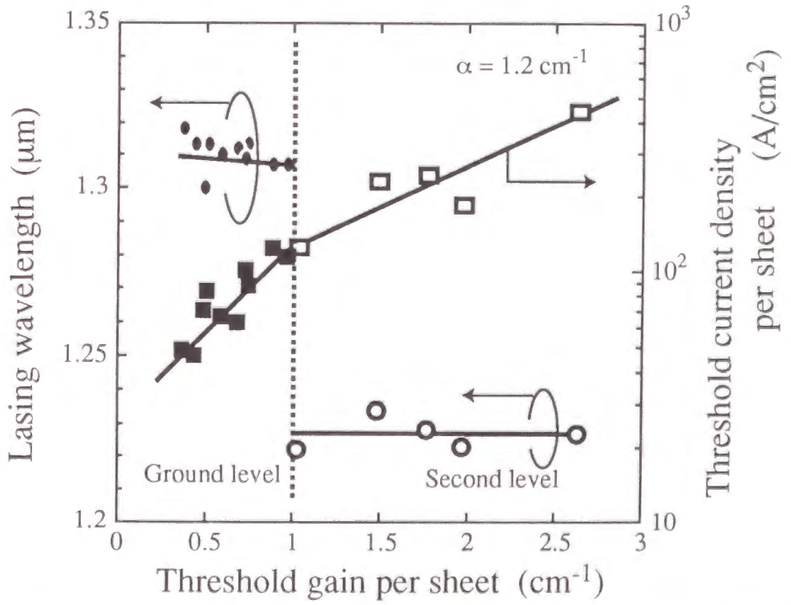

Figure 6-29 Lasing wavelength and threshold current density per sheet as a function of threshold gain per sheet. The threshold gain was calculated using mirror loss and internal loss of 1.2 cm^{-1}.

$$B_0(E-E_{cv}) = \frac{1}{\sqrt{2\pi}\xi_0}\exp\left[-\frac{(E-E_{cv})^2}{2\xi_0^2}\right] \qquad (6.\ 4)$$

where FWHM is given by $2.35\xi_0$. B_{cv} is the normalized homogeneous broadening function described by

$$B_{cv}(E-E') = \frac{\hbar\Gamma_{cv}/\pi}{(E-E')^2+\hbar^2\Gamma_{cv}^2} \qquad (6.\ 5)$$

which obeys a Lorentzian distribution with a FWHM of $2\Gamma_{cv}$. $|P_{cv}^{\sigma}|^2$ is the square of the momentum matrix element, and assuming that the dots have a spherical shape, it is equal to that in bulk materials as

$$|P_{cv}^{\sigma}|^2 = \frac{m_0^2}{12}\left(\frac{1}{m_e^*}-\frac{1+D'}{m_0}\right)\frac{E_{cv}(E_{cv}+\Delta)}{E_{cv}+2\Delta/3} \qquad (6.\ 6)$$

where m_e^* is the effective mass on the conduction-band edge, Δ is the spin-orbit splitting energy, and D' is the second-order perturbation term. To calculate the maximum material gain for the ground level, the author set $f_c = 1$ and solved Eq. (6. 3) using $n_r = 3.5$, $m_e^* = 0.044m_0$, $\Delta = 0.37$ eV, and $D' = 0$.

Figure 6-30 shows the calculated material gain for quantum-dot ground level. The author tested the cases for the several sets of parameters (N_D, ξ_0, Γ_{cv}). In the figure, curve (a) denotes present samples where the dot sheet density is 3 X 10^{10} cm^2, and inhomogeneous and homogeneous broadening is approximately 40 and 16 meV, respectively [38]. The calculated maximum value was 1.2 X 10^2 cm^{-1}. Now, the optical confinement factor per dot sheet in the diodes is calculated to be 1% or less, assuming several-percent coverage of InGaAs dots with a 4-nm $In_{0.17}Ga_{0.83}As$ overgrowth layer. Therefore, the material gain for the ground level of 1.2 X 10^2 cm^{-1} corresponds to a modal gain of 1.2 cm^{-1} or less, which agrees with the measurement. A larger modal gain is expected after the improvements in optical confinement and properties of the dot ensemble. The large optical confinement factor actually enabled 1.3-μm dot lasing with one sheet [19]. The effect of dot density and homogeneity is shown in Fig. 9. Curve (b) indicates the case when the dot sheet density becomes one-order larger than the

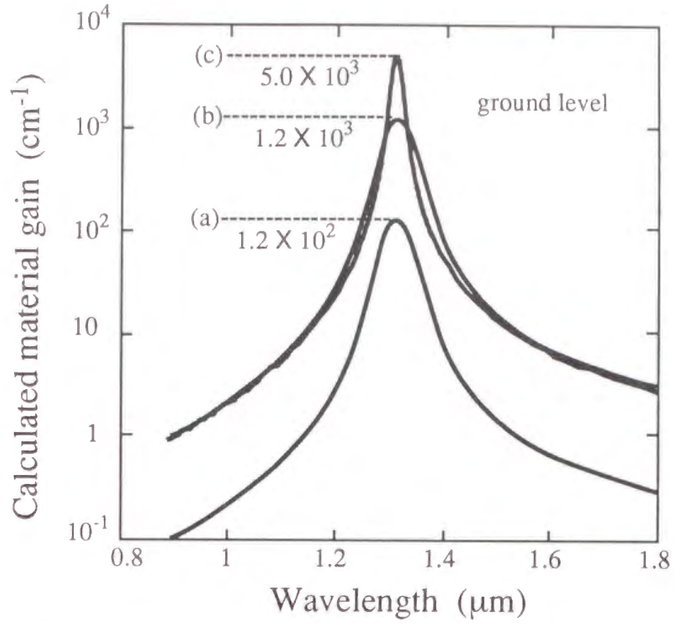

Figure 6-30 Calculated material gain of quantum-dot ground level: (a) [dot density, inhomogeneous broadening, homogeneous broadening] = [3 X 10^{10} cm^2, 40 meV, 16 meV], (b) [3 X 10^{11} cm^2, 40 meV, 16 meV], and (c) [4.5 X 10^{11} cm^2, 10 meV, 10 meV].

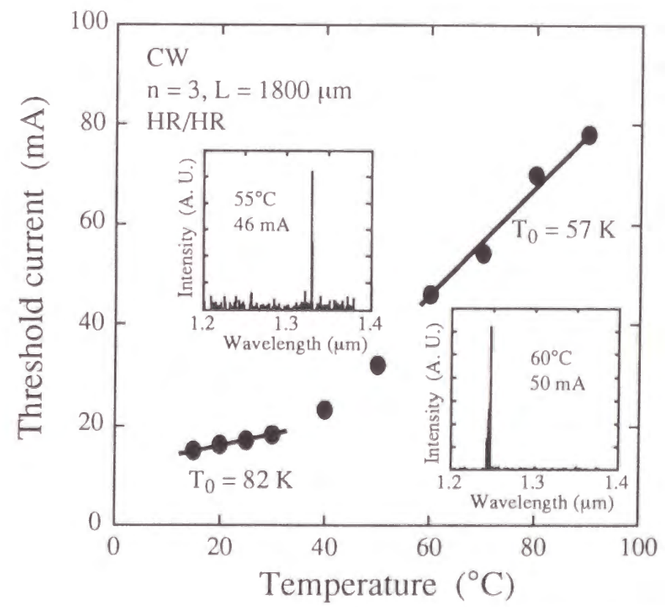

Figure 6-31 Temperature dependence of threshold current of laser with N = 3 and L = 1800 μm. Characteristic temperature was 82 K between 15 and 30°C. Insets lasing spectra shows that lasing level jumped from the ground level to the second level between 55 and 60°C.

present case. The material gain then becomes one order larger at a value of 1.2 X 10^3 cm^{-1}, which is comparable to the value of quantum wells [3]. Curve (c) indicates the case when the dot sheet density is 4.5 X 10^{11} cm^{-1}, which is the arithmetic maximum for 16-nm dots, and both the inhomogeneous and homogeneous broadening factors are 10 meV. In this case, material gain is expected to reach 5.0 X 10^3 cm^{-1}. The results clearly indicate that present quantum dots are required to improve sheet density and inhomogeneity in order to win a clear advantage in gain over quantum wells.

6-4-3 Temperature characteristics

Figure 6-31 shows the threshold current between 15 and 90°C for the laser where n = 3 and L = 1800 μm. As the temperature increased, the threshold current increased. The increase was enhanced between 40 and 60°C. The insets show the lasing spectra at 55 and 60°C, and indicate that the lasing level shifted from the ground level to the second level between the temperatures. The lasing level shift is probably caused by the thermal carrier excitation to the upper levels and the thermally induced loss of ground-level optical gain due to nonradiative recombination. Characteristic temperature, T_0, was determined to be 82 K between 15 and 30°C and 57 K between 60 and 90°C. T_0 decreased as the temperature was increased in this sample case. The author supposes that this is related to the thermally induced mechanical stress in a long cavity with a ridge structure. In many cases when L ≤ 900 μm, T_0 was comparable or higher in the high temperature range (60 - 90°C) than in the low temperature range (15 - 30°C). The author considers the reason for this as follows. While the thermal enhancement of nonradiative recombination and carrier excitation into upper levels causes low T_0, the state filling leading to carrier overflow requires high carrier density to occur at the second level having high state density [23]. Therefore, carrier overflow is small at the second-level-lasing threshold, which will cause high T_0.

There was the relationship between T_0 and n. Figure 6-32 shows the T_0 of 1.3-μm dot lasers at room temperature as a function of L for different values of N. Other reported data for N = 1 are superimposed [19, 39]. T_0 is shown to increase with an increase of L. The author supposes that this owes to small carrier overflow into the upper sublevels in long-cavity lasers; carrier density per dot at the threshold is reduced by the long cavity since threshold

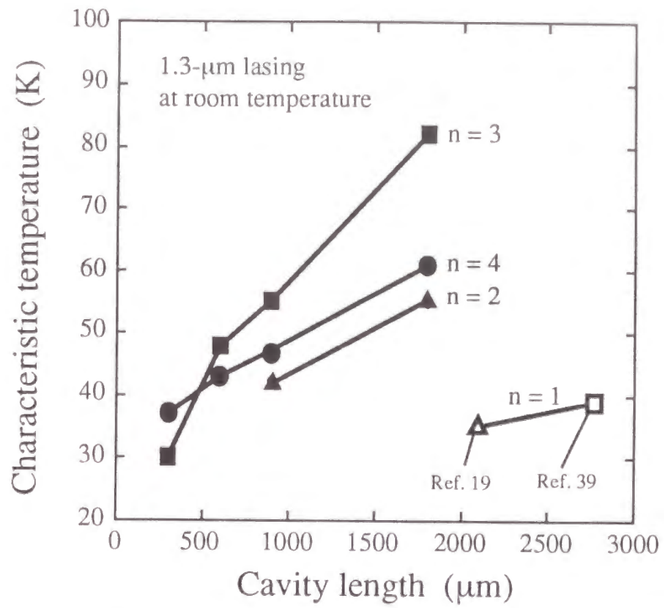

Figure 6-32 Characteristic temperature of 1.3-μm dot lasers at room temperature as a function of cavity length. Previous reported data where number of dot sheets was 1 are superimposed.

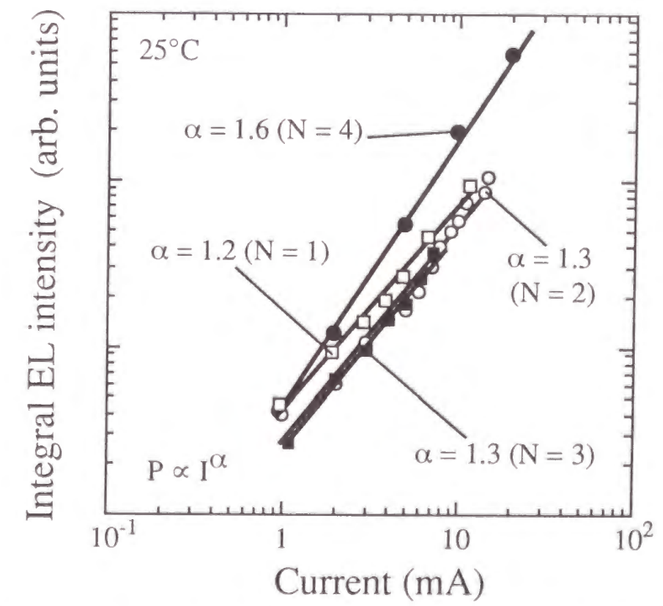

Figure 6-33 Integral electroluminescence intensity of quantum-dot lasers at 25°C as a function of injection current. As number of dot layers (N) increased from 1 to 4, the parameter a increased from 1.2 to 1.6.

gain gets small due to a decrease in cavity loss. Also, in Fig. 6-32, T_0 increased as N increased up to 3, but a further increase of N deteriorated T_0. The author supposes the reason for this as follows. The increase in N reduces the threshold gain per sheet and delays state filling at the ground level of the dot ensemble. These cause the reduction of both the carrier density per dot at the threshold and the number of overflow carriers, resulting in an increase of T_0. Meanwhile, the increase in N also magnifies lattice distortions in the active region, and probably enhances generation of the nonradiative recombination centers during epitaxial growth. This would deteriorate T_0.

To support the above estimation based on the results of N variation in Fig. 6-32, the author evaluated nonradiative recombination in laser diodes by examining spontaneous emission efficiency as a function of injection current.

Figure 6-33 shows the integral electroluminescence intensity of laser diodes at 25°C as a function of injection current under the lasing threshold. Absolute intensity was not calibrated among samples. The index, α, of the exponential relationship between current and integral electroluminescence (EL) intensity is denoted for each sample in the figure. α in these current ranges was the same as that in the excitation power dependence of photoluminescence, and increased near the lasing threshold since the electroluminescence was amplified between mirrors. α was larger than 1 in all samples, and increased as N increased. According to the theory on spontaneous emission intensity, $\alpha = 1$ if carrier consumption is dominated by radiative recombination, and $\alpha = 2$ if dominated by nonradiative recombination. The experiments suggest that the nonradiative effect was not negligible, supporting the low internal quantum efficiency found in Fig. 6-28. While α varied merely by 8% between N = 1 and 3, α increased by 23% from N = 3 to 4. The results suggest that generation of the nonradiative recombination centers were enhanced by the stacking of dot layers, and the enhancement was large when N > 3. This explains the result in Fig. 6-32, where T_0 decreased as N increased from 3 to 4. Thus, the author expects that higher T_0 will be obtained when the radiative efficiency of the structure is improved.

Low-temperature experiments were performed to estimate the laser performance when the nonradiative carrier consumption and thermal carrier excitation are eliminated. Figure 6-34 shows the light output versus injection current characteristics of CW laser with n = 4 and L = 300 μm at between 150 and 270 K. As temperature decreased, the threshold current

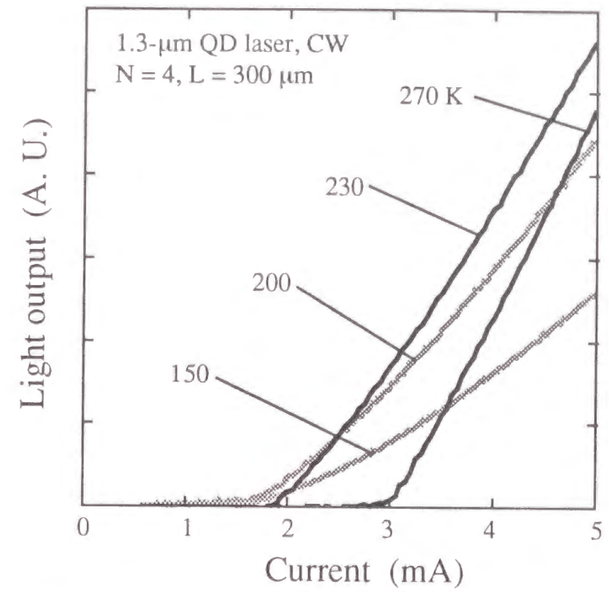

Figure 6-34 Light output versus injected current characteristics of CW laser with N = 4 and L = 300 μm between 270 and 150 K.

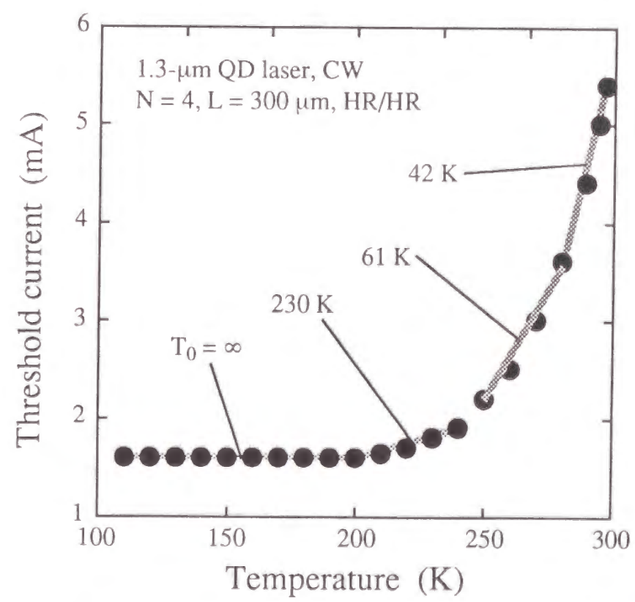

Figure 6-35 Threshold current as a function of temperature for laser diode with N = 4 and L = 300 μm. At low temperature, characteristic temperature was infinity and threshold current was 1.6 mA.

decreased below 2 mA. A unique behavior in the curves was observed [38]. While the curves at 270 and 230 K show typical lasing characteristics with a linear increase of the output power above a clear threshold, the curves at 200 and 150 K show a gradual increase of light output with a rather unclear threshold. The slope efficiency at 200 and 150 K was consequently quite lower than at higher temperatures. The author conjectured that these owe to differences of lasing mechanisms at the temperatures. At high temperatures, lasing occurs with the aid of homogeneous spectrum broadening due to the scattering of carriers, but at low temperatures, for the lack of the aid from broadening, lasing starts in sequence from the dot ensemble isolated in energy.

Figure 6-35 shows threshold current as a function of temperature between 110 and 300 K. As the temperature decreased from room temperature to under 200 K, T_0 drastically increased to infinity. It should be noted that with other previous dot lasers, such as SK dot lasers [40] and columnar dot lasers [23], the reduction of the threshold current was still observed at between 200 and 150 K (see Fig. 6-16). One explanation for the high T_0 at these temperatures is the deep potential of 1.3-μm dots that would be effective to prevent thermal carrier excitation into the continuum. Below 200 K, the threshold current reached as low as 1.6 mA. The data promises that a high T_0 is available with a low threshold current at room temperature if the nonradiative recombination is reduced in the 1.3-μm dot structure with deep potential.

The author then compared the optical properties of quantum dot lasers with and without an InGaAs-layer overgrowth on dots to indicate that the radiative efficiency and deep potential were actually the key points for achieving good temperature characteristics [41]. Ridge-type double heterostructure lasers were fabricated. Two types of dot layers, with and without the InGaAs-overgrowth layer, were used as the active layer. The number of dot sheets in the active layer was 2 or 3. The thickness of GaAs spacer layers separating the dot layers was 26 nm in all structures. The cavity length was 1800 μm and a 95% HR coating was applied to both facets. In cross-sectional TEM images of the samples, the author found that the sheet density of the stacked layers was not decreased for the case without an InGaAs-overgrowth layer (i.e., when dots were covered only by GaAs), but was decreased for the case with the overgrowth layer.

Figure 6-36 compares the photoluminescence spectra of samples for N = 2. For the measurements, p-type layers were removed by chemical etching, and a 647.1-nm Kr^+ ion

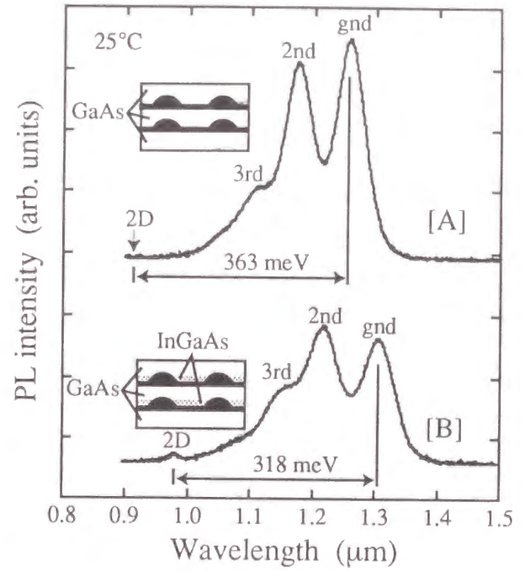

Figure 3-36 Photoluminescence spectra of two types of dots for N = 2 at 25°C. Cross-sectional dot structures are schematically shown in insets.

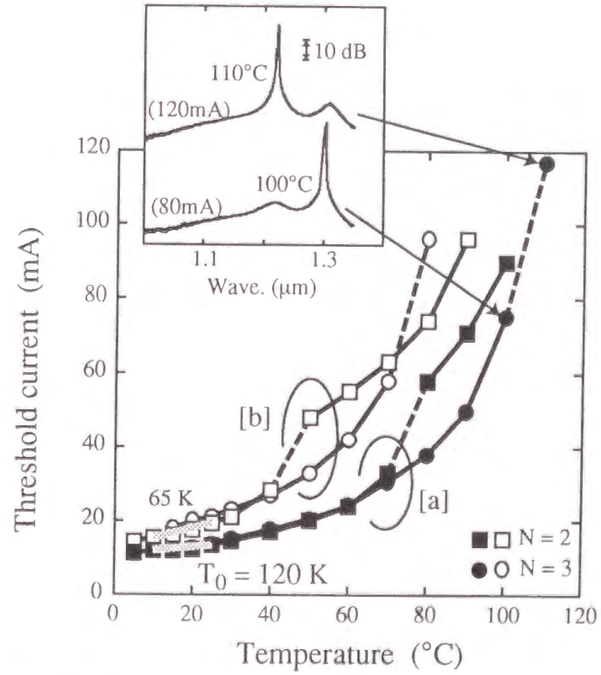

Figure 6-37 Temperature dependence of threshold current of lasers: (a) laser with 1.26-μm emission dots and (b) laser with InGaAs-covered dots. Inset lasing spectra indicate that the ground-level lasing occurred up to 100°C.

laser was used as an exciter. The excitation power density was about 60 W/cm^2. In the spectra, we can see multiple peak emissions corresponding to quantized discrete sublevels in quantum dots. In the upper spectrum, the emission wavelengths of the ground, second, and third levels were 1.26, 1.17, and 1.1 μm, respectively. In the lower spectrum of reference dots, which were covered by InGaAs followed by GaAs, the emission wavelengths of the ground, second, and third levels were 1.31, 1.22, and 1.16 μm, respectively. We suppose that an isolated weak peak at 0.98 μm in the lower spectrum is related to the two-dimensional (2D) structure composed of the wetting and overgrowth layer. Without the overgrowth layer, the wetting layer of SK dots emits at about 0.92 μm.

Figure 6-36 reveals four remarkable differences in the spontaneous emission spectra between the samples; 1) emission intensity of the ground level is stronger in the upper spectrum, 2) integrated intensity is larger in the upper spectrum, and 3) emission wavelength of the 2D structure gets longer due to the overgrowth layer. The ground-level emission intensity of GaAs-covered dots is about twice of that of InGaAs-covered dots, which is related the dot density and radiative recombination efficiency. Cross-sectional TEM images indicated that the dot volume density was about-10% higher for GaAs-covered dots than for InGaAs-covered dots. Integrated intensity suggests that carrier consumption through the nonradiative channel was higher in InGaAs-covered dots. The emission wavelength tells us that the energy separation between the ground level and the 2D layer was 318 meV for the reference sample while the energy separation for GaAs-covered dots was 363 meV. The energy separation of GaAs-covered dots is 45-meV larger than that of InGaAs-covered dots and, for example, 143-meV larger than that of 1.1-μm SK dot lasers [42].

Threshold current as a function of temperature is shown in Fig. 6-37. T_0 of GaAs-covered dot laser was determined to be 120 K between 5 and 25°C, which is quite large compared with that of previous dot lasers in Fig. 6-16. A remarkable increase in threshold current was observed in all samples, which are indicated by dashed lines. The remarkable increases were due to the lasing level shift from the ground level to the second level. The lasing level shift is caused by thermal carrier excitation from the ground level to the second level, that reduces the gain at the ground level. For a GaAs-covered dot laser with N = 3, a lasing level shift was observed between 100 and 110°C (i.e., the ground-level lasing up to 100°C was attained). In InGaAs-covered dot lasers, the threshold currents themselves and their increase with the temperature rise were larger than those in GaAs-covered dot lasers. T_0

between 5 and 25°C was 65 K, which is about half of that in GaAs-covered dot lasers. The lasing level jump was observed between 40 and 50°C for N = 2 and between 50 and 60°C for N = 3. Both of the critical temperatures are lower than those in GaAs-covered dot lasers.

These advantages enabled GaAs-covered dot lasers to exhibit good temperature characteristics. High volume density reduced carrier overflow due to the state filling effect at the ground level. High quantum efficiency resulted in a small effect of the thermal activation of the nonradiative channel. The deep potential suppressed carrier leakage into the continuum. These properties caused temperature-insensitive operation. The author supposes that future improvement in dot uniformity will also contribute to the high-temperature operation since it raises effective dot density. The results will help future designs of quantum dot laser structure aiming for high-temperature characteristics.

6-5. Summary

In this chapter, the author described the lasing characteristics of self-assembled InGaAs quantum dots on GaAs substrates. ALS dot lasers grown by MOVPE, columnar dot lasers grown by MBE, and 1.3-μm-emission dot lasers grown by MBE are investigated.

Using ALS dots, lasing at the three-dimensionally confined sublevel was demonstrated for the first time using magnet-optical measurements. Observed electroluminescence spectra indicated that the dot ground level was filled with an extremely low current injection level, suggesting that ultra-low threshold current density operation could be realized in quantum dot lasers. The small ground-level optical gain caused by low dot density and low emission efficiency limited the lasing in high-order-sublevel operation at low temperatures.

High sheet density and multiplication of the dot layers in growth direction was realized by columnar dots, which enabled low threshold current lasing at room temperature at the dot ground level. Dependence of lasing properties on cavity condition and temperature characteristics were discussed compared with those of SK dot lasers, indicating the advantages of columnar dot structure. Distinct jumping of lasing level during increases of injection current and temperature were demonstrated. The author showed that the high uniformity, emission efficiency, and density actually greatly improved the performance of

quantum dot lasers. Obtained low threshold current of 5.4 mA at 25°C was a record for an edge-emitting quantum dot laser in 1998.

Applying the growth methods of ALS dots to SK-dot formation in MBE, 1.3-μm CW lasing of quantum dots at room temperature was attained for the first time. The dots were grown with a combination of a low growth rate and InGaAs-layer overgrowth. A high dot density and the multiplication of the dot layers were successfully achieved and realized high gain. Several properties of 1.3-μm quantum dot lasers were demonstrated. A low threshold current of 5.4 mA was obtained for 1.3-μm ground-level CW lasing with a cavity length of 300 μm. Internal loss of the laser structure was estimated to be 1.16 - 1.31 cm^{-1}. Measured material gain closely agreed with theoretical estimation, quantitatively exposing the importance of raising dot density. The characteristic temperature of threshold current depended on the number of dot layers. The dependence of spontaneous emission intensity on injection current indicated that the lasing performances were still degraded by non-radiative recombination. Low-temperature characteristics of the lasers indicated that infinite characteristic temperature with a low threshold current will be achieved if the nonradiative recombination channel is eliminated with a deep dot potential. Without the InGaAs-layer overgrowth, the dot laser exhibited the characteristic temperature of 120 K at room temperature and ground-level lasing up to 100°C, indicating that the key points for achieving high-temperature characteristics are large volume density, deep potential, and high quantum efficiency.

References

[1] N. Chand, E. E. Becker, J. P. van der Ziel, S. N. G. Chu, and N. K. Dutta, Appl. Phys. Lett. 62, 1704 (1991).

[2] Y. Arakawa and H. Sakaki, Appl. Phys. Lett., 40, 939 (1982).

[3] M. Asada, Y. Miyamoto and Y. Suematsu, QE-22, 1915 (1986).

[4] H. Sakaki, Jpn. J. Appl. Phys. 28, L314 (1989).

[5] K. J. Vahala, IEEE J. Quantum Electron., 24, 523 (1988).

[6] T. T. J. M. Berendschet, H. A. J. M. Reinen, H. A. Bluyssen, C. Harder, and H. P. Meier, Appl. Phys. Lett. 54, 1827 (1989).

[7] K. Kash, A. Scherer, J. M. Worlock, H. G. Craighead and M. C. Tamargo, Appl. Phys. Lett. 49, 1043 (1986).

[8] T. Fukui, S. Ando, Y. Tokura and T. Toriyama, Appl. Phys. Lett. 58, 2018 (1991).

[9] H. Hirayama, K. Matsunaga, M. Asada, and Y. Suematsu, Electron. Lett., 30, 142 (1994).

[10] M. Tabuchi, S. Noda and A. Sasaki, in *Science and Technology of Mesoscopic Structures*, edited by S. Namba, C. Hamaguchi and T. Ando (Springer, Tokyo, 1992) pp. 379.

[11] D. Leonard, M. Kishnamurthy, C. M. Reaves, S. P. Denbaars, and P. M. Petroff, Appl. Phys. Lett., 63, 3203 (1993).

[12] N. Kirstaedter, N. N. Ledentsov, M. Grundmann, D. Bimberg, V. M. Ustinov, S. S. Ruvimov, M. V. Maximov, P. S. Kop'ev, Zh. I. Alferov, U. Richter, P. Werner, U. Gösele and J. Heydenreich, Electron. Lett., 30, 1416 (1994).

[13] D. Bimberg, N. Kirsteadter, N. N. Ledentsov, Zh. I. Alferof, P. S. Kop'ev, and V. M. Ustinov, 3, 196 (1997).

[14] H. Shoji, Y. Nakata, K. Mukai, Y. Sugiyama, M. Sugawara, N. Yokoyama and H. Ishikawa, Electron. Lett., 32, 2023 (1996).

[15] F. Heinrichsdorff, M.-H. Mao., N. Kirstaedter, A. Krost, and D. Bimberg: Appl. Phys. Lett., 71, 22 (1997).

[16] K. Mukai, Y. Nakata, H. Shoji, M. Sugawara, K. Ohtsubo, N. Yokoyama, and H. Ishikawa, Electro. Lett., 34, 1588 (1998).

[17] G. T. Liu, A. Stintz, H. Li, K. J. Malloy, and L. F. Lester, Electron. Lett., 35, 1163 (1999).

[18] K. Kamath, D. Klotzkin, and P. Bhattacharya, proc. IEEE Lasers and Electro-Optics Soc. 1997 Ann. Meet. pp. 498.

[19] D. L. Huffaker, G. Park, Z. Zou, O. B. Shchekin and D. G. Deppe, Appl. Phys. Lett., 73, 2564 (1998).

[20] Y. Nakata, K. Mukai, M. Sugawara, K. Ohtsubo, H. Ishikawa and N. Yokoyama, Ext. Abstr. The 46th Spring Meeting of The Japan Society of Applied Physics and Related Societies, 31aP-1, p. 376, 1999 (in Japanese).

[21] K. Mukai, Y. Nakata, K. Otsubo, M. Sugawara, N. Yokoyama and H. Ishikawa, abs. of Postdeadline paper in Conference on Lasers and Electro-Optics / Quantum Electronics and Laser Science Conference (Baltimore, USA), CPD-18 (1999).

[22] H. Shoji, K. Mukai, N. Ohtsuka, M. Sugawara,T. Uchida, and H. Ishikawa, IEEE Photon. Technol. Lett., 12, 1385 (1995).

[23] K. Mukai, Y. Nakata, H. Shoji, M. Sugawara, K. Ohtsubo, N. Yokoyama and H. Ishikawa, Proceeding of 10th Indium Phosphide and Related Materials (Tsukuba, Japan), pp. 345-348 (1998).

[24] K. Mukai, Y. Nakata, H. Shoji, M. Sugawara, K. Ohtsubo, Y. Sugiyama, N. Yokoyama, and H. Ishikawa, proc. of 16th IEEE International Semiconductor Laser Conference (Nara, Japan) 1998.

[25] Y. Nakata, Y. Sugiyama, T. Futatsugi, K. Mukai, H. Shoji, M. Sugawara, H. Ishikawa, and N. Yokoyama, Ext. Abs. The 58th Autumn Meeting of The Japan Society of Applied Physics, 2pM-4, p.233, 1997 (in Japanese).

[26] Q. Xie, A. Madhukar, P. Chen., and N. Kobayashi, Phys. Rev. lett. 75, 2542 (1995).

[27] M. Sugawara, Y. Nakata, K. Mukai, and H. Shoji, Phys. Rev. B, 55, 13155 (1997).

[28] H. Shoji, Y. Nakata, K. Mukai, Y. Sugiyama, M. Sugawara, N. Yokoyama and H. Ishikawa, technical digest of 2nd Opt. and Commun. Conf., 1997, Seoul, Korea, pp. 176-177.

[29] Y. Nakata, Y. Sugiyama, T. Futatsugi and N. Yokoyama, J. Crystal Growth, 175/176, 713 (1997).

[30] Y. Sugiyama, Y. Nakata, K. Imamura, S. Muto, and N. Yokoyama, Jpn. J. Appl. Phys., 35, 1320 (1996).

[31] K. Mukai, N. Ohtsuka, M. Sugawara, and S. Yamazaki, Jpn. J. Appl. Phys., 33, L1710 (1994).

[32] D. L. Huffaker, and D. G. Deppe, Appl. Phys. Lett., 73, 520 (1998).

[33] R. Murray, D. Childs, S. Malik, P. Siverns, C. Roberts, J.-M. Hartmann and P. Stavrinou, Jpn. J. Appl. Phys., 38, 528 (1999).

[34] H. Saito, K. Nishi, J. Lee and S. Sugou, Ext. Abstr. (45th Spring Meet. 1998); Japan Society of Applied Physics and Related Societies, 30a-PC-6, p. 491 [in Japanese].

[35] K. Mukai, Y. Nakata, K. Otsubo, M. Sugawara, N. Yokoyama and H. Ishikawa, IEEE Photonics Tech. Lett., 11, 1205 (1999).

[36] K. Mukai, Y. Nakata, K. Otsubo, M. Sugawara, N. Yokoyama and H. Ishikawa, J. Quantum Electron., 36, 472 (2000).

[37] M. Sugawara, *Semicond. & Semimetals*, vol. 60 Chap. 1 (Academic, NY, 1999).

[38] M. Sugawara, K. Mukai, and Y. Nakata, Appl. Phys. Lett., 74, 1561 (1999).

[39] G. Park, D. L. Huffaker, Z. Zou, O. B. Shckekin and D. G. Deppe, IEEE Photonics Tech. Lett., 11, 301 (1999).

[40] H. Shoji, Y. Nakata, K. Mukai, Y. Sugiyama, M. Sugawara, N. Yokoyama, and H. Ishikawa, Appl. Phys. Lett., 71, 193 (1997).

[41] K. Mukai, Y. Nakata, K. Otsubo, M. Sugawara, N. Yokoyama, and H. Ishikawa, Appl. Phys. Lett., to be published in June issue (2000).

[42] H. Shoji, Y. Nakata, K. Mukai, Y. Sugiyama, M. Sugawara, N. Yokoyama and H. Ishikawa, IEEE J. Selected Topics in Quantum Electronics, 3, 188 (1997).

Chapter 7

Conclusion

Fabrication, characterization, and application of self-assembled InGaAs/GaAs quantum dots have been investigated in this thesis. The author has placed special emphasis on i) a unique growth technique of 1.3-μm-emission quantum dots, ii) optical properties peculiar to quantum dots, such as multiple emission peaks from discrete energy levels and the phonon bottleneck effect, and iii) a development of quantum dot lasers inclusive of the first 1.3-μm CW lasing at room temperature.

In the following, the results demonstrated in this thesis are summarized.

Effect of lattice-mismatch on InGaAsP nanostructures

The author discussed the effect of lattice mismatches on nano-scale InGaAsP semiconductor crystals. First, strain-induced non-error-functional interdiffusion profile of InGaAsP/InP quantum wells was demonstrated. Lattice strain was introduced by intermixing of group-V atoms. The author has proposed a formula describing the interdiffusion profile of quantum wells, and showed how the formula accurately models interdiffusion in InGaAsP and AlGaAs quantum wells. It was shown that discontinuous concentration of group-V atoms was maintained at InGaAsP/InP interface during interdiffusion while concentration of group-III atoms was continuous at GaAs/AlGaAs interface where no lattice mismatch is generated. The author also discussed the difference between the interdiffusion mechanism in an InGaAs layer and in an InP layer. Next, the author investigated the dislocation multiplication process in strained InGaAs/InP quantum wells using X-ray topography to detect small stress relaxation in the early stages of dislocation multiplication. The author determined dislocation glide activation energy and a material-specific proportionality constant for Dodson and Tsao's empirical model. Using the results, the stress relaxation process during growth of strained

layers was simulated. Then, the discovery of self-assembled $In_{0.5}Ga_{0.5}As$ quantum dots on GaAs substrates after highly strained epitaxial growth was described. The self-assembled dots were grown by supplying InAs and GaAs monolayers alternately in MOVPE. One of the most striking properties of the dots was 1.3-μm emission.

Growth of self-assembled InGaAs/GaAs quantum dots emitting at 1.3 μm

The author found the self-assembly of 1.3-μm-emission quantum dots during an alternate supply of source materials (ALS dots). The growth technique is based on so-called atomic layer epitaxy (ALE) that uses self-limiting one-atomic-layer growth of InAs and GaAs. The author has presented two kinds of growth sequences for the ALS dots: i) an In-As-Ga-As sequence based on the concept of making monolayer superlattices by ALE, and ii) a newly developed In-Ga-As sequence. Quantum dots are characterized by their shape, size, composition, and emission wavelength. In particular, how the dots vary with an alternate supply cycle, growth temperature, and composition of buffer layers on which the dots are grown was explained. The author also exhibited significant finding that the temperature sensitivity of interband emission energy are suppressed in the self-assembled dots by an InGaAs-layer overgrowth. Photoluminescence spectra showed that emission energy shift with a temperature increase was nearly negligible above 150 K when $x \geq 0.25$. The results reveal the potential of InGaAs-covered dots in realizing temperature-insensitive lasing wavelengths in laser diodes by manipulating three-dimensional strain distribution.

Optical characterization of quantum dots

Optical characterization of quantum dots has been described by focusing on the original ALS quantum dots. One of the most significant features of ALS dots is 1.3-μm emission --- a suitable wavelength for optical data transmission systems. The author observed emission with multiple peaks from discrete energy levels in self-assembled quantum dots for the first time. Microprobe photoluminescence revealed macroscopic distribution of dot optical properties and sharp emission lines caused by a single or small number of dots. Other unique properties of ALS dots, such as harmonic-oscillator-type confinement potential, large wavelength tunability between 1.2 and 1.5 μm through size control, and radiative and nonradiative recombination lifetimes are also examined using optical diagnostic techniques, comparing ALS and SK dots to show the advantages of the alternate supply method.

Carrier relaxation in quantum dots

Carrier dynamics in ALS quantum dots have been discussed based on the findings from time-resolved photoluminescence measurements. The dots have a high crystal quality, which features narrow spectrum broadening and high emission efficiency, enabling pursuit of carrier dynamics among discrete sublevels. After a discussion on possible carrier relaxation processes into quantum dots, the author proposed a model of the carrier relaxation process in a quantum dot to describe the emission decay profile of sublevels. Electroluminescence and time-resolved photoluminescence data were then analyzed to provide recombination and relaxation lifetimes, suggesting the existence of phonon bottleneck in ALS dots. Experiments on annealed quantum dot samples were also presented to demonstrate the effect of retarded carrier relaxation on emission spectra.

Quantum dot lasers

The achievement of high-performance characteristics with quantum dot lasers, such as low threshold current, high output power, and the first 1.3-μm continuous wave (CW) lasing, have been described. After a primary trial to fabricate quantum dot lasers with ALS dots, the growth technique was inherited for quantum dot lasers grown by MBE. It was found that the technique was again effective to grow quantum dots with a high uniformity, high emission efficiency, and long emission wavelengths. The author achieved a low threshold current of 5.4 mA and a high output power of 110 mW at 25°C, which were records in 1998 for edge-emitting quantum-dot lasers. Also, the author attained the first 1.3-μm CW lasing of quantum dot lasers at room temperature. The author investigated the basic properties of the quantum-dot lasers, such as gain, internal loss, internal quantum efficiency and temperature characteristics, and discussed future subjects for the improvement of quantum dot lasers.

List of publications

Regular papers

1) "Interdiffusion process in InGaAs/InP quantum well structures", Kohki Mukai, Mitsuru Sugawara, and Susumu Yamazaki, Journal of Crystal Growth 115, 433 (1991).

2) "Interdiffusion process in lattice-matched $In_xGa_{1-x}As_yP_{1-y}$/InP and GaAs/$Al_xGa_{1-x}As$ quantum wells", Kohki Mukai, Mitsuru Sugawara, and Susumu Yamazaki, Physical Review B 50, 2273 (1994) / republished in *Selected Papers on Quantum Well Intermixing for Photonics*, series volume MS145 (SPIE Milestone, 1998) ISBN: 0819428566.

3) "Relaxation process in strained InGaAs/InP quantum wells studied by X-ray topography", Kohki Mukai, Mitsuru Sugawara, and Susumu Yamazaki, Journal of Crystal Growth 145, 752 (1994).

4) "Enhancement of thermal stability in $In_{0.53}Ga_{0.47}As$/InP quantum wells", Kohki Mukai, Mitsuru Sugawara, and Susumu Yamazaki, Journal of Crystal Growth 137, 388 (1994).

5) "Growth and optical evaluation of InGaAs/GaAs quantum dots self-formed during alternate supply of precursors", Kohki Mukai, Nobuyuki Ohtsuka, Hajime Shoji, and Mitsuru Sugawara, Applied Surface Science 112, 102 (1997).

6) "Slow Carrier Relaxation among Sublevels in Annealed Self-Formed InGaAs/GaAs Quantum Dots", Kohki Mukai and Mitsuru Sugawara, Japanese Journal of Applied Physics 37, 5451 (1998).

7) "Quantum-Dot Lasers Fabricated with Self-Assembled Microcrystals", Kohki Mukai, Yoshiaki Nakata, and Mitsuru Sugawara, Fujitsu Scientific and Technical Journal 34, 223 (1998).

8) "1.3-μm Continuous-wave Lasing Characteristics of Self-assembled InGaAs/GaAs Quantum

Dots", Kohki Mukai, Yoshiaki Nakata, Koji Otsubo, Mitsuru Sugawara, Naoki Yokoyama and Hiroshi Ishikawa, Journal of Quantum Electronics 36, 472 (2000).

Letters

1) "Dependence of dislocation multiplication on time, temperature, and stress distribution in strained InGaAs/InP quantum wells studied by x-ray topography", Kohki Mukai, Mitsuru Sugawara, and Susumu Yamazaki, Applied Physics letters 64, 2836 (1994).

2) "Self-Formed $In_{0.5}Ga_{0.5}As$ Quantum Dots on GaAs Substrates Emitting at 1.3 μm", Kohki Mukai, Nobuyuki Ohtsuka, Mitsuru Sugawara, and Susumu Yamazaki, Japanese Journal of Applied Physics 33, L1710 (1994).

3) "Controlled Quantum Confinement Potentials in Self-Formed InGaAs Quantum Dots Grown by Atomic Layer Epitaxy Technique", Kohki Mukai, Nobuyuki Ohtsuka, and Mitsuru Sugawara, Japanese Journal of Applied Physics 35, L262 (1996).

4) "Emission from discrete levels in self-formed InGaAs/GaAs quantum dots by electric carrier injection: Influence on phonon bottleneck", Kohki Mukai, Nobuyuki Ohtsuka, Hajime Shoji, and Mitsuru Sugawara, Applied Physics letters 68, 3013 (1996).

5) "Phonon bottleneck in self-formed $In_XGa_{1-X}As$/GaAs quantum dots by electroluminescence and time-resolved photoluminescence", Kohki Mukai, Nobuyuki Ohtsuka, Hajime Shoji, and Mitsuru Sugawara, Physical Review B 54, R5243 (1996).

6) "High photoluminescence efficiency of InGaAs/GaAs quantum dots self-formed by atomic layer epitaxy technique", Kohki Mukai, Nobuyuki Ohtsuka, and Mitsuru Sugawara, Applied Physics letters 70, 2416 (1997).

7) "Lasing with low threshold current and high output power from columnar-shaped InAs/GaAs quantum dots", Kohki Mukai, Yoshiaki Nakata, Hajime Shoji, Mitsuru

Sugawara, Koji Ohtsubo, Naoki Yokoyama and Hajime Ishikawa, Electronics Letters 34, 1588 (1998).

8) "Suppression of temperature sensitivity of interband emission energy in 1.3-μm region by an InGaAs overgrowth on self-assembled InGaAs/GaAs quantum dots", Kohki Mukai and Mitsuru Sugawara, Applied Physics Letters 74, 3963 (1999).

9) "1.3-μm CW Lasing of InGaAs/GaAs Quantum Dots at Room Temperature with a Threshold Current of 8 mA", Kohki Mukai, Yoshiaki Nakata, Koji Otsubo, Mitsuru Sugawara, Naoki Yokoyama and Hiroshi Ishikawa, IEEE Journal of Photonics Technology Letters 11, 1205 (1999).

10) "High characteristic temperature of near-1.3-μm InGaAs/GaAs quantum-dot lasers at room temperature", Kohki Mukai, Yoshiaki Nakata, Koji Otsubo, Mitsuru Sugawara, Naoki Yokoyama and Hiroshi Ishikawa, Applied Physics Letters, to be published in June issue (2000).

International conference proceedings

1) "Interdiffusion process in InGaAs/InP quantum well structures", Kohki Mukai, Mitsuru Sugawara, and Nakajima, 7th International Conference on Vapor Growth and Epitaxy (Nagoya, Japan) 1991.

2) "Interdiffusion Mechanism in InGaAs/InP Quantum Well Structures", Kohki Mukai, Mitsuru Sugawara, and Susumu Yamazaki, Material Research Society the fall meeting (Boston, USA) 1991.

3) "Relaxation process in strained InGaAs/InP quantum wells", Kohki Mukai, Mitsuru Sugawara, and Susumu Yamazaki, International Conference on Metalorganic Vapor Phase Epitaxy-7th (Yokohama, Japan) 1994.

4) "1.3-μm Emitting $In_{0.5}Ga_{0.5}As$ Quantum Dots on GaAs Substrates Grown by Atomic Layer Epitaxy Technique", Kohki Mukai, Nobuyuki Ohtsuka, Mitsuru Sugawara, and Susumu Yamazaki, 7th biennial workshop on Organo-Metalic Vapor Phase Epitaxy (Florida, USA.) 1995.

5) **Invited** : "Growth and Optical Evaluation of InGaAs/GaAs Quantum Dots Self-Formed during Alternate Supply of Precursors", Kohki Mukai, Nobuyuki Ohtsuka, Hajime Shoji, and Mitsuru Sugawara, 4th International Conference on Atomic Layer Epitaxy (ALE-4) (Linz, Austria) 1996.

6) "Phonon bottleneck in annealed self-formed InGaAs/GaAs quantum dots", Kohki Mukai, Nobuyuki Ohtsuka, Hajime Shoji, and Mitsuru Sugawara, Material Research Society fall meeting (Boston, USA) 1997.

7) "Low Threshold CW Lasing of Closely-Stacked Self-Organized InAs/GaAs Quantum Dots", Kohki Mukai, Yoshiaki Nakata, Hajime Shoji, Mitsuru Sugawara, Koji Ohtsubo, Toshiro Futatsugi, Yoshihiro Sugiyama, Naoki Yokoyama, and Hiroshi Ishikawa, International Conference on InP and Related Materials (Tsukuba, Japan) 1998.

8) "Low Threshold and High Output Power Lasing of Columnar-Shaped Self-Assembled InAs/GaAs Quantum Dots", Kohki Mukai, Yoshiaki Nakata, Hajime Shoji, Mitsuru Sugawara, Koji Ohtsubo, Yoshihiro Sugiyama, Naoki Yokoyama, and Hiroshi Ishikawa, 16th IEEE International Semiconductor Laser Conference (Nara, Japan) 1998.

9) "Quantum-dot lasers fabricated with self-assembled InGaAs/GaAs microcrystals grown by alternate supply of source materials", Kohki Mukai, Yoshiaki Nakata and Mitsuru Sugawara, International Topical Workshop on Contemporary Photonic Technologies (Sendai, Japan) 1999.

10) "Low threshold (8 mA) 1.3-μm CW lasing of InGaAs/InAs quantum dots at room temperature", Kohki Mukai, Yoshiaki Nakata, Koji Otsubo, Mitsuru Sugawara, Naoki Yokoyama and Hiroshi Ishikawa, Postdeadline paper: Conference on Lasers and Electro-

Optics / Quantum Electronics and Laser Science Conference (Baltimore, USA) 1999.

11) "Suppression of temperature sensitivity of interband emission energy by an InGaAs overgrowth on self-assembled InGaAs/GaAs quantum dots", Kohki Mukai and Mitsuru Sugawara, Conference on Lasers and Electro-Optics/Quantum Electronics and Laser Science Conference (Baltimore, USA) 1999.

12) **Invited** : "1.3-μm InGaAs/GaAs quantum-dot lasers", Kohki Mukai, Yoshiaki Nakata, Koji Otsubo, Mitsuru Sugawara, Naoki Yokoyama and Hiroshi Ishikawa, Conference on Lasers and Electro-Optics / Quantum Electronics and Laser Science Conference (California, USA) 2000.

13) "High characteristics temperature of near-1.3-μm InGaAs/GaAs quantum-dots lasers", Kohki Mukai, Yoshiaki Nakata, Koji Otsubo, Mitsuru Sugawara, Naoki Yokoyama and Hiroshi Ishikawa, Conference on Lasers and Electro-Optics / Quantum Electronics and Laser Science Conference (California, USA) 2000.

14) "1.3-μm continuous-wave lasing characteristics of self-assembled InGaAs/GaAs quantum dots", Kohki Mukai, Yoshiaki Nakata, Koji Otsubo, Mitsuru Sugawara and Hiroshi Ishikawa, The Third SANKEN International Symposium (Suita, Osaka) 2000.

15) "Continuous-Wave Lasing with Low Threshold current (5.4 mA) from Self-Assembled InGaAs/GaAs Quantum Dots at a Wavelength of 1.3 μm", Kohki Mukai, Yoshiaki Nakata, Koji Otsubo, Mitsuru Sugawara and Hiroshi Ishikawa, 5th Optoelectronics and Communications Conference (OECC 2000) (Chiba, Japan) 2000.

Books

1) "Interdiffusion in Lattice-Matched Quantum Wells and Self-Formed Quantum Dots Composed of III-V Semiconductors", Kohki Mukai,
Chapter 3 in 'Semiconductor Quantum Well Intermixing : Material Properties and

Optoelectronic Applications (E. H. Li, Editor)', vol.6 of *Optoelectronic Properties of Semiconductors and Superlattices* (Gordon & Breach, Amsterdam, 1999) ISBN: 9056996894

2) "Metalorganic vapor phase epitaxial growth of self-assembled InGaAs/GaAs quantum dots emitting at 1.3 μm", Kohki Mukai, Mitsuru Sugawara, Mitsuru Egawa, and Nobuyuki Ohtsuka,

Chapter 3 in 'Self-Assembled InGaAs/GaAs Quantum Dots (M. Sugawara Editor)', vol. 60 of *Semiconductors and Semimetals* (Academic Press, New York, 1999) ISBN: 0127521690

3) "Optical Characterization of Quantum Dots", Kohki Mukai, and Mitsuru Sugawara,

Chapter 4 in 'Self-Assembled InGaAs/GaAs Quantum Dots (M. Sugawara Editor)', vol. 60 of *Semiconductors and Semimetals* (Academic Press, New York, 1999) ISBN: 0127521690

4) "Phonon Bottleneck Effect in Quantum Dots", Kohki Mukai, and Mitsuru Sugawara,

Chapter 5 in 'Self-Assembled InGaAs/GaAs Quantum Dots (M. Sugawara Editor)', vol. 60 of *Semiconductors and Semimetals* (Academic Press, New York, 1999) ISBN: 0127521690

Acknowledgements

The author is sincerely indebted to his supervisor, Professor Shigeo Fujita, and co-supervisor, Professor Susumu Noda, and Professor Masao Kitano, Department of Electronic Science and Engineering, Kyoto University for their guidance and ample suggestions.

The author wishes to express sincere gratitude to managers at Fujitsu Laboratories, Dr. Hajime Ishikawa, Dr. Teruo Sakurai (at present, in Femtosecond Technology Research Association), Dr. Hajime Imai, Dr. Shigenobu Yamakoshi (at present, in Fujitsu Quantum Devices Ltd.), Dr. Hiroshi Ishikawa, Dr. Kazuo Nakajima (at present, in Tohoku University), Dr. Susumu Yamazaki, and Dr. Mitsuru Sugawara, for their support and hearty encouragement.

The author deeply acknowledges his colleagues at Fujitsu Laboratories, Mr. Nobuyuki Ohtsuka, Mr. Yoshiaki Nakata and Dr. Hajime Shoji, for significant technical support and fruitful discussion. The author is grateful to Mr. Koji Ohtsubo for his technical support in the experiments on laser diodes, and to Mr. Yoshiharu Kinoue for his assistance in photoluminescence measurements.

Finally, this thesis is dedicated to Ms. Sachiko Mukai, the wife of the author, who has given her invaluable support and continuous encouragement to the author during the course of this work.